Examination of Creatine Deposits and Environs in TgCRND8 Mouse Brain by Raman and FTIR Microspectroscopy

By

Avid Khamenehfar

A thesis submitted to
The Faculty of Graduate Studies
In partial fulfilment of
The requirements for the degree of

MASTER OF SCIENCE

Department of Chemistry
Faculty of Science
University of Manitoba
Winnipeg, Manitoba

Abstract

Alzheimer Disease (AD) is a progressive neurodegenerative disorder characterized by memory loss and dementia. The pathological hallmarks of AD include deposits of β-Amyloid peptides, neurofibrillary tangles (NFT), activated microglial cells, synaptic dysfunction and neuronal death. Both energy metabolism and the function of creatine kinase are known to be affected in Alzheimer diseased brain and in cells exposed to the β-amyloid peptide. Fourier Transform infrared (FTIR) and Raman microspectroscopy imaging techniques have proved to be important methods for in situ investigation of tissue sections from a transgenic mouse model for AD. With synchrotron FTIR microscopy, extensive deposits of crystalline creatine (Cr) had been discovered by previous students in our lab. Deposits were in hippocampal tissue of TgCRND8 mice, an AD model expressing doubly mutant (K670N/M671L and V717F) amyloid precursor protein. These deposits increased in size and number with age, compared to nontransgenic littermates.

In this thesis, regions of hippocampus and caudate of 5 pairs of transgenic mice and their non-transgenic littermate controls were mapped using Raman and IR microspectroscopy to find clues to Cr origin in transgenic mouse brain. Raman spectra obtained at higher spatial resolution (1-2 μm) were used for better delineation of the Cr crystalline deposits and their environs.

Since Cr can be endogenously synthesized in liver and kidney and carried out through the blood brain barrier by Cr transporters to get into the brain, blood vessels in the hippocampus of transgenic mice were analyzed by IR and Raman. The analyzed maps

show no co-localization found between these Cr deposits and the blood vessels. This suggests that the Cr deposits were formed in the brain.

Serial sections from 14 month-old mouse, previously imaged by FTIR, were analyzed by Raman microscopy. Maps of two plaques known to contain creatine were analyzed for Cr (symmetric CN_3^+ band at 830 cm^{-1}), lipid (CH_2 deformation band at 1440 cm^{-1}), and amyloid plaque (antiparallel β-sheet protein at 1670 cm^{-1}). No specific association between Cr deposits and either Aβ plaques or lipid membrane was detected. The maps were analyzed for other spectral markers such as sphingomyelin (CN^+ stretching mode at 730 cm^{-1}), nucleic acids (PO_2 symmetric band of DNA and RNA at 790, 1085 cm^{-1}; and a distinct band corresponding to RNA at 920 cm^{-1}), phospholipids (PO_2 symmetric band of phospholipids at 860, 1098 cm^{-1}; =CH bending of unsaturated lipid at 980 cm^{-1}) and amino acids mostly phenylalanine (distinct bands correspond to phenylalanine at 930, 1003 cm^{-1}; C=C deformation of phenylalanine 1590 cm^{-1}). No association was identified between these biochemical signatures and Cr deposits.

The known polarization dependence of some vibrational modes of Cr was used to estimate Cr crystal form, orientation and dimension. Processed IR images of pure Cr monohydrate crystal and of Cr deposits in brain tissue were acquired using a polarizer at settings from 0° to 180°. Analysis showed that the Cr streaks were formed as single crystals and not multiple microcrystalline deposits.

These results along with lack of any specific association between Cr deposits and any other biochemical signatures, indicate that Cr crystals were formed after snap-freezing and desiccation of brain tissue. Therefore, it can be speculated that Cr might be exist in solution form in vivo.

Acknowledgments

First and foremost, I would like to thank God for the knowledge and strength and guidance He provides me daily. I could not have accomlplished this without Him.

To my supervisor Prof. Kathleen M. Gough, thank you for encouragement and support. You saw my potential and believed in and supported me, and I thank you for that.

To my committee members, Dr. Mazdak Khajehpour and Dr. Melanie Martin. Your encourgment and advice were really important.

Thanks to all in our research group and Department of Chemistry.

Thank you also to my funding supports; University of Manitoba Graduate Fellowship (UMGF), Manitoba Graduate Scholarship (MGS), Alzheimer's Society of Manitoba Graduate Fellowship, McCrorrie-West Family Fellowship for Alzheimer Research, CIHR training Award, International Graduate Scholarship, and several awards and scholarships from Department of Chemistry.

Last but mostly important, special thanks to my mother and father. You are my shining light and inspiration. Thank you for being such amazing role models, and for encouraging me to always reach for the stars. I could not have done this without your support and encourage. Thanks my beloved brothers. Special thanks to my brother, Farbod. Your encouragemnet and support were really valuable.

Contents

List of Tables

List of Figures

List of Presentations

1. Faraz Khorasani, F., Khamenehfar, A., & Gough, K. M. Computational, FTIR and Raman study of Oriented Creatine Crystals in Brain Tissue from Alzheimer Disease Mouse Model. *Spec 2010*, Manchester, UK, June 28, 2010.

2. Khamenehfar, A., Faraz Khorasani, F., Kastyak, M., & Gough, K. M. FTIR and Raman Imaging Of Brain Tissue from Transgenic Mouse Models. *Manitoba Neuroscinece Network*, Winnipeg, June 14, 2010.

3. Isenor, M., Khamenehfar, A., Faraz Khorasani, F., Kastyak, M., Stitt, D., & Gough, K. M. FTIR and Raman Imaging of Biological Materials. *Graduate Student Poster Presentation*, University of Manitoba, May 25, 2010.

4. Khamenehfar, A., Szeghalmi, A., Del Bigio, M., Westaway, D., Julian, R., & Gough, K. M. Examination of Creatine Deposits and Environs in Brain Tissue from TgCRND8 Mice by Raman and FTIR Spectromicroscopy, *Health Science Graduate Students Association (HSGSA)*, Winnipeg, June 01-03, 2009.

5. Khamenehfar, A., Szeghalmi, A., Del Bigio, M.,& Gough, K. M. Examination of Creatine Deposits and Environs in Brain Tissue from TgCRND8 Mice by Raman and FTIR Microscopy, Federation of Analytical Chemistry and Spectroscopy Societies, *FACSS 2008*, Reno-NV, Sept 29, 2008.

6. Khamenehfar, A., Szeghalmi, A., Del Bigio, M., Westaway, D., Julian, R., & Gough, K.M. Raman Microscopy and Synchrotron FT IR Spectromicroscopy of Focally Elevated Creatine in Brain Tissue from AD Mice, *54th International Conference on Analytical Sciences and Spectroscopy (ICASS 2008)*, Montreal, August 06, 2008.

7. Khamenehfar, A., Gajjeraman, S., Del Bigio, M., Westaway, D., Julian, R., & Gough, K. M . Evaluation of Creatine Deposits in Brain Tissue of TgCRND8 Mouse Model of Alzheimer's Disease By Raman Microscopy and Synchrotron FT IR Spectromicroscopy, *CLS conference*, Saskatoon, June 11, 2008.

8. Khamenehfar, A., Del Bigio, M. R., Westaway, D., & Gough, K. M. Raman microscopy and infrared spectromicroscopy of focally elevated Creatine in brain tissue from Amyloid Precursor Protein (APP) transgenic mice, *91st Canadian Chemistry Conference (CSC2008)*, Edmonton–Canada, May 27, 2008.

List of Abbreviations

AD.....Alzheimer disease
ADP.....adenosine diphosphate
AGAT .....L-arginine: glycine amidinotransferase
ApoE .....apolipoprotein E
APP .....amyloid precursor protein
ATP.....adenosine triphosphate
Aβ..... amyloid β
BACE-1……beta-site amyloid precursor protein cleaving enzyme
BB-CK…….....cytosolic brain-type creatine kinase
CA ..... Cornu Ammonis
CK.....Creatine kinase
Cr.....Creatine
CRT..... Creatine transporter
DNA……...deoxyribonucleic acid
FPA ..... Focal plane-array
FT.....Fourier transform
GAA.....guanidine acetic acid
GAMT.....S-adenosyl-L-methionine:N-guanidinoacetate methyltransferase
IR..... Infrared
MCT.....mercury/cadmium telluride
MRS .....magnetic resonance spectroscopy
NFT..... neurofibrillary tangle
OCT.....Optimal Cutting Temperature
PS1 .....presenilin 1

PS2 .....presenilin 2

PCr ..... phosphocreatine

ROS..... reactive oxidizing species

RNA…….ribonucleic acid

uMt-CK……ubiquitous mitochondrial creatine kinase

Chapter 1

Introduction

1.1 Goals and objectives

The spectral signature of creatine (Cr) deposits was discovered in some of the IR plaque maps in the brains of transgenic mice (Rak, 2007; Gallant, 2007). The first publication reported the *in situ* detection of focally elevated Cr deposits in post mortem AD brain tissue and in Tg mouse brain (Gallant et al, 2006). The Cr deposits are sometimes found in the most aged control mice, but are fewer and much smaller compared to those observed in Tg mouse brain. The number and size of Cr deposits in hippocampus appear to increase with age (Kuzyk et al, 2010). The focally-elevated Cr deposits had not been previously reported before its discovery by Dr. Gough's research group (Rak, 2007; Gallant et al, 2006).

The goal of research in this thesis is to explore why more Cr found in transgenic mouse brain. In this project, I was trying to find clues to the origin of Cr in transgenic mouse brain by IR and Raman microspectroscopy. As the creatine deposits were identi-

fied in frozen and desiccated brain tissue, it was important to know whether these creatine crystals were formed after snap freezing and at desiccating of brain tissue.

Since Cr can be endogenously synthesized in the liver and kidney and carried out through the blood brain barrier (BBB) by Cr transporters (CrT) to get into the brain, blood vessels in the hippocampus of transgenic mice were analyzed by IR and Raman to understand whether any co-localization could be found between these Cr deposits and the blood vessels, alternating the creatine might be synthesized by microglial cells in brain tissue.

In this work, the regions of hippocampus and caudate of 5 pairs of TgCRND8 or Tg19959 (transgenic mice with the same mutations but maintained on a different genetic background) and their littermate controls were mapped using Raman and IR Microspectroscopy. After data collection, the results were analysed to determine whether any other biochemical signatures could be identified as being localized with the Cr deposits.

To investigate whether Cr deposits distributed ubiquitously in brain tissue, the caudate of Tg and non-Tg mice at different ages were IR mapped.

It was discovered by Veena Agrawal (a summer student in Dr. Gough's group, 2007-2008) that creatine spectra taken by synchrotron FTIR Microspectroscopy gave different spectra for various deposits. Spectra of pure Cr crystal were examined with polarized synchrotron light, and with thermal source FTIR and FPA, with polarizer to establish the oriented Cr spectral profiles. Since the polarized light could reveal Cr crystal orientation, FPA-FTIR maps of Cr deposits in caudate and hippocampus of 14 month-old TgCRND8 mouse were recorded, using a polarizer setting from 0° to 180°, and analyzed to estimate the form, orientation and dimension of crystalline Cr deposits. These IR maps were proc-

essed at 1305 cm^{-1} and 1405 cm^{-1} as these peaks exhibit extreme polarization effects and have less overlap with tissue bands compared to other Cr peaks. A combined experimental and theoretical study (in collaboration with Fatemeh Farazkhorasani, another graduate student in Dr. Gough's group) was undertaken to better understand Cr crystal structure and orientation. These theoretical calculations gave both vibrational modes and polarization information to enable a better interpretation of the Cr spectra.

Two imaging techniques, FTIR and Raman microscopy were used to investigate Cr deposits and surrounding tissue. FTIR and Raman Microscopy are compatible, that means the same section can be mapped by FTIR and then by Raman, repeatedly. The Raman spectra can be obtained at higher spatial resolution (1-2 μm for Raman compared to 5-10 μm for FTIR). These techniques have some advantages compared to other standard visualization techniques. For instance, staining methods, commonly used to study tissue sections, involve various solvent treatments; therefore, small soluble molecules like Cr would not be detected because of being washed away. Sample preparation for both IR and Raman methods involves snap freezing of tissue excised at time of animal sacrifice, cryosectioning and then desiccation of the sections; therefore, water is the only component removed, and no new components are added. These techniques are also non-destructive (note that illumination with infrared or visible light at very low power does not damage tissue), thus the sections remain suitable for further analysis such as X-ray fluorescence imaging (XRF) or immunostaining.

With discovery of Cr, the question remains whether detected Cr deposits have neuroprotective or neurotoxic effect in AD.

1.2 Previous work from this lab

Work completed by other members of Dr. Gough's lab is briefly reviewed here, followed by a description of AD, pathological hallmarks and the disease mechanisms. The role of inflammation and the possible connection to creatine is then described in more detail.

The research in the field of Alzheimer disease has been ongoing in Dr. Gough's group since 1999. The first studies on non-demented and Alzheimer's diseased (AD) autopsy human brain were followed by studies on TgCRND8 and littermate non-transgenic mouse brain sections with IR microspectroscopic mapping to evaluate β-Amyloid plaques in the tissue (Rak et al, 2007; Gallant et al, 2006; Ogg, 2002). TgCRND8, a transgenic mouse model of Alzheimer disease expressing a double mutant human amyloid protein precursor (APP_{695}), with the "Swedish" mutation (K670N/M671L) and the "Indiana" mutation (V717F), presents early amyloid plaque loads appearing at 3 months old (Woodhouse 2009; Herringa et al, 2008; Chishti 2001).

From the published results of this research group (Rak et al, 2007; Gallant et al, 2006), it has been illustrated that Fourier Transform Infrared and Raman Microscopy can be used to identify dense-core plaques, diffuse plaques and the surrounding elevated lipids in snap-frozen TgCRND8 mouse brain tissue sections (Rak et al, 2007). In using FTIR microscopy to analyze plaques, a spectral anomaly was noted in many infrared maps. This was determined later to be due to crystalline creatine (Cr) deposits in the brain tissue of TgCRND8 mouse. Cr is a small molecule found in tissue with high energy demands including the brain, and plays an important role in cellular energetic. The role of

the Cr/phosphocreatine (PCr) system in energy storage has been well established (Andres et al, 2008).

The deposits of Cr in brain tissue had previously escaped attention. The first publication reported the *in situ* detection of focally elevated Cr deposits in post mortem AD brain tissue and in Tg mouse brain, by infrared (IR) and Raman microspectroscopy (Gallant et al, 2006). It was shown that creatine was found more abundantly in hippocampus of mouse brain compared to their non-transgenic littermates and increased with age (Kuzyk et al, 2010).

1.3 Alzheimer Disease

Alzheimer Disease is the most common form of dementia; it is characterized by progressive deterioration of memory and higher cortical function that ultimately results in total degradation of memory and intellectual activities (Patterson et al, 2008; Apostolova et al, 2007). The major neuropathological changes in the brains of AD patients are neuronal death, activated microglial cells, and the presence of abnormal intra- and extra-cellular protein aggregates, known as neurofibrillary tangles and β-Amyloid plaques, respectively (Querfurth et al, 2010; Jakob-Roetne, 2009; Nelson et al, 2009). These histopathological lesions, prerequisites for a confirmed clinical diagnosis of AD after death, are found throughout the brain, usually more common in the hippocampus, a centre to transfer memory from short term to long term, and the cerebral cortex, which is involved in reasoning, memory, language and other important thought processing (Mattson et al, 2004). These brain regions are reduced in size in AD patients as the result of degeneration of synapses and neuronal death (Takahashi et al, 2010).

Unfortunately, many people all around the world suffer from this harmful disease and it is a huge drain on health care resources. Despite the progress made in AD research in the last decades, no reliable, effective long-term treatments are yet available (Panza et al, 2010).

Dr. Alois Alzheimer (1864–1915), who first described the disease, was a German psychiatrist and pathologist. In 1906, he carried out an autopsy on the brain of a 56-year-old woman who died after several years of progressive mental deterioration characterized by confusion and memory loss. In her cerebral cortex, he found strange bundles in neurons, which he termed neurofibrillary tangles, and accumulations of cellular debris around the neurons, which he termed senile plaques (Baek et al, 2002). He presented his findings at a meeting in late 1906, and published them in 1907, speculating that the tangles and plaques were responsible for patient's dementia (Herz, 2007).

Generally, the prevalence of AD increases with age, affecting approximately 1 to 3% of the population in the 6^{th} decade of life, 3 to 12 % of the population between 70 and 80 years, and up to 25 to 35 % older than 85 years (Walsh et al, 2004). It is estimated that 300,000 Canadians over 65 are affected by this neurodegenerative disorder and the number of people with AD is expected to grow due to the aging population (www.alzheimersociety.com). According to the World Health Organization, approximately 18 million people are currently living with Alzheimer disease worldwide. This number is predicted to become almost double by 2025 (www.sciencedaily.com).

1.4 Genetics of AD and risk factors

There are two main types of Alzheimer disease: sporadic or late-onset Alzheimer Disease (LOAD), and Familial Alzheimer Disease (FAD) or early-onset, the latter of which accounts for only about 5 percent of cases.

FAD is due to inherited genetic mutations, some of which include mutation in the presenilin 1 (PS-1) gene on chromosome 14, the presenilin 2 (PS-2) gene on chromosome 1, and the APP gene on chromosome 21 (Bettens et al, 2010; Shepherd et al, 2009; Herz, 2007). People with trisomy 21 (Down Syndrome) who have an extra gene copy develop AD symptoms at an early age (Bettens et al, 2010; Herz 2007; Selkoe et al, 2002).

Sporadic AD is a multifactorial disease, while its symptoms are similar to FAD. In addition to genetic abnormalities, several environmental factors may increase the risk of AD (Stampfer et al, 2006). It has been suggested by in vivo studies that history of head trauma and high cholesterol may increase the risk of occurrence of AD (Mattson et al, 2003; Lee et al, 2002). Researchers are investigating whether diseases that affect the heart and vascular (blood vessel) system may increase the risk of Alzheimer disease (Pereira et al, 2005). These conditions include high blood pressure, unhealthy cholesterol levels, and diabetes. There is some evidence that controlling these conditions may help prevent Alzheimer disease (Pereira et al, 2005). Insulin resistance may also be a risk factor for the development of AD (Iwata et al, 2004; Watson et al, 2003). Generally, insulin appears important for learning and memory. It has been reported that insulin can inhibit neurofibrilary tangle formation, stimulate α-secretase (Solano et al, 2000), and reduce the intracellular pool of Aβ in transgenic mouse brain (Zhao et al, 2004; Gasparani et al, 2001).

The causes of Aβ aggregation in sporadic cases of AD are not understood, but may include age-related increases in oxidative stress, impaired energy metabolism and disturbed ion homeostasis (Jakob-Roetne, 2009).

The mice studied in this thesis are TgCRND8, a transgenic mouse model of Alzheimer disease expressing a double mutated human amyloid protein precursor (APP_{695}), with the "Swedish" mutation (K670N/M671L) and the "Indiana" mutation (V717F). This transgenic mouse presents early amyloid plaque loads appearing at 3 month-old (Woodhouse 2009; Herringa et al, 2008; Chishti 2001). (See section 3.1 for more information)

1.5 Histopathological hallmarks of AD

Macroscopically, brain from individuals with AD shows a reduction of volume and enlarging of the ventricles, due to a loss of grey matter. The histopathological hallmarks of AD include Aβ plaques, neurofibrillary tangles, neuron and synaptic loss, activated glial cells, and deposition of Aβ in the small blood vessels (Congophil angiopathy) (Apostolova et al, 2007).

1.5.1 Amyloid beta plaques

In 1964, Aβ was identified in a fibrillar form within the senile plaques by electron microscopy (Terry, 1964). Since Aβ was identified as an important constituent of the amyloid-β aggregations that characterise the AD brain, this small peptide has received intense research focus as an important factor that contributes directly to development of the disease (Crouch et al, 2008). Aβ peptide is a natural product and is present in the brain and cerebrospinal fluid (CSF) of normal humans throughout life (Walsh et al, 2000).

Aβ is produced by proteolytic cleavage of the Amyloid Precursor Protein (APP) by β- and γ-secretases, respectively (Nerelius et al, 2009). APP is a transmembrane protein, expressed in many tissues and concentrated in the synapses of neurons (Crouch et al, 2008). Its primary function is unknown, although it has been reported as a regulator of synapse formation. In humans, the gene for APP is located on chromosome 21. It can be up to 770 amino acids long, with three isoforms: APP 695, APP 751, and APP 770. APP can be cleaved by three protein secretases: α, β, and γ in two different ways (Walsh et al, 2007). The non-amyloidogenic pathway includes the cleavage of APP by α- and γ-secretases, respectivly, and prevents the generation of Aβ (Figure 1.1A). On the other hand, as illustrated in Figure 1.1B, the beta-site amyloid precursor protein cleaving enzyme (BACE-1) initiates Aβ generation and the amyloidogenic pathway. The proteolytic cleavage of α, β and γ-secretase results in the generation of a truncated non-amyloidogenic peptide (P3) which does not play any role in Alzheimer disease (Hartmann et al, 2007).

Senile plaques are composed of aggregates of 39-43 amino acid Aβ peptide (Wirths et al, 2008). The Aβ in length with 40 and 42 amino acids are the main components of plaques. Aβ40 accounts for 90% of the total Aβ; Aβ42 aggregates much faster than Aβ40 and is more neurotoxic (Waldo et al, 2008).

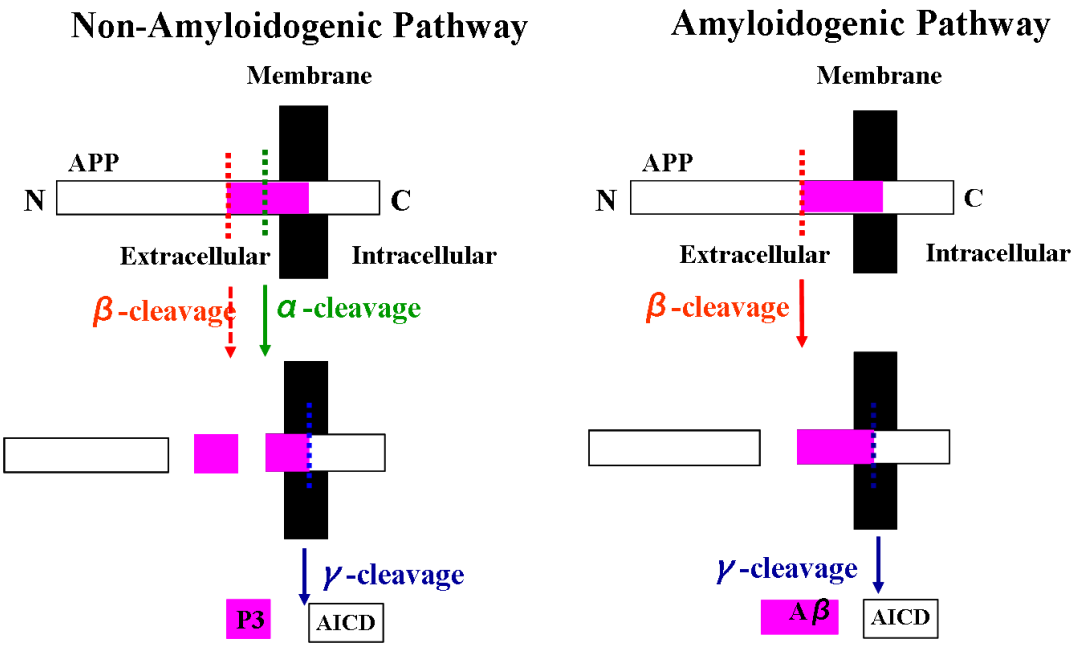

Figure 1.1: (A) NonAmyloidogenic and (B) amyloidogenic processing of APP by β-, α- and γ-secretase.

1.5.2 Neurofibrilary tangles

Neurofibrillary tangles are insoluble twisted fibers found inside the neurons. They consist of a protein called tau, which forms part of a structure called a microtubule (Maccioni et al, 2010; Rankin et al, 2008; Bandyopadhay et al, 2007). In Alzheimer disease, the hyperphosphorylated tau protein reduces affinity for microtbules, and ultimately cause the microtubles structure collapse (Alonso et al, 2008) (See section 1.6.2 for more information).

1.5.3 Synaptic dysfunction and neuronal loss

Synaptic dysfunction is a very early event. It can happen before reduction of acetylcholine level, and continue with plaque and tangles formation (Apostolova et al, 2007; Tiraboschi, 2000). Synaptic dysfunction is evident before synapses and neurons are lost (Coleman et al, 2004). A 50% decrease in synapse-to-neuron ratio in AD suggests that many surviving neurons have lost their synaptic function prior to cell death (Coleman et al, 2004). So far the exact causes of synaptic loss have not been completely understood. In AD, synaptic density correlates inversely with soluble amyloid beta levels but not amyloid plaques (Mucke, 2000). The oligomeric Aβ forms are synaptotoxic and severely interfere with synaptic function in the long-term (Kayed, 2003).

The earliest reduction in neuronal counts has been observed in entorhinal cortex (EC) and later shows up in CA1 region of hippocampus. Neuronal loss is ubiquitous in advanced AD (West et al, 2004). Generally, the regions of brain tissue, where more than 50% of the neuronal population is severely affected, are entorhinal cortex, olfactory nucleus, hippocampus and temporal neocortex (Apostolova et al, 2007; Duyckaerts et al, 2003). Although it was believed that neuroinflammation can threaten neurons, some evidence suggests that neurons themselves are able to produce inflammatory mediators (Heneka et al, 2007; Simard et al, 2006). It has been reported that glia and neurons can synthesize nitric oxide (NO) and proxynitrite ($ONOO^-$) which can cause neuronal dysfunction and cell death in vitro and in vivo (Heneka et al, 2007).

1.5.4 Activated microglia

Microglia cells form around 10% of all cells in the nervous system. They represent the first line of defence against invading pathogens (Brent et al, 2010; Napoli et al, 2009; Benhardi et al, 2006; Conde 2006). Under the pathological situation in AD, these cells become activated, migrate and surround damaged neurons to fight against Aβ plaque aggregations (Combs et al, 2009; Fetler et al, 2005). They also undergo dramatic morphological changes (enlarged size and distorted shape) and release a variety of pro-inflammatory mediators including cytokines, and free radical species both of which are neurotoxic (Heneka et al, 2007; Mark et al, 2005). Along with microglia, astrocytes directly react and contribute to defence against Aβ plaque aggregation (Heneka et al, 2007). Although it is generally accepted that Aβ deposition is a potent glial activator, activation of microglia and astrocytes could be an early event in the disease, occurring even in the absence of insoluble Aβ aggregation (Nunomura et al, 2001). It has been reported that in 3 month old APP transgenic mice, both cognitive deficits and focal glial cytokine production has been observed well before Aβ plaque deposition (Heneka et al, 2005). It means at least at the beginning of the disease, the senile plaques do not cause glial activation, and the neuroprotective effect of glial cells is a response against small Aβ oligomers or protofibrils instead of senile plaques (Schlachetzki et al, 2009; White et al, 2005).

1.6 Disease mechanism

Having depicted the pathological hallmarks, hypotheses concerning the disease mechanism are described here.

1.6.1 Amyloid beta cascade hypothesis

For over a decade, the main argument of the "Amyloid Cascade Hypothesis" has maintained that accumulated Aβ is the principal cause leading to both sporadic and FAD (Pimplikar et al, 2009; Jakob-Roetne et al, 2009; Hardy et al, 1992; Selkoe, 1991). This hypothesis implies that non-fibrilar forms of Aβ, including small oligomers and protofibrils (PF), may be responsible for memory impairment in AD human patients and AD animal models (Cerpa et al, 2008; Walsh et al, 2007; Klein WL, 2004). The insoluble amyloid fibril deposits of Aβ were thought for a long time to contribute to the progression of dementia of AD (Hardy et al, 2002). However, a poor correlation was obtained between the insoluble fibrilar Aβ aggregation with the progression of AD (Bharadwaj et al, 2009; Pierrot et al, 2008; Cerpa et al, 2008; Walsh et al, 2007). In contrast, soluble Aβ oligomers have been found in the brain of AD patients (Yu et al, 2009), and the loss of synapses and cognitive perception seems to correlate better with soluble oligomers of Aβ 42. Increasing evidence suggests that these early stage oligomers of Aβ may be much more important in AD (Jakob-Roetne et al, 2009). The levels of Aβ oligomers and its affect on altered synaptic morphology were shown to be increased in hippocampus and cortex of AD patients in the absence of amyloid plaques and NFT as well (Tkahashi et al, 2004; Funato et al, 1999). These results suggest that accumulation of Aβ oligomers occurs very early in the disease process and is linked to memory failure in AD (Kawarabayashi et al, 2004).

The Aβ cascade hypothesis also considers that amyloid plaques are formed by Aβ42 rather than Aβ40 (Jan et al, 2008; D'Andrea et al, 2001). Aβ42 can develop dense-cored

plaques, diffuse plaques and vascular amyloid deposits, while Aβ40 fail to do so (Jan et al, 2008; McGowan et al, 2006).

Amyloid pathology in AD may occur as a result of increased intracellular Aβ levels. Neurons in the hippocampus and cortex from the brain of Down's syndrome patients showed strong intraneuronal Aβ42 immunoreactivity, which declined with the deposition of extracellular Aβ plaques (Busciglio et al, 2002). It has also been demonstrated that Aβ plaques are dynamic structures; Aβ can be internalized again, thereby increasing the intraneuronal pool of Aβ42, which in turn increases the neurotoxic intracellular events (Friedrich et al, 2010; Christensen et al, 2009; Billings et al, 2008; Wirths et al, 2004).

1.6.2 Tau hypothesis

The hyperphosphorylated forms of tau protein were discovered during the 1980s (Kosik et al, 1986). Tau is a microtubule-associated protein that stabilizes the cytoskeleton, constantly undergoing phosphorylation and dephosphorylation to achieve this (Alonso et al, 2008; Rankin et al, 2008; Stoothoff et al, 2005). In adult human brain, six isoforms of tau ranging from 352 to 441 amino acids are present (Lucas et al, 2001). In AD, tau neurotoxicity is, at least in part, due to hyperphosphorylation of all six isoforms leading to reduced microtubule binding, destabilization of the cytoskeleton, reduced axonal transport (Stoothoff et al, 2005) and insoluble intracellular fibril formation (Maccioni et al, 2010; Alonso et al, 2008; Kobayashi et al, 2003). As a result of neuronal death, oligomeric forms and tau filaments are released to the extracellular environment, and contribute to activation of microglial cells leading to progressive neuronal degeneration (Maccioni et al, 2010; Gong et al, 2010; Ramos et al, 2006).

According to the amyloid cascade hypothesis, Aβ aggregation causes inflammation that is a part of the pathology of AD, and leads to hyperphosphorylation of tau protein. It has been shown that in the absence of fibrils, small oligomers stimulate tau phosphorylation in mature cultures of hippocampal neurons; therefore, Aβ oligomer activity may be directly linked to tau hyperphosphorylation in AD pathology (De Felice et al, 2008). NFTs are reported to lead to dementia in the absence of amyloid plaques (Ramos et al, 2006). The precise molecular mechanism of such toxicity is not clear, as tau is modified by a series of complex methods, such as hyperphosphorylation, glycosylation, and nitration (Alonso et al, 2008). The relative toxic effect of NFTs to cells is still controversial.

According to the dual pathway hypothesis, Aβ aggregation and tau hyperphosphorylation can be linked by separate mechanisms; resulting in synaptic dysfunction and neuronal death (Small et al, 2008).

1.6.3 Oxidative stress

Currently it is believed that oxidative stress plays a significant role in AD pathogenesis (Ansari et al, 2010). A considerable number of oxidative stress markers are found in the brain of AD patients associated with plaque aggregation and NFT (Martinez et al, 2010; Butterfield et al, 2001). Indirect evidence of oxidative stress in AD brains comes from studies of AD patients treated with antioxidant like Vitamin E, and 17-Estradiol, phenolic compound, display a postponement in progression of disease (Uttara et al, 2009; Pratico, et al, 2008; Green et al, 2000). However, from another publication, it was reprted that an antioxidant diet reducing oxidized end products could not reduce plaque aggregation and cognitive deficite in APP mice (Siedlak et al, 2009).

Aβ peptides have been reported as a source of oxidative stress in this neurodegenerative disorder (Nunomura et al, 2010). H_2O_2 is directly generated during the process of Aβ aggregation (Koppenal et al, 2004). In the presence of Fe^{2+}, it can generate $OH^{\cdot}$ (Fenton reaction) (Uttara et al, 2009) and cause oxidative stress, which in turn may induce Aβ production (Jackob-Roetne et al, 2009).

This cycle of oxidative stress and Aβ accumulation eventually leads to neurodegeneration (Xu et al, 2008). Oxidative stress can induce amyloidogenic processing of βAPP, resulting in production and aggregation of Aβ as a result of the increased activity of β-secretase (Quiroz-Baeza et al, 2009).

Several lines of evidence suggest that synaptic dysfunction induced by Aβ occurs through oxidative stress mediated mechanisms (De Felice et al, 2008). It is also known that mitochondrial dysfunction often leads to excessive generation of free radicals and subsequent oxidative damage (Pereira et al, 2005). Generally, oxygen takes part in glucose break down in mitochondria through oxidative phosphorylation and generates ATP. Any mutation in mitochondrial DNA leads to impaired ATP generation, preventing oxidative phosphorylation (Mancuso et al, 2008; Guido et al, 2000). Neurons require more oxygen and glucose consumption to generate ATP pool for normal functioning of brain; therefore, they are more susceptible toward oxygen overload and generation of free radicals (Pereira et al, 2005; Lepoirve et al, 1994). In the normal situation, 1-2% of consumed O_2 is converted to reactive oxygen species (ROS) but in aged brain this number goes up because of low regenerative capacity of aged brain (Pereira et al, 2005).

Some important Reactive Oxygen Species (ROS) are hydrogen peroxide (H_2O_2), highly reactive hydroxyl radicals ($OH^{\cdot}$), and nitric oxide radical ($NO^{\cdot}$). $OH^{\cdot}$ can react

with Aβ to further promote Aβ aggregation. As mentioned above, damaged mitochondria and activated microglia act as reservoir of ROS. Free radicals have been reported to contribute to neuronal loss in AD (Uttara et al, 2009). The brain is also rich in molecules such as unsaturated fatty acids that are susceptible to oxidative damage. Double bonds of unsaturated fatty acids are vulnerable to attack by free radicals and ultimately cause chain reactions to damage neighbouring unsaturated fatty acids (Butterfield et al, 2002). Oxidative overload in neuronal microenvironment causes oxidation of lipids, and proteins. The generation of lipid peroxidation products and the lipoperoxidation of membranes are associated with amyloid plaques in Tg mice and there is a correlation between amyloid plaques and lipid peroxidation in AD (Uttara et al, 2009). Antioxidant therapy has been examined in scavenging ROS to postpone disease progress (Pratico, et al, 2008). However, it has not been shown to prevent neuronal degeneration.

1.6.4 Amyloid beta toxicity

Numerous studies show that Aβ42 has a neurotoxic effect (Gotz et al, 2008). Amyloid beta is postulated to cause cognitive deficits and neuronal damage, mitochondrial dysfunction, increasing inflammation in the brain, the production of the reactive oxygen species (ROS), interruption of synaptic transmission, and intracellular calcium dyshomeostasis (Querfurth et al, 2010; Nerelius et al, 2009; Kawahara et al, 2009; Tanzi et al, 2005; Reddy et al, 2005).

Generally, Aβ readily interacts with other Aβ molecules to progressively form a wide range of oligomers and soluble aggregates (Nerelius et al, 2009). Continued amyloidogenesis gives rise to the high molecular weight insoluble Aβ fibrils. Initial AD research

focused on extracellular Aβ fibrils. Although it is still not very clear whether the Aβ oligomers or fibrils are the most important toxic species, it has been shown that Aβ fibrils induce extensive dystrophic neurites, but only modest neuronal death. On the other hand, the Aβ oligomers produced extensive neuronal death (Nerelius et al, 2009; Waldo et al, 2008; Walsh et al, 2007). Recently, more attention has been focused on oligomers (Walsh et al, 2005). The soluble Aβ oligomers have been shown to inhibit hippocampal long term potentiation and cause memory loss and synaptic dysfunction when injected into rat brain (Cerpa et al, 2009).

On the basis of Aβ hypothesis, while extracellular amyloid aggregation is one of the most important pathological hallmarks of AD, intracellular Aβ may be even more important than extracellular Aβ (Friedrich et al, 2010; Nunomura et al, 2009). Intraneuronal Aβ accumulation has been reported to commonly precede extracellular Aβ deposition in several familial AD-related mutant PS-1 transgenic mice (Ohyagi et al, 2008). It has also been demonstrated that as Aβ plaques are dynamic structures, Aβ can be internalized again, thereby increasing the intraneuronal pool of Aβ42, which ultimately results in various pathogenic mechanisms such as mitochondrial toxicity and synaptic damage (Ohyagi et al, 2008; Wirths et al, 2004). While prevention of Aβ production and anti-Aβ immunotherapies are likely to attenuate both intraneuronal and extracellular Aβ toxicity, more specific anti-intraneuronal Aβ therapies may be useful (Ohyagi et al, 2008).

Some studies demonstrate that lipids, surrounding the Aβ plaque aggregate, can revert aggregated Aβ fibrils into neurotoxic protofibrils (Martins et al, 2008). Injection of such reverted protofibrils into mice reveals the same memory impairment as protofibrils

formed from monomeric Aβ (Martins et al, 2008). It means that the step from protofibril to fibril formation can be reversible.

1.6.5 Inflammation in AD

The involvement of inflammatory processes in the pathogenesis of AD is shown from studies indicating that use of non-steroidal anti-inflammatory dugs significantly reduces the risk of disease (Moore et al, 2010; Szekely et al, 2010; Stewart et al, 1997). The inflammatory reaction is the first line of protection against Aβ aggregation, but an excessive inflammatory response can be gradually harmful (Schlachetzki et al, 2009). Generally, the inflammatory process involves microglia cells, and astrocytes. The presence of activated microglia surrounding Aβ aggregation supports the postulated role of these cells in the clearance of amyloid aggregation (Rogers et al, 2002). Microglia activation in AD was discovered two decades ago, and activated microglia are generally believed to be involved in AD-associated inflammatory response (Heneka et al, 2007), although the precise role of microglial cells in AD pathogenesis remains to be calrify.

Before the development of clinical symptoms for AD, microglia becomes activated by Aβ possibly in order to prevent plaque formation or restrict plaque growth (Rodriguez et al, 2010; Schlachetzki et al, 2009). Activation of microglia results in enlarged size, and increased secretion of cytokines, reactive oxygen intermediates and nitric oxide, all of which contribute to neuronal dysfunction and cell death. As the disease progress, microglia contribute to altered calcium homeostasis, increased production of ROS, neuritic and synaptic dysfunction caused by oxidative stress, and possibly generation of tangles, ultimately causing neuronal death (Butterfield et al, 2002; Selkoe, 2001). Over the following

years, more plaques and NFT are generated, and the patient develops severe dementia (Schlachetzki et al, 2009).

Although the role of astrocytes in the inflammatory process associated with neurodegenerative disorders is not very clear, it is known that activated astrocytes produce high levels of pro-inflammatory cytokines, ROS, similar to and overlapping with those produced by microglia (Bernhardi et al, 2007). The degree of inflammation has been reported to correlate with brain atrophy and the severity of dementia in early AD (Parachikova et al, 2006; Cagin et al, 2002). Activated microglia can be found very early in disease progression. In the APP/PS1 AD transgenic mouse model, microglial activation has been observed at 4-6 months of age, along with the deposition of amyloid plaques (Ruan et al, 2009; Wirths et al, 2008). In the single APP mouse model, microglial activation has been reported before the onset of amyloid deposition, possibly in order to fight against oligomers (Heneka et al, 2005).

1.7 Creatine/Phosphocreatine system

Since elevated Cr has been found in Tg mouse model and it is the focus of this study, its role in the body is described here.

The creatine (N-aminoiminomethyl-N-methylglycine) /phosphocreatine system plays a crucial role in energy metabolism in tissue with high demand for energy, such as muscles and brain. This shuttle system can maintain ATP/ADP homeostasis catalyzed by creatine kinase (CK) as shown in the following reversible reaction (Figure 1.2) to transfer phosphate group from ATP to Cr, and form ADP and phosphorylcreatine (PCr) (Brosnan et al, 2007).

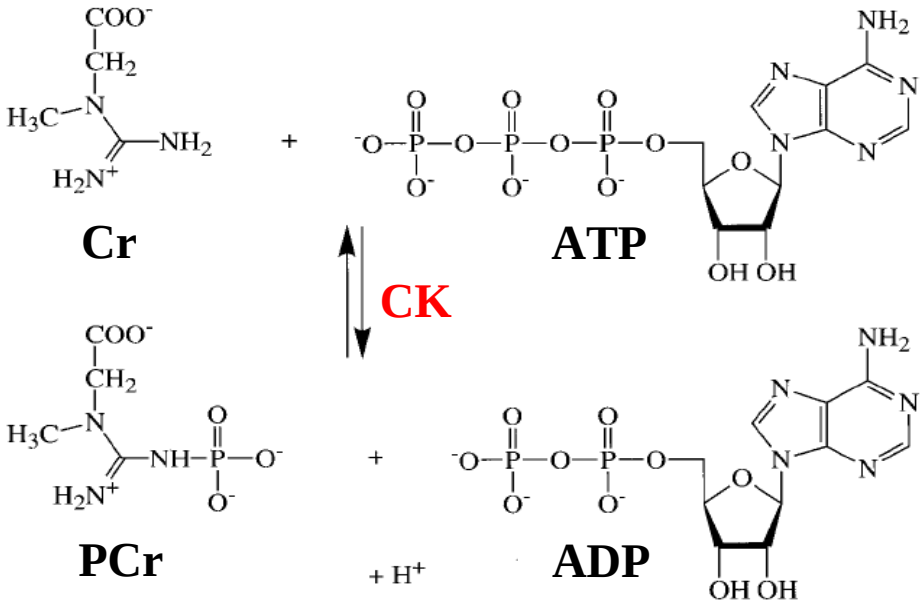

Figure 1.2: Cr/PCr shttle system

The major energy-consuming process in neuronal cells is the transport of ions by the Na^+/K^+-ATPase (Magistretti et al, 1999). It has been proven that the overall ATP level does not change significantly because it can be continuously regenerated from the large pools of PCr through the CK reversible reaction (Brosnan et al, 2007; Wallimann T, 1992). In brain, CK has been shown to be associated with ATP/ADP homeostasis, calcium homeostasis, and facilitation of glutamate uptake into vesicles (Andres et al, 2008; Brosnan ME, 2007). Two isoenzymes of CK are uMtCK, located in the mitochondrial intermembrane space, and BB-CK, cytosolic brain-type creatine kinase (Schlattner U, 2005). The creatine transporter (CRT) is also localized in the mitochondrial membrane, which means Cr/PCr can be found in mitochondria in addition to the cytosol.

Neuroprotective and antioxidant effects of Cr were recently reported (Adhihetty P, 2008; Nivaggioli B, 2007). Some studies have shown that Cr supplementation can sup-

port maintenance of mitochondrial function and preservation of ATP levels (Bruno et al, 2010; Adhihetty et al, 2008; Andres et al, 2008). Cr supplied from Cr supplementation is phosphorylated inside the neurons by the catalytic activity of CK, leading to an increasing PCr/ATP ratio, thus a higher energy charge in the cell. However, this procedure can not happen if CK is damaged by oxidative stress.

1.7.1 Creatine synthesis in the body

Creatine is a guanidine compound synthesized from the amino acids arginine, glycine and ornithine (Andres et al, 2008; Brosnan et al, 2007). Cr is taken up in diet containing fresh meat or fish. As illustrated in Figure 1.3, Cr can be endogenously synthesized in the kidney and liver by a two step synthesis involving the enzymes L:arginine glycine amidino transferase (AGAT), producing guanidine acetate (GAA) as an intermediate being transported between both sites through the bloodstream (Andres et al, 2008; Wyss et al, 2000), and S-adenosyl-L-methionine:N-guanidinoacetate methyltransferase (GAMT) to produce creatine in liver which is the main organ of endogenous Cr synthesis (Braissant et al, 2005).

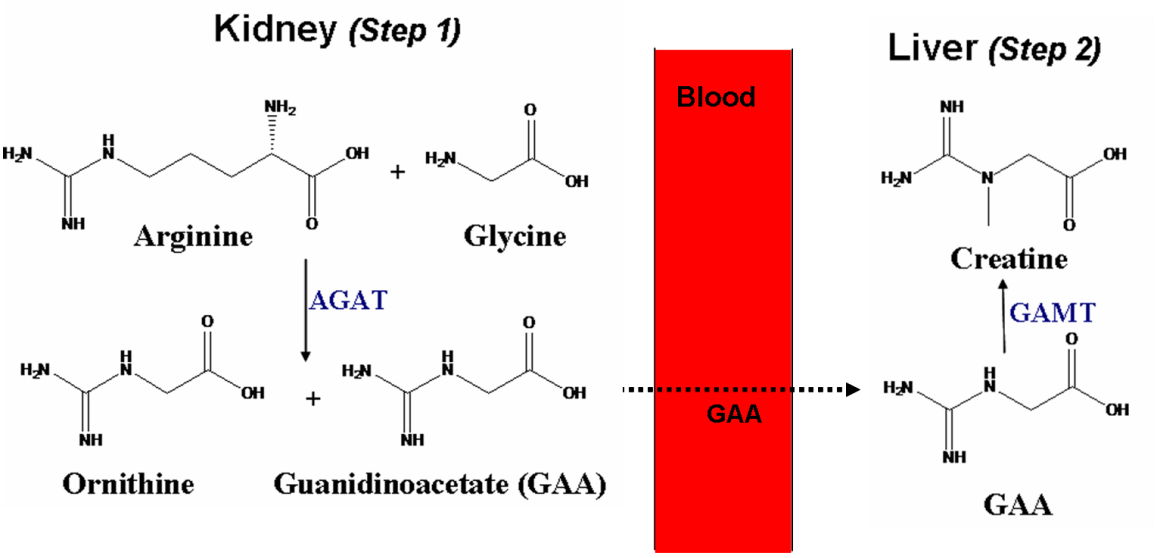

Figure 1.2: Synthesis of creatine. L-Arginine:glycine amidinotransferase **(**AGAT) catalyses the transfer of an amidino group from Arginine to Glycine to form ornithine and Guanidinoacetate (GAA) in kidney (step 1) and transfer GAA through the blood to liver. In the liver (step 2), Guanidinoacetate N-methyltransferase (GAMT) methylates GAA to produce Cr in liver and transfer it to the body by Creatine transporter (CRT).

To get into the brain, Cr has to be carried by CRT across the blood-brain barrier (BBB) and then it can be actively taken up from the extracellular fluid of the brain by cells that express CRT (Braissant et al, 2007; Ohtsuki et al, 2002). It has been reported that CRT is expressed in neurons and oligodendrocytes (Beard et al, 2010; Braissant et al, 2001). GAMT immunoreactivity is very strong in oligodendrocytes, moderate in astrocytes, and not detected in neurons (Urenjak et al, 1993). This leads to the conclusion that Cr in neurons is synthesized in part from glial cells surrounding the neurons, indicating possible transportation of Cr from glial cells to neurons (Beard et al, 2010; Tachkawa et al, 2004). An additional source of Cr synthesis is glial cells involving the AGAT and GAMT enzymes to produce Cr. CRT carries Cr and it is taken up by neurons to play a role in ATP/ADP homeostasis (Andres, 2008; Brewer, 2000).

1.7.2 Disturbed energy metabolism in AD

The energy impairment in diseased and elderly brain has been investigated during the last decade (Andres et al, 2008; Griffiths et al, 2008; Bürklen et al, 2006; Parihar et al, 2006). Mitochondrial dysfunction often leads to the excessive generation of free radicals and subsequent oxidative damage, which can contribute to the aging process (Mancuso et al, 2008; Lustbader et al, 2004). Studies of patients and transgenic mouse brain indicate that the Aβ-binding alcohol dehydrogenase (ABAD) interacts with Aβ in the mitochondria to increase free-radical generation in neurons (Lustbader et al, 2004). There is another hypothesis that the characteristic loss of synapses in AD arises in part from mitochondrial dysfunction (Pereira et al, 2005). It is reasonable that increased oxidative modification of brain proteins may disturb neuronal functions by decreasing activities of key metabolic enzymes and affecting cellular signalling systems (Uttara et al, 2009; Aksenov et al, 2000). Brain energy metabolism is characterized by high and fluctuating rates of ATP synthesis. A high level of CK, catalyzing the reversible transfer of the phosphate group of PCr to ADP in order to regenerate ATP, is reached in the brain. PCr/Cr/ATP levels are regulated by the enzyme CK.

Damage to the CK function may be an important part of a neurodegenerative pathway that leads to neuronal loss in the brain (Andres et al 2008; Bürklen et al, 2006; Aksenov et al, 2000). BB-CK has been shown to be significantly inactivated by oxidation in AD patients, and it is one of the biochemical markers of the Central Nervous System (CNS) cell damage in AD (Bürklen et al, 2006). A direct connection between AD and uMt-CK was discovered when it was shown that it can interact with the short cytoplasmic tail of APP family proteins, and affects the correct import of uMtCK into mitochondria and thus

would negatively interfere with cellular energetics (Li et al, 2005). It has been revealed that mice lacking both brain isozymes of CK show severely impaired spatial learning and reduced body weight (Streijger et al, 2005). The inactivation of PCr causes an increase in the level of Cr. It should be noted that the PCr is depleted at death, and Cr remains as the only existing form.

1.7.3 Focally elevated Cr deposits in AD brain tissue

Discovery of creatine deposits in the brains of transgenic mice raises many questions about its role in this neurodegenerative disorder. Decreased brain metabolism is always associated with AD (Andres et al, 2008; Parihar et al, 2006; Blass et al, 2002). The role of Cr/PCr system in energy metabolism has been recognized. Intracellularly, under normal energetic conditions, 2/3 of total Cr is in the form of PCr (Wallimann, 1994). During cellular energy stress, mitochondrial function is disrupted, and ATP levels are reduced (Mancuso et al, 2008; Casley et al, 2002). CK is very sensitive to oxidative stress; therefore, under this situation, oxidation of CK isoenzymes, BB-CK and uMtCK, could limit PCr formation, consequently reducing PCr/Cr ratio in vivo (Andres et al, 2008; Li et al, 2006). Some part of Cr is synthesized in microglial cells in brain. Under massive neuronal death, Cr trafficking between glial cells and neurons could be limited, because the uptake of Cr via CRT is associated with Na^+/ K^+ to transport into the neuron; ultimately, the result is accumulation of Cr in the extracelluar space gradually, that shows up as significant amounts of Cr released in the extracellular space (Straumann et al, 2005; Tachikawa et al, 2004). The other way that Cr can be released in the extracellular space can be leakage of Cr from dying neurons (Burklen et al, 2006).

As explained more in section (1.6.5), AD is accompanied by activated microglial cells (Moore 2010; Schlachetzki et al, 2009); therefore, inflammation and an increase in the number of glial cells could provide additional source of Cr because more Cr can be produced and released in the extracellular space.

In next chapters, IR and Raman microspectroscopic techniques, which were used in this work, are introduced, followed by description in more detail about results, discussion, conclusion, and future works.

Chapter 2

FTIR and Raman Spectromicroscopy

2.1 Fourier Transform Infrared Spectroscopy

Infrared spectrometers have been commercially available since the 1940s. With the advent of Fourier Transform Infrared spectroscopy, the time required to obtain good quality data has been shortened.

Infrared studies are based on the absorption of the electromagnetic radiation that lies between 1 and 1000 μm. This spectral range is sub-divided into three areas: near IR (1-2.5 μm), mid-IR (2.5-25 μm) and Far-IR (beyond 25 μm). The mid-IR region provides more information about the structures of compounds and is used to identify functional groups of organic compounds (Rouessac et al, 2007). For a molecule to be infrared active, the electric dipole moment must change during the vibration (Stuart, 2003). This technique is very suitable for biological investigation because many common biomolecules such as proteins, lipids, nucleic acids and carbonhydrates have characteristic and well-known vibrational fingerprints (Stuart, 2004; Dumas et al, 2003).

2.1.1 Principles of IR spectroscopy

In the classical model, when the frequency of specific vibration is equal to the frequency of IR radiation directed on the molecule, the molecule may absorb the radiation. The simplest vibration of a bond in a molecule can be modelled with two masses which are connected by a spring. One mass is stationary and the other one moves back and forth (Rouessac et al, 2007).

According to the classical mechanics, when the moving mass or atom moves back and forth, the restoring force can be described by Hooke's law:

$$F = -kx \tag{1}$$

where F is the restoring force of the spring, k is the force constant of the spring, and x is the displacement of moving mass. The potential this energy of this harmonic oscillator changes when the atom or mass moves back and forth from the equilibrium position. The minimum potential energy occurs when the moving atom is at the equilibrium position. The potential energy, U, is obtained by integration of:

$$f = -\frac{dU}{dx} \Rightarrow -K.x = -\frac{dU}{dx} \Rightarrow dU = K.x.dx \tag{2}$$

$$\int_0^U dU = K \int_0^x x.dx \Rightarrow U = \frac{1}{2} K.x^2 \tag{3}$$

The change in potential energy of a harmonic oscillator as a function of x (internuclear distance) is shown in Figure 2.1.

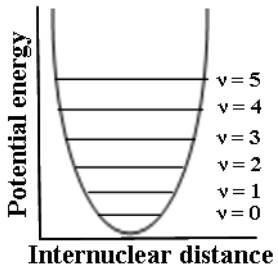

Figure 2.1: The potential energy of the harmonic oscillator

The frequency of vibration depends on reduced mass and force constant of the spring or bond can be described as:

$$\nu_{vib} = \frac{1}{2\pi}\sqrt{\frac{k}{\mu}} \tag{4}$$

In this expression, μ is the reduced mass of the system which is:

$$\frac{1}{\mu} = \frac{1}{M_A} + \frac{1}{M_B} \tag{5}$$

where M_A and M_B are the atomic masses of the individual atoms; therefore, frequency of IR absorptions depends on the masses of the atoms and the strength of the bond.

the $\bar{\nu}$ in units of cm^{-1} is equal to:

$$\bar{\nu} = \frac{1}{2\pi c}\sqrt{\frac{k}{\mu}} \tag{6}$$

This model resembles the chemical bond linking two atoms on condition that the quantum theory is applied. A bond whose frequency of vibration is *v* can absorb incident light of an identical frequency. In the quantum mechanical model, it can be shown that the energy of allowed states (ε_{vib}) will be defined as:

$$\varepsilon_{vib} = h\nu(V + \frac{1}{2}) \tag{7}$$

$$\varepsilon_{vib} = (V + \frac{1}{2}) \frac{h}{2\pi} \sqrt{\frac{k}{\mu}} \tag{8}$$

In this expression, V=0,1,2,… is called the vibrational quantum number. According to quantum mechanics, only certain vibrational energy state are allowed (Rouessac, 2007; Griffiths, 2007). As most molecules at room temperature are at the ground vibrational state, transitions are typically to the first vibrational exited state. The lowest energy level, called zero point energy, is equal to ½ $h\nu_{\text{vib}}$, and the next vibrational level has 3/2 $h\nu_{\text{vib}}$ energy. According to the selection rule for harmonic oscillator, only transitions to the next energy level are allowed; therefore, the molecule will absorb an amount of energy equal to $h\nu_{\text{vib}}$. However, the transition can sometimes happen from v=0 to v=2 or v=3 called overtones in an IR spectrum and they are of lower intensity than the fundamental band. This is because the harmonic oscillator model is inadequate to describe vibration properly.

Since the bond can break, a molecule is actually an anharmonic oscillator. The Morse oscillator offers a more accurate model for vibrations of higher energy levels. Using Morse function produces a curve for potential energy versus interneuclear distance (Figure 2.2). The equation is defined as:

$$U(r - r_e) = D_e(1 - e^{-\alpha(r - r_e)})^2 \tag{9}$$

This function involves the dissociation energy D_e in units of cm^{-1} and α parameter which can be obtained from:

$$\alpha = \pi \nu_e (\frac{2\pi}{D_e})^{1/2} \tag{10}$$

Where the ν_e can be obtained from:

$$\Delta\varepsilon_e = h\nu_e \tag{11}$$

$\Delta\varepsilon_e$ is the vibrational energy spacing that corresponds to the curvature of the potential energy function around the equilibrium bond length.

As illustrated in Figure 2.2, potential energy curve described under this system deviates significantly from that of the harmonic oscillator at higher energy levels (Figure 2.1). The energy levels become more closely spaced with increasing internuclear distance in the anharmonic oscillator; eventually the increasing energy becomes sufficient to cause dissociation of the bond. After dissociation the potential energy will be constant.

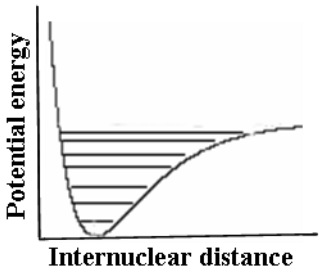

Figure 2.2: The potential energy of the anharmonic oscillator

The situation becomes more complex for polyatomic molecules, where molecular vibrations include bonds stretching, bending, twisting, scissoring, etc. In a molecule, each atom has 3 degrees of freedom. A polyatomic molecule of N atoms has 3N total degrees of freedom. However, 3 degrees of freedom are required to describe translation; and 3 degrees of freedom correspond to rotation of entire molecule; therefore, for nonlinear molecules, 3N-6 degrees of freedom are possible for fundamental vibrations, also called normal modes of vibration. For non-linear molecules, 3N-5 normal modes of vibration are possible because only 2 degrees of freedom are needed to describe rotation. Among these normal modes of vibration, those ones that produce change in dipole moment can

result in an IR activity. The electrical field of incident light can interact with the molecule and transfer its energy to the molecular vibration (Rouessac, 2007).

Various types of vibrational modes are illustrated in Figure. 2.3.

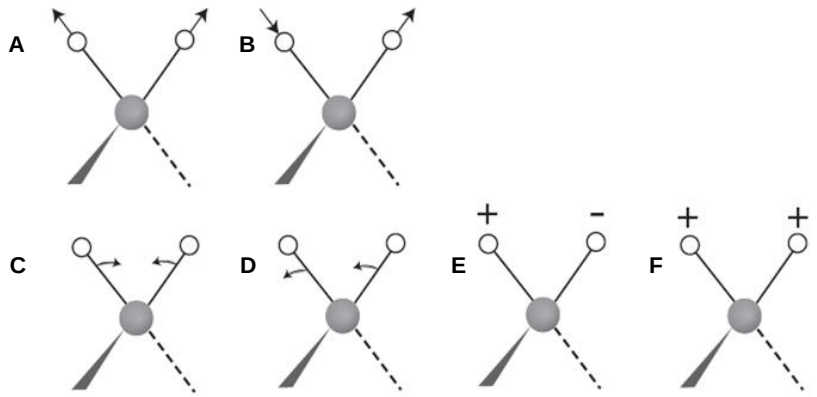

Figure 2.3: Vibrational modes for a non-linear group (CH_2). (A) Symmetric Stretching, (B) Asymmetric stretching, (C) Scissoring (in-plane, bending), Rocking (in-plane, bending), (E) Twisting (out of plane, bending), (F) Wagging (out of plane, bending)

2.1.2 Infrared spectroscopy instrumentation

In simple terms, IR spectra are obtained by detecting changes in absorption (or transmittance) intensity as a function of wavenumber. Early instruments were dispersive. Most present-day commercial instruments measure IR radiation using Fourier transform spectrometers.

Dispersive spectrometers

Dispersive spectrometers were introduced in the mid-1940s. A dispersive IR spectrometer consists of radiation source, sample chamber, monochromator and detector. In a typical dispersive IR spectrometer, incident IR light from a broad-band source passes

through the sample and is dispersed by a monochromator with a slit to select only a small band width. The selected portion of the light goes to the detector, which generates an electrical signal and ultimately results in a recorder response. Most dispersive spectrometers have a double-beam design in which two equivalent beams from the source pass through the sample and reference chambers, respectively. By using an optical chopper such as a sector mirror, the reference and sample beams are alternately focused on the detector (Rouessac, 2007).

The whole idea for a dispersive instrument is that it is based on rejection of all of the other light and acceptance of only very small range of wavelengths of light, after dispersing all other light; therefore, only a small portion of the spectrum is detected at one time.

Non-Dispersive spectrometers

Fourier transform spectrometers have replaced dispersive instruments for most applications due to their speed and sensitivity. In FTIR spectroscopy, all frequencies are examined simultaneously instead of viewing small region of frequency sequentially. This technique has greatly extended the capabilities of infrared spectroscopy and been applied to many areas such as biological materials, polymers and petrochemical compounds.

The basic components of an FTIR spectrometer are light source, interferometer, sample chamber, detector, amplifier, convertor of analogue to digital and computer. Generally, the radiation emerging from the source is passed through an interferometer to the sample before reaching the detector (Figure 2.4). In FT-IR spectroscopy, the entire spectrum is collected as time domain function, and is converted mathematically into the frequency domain (Salzer, 2009; Rouessac, 2007; Griffiths, 2007).

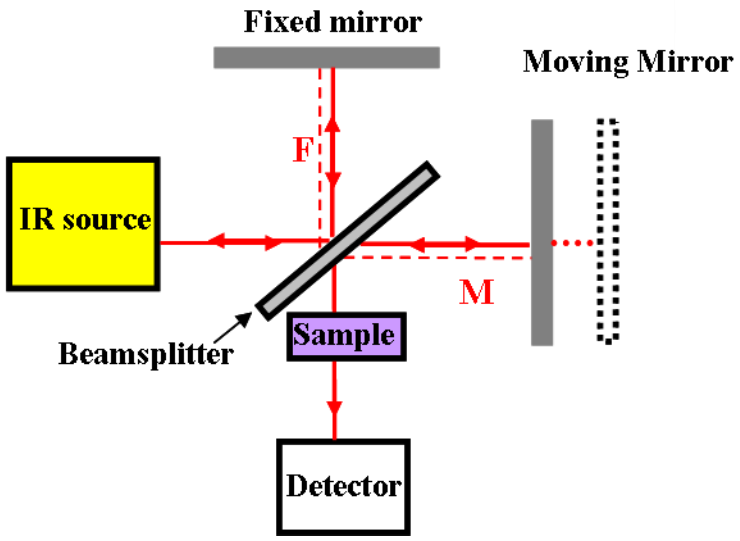

Figure 2.4: Schematic of FTIR spectrometer

2.1.3 Principles of Fourier Transform Infrared Spectroscopy

FT-IR instruments are based on the Michelson interferometer, which consists of three active components: fixed mirror, moving mirror and the beamsplitter (Griffiths, 2007). In Mid-IR, beamsplitter is made of potassium bromide or caesium iodide.

If a collimated beam of monochromatic radiation of wavelength (λ) is passed into an ideal beamsplitter, 50% of incident radiation will be reflected to fixed mirrors while 50% will be transmitted to the moving mirror. Then, these two beams are reflected back from the two mirrors, returning to the beamsplitter to recombine. Half of the beam reflected from the mirrors is transmitted through the beamsplitter after recombining and passed through the sample while the remainder is reflected back to the source. The optical path difference, called the retardation (δ), is defined as the difference in the distance traveled by the light going to the two mirrors and back, and is equal to 2(M – F). It is important to note that the interferogram will be recorded as a function of mirror displacement. For in-

stance, if the moving mirror is displaced by λ/2 cm, the retardation will be λ cm, and the beams will be in phase and they will interfere constructively. On the contrary, if the moving mirror is displaced λ/4 cm, the retardation will be λ/2 cm. In this case, after recombination of the beams from the two mirrors, the retardation will be λ/2; therefore, they will interfere destructively. Whenever the moving mirror is displaced at a constant velocity, the signal at the detector will be sinusoidal. The intensity $I(\delta)$, which is a function of retardation or time, is a cosine wave function and is defined as:

$$I(\delta) = \frac{1}{2} I(\bar{\nu}).\cos(2\pi\bar{\nu}\delta) \tag{12}$$

In reality, there is no beamsplitter to transmit exactly half of the radiation and reflect the remainder; therefore, apart from power of the beam, some other factors, such as the efficiency of beamsplitter, the amplitude of the interferogram, and detector response will be important. If a frequency-dependent factor is introduced into the above equation, then:

$$I(\delta) = \frac{1}{2} C(\bar{\nu}).f(\bar{\nu}).\cos(2\pi\bar{\nu}\delta) \tag{13}$$

$C(\bar{\nu})$ is frequency dependent correction function that encodes the instrument terms such as beamsplitter, amplifier, detector, and internal mirrors. $f(\bar{\nu})$ is also a frequency dependent function and is described as source intensity for example the frequency intensity output from the light with or without the sample.

If $\frac{1}{2} C(\bar{\nu}).f(\bar{\nu})$ is substituted by $B(\bar{\nu})$, then:

$$I(\delta) = B(\bar{\nu}).\cos(2\pi\bar{\nu}\delta) \tag{14}$$

The interferogram is mathematically related to the spectrum by the Fourier transform. Therefore:

$$B(\bar{\nu}) = I(\delta).\cos(2\pi\bar{\nu}\delta) \tag{15}$$

These two above equations are called a cosine Fourier transform pair. $I(\delta)$ is called the interferogram, while the plot of $B(\bar{\nu})$ is known as the spectrum.

When various frequencies are emitted by light source, the interferogram and spectrum are represented by the integral:

$$I(\delta) = \int_{-\infty}^{+\infty} B(\bar{\nu}).\cos(2\pi\bar{\nu}\delta).d\bar{\nu} \tag{16}$$

$$B(\bar{\nu}) = \int_{-\infty}^{+\infty} I(\delta).\cos(2\pi\bar{\nu}\delta).d\delta \tag{17}$$

FT-IR spectroscopy can be considered as time-domain spectroscopy (Figure 2.5A), because the entire spectrum is collected as the mirror moves at a constant velocity; then, it is converted mathematically into the frequency domain (Figure 2.5B).

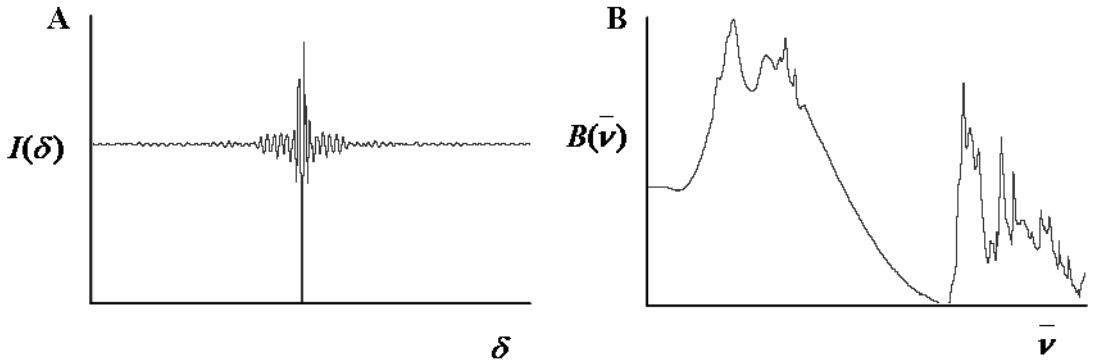

Figure 2.5: (A) Interferogram (A), and (B) spectrum

2.1.4 Advantages of FTIR versus dispersive infrared spectrometer

The two most important advantages of FTIR spectroscopy are Fellgett (or multiplex) advantage and Jaquinot (or throughput) advantage.

In FTIR spectroscopy, all wavelengths are detected simultaneously and at many times in one interferogram. A large number of spectra can be acquired rapidly and averaged, to increase S/N ratio. This is known as the Fellgett or multiplex advantage.

Another benefit of the FTIR spectrometer is that in this instrument there is no slit to throw away any intensity from the light source; therefore, it is possible to get the brightness of light. This is called Jacquinot advantage and also increases the S/N ratio.

FTIR interferometers are also much faster, more reproducible, and more sensitive compared to dispersive spectrometers (Griffiths et al, 2007). These advantages have caused the common choice of FTIR over dispersive instruments.

2.1.5 Instrumentation for Infrared microspectroscopy

The major advance in the kinds of biological samples that can be analyzed by FTIR occurred with the introduction of the commercial FTIR microscope in the 1980s. An IR microspectroscope combines the molecular-level information of FT-IR spectroscopy with the spatial resolution of microscopy. The factors that will influence the performance of an IR spectromicroscope include the optics, light source and detector.

Early work in this lab was done at synchrotron with single pixel raster scan mapping. With this technique, software allows to collect the spectrum of the small pixel at the centre. A series of spectra can also be acquired by raster scanning the sample, to allow for spectral analysis over broad areas of a sample. With single-point measurements, the aperture size can be reduced considerably more by using synchrotron radiation as compared to radiation produced by a thermal light source. With a globar light source, the aperture needs to be at least 20 μm. Using a synchrotron source, the aperture can be reduced until

resolution becomes diffraction-limited. It should be note that the spatial resolution is limited by wavelength of light, brightness of light source, and the aperture size. When the aperture size become equal to the wavelength of the light passing through, diffraction of light becomes evident. For microscopes using a single aperture, the spatial resolution at the diffraction limit is approximately $2\lambda/3$, while the limit for confocal microscopes, using a second aperture, is approximately $\lambda/2$ (Salzer, 2009; Miller, 2005). With a conventional thermal light source, the best spatial resolution that can be obtained is approximately 20 μm, well below the diffraction limit for mid-IR region.

Two types of detectors are used for this FTIR microscope: Focal Plane Array (FPA) and single element detector.

Figure 2.6B illustrates FPA-FTIR microscope which was used for IR data collection in this project at University of Manitoba (Figure 2.6). In this instrument, a globar light source, which is the most common thermal light source, is used for the IR spectrometer. A globar is a silicon carbide rod that is electrically heated up to 1000 to 1650 °C to emit continuous IR radiation. The light from the globar light source travels through the spectrometer, then into the IR microscope, onto the sample, and finally is collected at the detector. The FPA detector (Figure 2.6B) consists of an array of IR detector elements that enables spectra at each pixel to be collected simultaneously, while the interferometer portion of the system allows all the spectral frequencies to be measured concurrently. By using FPA detector, collection of large IR images is dramatically improved (Salzer, 2009; Bhargava, 2005). For instance, our FPA-FTIR miscrospectroscope equipped with a 64 x 64 pixel focal plane array detector enables simultaneous detection of 4096 individual spectra in a few minutes. For instance, it is possible to take a single tile map including

4096 pixel in 7 min by 128 scan number, while to collect the 4096 single pixel raster scan with globar light source, it will take around 20 days.

The single point detector that is used in this instrument is a single element detector (Figure 2.6B). With single-point detector, an aperture is used to limit the spot size of the light before it reaches the sample, defining the size of the pixel, where a spectrum will be acquired.

Mercury cadmium telluride (MCT), a semiconductor, is the most common single element detector in IR spectromicroscopes. When radiation strikes the MCT detector, electrons in the semi-conducting surface are excited to a higher conducting state, and the magnitude of this change is a function of the power of the incident radiation. Sensitivity of MCT detectors improves when cooled down to liquid nitrogen temperature (77K).
As illustrated in Figure. 2.6C, in order to allow mapping, the instrument has a computer-controlled sample stage.

This FPA-FTIR microscope, like most of the IR microspectroscopes, can operate in either transmission or reflectance mode. In transmission mode, the light from the source passes through the sample and onto the detector (Figure 2.6D (top)). In reflectance mode, the light passes through the sample, reflects from the substrate, and passes through the sample again before going to the detector (Figure 2.6D (bottom)). The spectrum of a sample mounted on a reflective substrate is called a transflection spectrum.

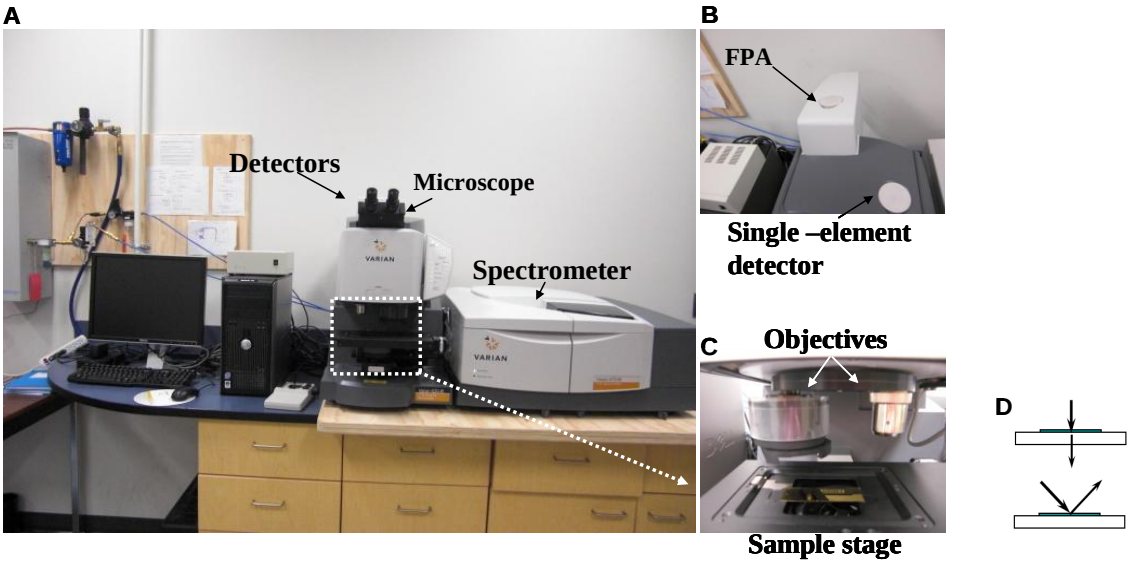

Figure 2.6: Schematic of FPA-FTIR microscope. Experimental set up at University of Manitoba. Varian 670 spectrometer, equipped with a Varian 620 microscope. (A) FPA-FTIR microscope (B) A close-up of the detectors (top: FPA detector; bottom: Single point detector, and (C) sample stage. (D)The path of the light through the sample with the transmission (top) and reflectance (bottom) set-ups.

In comparison to FPA detectors, the slowness of data acquisition in point mapping with a globar source generally prevents the examination of large sample regions at high spatial resolution. FPA detectors give the opportunity to collect fast IR images over large areas because of the sensitivity and readout speed (Salzer, 2009; Bhargava, 2005).

Synchrotron FTIR Microspectroscopy

A synchrotron is an extremely bright radiation source which may be used as the light source in FTIR microscope. Synchrotron FTIR (sFTIR) microscopes provide chemical information of components at diffraction limited spatial resolution and increased the S/N ratio achievable in the same amount of time. A synchrotron is a particle accelerator in which electrons travel at close to the speed of light. The path of the electrons is bent by

magnetic fields. The change in path causes the electrons to change acceleration and emit electromagnetic radiation, light that is known as synchrotron radiation. Synchrotron light has several unique properties. It is low noise, polarized, highly collimated and spans from high energy x-rays to the infrared region. Most importantly it is very bright. In the IR region, it is around 1000 times more intense than a blackbody source such as a globar for the same spot size (Salzer, 2009; Miller, 2005). In a sFTIR microscope, light from the synchrotron ring travels through the beamline into the interferometer, then into the IR microscope.

With single-point measurements, the aperture size can be reduced more by using synchrotron radiation as compared to radiation produced by a globar source. When the aperture setting is around 100 μm, the globar source is quite bright, while for samples where spatial resolution of interest is less than 20 μm, diffraction effects become appeared and synchrotron radiation is recommended. For samples where the spatial resolution of interest is greater than 20 μm, a conventional globar source will suffice, and there is little or no advantage to using a synchrotron source (Salzer, 2009; Miller, 2005).

As mentioned above, synchrotron radiation is 1000 times brighter than a globar light source; therefore, this brightness advantage allows smaller regions to be probed with acceptable S/N ratio. It is important to note that its brightness is because the effective source size is very small and the light is emitted into a narrow range of angles (Salzer, 2009; Miller, 2005).

2.1.6 Infrared analysis of biological samples

IR spectroscopy is a valuable technique to elucidate comprehensive structural information of numerous biological samples. This technique is capable to analyse a wide range of components with only small amounts of sample preparation. It is also a non-destructive technique, so the sample is available for other analyses such as staining. IR microspectroscopy has been applied to biological materials. With the development of FTIR spectrometers, particularly with synchrotron IR sources, great improvements have been made in the quality of data (Salzer, 2009; Miller et al, 2005). FPA-FTIR microspectroscopes increase the speed of data collection (Bhargava R, 2005). Biological tissues are composed of various types of molecules and the average molecular composition of the sample can be detected with IR, by analyzing bands due to the functional groups found in proteins, lipids, and other molecules (Stuart, 2004).

IR spectroscopy is widely used to study proteins (Movasaghi et al, 2008; Barth, 2007; Stuart, 2004). Proteins are linear polymers of amino acids linked through the peptide bond, and folded into three-dimensional structures. The amide bonds of proteins display three characteristic absorbance bands including the amide I (represent 80% of the C=O stretching vibration of the amide group coupled to the N-H bending and C-N stretching; profile ranges from 1600-1700 cm^{-1}), the amide II (represent 60% N-H bending with 40% C-N stretching; profile ranges from 1500-1600 cm^{-1}) and the amide III (profile from 1200-1350 cm^{-1}). The amide I band is broad and very complex. An amide I between 1662-1650 cm^{-1} usually indicates α-helix, and 1640-1620 indicates β-sheet; therefore, it can be used to evaluate relative levels of β-sheet and α-helix within amyloid- β plaque aggregation.

IR spectroscopy has been applied to the study of membrane lipids (Movasaghi et al, 2008; Stuart, 2004). Lipids are water insoluble compounds that act as membrane components and energy stores. Fatty acids which are the building blocks of many lipids are composed of a long hydrocarbon tail and carboxyl head group. Membrane lipids are fatty acids esters of glycol. They are usually two fatty acids and one head group (Figure 2.7B), and categorized according to their head group, and include glycerophospholipids, sphingolipids. The spectra of lipids are based on CH_2 symmetric stretching (2851 cm^{-1}), CH_3 symmetric stretching (2871 cm^{-1}), CH_2 asymmetric stretching (2922 cm^{-1}), CH_3 asymmetric stretching (2956 cm^{-1}), CH_2 deformation (1466 cm^{-1}), and C=O stretches are indicated between 1740 and 1715 cm^{-1}. For phospholipids, the symmetric P=O stretching of PO^{2-} groups are found at around 1090 to 1080 cm^{-1} and asymmetric P=O stretching of PO^{2-} groups are obtained at around 1250 to 1220 cm^{-1}. Phosphate and carbonyl are also indicators for DNA and RNA.

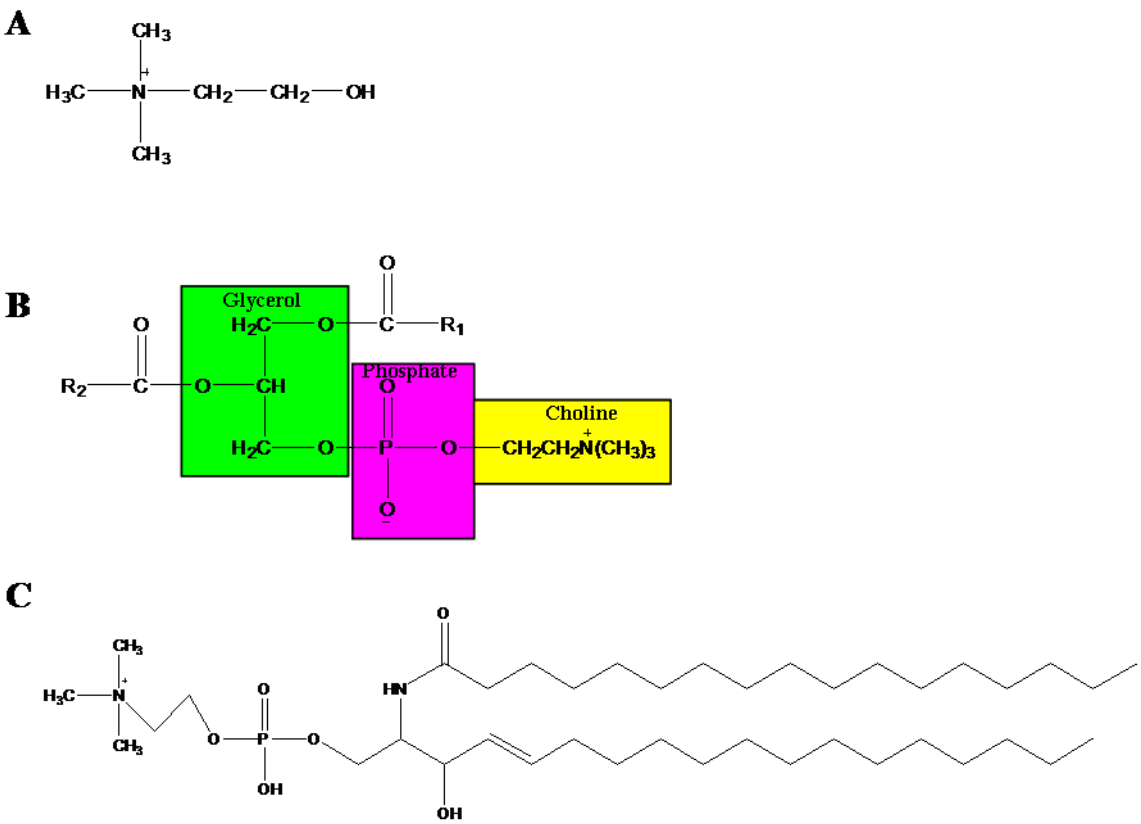

Figure 2.7: The structure of A) Choline, (B) Phosphatidylcholine which is the main constituent of cell membrane, (C) Sphingomyelin which makes up the myelin sheath and is a major constituent of brain tissue.

2.2 Raman Spectroscopy

Raman spectroscopy is a technique for recording molecular vibrations that derives from two photon, inelastic light scattering process. With Raman spectroscopy, a photon is scattered by a sample molecule and loses or gains energy during the process (Ozaki et al, 2008). This energy exchange is characteristic for a particular vibration in the molecule. This spectroscopic technique is simple, nondestructive, and only small amounts of material with minimum sample preparations required. This spectroscopy technique provides molecular-level information, allowing investigation of functional groups, bonding types, and molecular conformations, spectra provide direct information about the biochemical composition of the sample (Bista 2009; Shih 2009).

2.2.1 Principles of Raman spectroscopy

When monochromatic radiation is incident upon a molecule, it may be reflected, absorbed or scattered in some manner. In Raman technique, it is the inelastic scattering of the radiation that occurs and can tell about the sample's molecular structure.

The incident light with the frequency v_0 upon a certain molecule brings a number of photons with the energy hv_0 to the molecule. Most photons interacting with molecules do not change their energy during the collision; it means that they have an elastic collision. This is called Rayleigh scattering, and consists of scattered photons having the same frequency as the incident light. If an incident photon transfers an hv quantum of energy to the molecule, the frequency of the scattered photon becomes equal to v_0-v. This is called Stokes Raman scattering, and arises when energy from the photon is transferred to the molecule, raising it to a higher energy state. In some cases, the incident photon receives

the $h\nu$ energy, the energy of the scattered photon rises to $h(\nu_0+\nu)$, and the frequency of the scattered photon becomes $\nu_0+\nu$. This is named Anti-Stokes scattering, and is due to collision between a photon and a molecule in an excited state. The molecule transfers energy to the photon and returns to the ground state. As the molecules are normally in the ground state, Stokes Raman scattering occur more frequently rather than anti-Stokes Raman scattering.

Intensity of scattered radiation versus wavenumber forms a Raman spectrum that is unique for each individual substance (Ozaki et al, 2008).

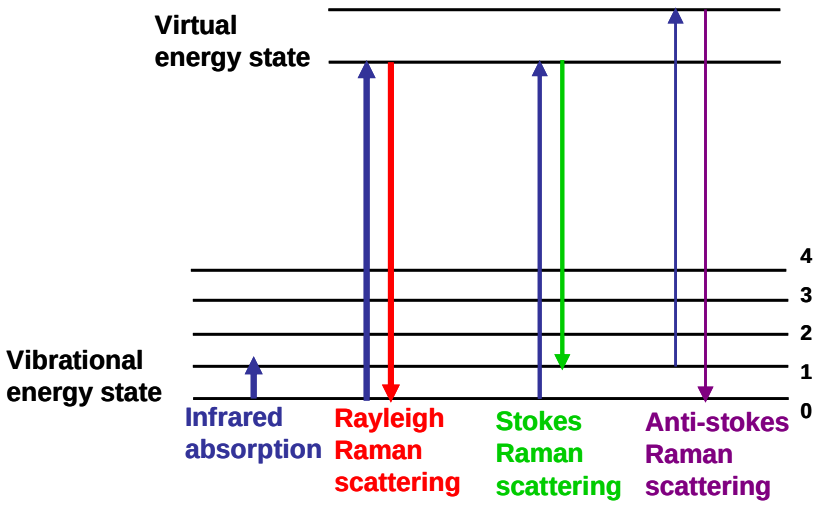

Figure 2.8: Energy level diagram to show elastic and inelastic Raman scattering

We can describe the elastic and inelastic scattering according to classic theory of Raman effect (Ozaki et al, 2008; Winefordner, 2000). When a molecule is subjected to the beam of electromagnetic radiation (EMR) with frequency (ν_0), the oscillatory electric field (E) of the EMR changes the distribution of electron cloud within the molecule.

When the electric field is weak enough, the induced polarization (*P)* is proportional to this electric field and defined by following equation:

$$P = \alpha \,.\, E \tag{18}$$

The polarizability can be defined as how easily the electron cloud becomes distorted. As the vectors *P* and *E* are generally in different directions, the polarizability shown by *α*, a tensor quantity that is called polarizability tensor:

$$\begin{pmatrix} P_x \\ P_y \\ P_z \end{pmatrix} = \begin{pmatrix} \alpha_{xx} & \alpha_{xy} & \alpha_{xz} \\ \alpha_{yx} & \alpha_{yy} & \alpha_{yz} \\ \alpha_{zx} & \alpha_{zy} & \alpha_{zz} \end{pmatrix} \begin{pmatrix} E_x \\ E_y \\ E_z \end{pmatrix} \tag{19}$$

Raman scattering is based on the effects of molecular vibrations on the tensor polarizability, α, in equation (18). If we assume that *P* and *E* are values along one coordinate axis, the oscillatory electric field of electromagnetic radiation is governed by:

$$E = E_0 \,.\, cos2\pi\nu_0 t \tag{20}$$

where ν_0 is the frequency of the laser light. The molecular vibrations are usually considered to be composed of normal modes, Q_j , of which there are *3N-6* for non-linear and *3N-5* for a linear molecule with *N* atoms and can be defined as:

$$Q_j = Q_j^0 . \cos 2\pi\nu_j t \tag{21}$$

where ν_j is the frequency of the *jth* normal mode. The polarizability of electrons in the molecule will be modulated by the molecular vibration so that:

$$\alpha = \alpha_0 + (\frac{\partial \alpha}{\partial Q_j}) Q_j + ... \tag{22}$$

As already mentioned, the polarization (*P*) is the product of E and α. Since *cos(a).cos(b)=[cos(a+b)+cos(a-b)]/2*; therefore, the polarization is equal to:

$$P = \alpha_0 E_0 \cos 2\pi \nu_0 t + E_0 Q_j^0 (\frac{\partial \alpha}{\partial Q_j}) \frac{\cos 2\pi(\nu_0 + \nu_j)t + \cos 2\pi(\nu_0 - \nu_j)t}{2} \quad (23)$$

This equation demonstrates that light will be scattered at three frequencies. The first term is Rayleigh scattering, which is at the same frequency as the laser ($\nu_0 = \nu_j$). The second term is anti-Stokes Raman scattering, which occurs at $\nu_0 + \nu_j$ and the third term is Stokes Raman scattering at $\nu_0 - \nu_j$. It is important to note that only vibrations that change the polarizability (consequently $(\frac{\partial \alpha}{\partial Q_j}) \neq 0$) yield Raman scattering. This statement is the basis of the primary selection rule for Raman scattering.

2.2.2 Raman spectroscopy instrumentation

Four major elements for a Raman instrument are: the light source (laser light), spectrometer, detector and optical setup.

Lasers

Raman spectrometers that operate at laser wavelengths up to 785 nm are most common in dispersive systems, while those ones with laser at 1064 nm and above are usually employed in FT-Raman systems.

It is important to note that the high photon flux produced by laser 514 nm (air cooled Ar ion) and 633 nm (He-Ne laser) can cause sample oxidation; therefore, samples can be damaged if high percentage of laser power is used. The most practical choice for biological samples is a diode laser which produces light of 785 nm. This laser is suggested for experiments with biological samples, because a number of components present in such samples usually fluoresce strongly under 500-700 nm light. Fluorescence will be very strong and will obscure the Raman scattered light (see section 2.2.5).

Spectrometer

There are two types of spectrometer: Dispersive and Non-dispersive.

The dispersive spectrometers are based on dispersing the scattered radiation by a grating. These spectrometers are used with the system equipped with visible and up to 785 nm excitation.

Nondespersive Raman spectrometers are almost exclusively associated with FT modulation of the signal and do not include physical separation of the wavelength. This spectrometer is used in FT-Raman instruments with the excitation at 1064 nm. FT-Raman was not used in this work and is not described further.

Detector

Charge coupled devices (CCD) are popular in Raman instruments. CCD detectors are produced from silicon or other semiconductors. These detectors consist of two-dimensional arrays of pixels, such that each of them can be considered as an independent detector. The horizontal pixels are calibrated corresponding to wavenumber axis, while the vertical pixels measure the strength of Raman signal. The image on the CCD camera is an electric Raman signal that is then converted into a spectrum.

Optics

There are two common configurations: 90° and 180°. The 180° configuration is most convenient for a microscope. In this configuration, the incident laser beam and scattered light are on the same axis. There are different ways to combine lenses and mirrors to form a proper setup in the instrument. In section (2.2.4), more information about the optics in Raman Microscope will be given.

2.2.3 Raman microscopy

Raman microscopy involves connecting a Raman spectrometer to a regular microscope (Salzer, 2009). This technique was developed in 1970s in order to be capable to probe the molecular changes associated with biological samples (Salzer 2009, Ferraro et al, 2003).

This technique combines the spatial resolution of microscopy with the molecular-level information of Raman spectroscopy. The map of area on the sample can be processed to create a false colour image that represents intensity of peaks of interest on a color scale, also called chemical mapping. Like FTIR spectromicroscopy, this technique is non-destructive, and needs minimum sample preparation. The sample is sectioned, and mounted on the appropriate substrate and examined, so nothing is added or taken away from it except water.

Raman microscopy is attractive because spatial resolution is improved (1-2 microns) by an order of magnitude compared to conventional globar FTIR microscopy. It is possible to focus visible or Near-IR laser light to a much smaller spot size compared to mid-IR radiation. FTIR and Raman imaging techniques are compatible; therefore, the same section may be mapped by FTIR and then by Raman microscope to probe a small area, repeatedly.

2.2.4 Instrumentation of Raman microscope

A Raman microscope is composed of different parts (Figure 2.8). The first part is the laser source. As shown in Figure 2.8B, there are three laser lines in the Renishaw Invia Raman microscope that was used in this project. The Ar ion laser, producing 514 nm

wavelength, gets very hot and is air-cooled; a fan turns on automatically to cool it down whenever it is used. The second laser line is a He-Ne laser which produces light of 633 nm and generates more fluorescence in biosamples compared to diode lasers. The third laser line, highly recommended for biological samples, is a 785 nm diode laser.

Before the light comes into the spectrometer, there are optics for each laser line (Figure 2.10C). These optics catch the beam and send it to the spectrometer. Right before entering the spectrometer, there is a set of four arms that carry neutral density filters (50, 10, 1, 0.001%) (Figure 2.10D); therefore, by combining them, we can choose a wide range of laser power. When the laser beam comes into the spectrometer (Figure 2.10E), one appropriate optic sends the laser beam to the focusing and collimating optic which is optimized for a particular wavelength. Whenever a laser line is chosen, the proper optic automatically moves to place. Then the laser beam is reflected from another mirror and sent to the rotary dial which is located on the top of spectrometer. This part also contains optics, which are selective to each of the wavelengths and ultimately send the laser beam to the sample mounted on the sample stage. As illustrated in Figure 2.10F, there are 4 different objectives (5, 20, 50, 100x) that permit imaging from large scale rapid survey to sub-cellular high resolution maps. Each of these objectives transmits visible light. The 50x objective is recommended for mapping of most of the biological tissues, and has the best quality; at this magnification, the laser spot size that we can get onto the sample is 2 microns.

The microscope is a regular microscope that transmits visible light. After the laser light hits the sample, scattered light is collected at 180°, although the light can be scattered in various directions. All of the light comes back through the arm, placed between

microscope and spectrometer, and is collected through an aperture. A filter blocks the Rayleigh scattered light. The light that comes through includes the whole spectrum of Raman scattered light; it passes through a grating to be dispersed and is finally imaged on the CCD detector. By choosing extended scan, the grating position is automatically changed to get each portion of the spectrum

Photographs of the Renishaw Invia Raman Microscope are shown in Figure 2.9.

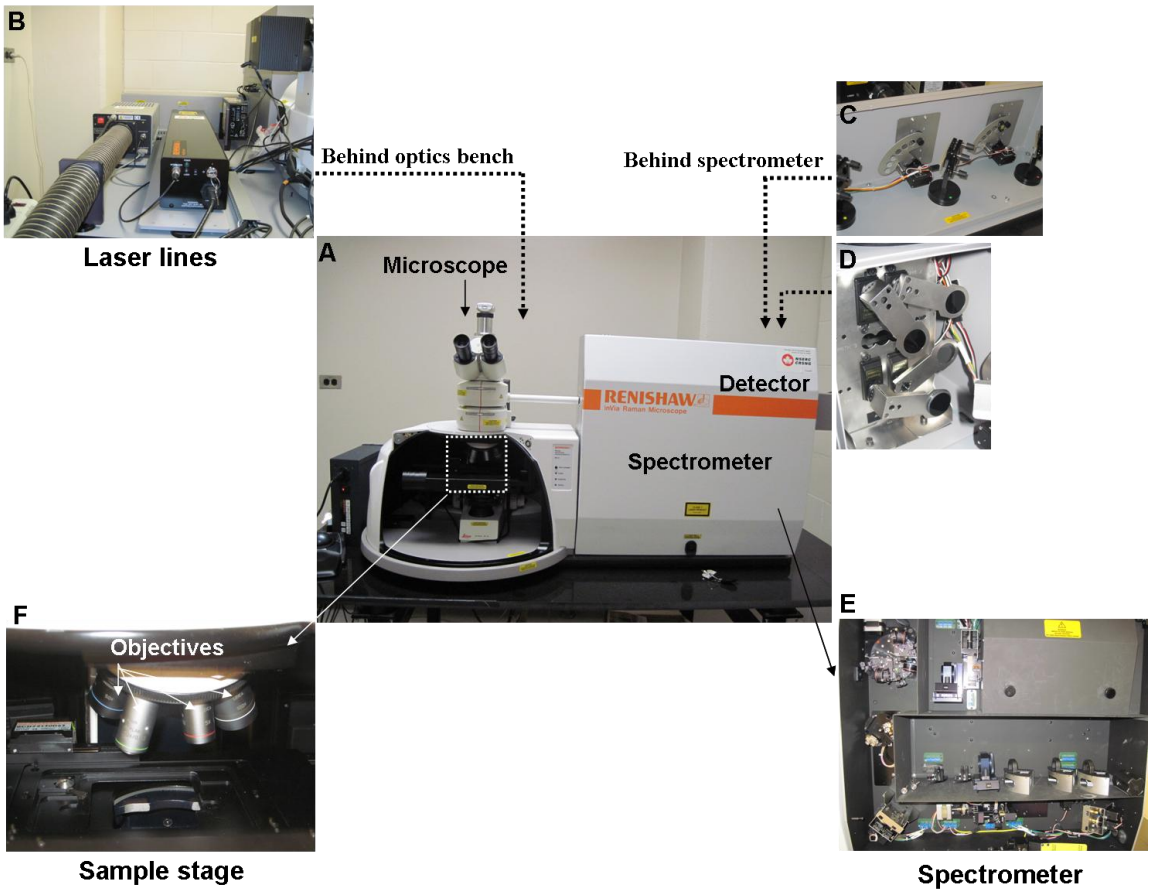

Figure 2.9: Photographs of the Renishaw InVia Raman microscope. experimental set up at University of Manitoba. (A) Raman microscope (B) A close-up of the laser lines from left to right: Air cooled Ar ion (514nm), He-Ne laser (633 nm), Diode laser (785nm), (C) A close up of optics and (4) neutral density (ND) filters, (E) Inside the spectrometer, (F) a close-up of sample stage and objectives (5, 20, 50, 100x).

2.2.5 Raman scattering and fluorescence

The Raman scattering process competes with fluorescence, because the fluorescence is generated very easily. It happens on the same time scale as Raman. As illustrated in Figure 2.10A, photon may be inelastically scattered. The incident photon transfers an hv_0 quantum of energy to the molecule, and the energy of the scattered photon becomes equal to $h(v_0\text{-}v_i)$. The Raman scattering happens with very low probability (one in a million). In fluorescence, the incident light with the same hv_0 energy excites the molecule to some higher excited electronic state (Figure 2.10B). The molecule relaxes a little and then hv (fluorescence) is emitted and molecule returns to ground state. The fluorescence happens with very high probability (99.99% compared to Raman scattering which can happen one in a milllion).

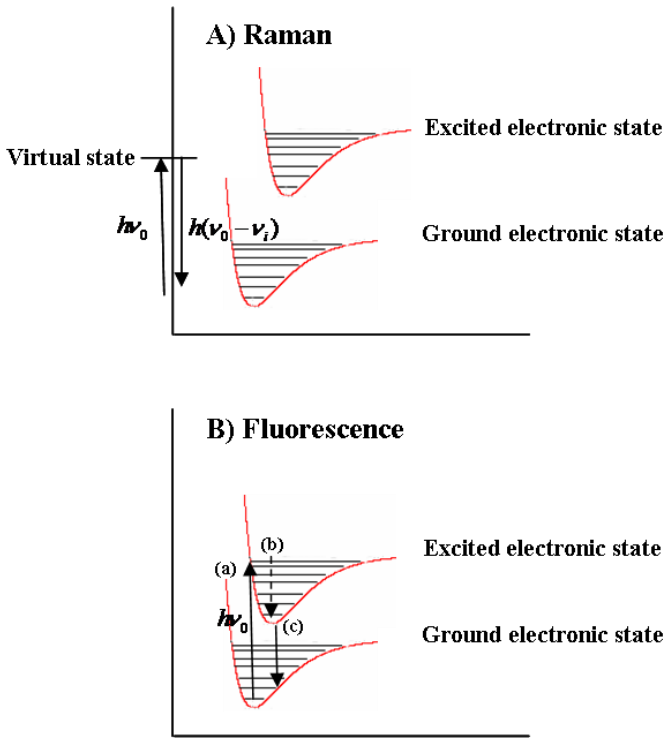

Figure 2.10: Raman scatter *vs.* fluorescence

Fluorescence is really strong particularly when the biological samples are probed; therefore, a huge amount of fluorescence is observed from biological molecules. This is the reason why a laser at 785 nm is suggested for biological samples because the laser with longer wavelength, lower energy can not excite the molecule to higher excited electronic state; therefore, the probability of causing fluorescence is less compared with lasers with shorter wavelength (He-Ne laser and Ar ion laser).

2.2.6 Raman analysis of biological samples

Raman microscopy has been employed for the characterization of biological molecules, particularly proteins and lipids (Köhler et al, 2009; Movassaghi et al, 2007; Krafft et al, 2005; Ong et al, 1999), for many years. This technique can provide valuable structural information about many components, just as with FTIR. The region from 3232 to 3300 cm^{-1} contains broad peaks due to O-H and N-H stretching. The C-H stretching vibrations dominate the region from 2960 to 2851 cm^{-1} (asymmetric vibration of CH_3 at 2960 cm^{-1}, asymmetric vibration of CH_2 at 2934 cm^{-1}, symmetric vibration of CH_3 at 2885 cm^{-1}, and symmetric vibration of CH_2 at 2851 cm^{-1}). The C=O stretching vibrations of lipid groups are found at 1730-1750 cm^{-1}. Several bands due to C-H deformation modes are found both at 1300 $cm^{-1}$and 1440-1454 cm^{-1}. The asymmetric P=O stretch of phospholipids occurs at 1085 cm^{-1} and the symmetric P=O stretch at 1065 cm^{-1}. CN stretching modes from the choline head in phosphatidylcholine and sphingomyelin (Figure 2.7) are found between 700 and 720 cm^{-1}. The Raman spectra of proteins exhibit absorption bands associated with their characteristic amide group. The region from 1655 to 1672 cm^{-1} contains the amide I bands of proteins (Amide I; antiparallel β-sheet at 1672

cm^{-1}, α-helix at 1655 cm^{-1}. The amide II and III bands of proteins are found at 1545-1555 and around 1280 cm^{-1}, respectively. Some peaks unique to Raman are also seen. For example, at 1003 cm^{-1}, there is a very strong sharp peak from phenylalanine. This is diagnostic for protein in general.

Chapter 3.

Materials and methods

3.1 Transgenic mouse model

The transgenic mice used in this project were provided by the Centre for Research in Neurodegenerative Disease (CRND) at the University of Toronto, by Dr David Westaway, presently at the University of Alberta.

The first set of 16 included TgCRND8 mice and non-transgenic littermates at 5 months and 11 months was provided. Subsequently, a second set of 25 much older animals included TgCRND8, control littermates, and Tg19959 and control littermates was provided. The brain tissues were sent from CRND and processed at the University of Manitoba by Dr. Gough and previous members of Dr. Gough's group in 2002 and 2004. Labels beginning Tg are for 2002 sets, labels beginning A are the 2004 set. A selection of tissue from both sets was studied in this work (see Table 3.1).

Table 3.1: Age and sex of transgenic and non-transgenic littermate mice.

Mouse	Sex	Age (day)	Genotype
A04	M	504	Tg(KM670/671NL+V717F)8 -/- (C3H/C57)
A03	F	504	Tg(KM670/671NL+V717F)8 +/- (C3H/C57)
A06	M	478	Tg(KM670/671NL+V717F)8 -/- (C3H/C57)
A05	M	478	Tg(KM670/671NL+V717F)8 +/- (C3H/C57)
A13	F	429	Tg(KM670/671NL+V717F)8 -/- (C3H/C57)
A14	F	429	Tg(KM670/671NL+V717F)8 +/- (C3H/C57)
Tg12	F	330	Tg(KM670/671NL+V717F)8 -/- (C3H/C57)
Tg3	F	330	Tg(KM670/671NL+V717F)8 +/- (C3H/C57)
A24	M	241	Tg(KM670/671NL+V717F)19959 -/-
A25	M	241	Tg(KM670/671NL+V717F)19959 +/-
Tg7	F	150	Tg(KM670/671NL+V717F)8 -/- (C3H/C57)
Tg4	F	150	Tg(KM670/671NL+V717F)8 +/- (C3H/C57)

TgCRND8 and Tg19959 mouse model

TgCRND8 is a transgenic mouse model of Alzheimer disease expressing a double mutated human amyloid protein precursor (APP_{695}), with the "Swedish" mutation (K670N/M671L) and the "Indiana" mutation (V717F), expressed in C3H/C57 back-ground strain. As shown in Figure. 3.1, the mutations are found at the N- and C- boundaries of the Aβ fragment, near the β- and γ secretase cleavage sites. TgCRND8 mouse brain is characterized by many β-amyloid plaques, reduced neuronal and axonal staining, white matter demyelination, glia reaction and inducible nitric oxide synthase immunore-

activity (Belluci etal, 2006). This transgenic mouse model has the subject of numerous studies (Woodhouse et al, 2009; Herring et al, 2008; Belluci et al, 2007; Rak et al, 2007; McGowan et al, 2006; Gallant et al, 2006; Belluci etal, 2006; Dudal et al, 2004; Chishti et al, 2001).

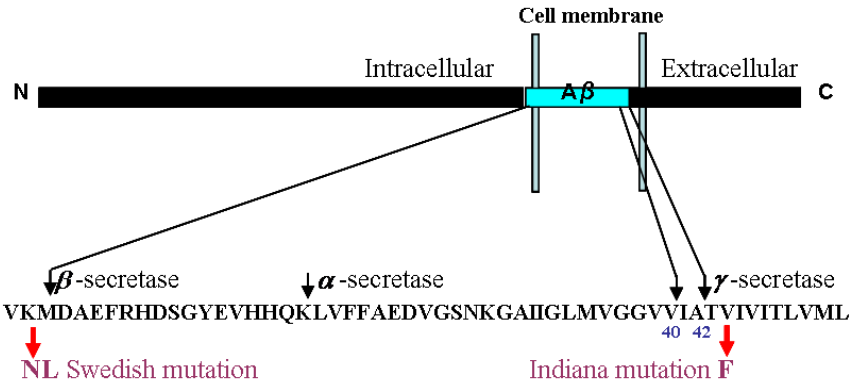

Figure 3.1: Schematic of TgCRND8 double genetic mutation

TgCRND8 mice have been characterized with conventional histological and immunological methods (Chishti et al, 2001). They have normal hippocampus size and neuronal structure, but show early plaque pathology. Both diffuse and dense cored plaques were detected as early as 9-10 weeks of age and increased with age (Chishti et al, 2001). Diffuse plaques (4G8 positive) appeared first in the neocortex and amygdala, then in the hippocampal formation, and lastly in the thalamus (Dudal et al, 2004). Dense cored plaques are associated with dystrophic neurites at 5 months of age (Dudal et al, 2004; Chishti et al, 2001). The plaque formation is concurrent with the appearance of activated microglia cells and shortly followed by clustering of activated astrocytes around dense cored plaques at 13-14 weeks of age (Dudal et al, 2004). It has been reported that TgCRND8 is a suitable transgenic mouse model to study the relationship between the fi-

brillogenic process and the inflammatory response during the brain amyloidogenic process (Dudal et al, 2004). At 6 months, the levels of Aβ40 and Aβ42 are 190 and 510 times normal, respectively (Chishti et al, 2001). The mice show deficits in spatial learning, as measured by the Morris water maze test for spatial memory, from three months of age (Chishti et al, 2001). Behavioural testing revealed that cognitive impairment coincides with plaque development and progresses with age (Hyde et al, 2005).

The Tg19959 mice contain the same mutations to APP_{695} but are maintained on a different genetic background compared to the TgCRND8 mice and display plaque formation beginning at approximately 3 months of age (Li et al, 2004).

3.2 Sample preparation

3.2.1 Brain tissue preparation

Animals were killed by cervical dislocation; brains were removed and bisected sagitally along the midline. The left half of the brain was covered in OCT (Optimal Cutting Temperature, Sakura, Tokyo, Japan) medium and snap-frozen by immersion in liquid nitrogen for 30 second, and stored in -80°C until needed. For IR and Raman microscopy, pristine tissues were cryosectioned at 8 μm tickness and mounted on Mirr-IR slides and gold coated silicon chips. All these steps were performed by Dr. Gough and former members of the group; I undertook IR and Raman data collection from previously sectioned samples.

The right half of the brain was placed in cold 3% paraformaldehyde in 0.1 M Phosphate buffered saline (PBS) for fixation, then dehydrated and embedded in paraffin. For this thesis, some additional sections of flash frozen brain tissue of A05 and A06, 478

days Tg and non-Tg control littermate, were cryosectioned by Dr. Marzena Kastyak (a member of Dr. Gough's group) and me; stored at -80°C till required for Congo-red and 4G8 antibody staining methods.

Animals were treated in accordance with the guidelines of the Canadian Council of Animal Care. Protocols were approved by the University of Toronto and the University of Manitoba.

3.2.2 Creatine crystal preparation

In order to obtain reference spectra of creatine crystals, some creatine monohydrate powder, purity > 99% (C3630, Sigma), was dissolved in distilled water, and a small amount was placed on a gold coated silicon wafer (manufactured at Clean room, Electrical Engineering Department at University of Manitoba). A more dilute solution (approximately 0.5 mg/ml) gave better crystals. The slide was left to dry at room temperature in a desiccator overnight; thin crystals that were suitable for spectromicroscopic analysis formed readily. Several creatine crystals on various gold silicon chips were prepared and the best crystals were chosen for IR and Raman data collection.

3.3 FTIR and Raman Microscopy

3.3.1 FPA-FTIR data acquisition

Spectra were obtained with the Varian 670 spectrometer, attached to a Varian 620 microscope equipped with a single element detector and a focal plane array (FPA) detector. The single element detector was MCT with a spectral range of 8000-450 cm^{-1}. This

detector can acquire spectra from samples as small as 20-10 μm. The 64 x 64 pixel FPA detector enabled simultaneous detection of 4096 individual spectra in a few minutes. The size of each single tile map was 350 x 350 μm and the pixel resolution was 5.5 x 5.5 μm. FPA detector covered the IR spectral range from 4000 to 900 cm^{-1}; spectra were recorded at 4 cm^{-1} spectral resolution. All spectra were taken in transflection mode using Happ-Genzel apodization function. All the spectra were saved in log (1/R) format. As already mentioned in section 2.1.5, in transflectance mode, the light passes through the sample and is then reflected from the slide, therefore, making two passes through the tissue; ultimately, the absorbance is defined as log(1/R), where R is the ratio of the signal from brain tissue and that of background recorded from a clean region of the substrate.

Images including both single tile maps and multiple tile mosaics were collected across the caudate and hippocampus of transgenic mice and non-transgenic control littermates, then processed with Varian Resolution-Pro software. Results were analyzed for distribution of Cr, lipid and plaque aggregation across the hippocampus and caudate of transgenic mouse at different ages (5, 8, 11, 14, 17 months). A sum of 128 scans were accumulated in order to increase S/N ratio. Background scans were acquired first and the sample spectra were ratioed against the background.

To analyze the effect of polarized light on the spectra of crystalline creatine deposits in brain tissue, single tile images of neat creatine crystals prepared on a gold slide and lying at horizontal or vertical to the stage were taken without polarizer, and with polarizer (0° and 90°), then processed on the same peaks selected for brain tissue. In addition, several single tile images were acquired in hippocampus and caudate with a Varian FPA-FTIR microscope and a 64 x 64 Focal Plane Array detector, using polarizer angles of 0°

to 180°, at 10° intervals. The polarizer is inserted above the objectives for infrared polarization studies and could easily be adjusted manually to allow for spectral acquisition at different polarization. Background scans of clean gold slide were also acquired for each polarizer angle of 0° to 180°, at 10° intervals, before taking single tile images of brain tissue. All data were processed with specific focus on peaks at 1304 cm^{-1} and 1404 cm^{-1}, as these exhibited extreme polarization effects and had less overlap with tissue bands compared to other Cr peaks (See chapter 4 for further information).

3.3.2 Synchrotron FTIR data acquisition

Synchrotron FTIR (sFTIR) data were recorded on a Nicolet Magna 550 FTIR with a Nicolet Magna 860 FTIR with Spectra Tech Continnum IR microscope (SRC, University of Wisconsin, Madison, WI, USA). Some single Cr crystal spectra at different orientations were also taken at SRC by Dr. Gough in October 2007. In addition, maps were acquired by Meghan Gallant (M.Sc. 2008, Dr. Gough's group) across the hippocampus of transgenic mice, using a step size of 10 microns and aperture of 12 × 12 μm^2. These sFTIR maps were reprocessed by me with Omnic/Atlμs software (Version 7.3, Thermo-Nicolet). Results were analyzed for distribution of Cr deposits across the hippocampal serial section tissue of 14 months old transgenic mouse. All of the sFTIR data were acquired at SRC previously, and I re-processed the data for creatine deposits at 1410-1384 cm^{-1} instead of 1305 cm^{-1}, because it was discovered by Veena Agrawal (summer student in Dr. Gough's group 2007-2008) that creatine spectra taken by synchrotron FTIR Microscope gave different spectra for various deposits. A depth profile through nine consecutive sections on a plaque located inside the dentate gyrus of 14-month old

TgCRND8 mouse were acquired by Nicolet Magna 550 FTIR with Continuum IR microscope (SRC, University of Wisconsin, Madison). These maps were taken by Alex Kuzyk and Veena Agrawal, and analyzed for lipid, protein, creatine, and dense core plaque with Omnic/Atlμs software (Version 7.3; Thermo-Nicolet) (Kuzyk et al, 2010).

3.3.3 Raman data acquisition

Spectra of TgCRND8 mouse brain and pure Cr (Sigma), mounted on gold-coated silicon chips, were recorded with a Renishaw inVia Raman microscope. The parameters required for successfully mapping brain tissue with Raman microscope such as laser wavelength, spatial resolution, exposure and acquisition time were determined to permit Raman mapping of Cr deposits in transgenic mouse brain (See chapter 4 for more detail). One of the problems in taking the spectra of brain tissue is that with higher energy wavelengths, the sample may burn and two charcoal bands appear at 1589 cm^{-1} and 1324 cm^{-1}. To reduce the risk of damaging the specimen, it was found out the 10% of 785 nm diode laser as the light source was adequate to reduce the risk; therefore, 21 mW of 785 nm laser excitation from a diode laser was used to generate the Raman scattering under a 50x objective. As explained in section 2.2.4, 50x objective has the best quality; therefore, all the maps and spectra were acquired at this magnification with 2 μm spatial resolution.

With the 50x objective and 1200 l/mm grating, spectra were obtained with 1 cm^{-1}/pixel spectral resolution and spatial resolution of 2 μm. The exposure time for all the streamline maps was 300 second to improve S/N ratio.

With WiRE software, there is an option to minimize the cosmic ray and the laser exposure on sample during taking spectra. Cosmic rays are highly energy particles passing

through the CCD detector, generating electrons that are interpreted as signal in spectrum. The position and time of occurrence of cosmic ray is completely random. Cosmic rays appear much more frequently in scans with long exposure time. These peaks can be removed by activating cosmic ray removal through the acquisition set up software. By using this option, two extra accumulation are performed. Another option through acquisition set up is minimize laser exposure on sample to close the laser shutter when data is not collected during the time switching from one row of maps to the next one.

Silicon calibration was performed before collecting data with the same laser line used for data collection. The static scan should be centered at 520 cm^{-1}; 1s exposure time, 1 accumulation, and 10% of 785 nm laser power were chosen as adequate. This calibration was done to ensure the instrument is calibrated to the Si peak at 520 cm^{-1} and that the number of counts was sufficient. Two options of scanning are possible on software: static and extended scan. Static scan covers very small wavenumber range (about 200 cm^{-1}) either side of the chosen centre. A static scan is quicker than extended scan, but only covers a limited range of spectrum. With choosing this option, the grating position is automatically changed. Raman spectra were recorded across a spectral range of 600 to 3100 cm^{-1} to get each portion of the spectrum.

Maps were collected in the caudate and hippocampus of transgenic mice, and processed with WiRE software (version 3.0, Renishaw) for distribution of Cr, lipid and plaque aggregation in the hippocampus and caudate of transgenic mouse brain. The brain tissue regions mapped by Raman microscope were processed at 830 cm^{-1} to identify Cr deposits since this band is very strong for Cr crystal.

Spectra of pure Cr were recorded on gold-coated silicon wafer attached to a glass slide. Raman spectra of pure Cr monohydrate crystals were collected with polarizer placed into the laser pathway between microscope and spectrometer. The polarizer is comprised of two parts: a polarizer and a half-wave plate which rotates the light by 90°. Single spectra of neat Cr crystals were collected using polarizer and half-wave plate to determine the effect of polarized light on spectra of oriented Cr crystals (See chapter 4 for more information).

3.4 Theoretical calculations

All the calculations were performed with Gauss View molecular visualization program and GAUSSIAN03 Package by Fatemeh FarazKhorasani (Ph.D. student in Dr. Gough's group).

The optimized geometry and vibrational spectrum of Creatine monohydrate ($Cr.H_2O$) was modelled using density functional theory (DFT) by B3LYP correlation functional with the 6-311G (d,p) basis set, to obtain optimized geometry and vibrational modes. The starting geometry of the molecule was extracted from its single-crystal neutron structure, followed by converting X-ray fractional coordinates to Gaussian input (Cartesian coordinates) using Mol2Mol (version 5.6.1) software. The geometry was fully optimized before proceeding to vibrational calculations.

Chapter 4.

Results

Previous research in Dr. Gough's group included acquisition and analysis of infrared maps of the Aβ plaques that characterize Alzheimer Disease (Rak, 2007; Gallant, 2007; Ogg, 2002). In using IR technique to analyze plaques, a spectral anomaly was noted in many infrared maps. A literature search suggested a match between the IR spectra of pure creatine and the unknown compound. The discovery was first published in JBC 2006 (Gallant et al, 2006). In a recent paper, it was illustrated that creatine was found more abundantly in hippocampus of transgenic mouse brain compared to their non-transgenic littermates and increased with age (Kuzyk et al, 2010).

The goal of research in this thesis is to explore why more Cr was found in transgenic mouse brain and whether it is a marker of AD. As the creatine deposits were identified in frozen and desiccated brain tissue, it was important to investigate whether these creatine crystals were formed after snap-freezing and desiccating of brain tissue. Cr deposits were mapped in hippocampus and caudate of transgenic mouse for understanding possible co-localization between Cr, lipid and plaque, and also to learn more about the shape and spatial extent of the deposits.

Figure 4.1A illustrates the sagittal section of 14 month-old TgCRND8 mouse brain to show hippocampus, cortex and caudate, regions of interest that were mapped in this work. The unstained, flash frozen tissue was sectioned at 8 μm thickness, and mounted on gold coated silicon wafers to map with IR and Raman and process for levels of Cr, lipid and plaque.

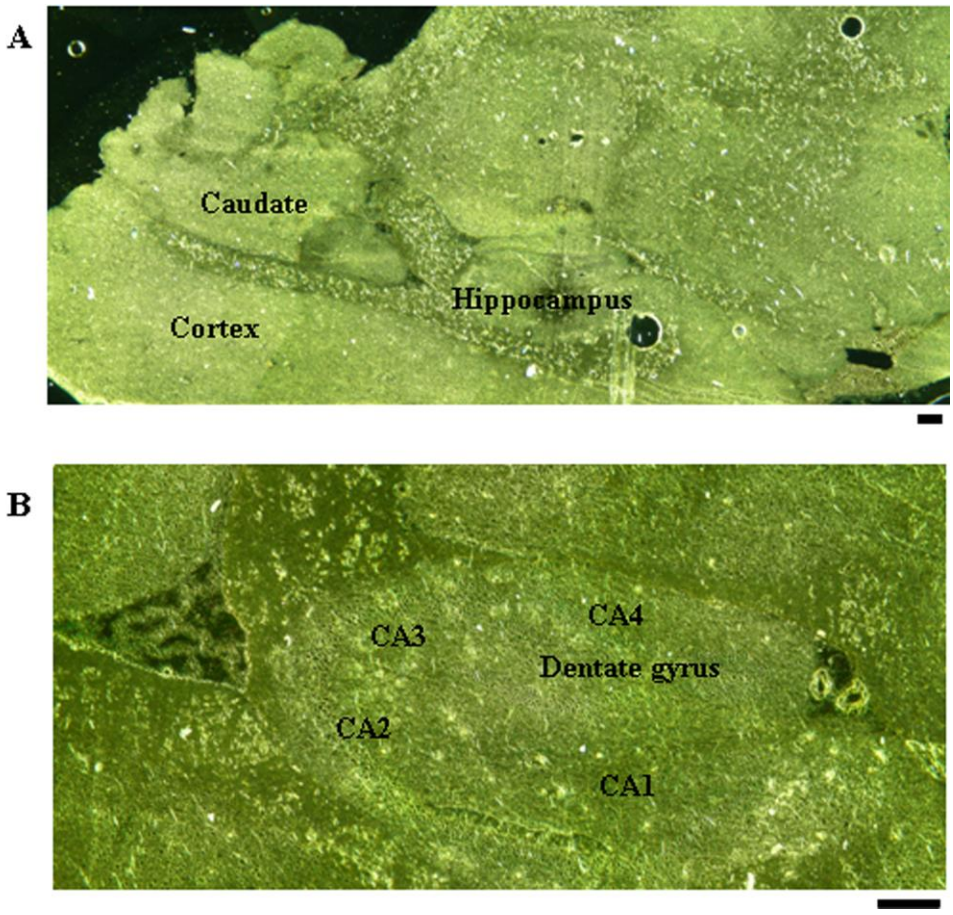

Figure 4.1: Sagittal section of the 14 month-old TgCRND8 mouse brain. (A) Sagittal section of transgenic mouse brain showing major regions of interest mounted on gold silicon slide and (B) a close up of the hippocampus. Densely packed neurons are located in the dentate gyrus and the Cornu Ammonis (CA) which is subdivided into four regions: CA1, 2, 3,4. Scale bar = 200μm.

4.1 Parameter optimization with Raman microscope

Spectra of pure Cr monohydrate, and Cr in transgenic mouse brain tissue and some biochemical signatures like lipid, amyloid plaque, phenylalanine, and CN^+ mode of choline head group of sphengomyeline in TgCRND8 mouse brain were recorded with Renishaw InVia Raman microscope. Before taking maps, the parameters required for successfully mapping brain tissue with the Raman microscope such as laser wavelength, spatial resolution, exposure time and laser power were determined to permit Raman mapping of Cr deposits and environs in transgenic mice.

In order to understand which laser wavelength is suitable for this study, some single scan tests were acquired on cortical tissue by using 10% laser power at 633 nm (He-Ne laser) as the light source. As shown in Figure 4.2A, the test was performed with 1s exposure time and 1 accumulation. In this test, automatic cycles were used to view at least 30 spectra. The background fluorescence was about 4500-5000 counts, fluorescence was observed with each cycle, and no tissue peaks were observed. With this laser power, no charcoal band was seen at 1589 cm^{-1} and 1324cm^{-1}; therefore, this laser power did not burn the brain tissue. The exposure time is the time that the detector is exposed to Raman signal. Longer exposure time gives better signal to noise ratio. However, a sample like brain tissue has a high fluorescence background. A long scan will saturate the detector, whereas several short scans will not. This allows an improvement in the signal to noise ratio; therefore, the single scan test was repeated with the same exposure time and 10 scans were accumulated. The background fluorescence was approximately 25600-28400 counts and like the first test, fluorescence was observed with each cycle, but no tissue peaks were obtained (Figure 4.2B). Even by increasing the accumulation to 100, no

change was observed (Figure 4.2C). The background fluorescence with 100 accumulations was 230000-250000 counts.

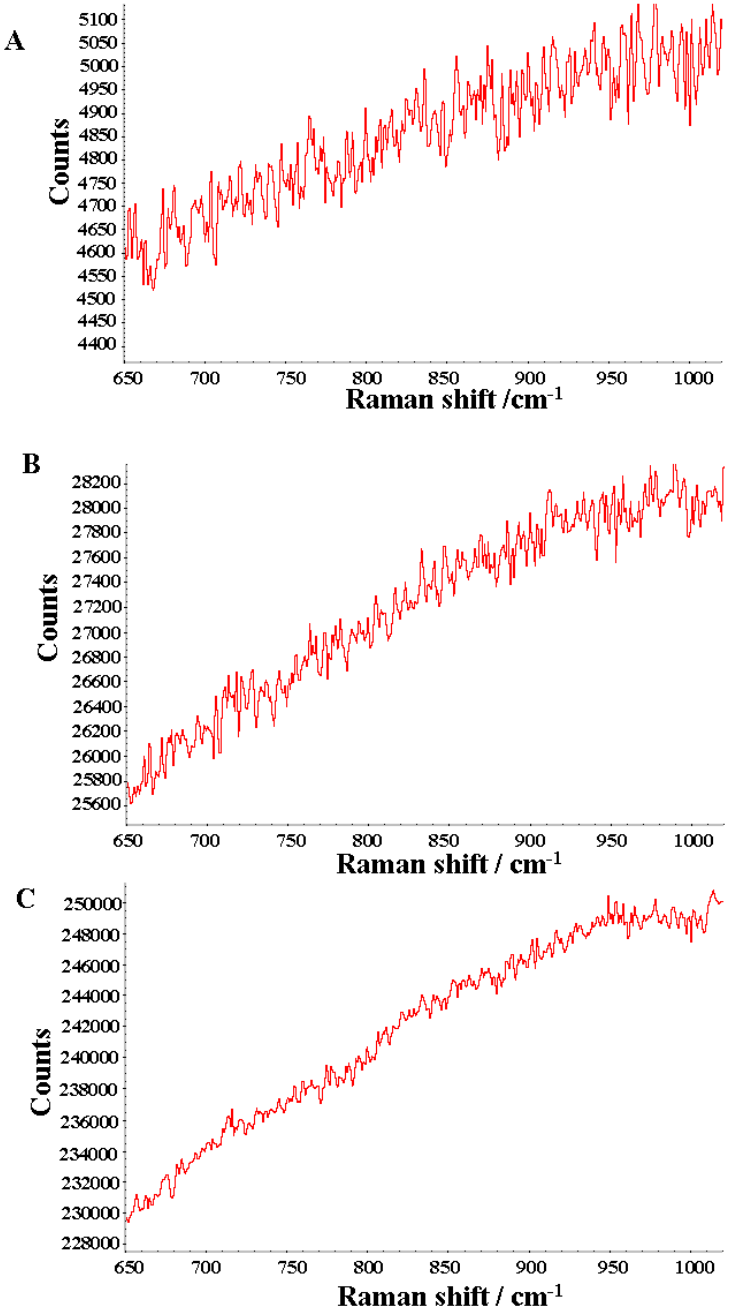

Figure 4.2: Laser wavelength optimization. Raman spectra taken by 10% Laser 633 nm applied 1s exposure time; accumulation (A) 1, (B) 10, and (C) 100, respectively. No peak was observed even by increasing accumulation.

In the next step, another spot in cortical region of brain tissue was illuminated with 50% of 633 nm laser light. As shown in Figure 4.3, although there were few other peaks, two charcoal strong bands were observed at 1589 cm^{-1} and 1324cm^{-1}; therefore, increasing the laser power could not be helpful when He-Ne laser applied.

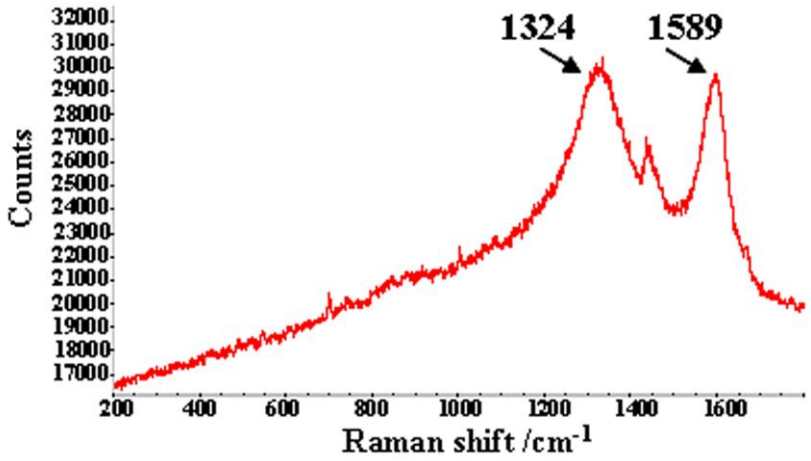

Figure 4.3: Charcoal bands observed by taking spectra with 50% power at 633 nm, He-Ne laser.

As mentioned in section 2.2.4, He-Ne laser (633 nm) can excite more fluorescence compared to the longer wavelength diode laser (785 nm). The fluorescence is generated very easily and it happens on the same time scale as Raman (see section 2.2.5 for more information). Fluorescence is really strong particularly when the biological samples like brain tissue are examined. This is the reason why laser 785 nm was used in this study because the laser with longer wavelength can not excite the molecule to higher excited electronic state; therefore, the probability of causing fluorescence is less. As shown in Figure 4.4, the white matter spectra in cortex region was taken with 5% (Figure 4.4), 10% (Figure 4.5) and 50% (Figure 4.6) laser 785 nm , 1s exposure time, and accumulation 50. Ac-

cording to minimize the background fluorescence, these spectra were taken by static scan, centered at 850, 1050, 1400, 1600 cm^{-1}. Although the signal to noise ratio was improved by increasing the laser power, the background fluorescence obtained by these laser powers was 5500-10000, 14000-26000, 25000-56000 counts, respectively (Figure 4.4B-D). In this work, 10% laser 785 nm was chosen in order to do data collection with minimum risk of sample burning and to get less background fluorescence. With this laser power, 21 mW of diode laser power, measured by powermeter, was used to generate Raman scattering under 50x object.

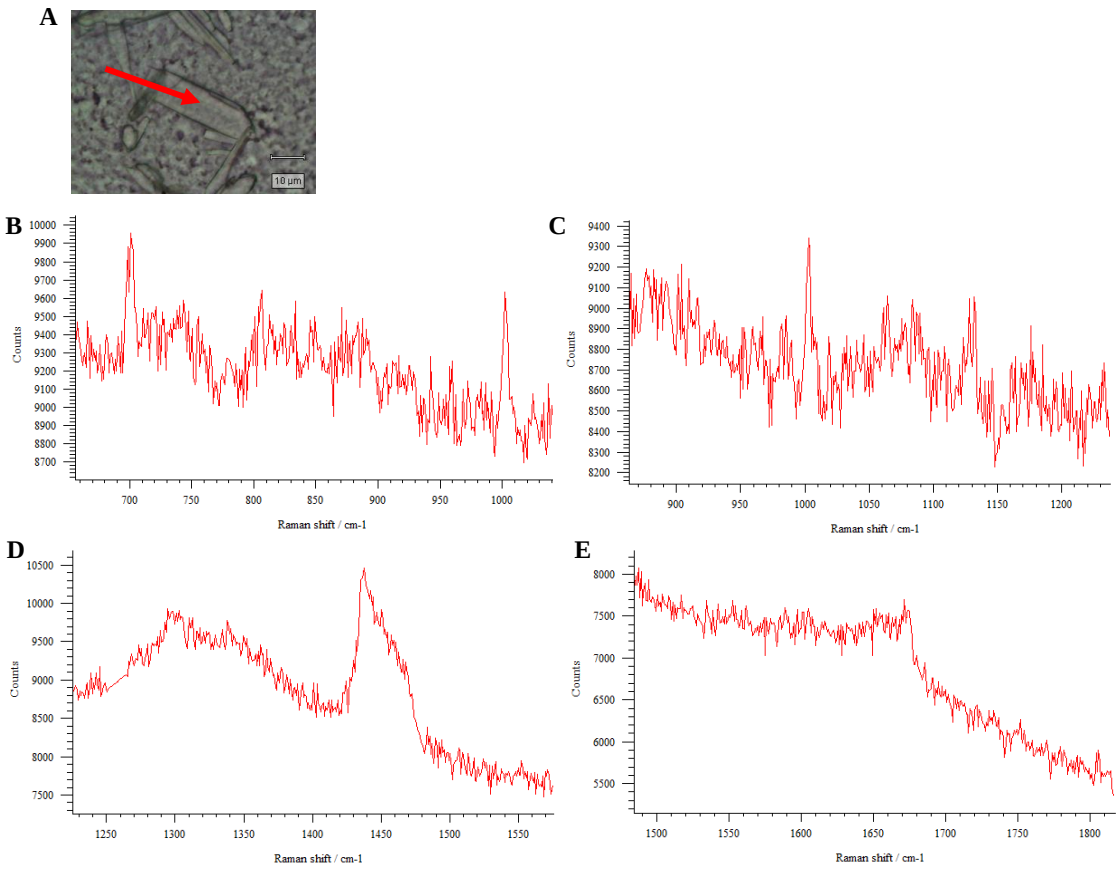

Figure 4.4: Laser power optimization. (A) White matter was selected to take spectra with 5% laser 785 nm in the region between (B) 760-1050 cm^{-1}, (C) 870-1240 cm^{-1}, (D) 1230-1570 cm^{-1}, (E) 1540-1810 cm^{-1}.

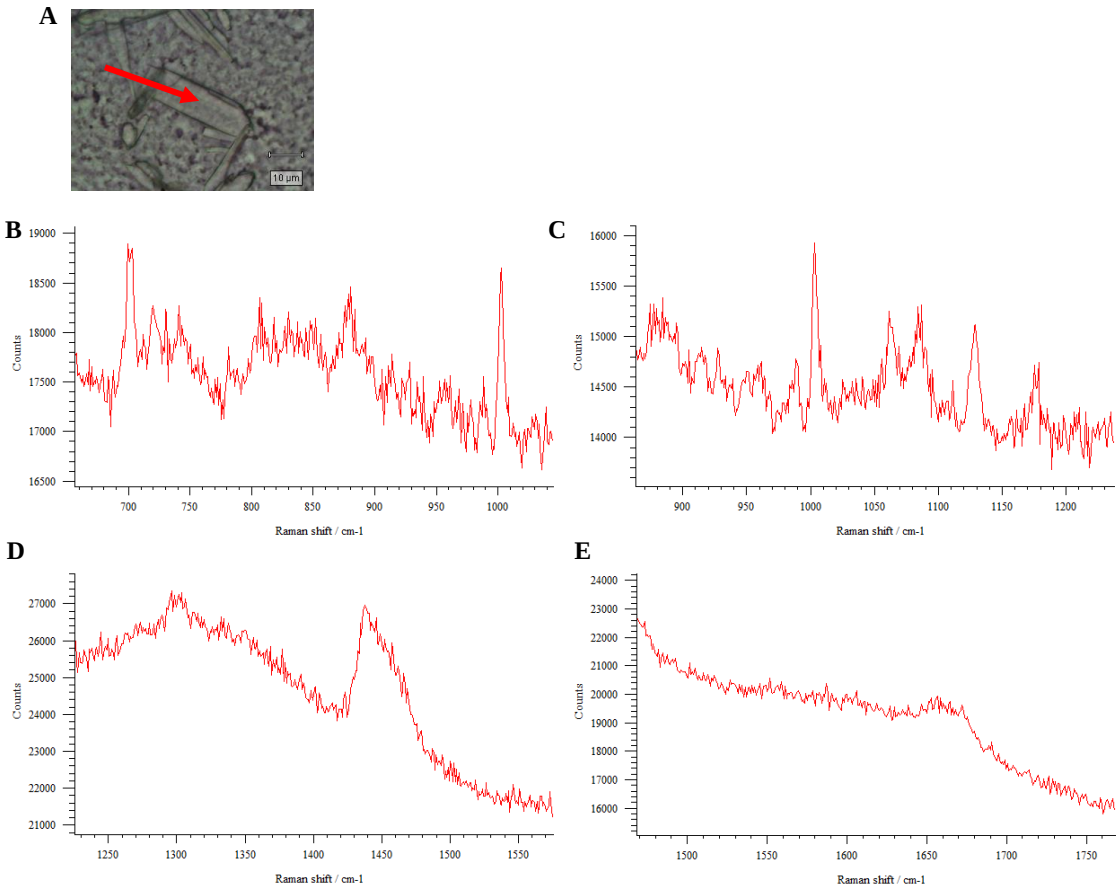

Figure 4.5: Laser power optimization. (A) White matter was selected to take spectra with 10% laser 785 nm in the region between (B) 760-1050 cm^{-1}, (C) 870-1240 cm^{-1}, (D) 1230-1570 cm^{-1}, (E) 1540-1810 cm^{-1}.

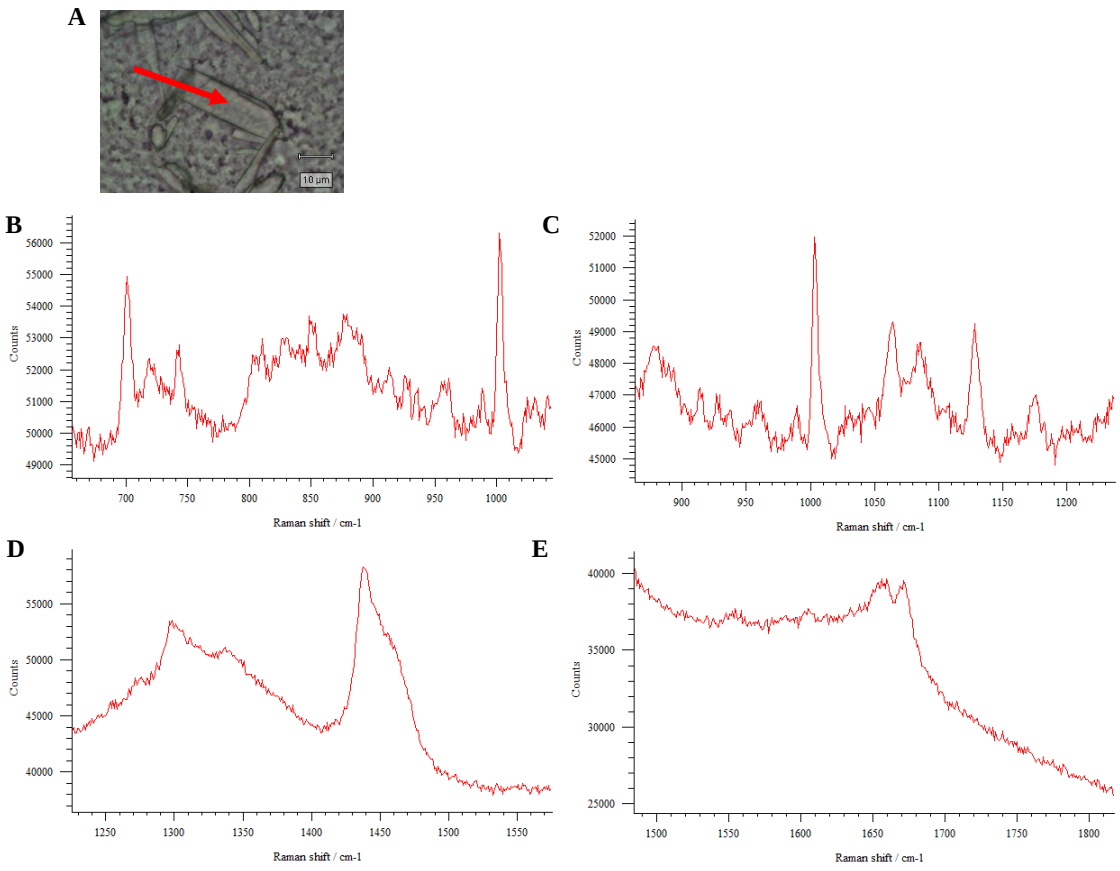

Figure 4.6: Laser power optimization. (A) White matter was selected to take spectra with 50% laser 785 nm in the region between (B) 760-1050 cm^{-1}, (C) 870-1240 cm^{-1}, (D) 1230-1570 cm^{-1}, (E) 1540-1810 cm^{-1}. S/N ratio was improved by increasing laser power, but higher background fluorescence is very distinctive.

To determine the optimal exposure time, three streamline maps were taken in gray matter of caudate region with 100, 200, 300 s exposure time and 10% of 785 nm laser light. All of the maps were analyzed with WiRE 3.0 software. Streamline image acquisition is high speed spectral collection at varying lateral sample positions; therefore, it can permit fast data collection compared to point by point map particularly when a large area is required to be mapped. As illustrated in Figure 4.7, the S/N ratios would have been better by using 300 s exposure time. In addition, the background fluorescence obtained for these exposure time was about 600, 1560 and 2600 counts, respectively. As shown in

Figure 4.7, by using 100 s and 200 s exposure time, just the phenylalanine peak at 1003 cm^{-1} was observed. While in 300s exposure time, apart from phenyalanine band, other peaks at 740 cm^{-1} and 980 cm^{-1} became apparent.

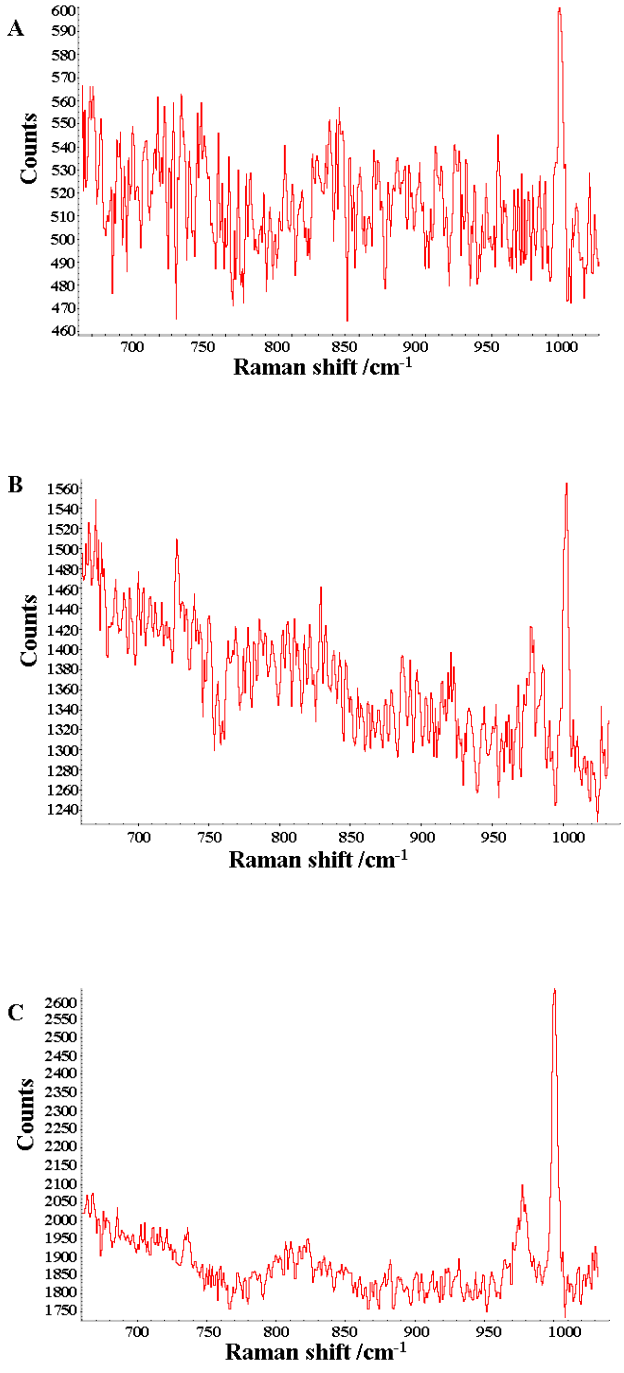

Figure 4.7: Exposure time optimization. Maps were taken by (A) 100s, (B) 200s, (C) 300 s exposure time.

All Raman maps of the brain tissue mounted on gold-coated silicon chips were recorded with 300 s exposure time and 10% power with 785 nm laser.

With Raman data collection, it is important to get the laser light as narrow as a spot size in order to observe the biochemical signatures located exactly in that area. The spectral acquisition setup on WiRE software allowed choosing the pinhole option. Technically, when the pinhole applied, the aperture size is reduced; therefore, it can improve the beam profile. As Figure 4.8A shows, the line focus laser can illuminate even the area out of the box, while the pinhole (Figure 4.8B) just focus on a small area to illuminate only that particular spot size.

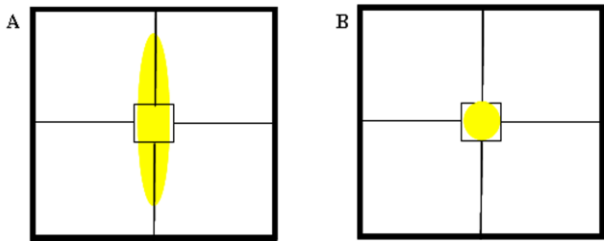

Figure 4.8: Schematic of line focus laser *vs.* pinhole

To study the effect of pinhole, the small maps were collected with and without pinhole on gold silicon slide by Kosta Jilkin (summer student in Dr. Gough's lab) and analyzed with both of us. As illustrated in Figure 4.9A, when the vertical line was mapped without pinhole, the silicon peak intensity started decreasing 10μm before the border of silicon-gold and the silicon band at 520 cm^{-1} was appeared even 10μm far away from the interface; while with utilizing pinhole, the Raman intensity of silicon band was very sharp before the silicon-gold interface and it was extinguished at the border line (Figure 4.9A, blue line). This test was tried for horizontal line, and there was no differ-

ence between the results obtained with pinhole and without pinhole (Figure 4.9B). It could point that the advantage of pinhole is for taking vertical map not the horizontal one.

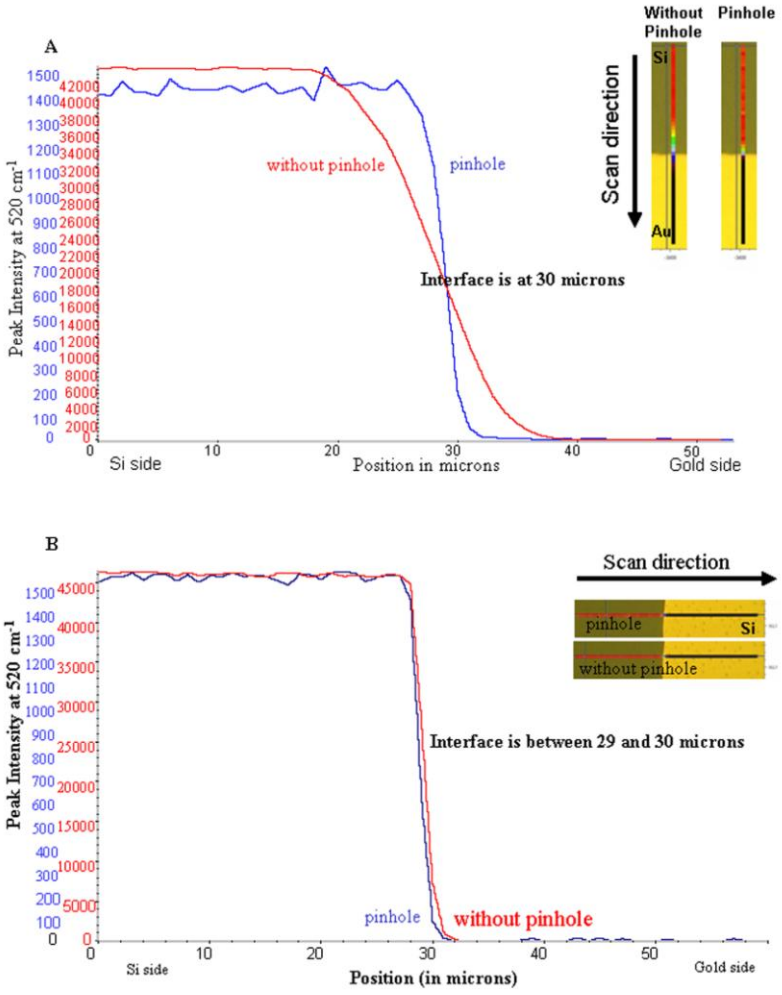

Figure 4.9: Peak intensity of silicon versus position of (A) vertical mapped line and (B) horizontal mapped line with pinhole (blue line), and without pinhole (red line)

To investigate the effect of pinhole on brain tissue spectra, some single scan tests were acquired on caudate tissue by using 10% laser power at 785 nm as the light source. As shown in Figure 4.10A-F, the test was performed first with 1 accumulation and 10, 20, 50, 100, 200, 300s exposure time. The signal to noise ratio was very low and just in

the spectra taken by 300s exposure time, two bands were observed at 640 cm^{-1} and 980 cm^{-1}. In other spectra, no significant tissue peak was obtained.

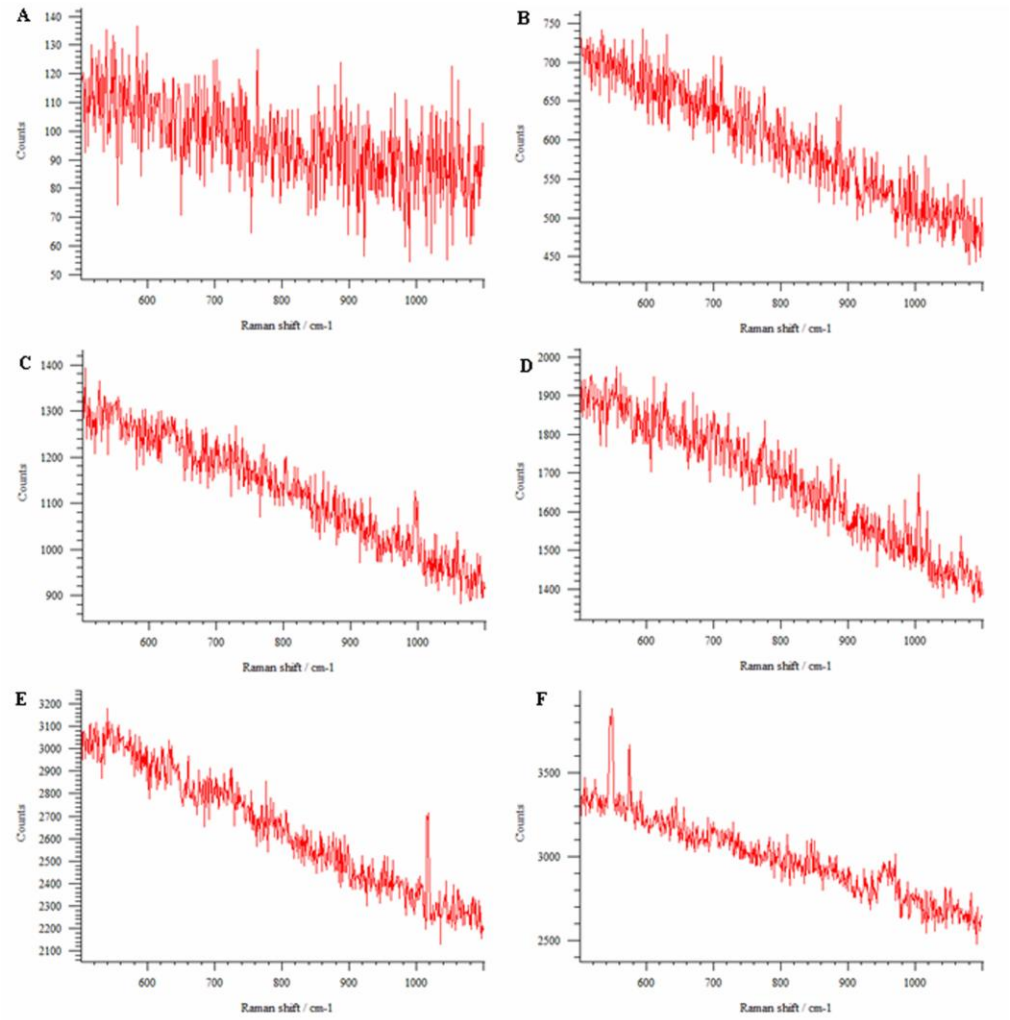

Figure 4.10: The Raman extended spectra taken with pinhole. Spectra were taken with using 1 accumulation and (A) 10, (B) 20, (C) 50, (D) 100, (E) 200, (F) 300s exposure time. All spectra were taken with 10% laser 785 nm. Spectral resolution and spatial resolution were 1 cm^{-1}/pixel and 2 µm , respectively. To get the extended spectra between 600-1800 cm^{-1} with pinhole, it took 5.5, 6.5, 8, 13, 26, 39 minute with 1 accumulation and 10, 20, 50, 100, 200, 300s exposure time, respectively.

In the next step, the single spectra were collected by using 10s exposure time and accumulation 10, 20, 50. Like the previous test, the signal to noise ratio was very low and no peak was observed (Figure 4.11 A-C).

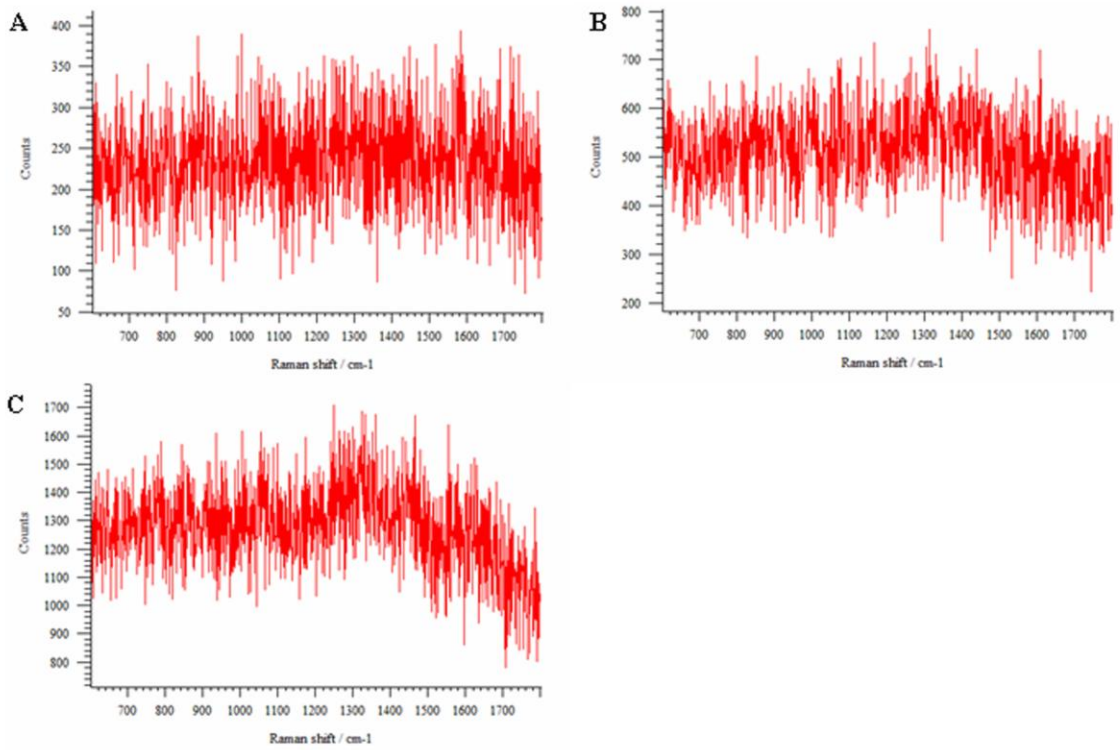

Figure 4.11: The Raman extended spectra taken with pinhole. Spectra were taken with using 10s exposure time and accumulation (A) 10, (B) 20, (C) 50. All spectra were taken with 10% laser 785 nm. Spectral resolution and spatial resolution were 1 cm^{-1}/pixel and 2 μm , respectively. To get the extended spectra between 600-1800 cm^{-1} with pinhole, it took 15, 30, 52 minute with 10s exposure time and accumulation 10, 20, 50, respectively.

The comparison of S/N ratio in two spectra taken without pinhole and with pinhole are present in Figure 4.12A and 4.12B, respectively. The exposure time in both spectra was 10s and the difference was only in accumulation which was 10 and 200 for taking spectra without and with pinhole, respectively. These parameters were chosen to get approximately the same S/N ratio (approximately equal to 3). As shown in Figure 4.12A-B, Cr bands were observed at 830, 916, 982 and 1054 $cm^{-1.}$ The other distinctive bands correspond to lipid bands at 1300, 1420, 1650 cm^{-1} and phenylalanine at 1003 cm^{-1}. To get the extended spectra between 600-1800 cm^{-1} with pinhole, it took 264 min while without pinhole it was 15 min. Empirically, this method can be useful when just very small point by point map is required to be collected, but for larger maps, time consuming is an impor-

tant issue and using pinhole is not feasible. This is the reason why all of the maps were collected by utilizing line focus laser instead of pinhole in this work.

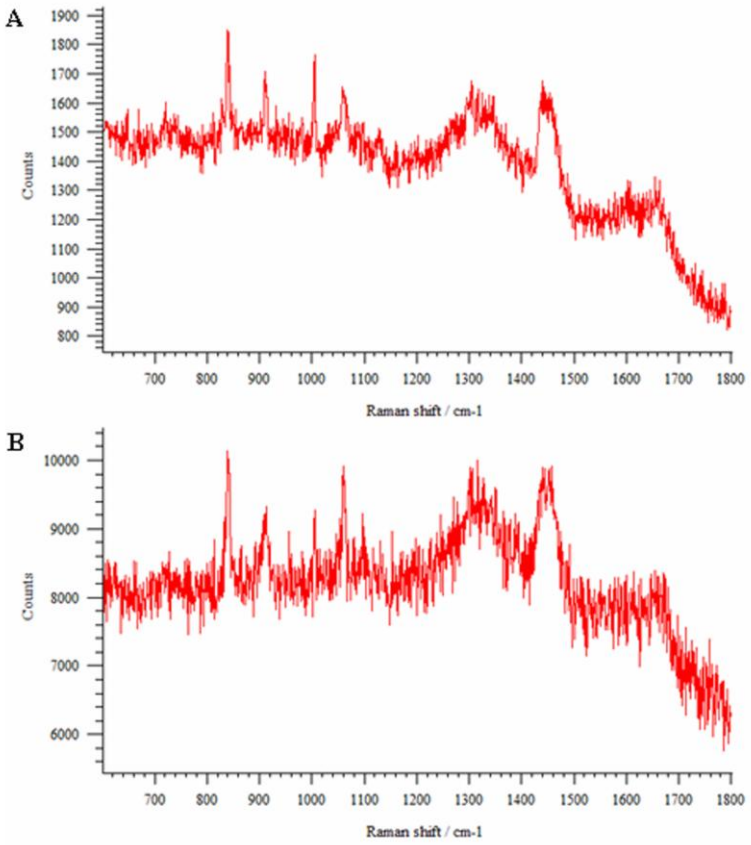

Figure 4.12: The Raman extended spectra taken (A) without pinhole and (B) with pinhole. Both spectra were taken with 10% laser 785 nm. Spectral resolution and spatial resolution were 1 cm^{-1}/pixel and 2 µm. The exposure time in both spectra was 10s and the difference was only in accumulation which was 10 and 200 for taking spectra without and with pinhole, respectively. The S/N in both spectra was around 3.

The Renishaw Invia Raman Microscope used for this research consists four different objectives (5, 20, 50, 100x) that permit imaging from larg scale rapid survey to sub-cellular high resolution maps. In this thesis, the 50x objective, having the best quality, was used for mapping of all the mouse brain samples. It should mention, although with this objective the laser spot size is supposed to be 2 microns, the spot size for the diode

laser 785 was actually a line; therefore, the spot size as determined by the microscope was slightly blurred in the y direction.

4.2 IR and Raman spectra of biochemical signatures in brain tissue

IR and Raman mapping were performed in the hippocampus and caudate of Tg and non-Tg control mice. Characteristic IR and Raman spectra for white matter, gray matter, plaque, neuron, and Cr in the transgenic mouse brain are shown in this section. The tissue bands were referred to literatures (Köhler et al, 2009; Movasaghi et al, 2008; Barth, 2007; Ellepola et al, 2006; Krafft et al, 2005; Stuart, 2004) . To characterize both IR and Raman Cr crystal vibrational modes, we performed combination of experimental and theoretical studies (using Gaussian software in collaboration with Fatemeh Farazkhorasani, another graduate student in Dr. Gough's group).

Tables 4.1& 4.2 summarize the main IR and Raman spectral peak positions of biological molecules in mouse brain tissue.

Table 4.1: Assignments of peaks in IR spectra of brain tissue

(Movassaghi 2007; Barth 2007; Stuart 2004; Wood et al, 1998; Dovbeshko et al, 1997; Fabian et al, 1995)

Peak position (cm^{-1})	**IR Assignment**
3400-3500	O-H stretching
3300-3200	N-H stretching
2956	Asymmetric CH_3 stretching in Lipid
2922	Asymmetric CH_2 stretching in Lipid
2871	Symmetric CH_3 stretching in Lipid
2852	Symmetric CH_2 stretching in Lipid
1670	C=O band in lipid
1662-1652	Amide I (α- helix)
1630-1620	Amide I (β-sheet)
1550	Amide II of proteins
1515	Tyrosine band
1466	C-H deformation of CH_2 in Lipid
1448	CH_2 scissoring in creatine
1423	δ(CH2), ν (CN), NH2 rock in creatine
1405	$\delta(CH_3)$ in creatine
1392	ν (COO^-), H_2O Scissor, CH_2 wag in creatine
1310	Amide III of proteins
1305	δ (CH2), NH2 rocking in creatine
1200-900	Sugar ring modes: C-O and C-C stretching, C-O-H and C-O-C deformations of carbohydrates
1250-1220	Asymmetric P=O stretching of PO^{2-} groups
1090-1085	Symmetric P=O stretching of PO^{2-} groups

Table 4.2: Assignments of peaks in Raman spectra of brain tissue

Peak position (cm^{-1})	**Raman Assignment**
3700-3450	N-H and O-H stretching modes
3550	O-H stretching
3232	N-H stretching
2960	Asymmetric vibration of CH_3 (γ_{as}) in lipid
2934	Asymmetric vibration of CH_2 (γ_{as}) in lipid
2885	Symmetric vibration of CH_3 (γ_s) in lipid
2851	Symmetric vibration of CH_2 (γ_s) in lipid
1670	Amide I (Antiparallel β-sheet)
1650	Amide I (α- helix)
1553	Amide II (α-helix, main secondary structure of protein and random coil)
1430-1440	CH_2 deformation of lipid
1445-1460	CH_3 asymmetric deformation, CH_3 bending modes of protein
1340	C-H bend, Phe
1300	CH_2 twisting mode of lipid
1296	Phospholipid CH2 twist and wagging, Amide III
1089	PO_2 asymmetric band of phospholipids
1085	PO_2 asymmetric band of nucleic acid (DNA and RNA)
1070	Glucose
1065	C=O stretching and C-O-C stretching and PO_2 symmetric stretch
1060-1095	PO_2^- stretching mode (DNA/RNA)
1054	Asymmetric vibration of C-N, CH_3 twisting in creatine
1032	CH_2CH_3 bending modes of phospholoipids
1030	Phenylalanine, CN stretching
1003	Breathing mode of phenylalanine of proteins
982	CH_2 rocking in creatine
980	C-C stretching β-sheet; =CH bending (unsaturated Lipid)
972	C-C backbone (Collagen assignment)
920	Distinct band corresponding to RNA
916	Symmetric vibration of (C-COO^-), NH_2 wagging in creatine
875	C-C stretching β-sheet
860	PO_2 asymmetric band of phospholipids
830	Symmetric stretching mode of the three CN^+ bonds in creatine
790	PO_2 asymmetric band of DNA and RNA
730	CN^+ stretching mode from the choline head in sphingomyelin
620	C-C twisting mode of Phenylalanine

4.2.1 IR and Raman spectra of white matter, gray matter, plaque and neuron in mouse brain tissue

IR spectra of mouse brain show absorption peaks due to the functional groups of the biological molecules. All IR spectra were taken in transflection mode using happ-Genzel appodization function and spectral resolution of 4 cm^{-1}, pixel resolution 5.5 x 5.5 μm.

The white matter and gray matter spectra shown in Figure 4.13 were mapped and processed for lipid distribution. The region from 3700-3100 cm^{-1} contains broad peaks corresponding to OH and NH stretching. The strong peaks at 2956 $cm^{-1}$and 2922 cm^{-1} are due to CH_3 and CH_2 asymmetric stretch modes and peaks at 2871cm^{-1} and 2851cm^{-1} are corresponded to CH_3 and CH_2 symmetric stretch modes, respectively. Gray matter shows very low intensity of the symmetric stretch CH_2 peak at 2851 cm^{-1} and carbonyl band at 1670 cm^{-1} (Fabian et al, 1995). Contrastingly, white matter which has high lipid content, displays high intensity of the lipid bands (Figure 4.13).

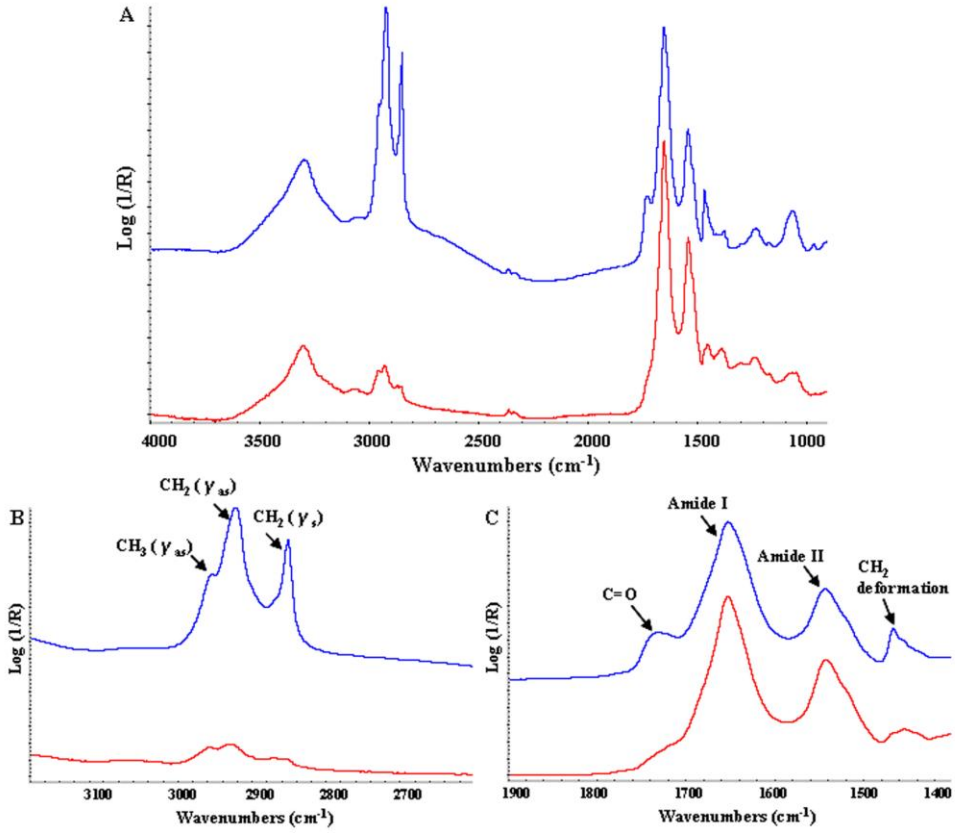

Figure 4.13: IR spectra of white matter and gray matter. (A) White matter (blue spectrum) has a high lipid concentration, causing intense CH_2 absorption. Contrastingly, Grey matter (red spectrum) shows low intense CH_2 absorption. (B) Enlarged IR spectra of white matter and grey matter between 3200-2600 cm^{-1} and (C) between 1900-1350 cm^{-1}.

The IR spectra of the neurons, densely-packed in the dentate gyrus, are characterized by low intensity of the symmetric CH_2 stretch peak at 2851 cm^{-1} and carbonyl band at 1670 cm^{-1}. As Figure 4.14B shows, the amide I band of proteins found at around 1665 cm^{-1} is due to α-helix in neurons, while the spectrum of plaque core as displayed in Figure 4.14B indicates a shoulder of α-helix at 1665cm^{-1} and small peaks between 1630-1620 cm^{-1} which is related to β-sheet secondary structure (Yoshida et al, 1997; Fabian et al, 1995).

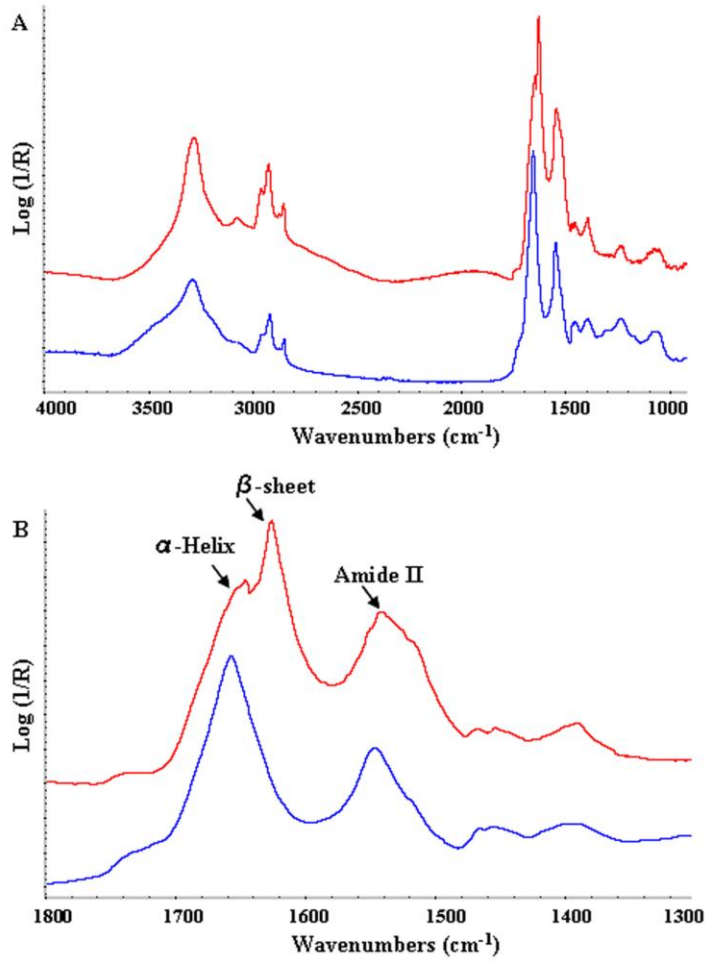

Figure 4.14: IR spectra of plaque and neuron. (A) IR spectra of plaque and neuron in hippocampus region is shown in the region between 4000-1000 cm^{-1}, and (B) enlarged between 1800-1300 cm^{-1}. Amyloid plaque shows a distinct Amide I doublet of β-sheet and α-helix compared to neuron which shows one peak at 1665 cm^{-1} due to α-helix.

Figure 4.15 illustrates the characteristic Raman spectra of lipid distribution in white matter and gray matter from 14 month-old TgCRND8 mouse brain mounted on gold-silicon chip slide. The difference between white matter and gray matter is useful to display morphology of tissue (Figure 4.15A&B). Raman spectra from white matter (red spectrum) and grey matter (blue spectrum) from 600-1700 cm^{-1} (Fig 4.15C) and 2650-4000 cm^{-1}(Fig 4.15D) were acquired with Renishaw inVia Raman microscope by using

10% laser power 785 nm. The spectra were performed with 10s exposure time and 30 accumulations. White matter shows typical profile of high lipid content, including many fatty acid ester peaks, and some protein bands. Gray matter is distinguished mainly by protein proxy: distinctive phenylalanine peak at 1003 cm^{-1}. The peaks at 2960 cm^{-1} and 2934 cm^{-1} are due to asymmetric CH_3 and CH_2 and peaks at 2885 cm^{-1} and 2851 cm^{-1} are due to symmetric CH_3 and CH_2, respectively (Köhler et al, 2009; Kolijenovic et al, 2005; Ong, 1999). The main differences for the two types of tissues were observed in the region of CH_2 stretching at 2851 cm^{-1} and bending modes at 1430-1440 cm^{-1} due to CH_2 deformation mode for lipid (Köhler et al, 2009; Krafft et al, 2005). This is consistent with the fact that the white matter of the brain tissue is rich in lipid membrane containing long acyl chain of CH_2 groups whereas the gray matter contains more cellular material: protein, sugar, phosphate, nucleic acid. The peak at 1445-1455 cm^{-1} is due to CH_3 bending mode of lipid (Köhler et al, 2009; Kateinen et al, 2007) and protein (Köhler et al, 2009; Lakshimi et al, 2002). Another peak that helps to differentiate the white matter and grey matter is that at 1300 cm^{-1}. This peak is particularly strong in the white matter compared with that in the gray matter and is assigned to the CH_2 twisting modes (Köhler et al, 2009). The other peak which is very strong in white matter is at 720-730 cm^{-1} due to CN^+ stretching mode from the choline head in phosphatidylcholine and sphingomyeline (Malini et al, 2006).

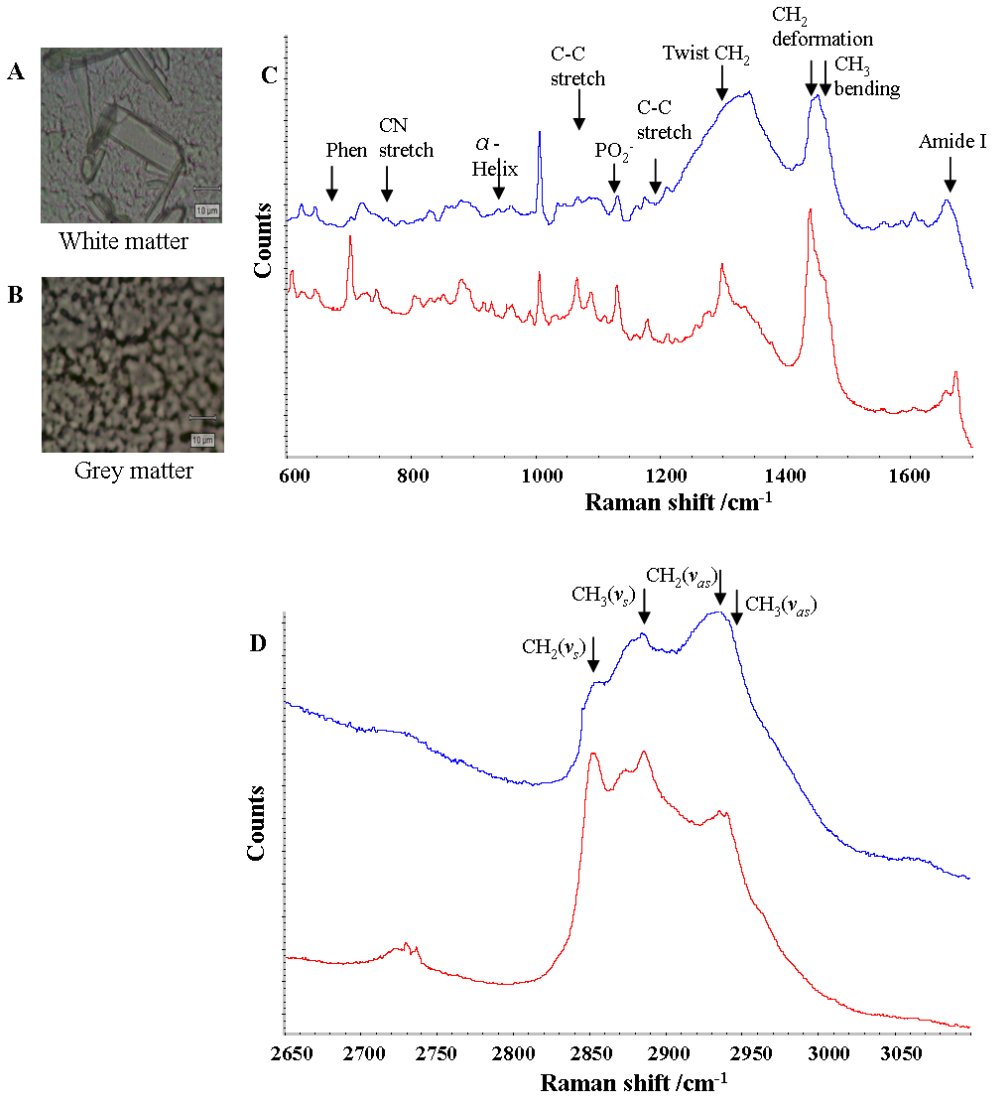

Figure 4.15: Raman spectra of white matter and grey matter. (A) Photomicrograph of white matter and (B) grey matter in caudate taken with 50x objective, 10% laser power 785 nm, 10s exposure time and 30 accumulations. Scale bar = 10 μm. (C) White matter (red spectrum), grey matter (blue spectrum) is shown in the region between 600-1700 cm^{-1}, and (D) 2650-4000 cm^{-1}. The white matter contains significant amount of lipids compared to grey matter.

Raman spectra collected with 785 nm laser excitation over the region 500-1800 cm^{-1} were obtained from a plaque in CA4 region of hippocampus and a neuron, located in the dentate gyrus (Figure 4.16). The Amide I peak of proteins, found at around 1650 cm^{-1}, is

due to α-helix in neurons (Ellepola et al, 2006), while the spectrum of plaque core as shown in Figure 4.16D indicates a broad band around 1670 cm^{-1} which is related to β-sheet secondary structure (Ellepola et al, 2006).

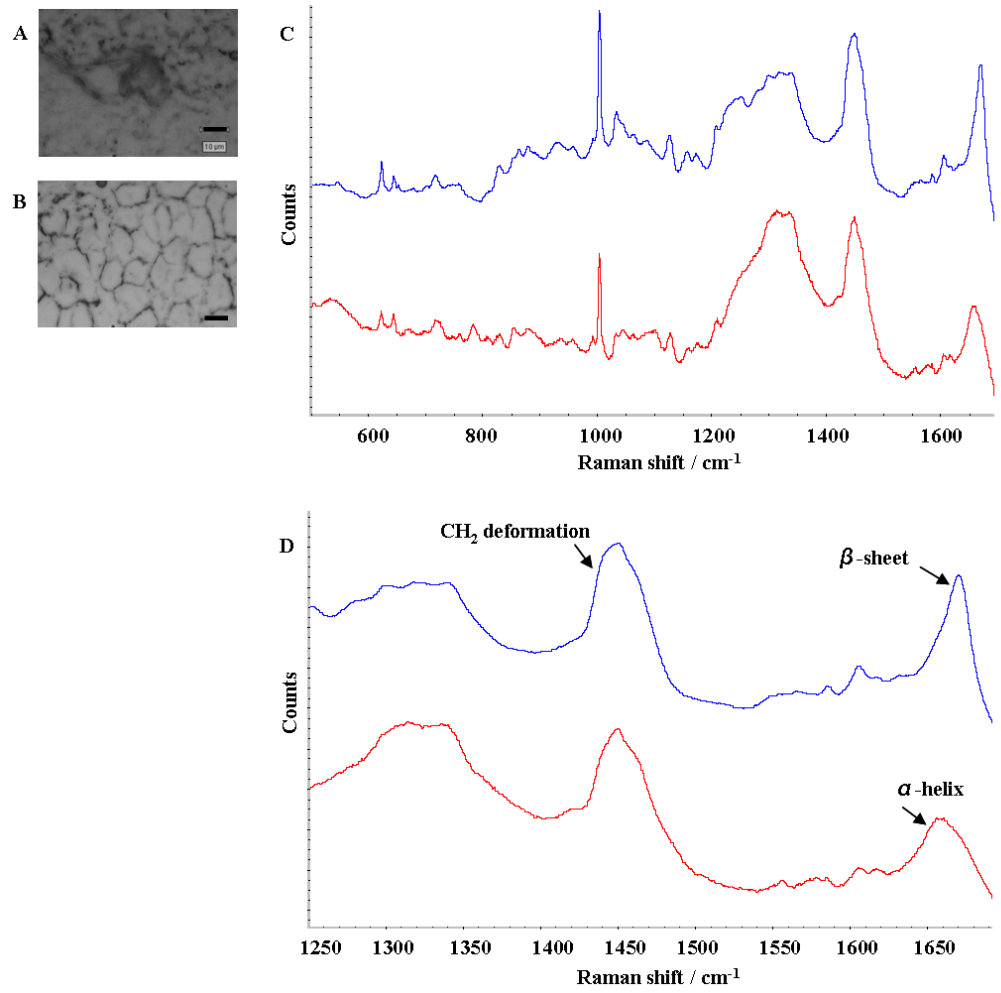

Figure 4.16: Raman spectra of plaque and neuron. (A) Photomicrograph of plaque in CA4 region of hippocampus and (B) neuron, located in the dentate gyrus taken with 50x objective, 10% laser power 785 nm, 10s exposure time and 30 accumulations. Scale bar = 10 μm. (C) Raman spectra of plaque and neuron in hippocampus region is shown in the region between 500-1700 cm^{-1} and (D) enlarged between 1250-1700 cm^{-1}. The peak at 1650 cm^{-1} is due to α-helix in neurons, while the spectrum of β-sheet was observed at 1670 cm^{-1}.

4.2.2 IR and Raman creatine peak assignments from experimental and theoritical studies

In this thesis, we investigate the vibrational modes of creatine to calrify the spectral analysis of creatine crystals found in barin tissue. Experimental results obtained from FTIR and Raman were compared with calculations at B3LYP/6-311G (d,p) level of theory. The theoretical calculation was performed by Fatemeh FarazKhorasani (Graduate student in Dr. Gough's lab). A detailed vibrational analysis of Cr was carried out based on density functional theory (DFT) calculations of the neutral, anionic, cationic, and Cr monohydrate form to characterize the principal bands chosen for Cr identification. Particular bands which show the most affect when polarizer applied (see section for more information) for IR and Raman analysis were characterized through DFT calculations, performed within the Gaussian program with the B3LYP functional and 6-311G (d,p) basis set. From all of the computed forms, the results obtained with Cr monhydrate were much closer to the experimental acquired data.

Two orientations of the creatine monohydrate optimized structure are displayed in Fig. 4.17. It can be seen that a CN_3 stretching coordinate (green arrows, left figure) must lie in a plane that is nearly perpendicular to the plane of a COO^- stretching coordinate (blue arrows, right figure), while the C-C bond is perpendicular to both. These intrinsic features of the structure are postulated to be the basis of the responses observed in modes excited by polarizations of light.

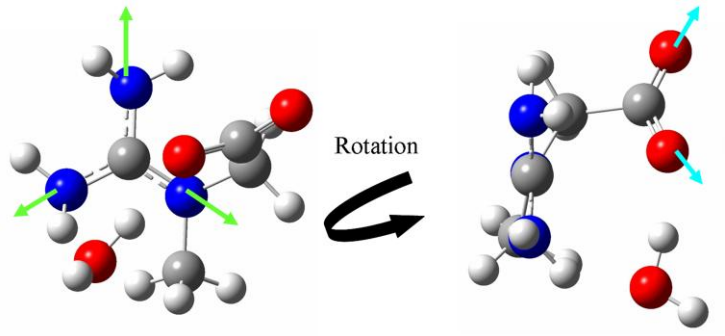

Figure 4.17: Creatine monohydrate after optimization-rotated aspect to show CN_3 relative to COO^-.

Figure 4.18 illustrates the atom numbering of Cr monohydrate. The calculated IR spectra in the region of interest are dominated by 5 well-resolved bands at 1275, 1321, 1331, 1455, and 1478 cm^{-1} (Table 4.3). Based on Table 4.3, the observed 1305 and 1405 cm^{-1} peaks might be assigned to CH_2 deformation + NH_2 rocking and CH_3 deformation that appear in 1275 and 1455 cm^{-1}, respectively. These two bands are the most affected bands when polarizer was utilized (see section 4.5 for more information about orientation dependence of this IR bands). In addition, the experimental peak at 1392 cm^{-1} and 1423 cm^{-1} are related to symmetric vibration of C4O8O9 + CH_2 wagging and CH_2 deformation + CN stretching, NH_2 rocking which can be seen at 1321, and 1331 cm^{-1} in the theoretical calculations, respectively.

As illustrated in Table 4.3, the very strong Raman band at 830 cm^{-1} is due to the symmetric stretching mode of the three CN^+ bonds. This mode was very distinctive in the Raman spectra of brain tissues; therefore, it was selected for identification of Cr distribution, and pure Cr crystal. The relative intensities of bands at 912, 982, and 1054 cm^{-1} were stronger with polarizer & half-wave plate compared to using polarizer. These Cr bands (912, 982, 1054 cm^{-1}) are assigned to symmetric vibration of C3C4OO$^-$, CH_2 de-

formation, and symmetric vibration of CN_3 + CH_3 rocking, respectively. These Raman peaks were present at 812, 853, 964, 1040 cm^{-1} in theoretical calculation, respectively. The depolarization ratios from the calculation for these three bands were 0.07, 0.27, 0.10, respectively. A Raman band with the depolarization ratio less than 0.75 is polarized band.

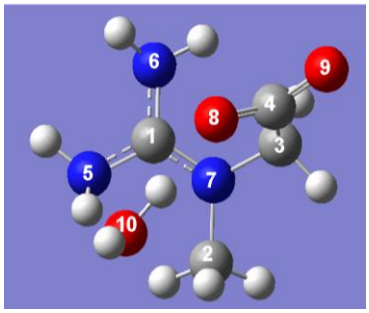

Figure 4.18: Atom numbering of $Cr.H_2O$

Table 4.3: IR and Raman assignments of the most affected modes in Cr.

Modes	**Experimental**				**Calculation**				
	IR		**Raman**		**IR**		**Raman**		
	Frequency	**Intensity**	**frequency**	**counts (*10^3)**	**Frequency**	**Intensity**	**frequency**	**activity**	**Depol-arization ratio**
CH_2 scissor	1448	0.18			1478	15.14			
$\delta(CH_3)$	1405	0.04			1455	15.39			
$\delta(CH_2)$, ν (CN), NH_2 rock	1423	0.26			1331	13.85			
ν (COO^-), H_2O Scissor, CH_2 wag	1392	3.53			1321	213.61			
δ (CH_2), NH_2 rock	1305	0.62			1275	30.37			
ν (CN_3), CH_3 rock			1054	17			1040	15.18	0.10
δ (CH_2)			982	6.5			964	3.24	0.27
ν (C-COO^-), δ(O=C=O)			916	20.8			853	9.80	0.07
ν (CN_3), OH wag			830	56			812	10.25	0.10

ν: stretching; w: wagging; δ: deformation, frequencies (cm^{-1})

FTIR and Raman are effective microspectroscopic thecinques for molecular structure determination especially when coupled with theoritical methods.

Figure 4.19 displays IR spectra of creatine in brain tissue (red spectrum), pure creatine (blue spectrum), and normal tissue (green spectrum) taken in the region between 4000-1000 cm^{-1}. As obtained from theoritical studies, the peaks at 1305 cm^{-1} due to deformation of CH_2 + NH_2 rocking and the peak at 1405 cm^{-1} assigned to deformation of CH_3 were used for identification of creatine in brain tissue, because these peaks had less overlap with tissue bands compared to other Cr peaks. Another distinct Cr peak observed at 1392 cm^{-1} is due to symmetric vibration of COO^- and CH_2 wagging. As shown in Figure 4.19B, all three peaks, 1305 cm^{-1} and the doublet at 1392 and 1405 cm^{-1} were observed with FPA-FTIR spectra; however the creatine spectra taken by synchrotron FT-IR gave different spectra for various deposits (see section 4.5.1 for more detail).

The normal tissue spectra (green spectrum) were composed of the broad absorbance at 3300 cm^{-1} which is due to NH and OH stretching (Dovbeshko et al, 1997). The peaks at 2956 cm^{-1} and 2922cm^{-1} are due to asymmetric CH_3 and CH_2 and peaks at 2871 cm^{-1} and 2851 cm^{-1} are due to symmetric CH_3 and CH_2, respectively. Amide I band of proteins was found at 1660 cm^{-1}, followed by the amide II 1550 cm^{-1}, amide III and phosphate assigned at 1240cm^{-1}. The peak at 1080 cm^{-1} is due to symmetric phosphate stretch overlapped with sugar bands (Wood et al, 1998).

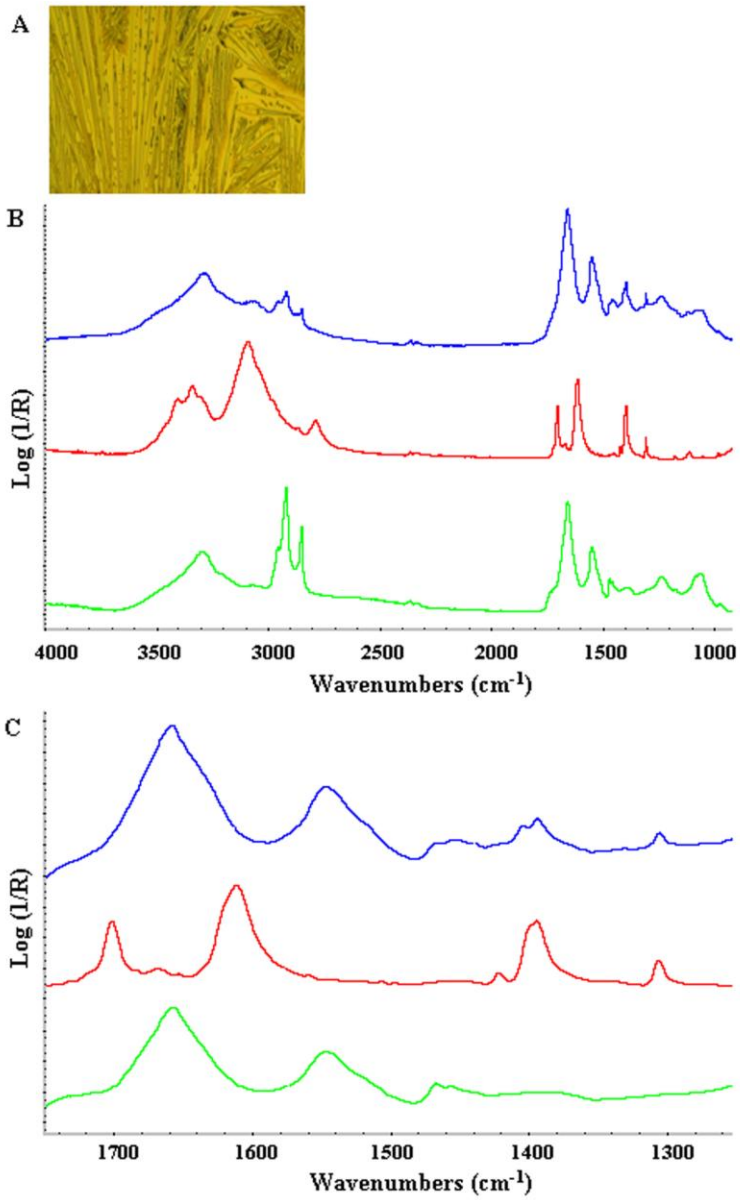

Figure 4.19: Identification of creatine in mouse brain tissue by IR microscope. (A) Pure Cr monohydrate crystals taken by 15x objective. (B) The IR spectrum of creatine in brain tissue (red spectrum), pure creatine (blue spectrum), and normal tissue (green spectrum) is shown in the region between 4000-1000 cm^{-1}, and (C) enlarged between 1800-1250 cm^{-1}. The peaks at 1305 cm^{-1} and 1405 cm^{-1}were used for identification of Cr in brain tissue, because these peaks had less overlap with tissue bands compared to other Cr peaks.

Figure 4.20 displays the Raman spectra of creatine in brain tissue (red spectrum), pure creatine (blue spectrum), and normal tissue (green spectrum) taken in the region between 550-1650 cm^{-1}. The spectra were recorded with spectral resolution of 1 cm^{-1}/ pixel and spatial resolution of 2 μm. As illustrated in Figure 4.20B, the very strong Raman band at 830 cm^{-1} is due to the symmetric stretching mode of the three CN^{+} bonds. This bond is very distinctive in the Raman spectra of tissues and was selected for identification of Cr distribution, and pure Cr crystal. The other Cr bands observed in both pure Cr spectrum and Cr in brain tissue are peaks at 916 cm^{-1}, assigned to symmetric vibration of (C-COO^{-}) and O=C=O deformation; a peak at 982 cm^{-1} assigned to CH_2 rocking, and a peak at 1054 cm^{-1} assigned to asymmetric vibration of CN, and CH_3 twisting. As displayed in Figure 4.20B, in normal tissue and Cr in brain tissue spectrum, two strong bands were observed at 730 cm^{-1} and 1003 cm^{-1}, assigned to CN stretching mode from the choline head in sphyingomyelin and breathing mode of phenylalanine, respectively (Chan et al, 2006; Krafft et al, 2005).

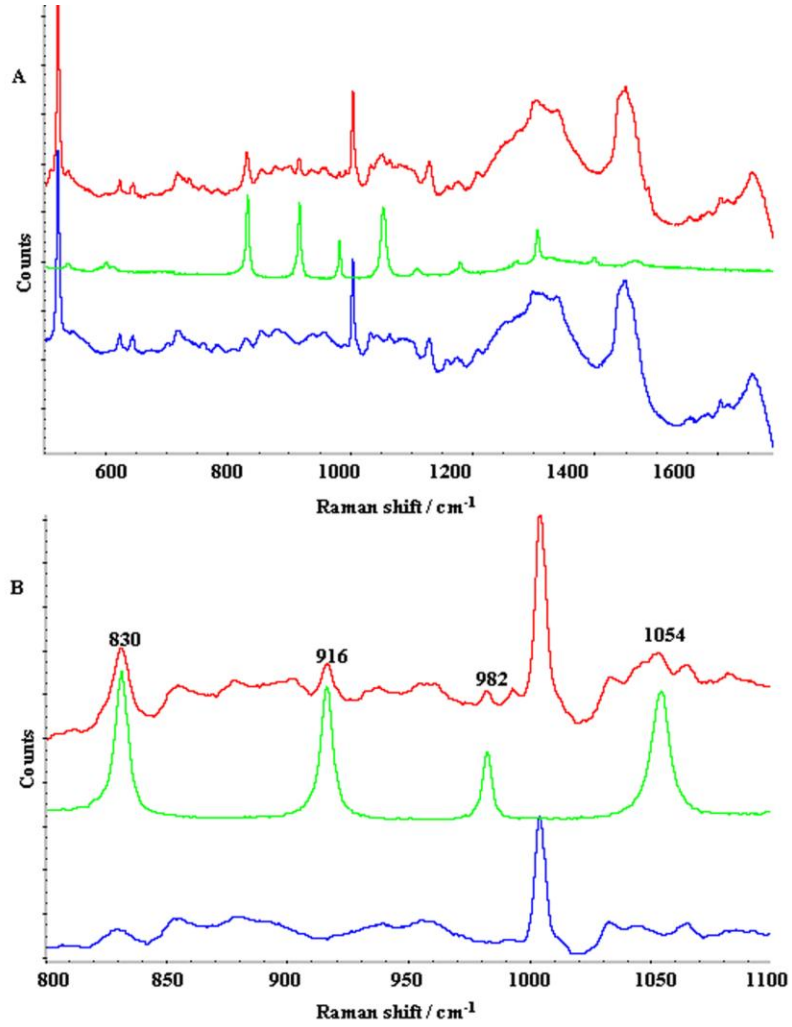

Figure 4.20: Identification of creatine in mouse brain tissue by Raman microscope. (A) The Raman spectrum of creatine in brain tissue (red spectrum), pure creatine (blue spectrum), and normal tissue (green spectrum) is shown in the region between 550-1650 cm-1and and (B) enlarged between 800-1100 cm-1. The peak at 1650 cm^{-1} The peaks at 830, 916, 982, and 1054 cm^{-1} were used for identification of creatine in brain tissue.

4.3 Infrared and Raman analysis processing tools

Characteristic IR absorbance bands were used to analyze IR spectra for creatine, lipid and plaque distribution. Data acquired with Thermo-Nicolet FTIR continuum microscope at SRC, University of Wisconsin, were reprocessed at 1408-1384 cm^{-1}, because the creatine spectra taken by synchrotron FTIR Microscope gave different spectra for various deposits. All data acquired by Varian FPA-FTIR microscope were analyzed by using Resolution-Pro software to investigate the effect of synchrotron polarized light on Cr crystal orientation in brain tissue. Since IR and Raman spectromicroscopy techniques are compatible, the same region was imaged by Raman at higher spatial resolution (2 μm). All the Raman data were analyzed by using WiRE software.

4.3.1 IR Processing using Omnic software

For reprocessing of Cr to investigate Cr distribution in serial sections from the hippocampus of 14 months transgenic mouse with Omnic/Atlμs, the absorbance at 1412 cm^{-1} and 1380 cm^{-1} were set as baseline values, and the area of peak between 1408-1384 cm^{-1} was measured (Figure 4.21). The colours ranging from blue (low) to red (high) were assigned to display the distribution of creatine peaks.

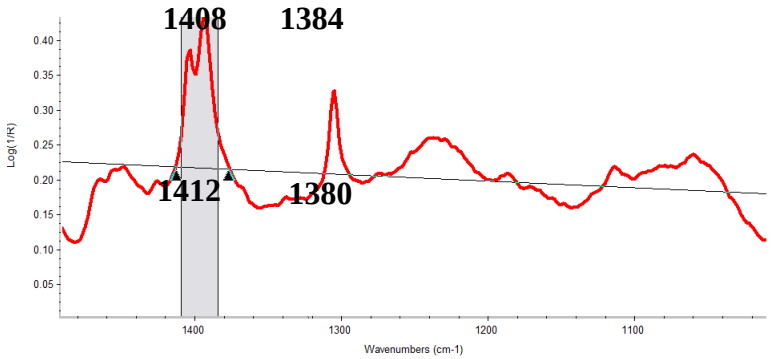

Figure 4.21: Creatine processing parameter using Omnic/Atlμs software processed at 1410-1384 cm^{-1}.

4.3.2 IR Processing using Resolution-Pro software

More than 200 FPA-FTIR maps were taken and analyzed for creatine, lipid and plaque distribution in mouse brain tissue. Maps were created by representing the distribution and intensity of peaks of interest on a color scale from blue (low) to red (high). To study the effect of polarized light, all data obtained with polarizer were processed with specific focus on peaks at 1305 cm^{-1} (1308-1302 cm^{-1}, baseline 1316, 1294 cm^{-1}) (Figure 4.22A) and 1405 cm^{-1}(1408-1402 cm^{-1}, baseline 1410, 1400 cm^{-1}) (Figure 4.22B), as these exhibited extreme polarization effects and had less overlap with tissue bands compared to other Cr peaks.

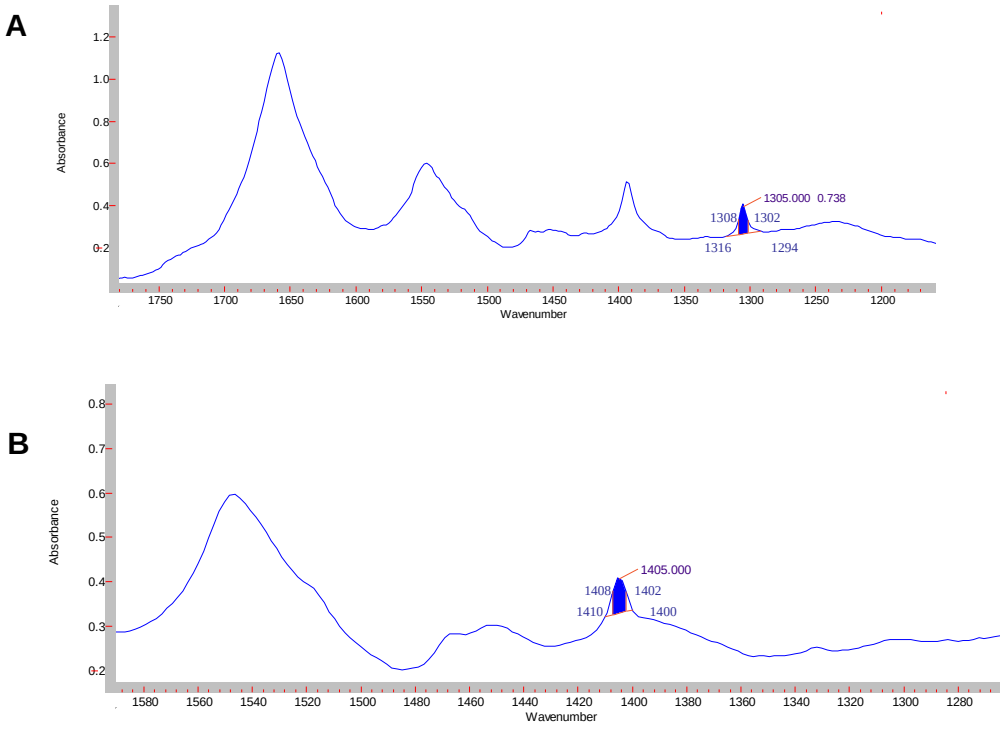

Figure 4.22: Creatine processing parameter using Resolution Pro-software. (A) Processed at 1305 cm^{-1}, and (B) 1405 cm^{-1}.

Aβ plaque was processed through a ratio of the β-sheet Amide I (1662-1665cm^{-1}, base line 1806-900cm^{-1}) to α-helix Amide I (1630-1620cm^{-1}, base line 1806-900cm^{-1}). These parameters for Aβ plaque processing were set up by Dr. M. Rak (former Ph.D. student in Dr. Gough's group).

For lipid analysis, maps were processed using parameters for the symmetric CH_2 band of 2858-2844 cm^{-1}, base line 3012-2750 cm^{-1} (Figure 4.23A) , and for lipid carbonyl band of 1750-1720 cm^{-1}, base line 1761-1704 cm^{-1} (Figure 4.23B).

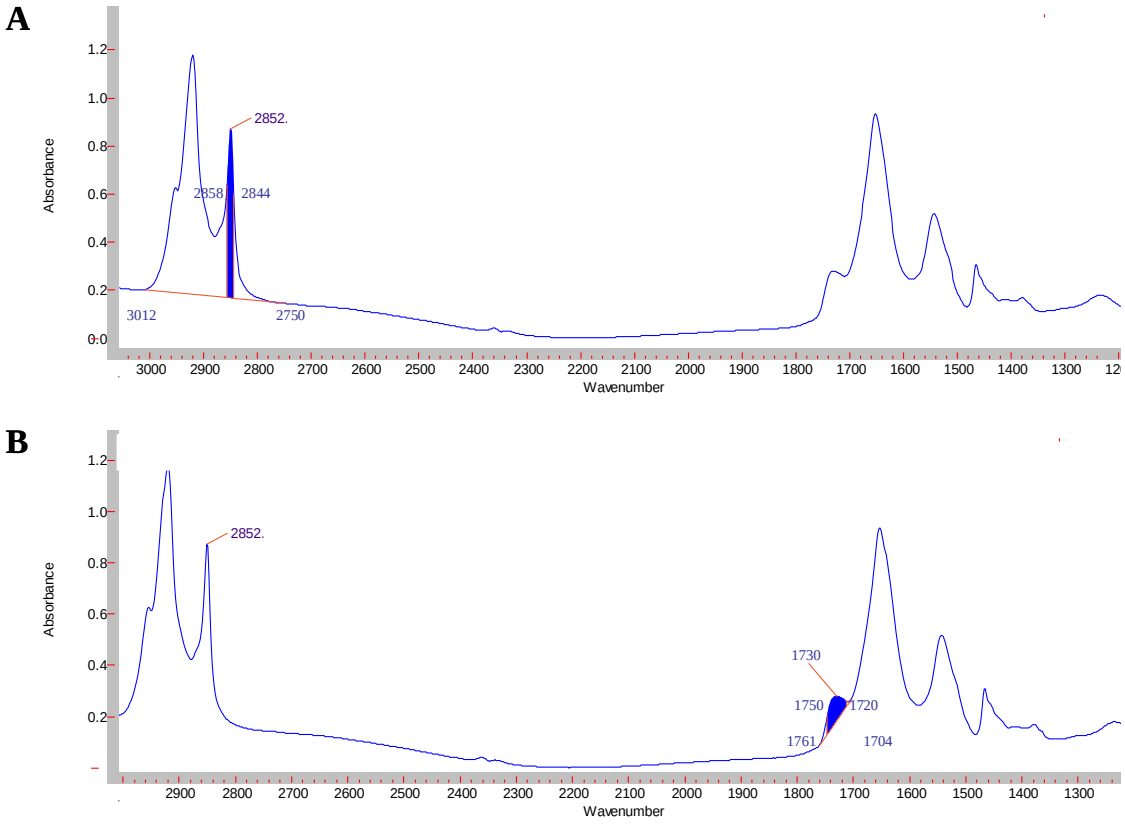

Figure 4.23: Lipid processing using Resolution-Pro software. (A) Processed for symmetric CH_2 band at 2852 cm^{-1} and (B) lipid carbonyl band at 1730cm^{-1}.

4.3.3 Raman processing using WiRE software

All maps were analyzed with WiRE software (version 3.0, Renishaw). A processing option that measures signal to baseline was used to create false colour map display from collected data. Signal to baseline processing option used two vertical cursors to define the limit between which the integrated area was calculated. The LUT control was used to change the colour and brightness of a created map. The colors ranging from black (low) to white (high) were assigned to show the distribution and intensity of peaks of interest.

For analysis of Cr with WiRE software, the brain tissue maps were processed at 830 cm^{-1} because this band is very strong for Cr crystal and has less overlap with tissue bands compared to other Cr peaks. The peak area at 830, 914, 992, 1054 cm^{-1} were found to be adequate to confirm detection of all Cr deposits within the tissue. All of the Raman maps were processed at 830 cm^{-1} assigned to symmetric CN^{+} stretch band to identify Cr in brain tissue. As shown in Figure 4.24, the signal to baseline was taken between 824 cm^{-1} and 848 cm^{-1} for Cr.

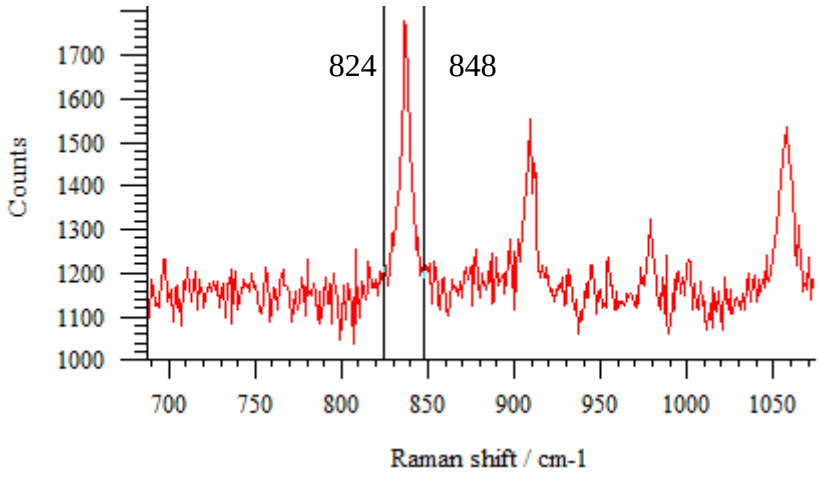

Figure 4.24: Creatine processing parameters using WiRE software

For analysis of Aβ plaques, all the Raman maps were processed at peak area 1670 cm^{-1} which is assigned to anti-parallel β-sheet. As illustrated in Figure 4.25, the signal to baseline was taken between 1657-1680 cm^{-1} for detection of Aβ dense cored plaques within the tissue.

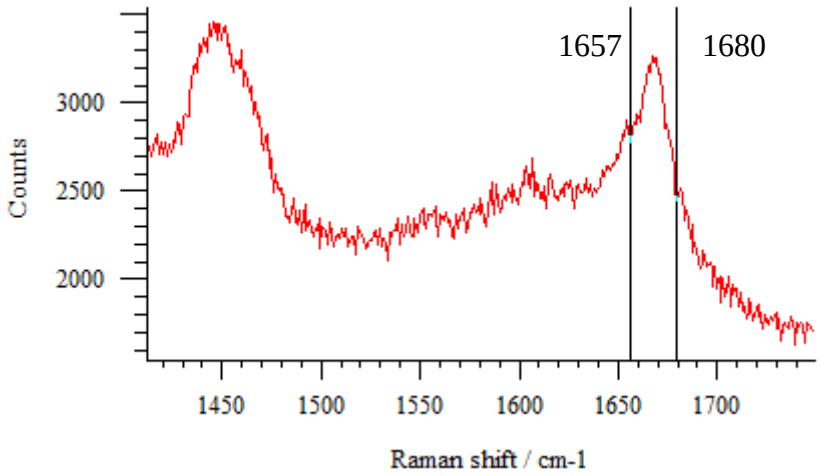

Figure 4.25: Plaque processing parameters using WiRE software.

Maps were processed using parameters for the CH_2 deformation band of lipid at 1440 cm^{-1} and for CN stretching of sphingomyelin at 730 cm^{-1}. For analysis of lipid, a strong peak at 1430-1440 cm^{-1} was selected and the area between 1420-1460 cm^{-1} was evaluated (Figure 4.26A). As illustrated in Figure 4.26B, to create the map based on the intensity of the CN stretching mode at 730 cm^{-1}, the area between 706 and 750 cm^{-1} was taken.

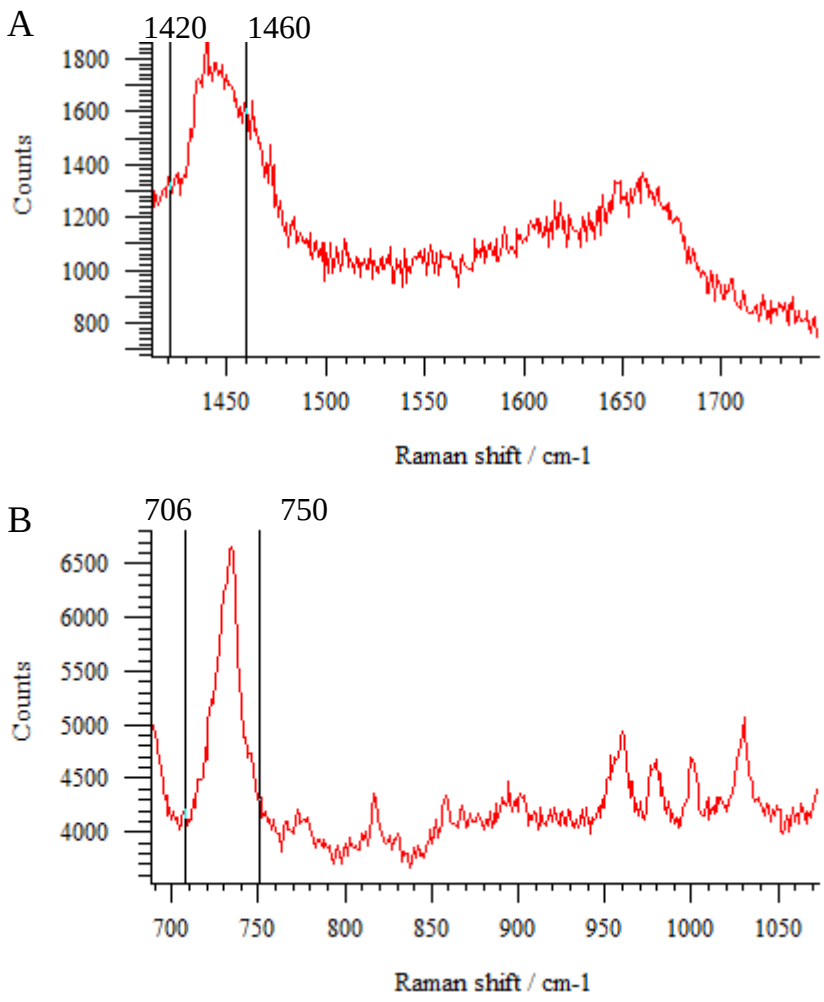

Figure 4.26: Lipid processing parameters using WiRE software. **(**A) Processing of lipid (CH_2 deformation of at 1440 cm^{-1}) and B) sphingomyelin (CN^+ stretching mode at 730 cm^{-1}).

4.4 Analysis of creatine and distribution of creatine in mouse brain tissue

As mentioned, with using FTIR imageing to study snap-frozen, unfixed tissue sections from transgenic mouse brain, some unusual spectral signature was initially found in several maps (Rak, 2007). This spectrum was identical to spectra observed in IR maps of human AD brain (Ogg, 2002). A spectral library search identified it as Creatine. The first publication reported the in situ detection of focally elevated creatine deposits in Tg mouse brain and post mortem AD brain tissue (Gallant et al, 2006). It was shown that creatine was found more in size and number in hippocampus of mouse brain compared to their non-transgenic littermate and increased with age (Kuzyk et al, 2010).

In this thesis, the main goal was to find clues to the origin of creatine in transgenic mouse brain tissue. Since the creatine deposits were found in frozen and desiccated brain tissue, it was important to investigate whether these creatine deposits were formed after snap freezing and dessication of brain tissue or any other possibility cause formation of these crystals like synthesis in situ or transfering cross blood brain barrier.

In this section the imaged blood bvessels were explained, followed by a discription of depth profile of creatine and environs by Raman microscope and imaged large area of caudate by FPA-FTIR.

4.4.1 Creatine deposits and blood vessel

Processed IR maps revealed that almost all of the larger deposits, found in the older transgenic mice, took the form of streak and these larger deposits were not usually associated with plaques (Rak M, 2007). Since Cr can be endogenously synthesized in the liver

and kidney and carried out through the blood brain barrier (BBB) by Cr transporters (CrT) to get into the brain, this could point to an association with blood vessels and Cr deposits. To understand it better, two blood vessels in hippocampi of four transgenic mice was mapped in different ages (8, 11, 14, 17 months-old) by FPA-FTIR microscope. Figure 4.27, Row A1-4 illustrate blood vessel in hippocampus region of these four transgenic mice. All maps were taken by Varian FPA-FTIR Microscope. The 64 x 64 element FPA detector simultaneously collected 4096 spectra from an area of analysis of 350 x 350 μm in spatial resolution 5.5 x 5.5 μm. Each pixel on the FPA gave an individual IR spectrum. In order to get the highest S/N ratio, 1028 scans were summed for the single tile map. The acquisition time with this scan number was 53 min. All spectra were collected in reflectance mode from 4000 to 900 cm^{-1} at 4 cm^{-1} spectral resolution, using Happ-Genzel apodization function. The background spectra were taken both on Mirr-IR slide and gold silicon chips slide since two transgenic mice (5 and 8 month-old) were mounted on Mirr-IR and the others (14 and 17 month-old) were mounted on gold coated silicon slide. IR maps were processed for Cr at 1410-1384 cm^{-1} (Row B1-4), lipid symmetric CH_2 stretching band at 2853 cm^{-1} (Row C1-4) and for lipid carbonyl at 1733 cm^{-1} (Row D1-4). In the colour scale, red corresponds to high intensity and dark blue to no signal. As shown in Figure 4.27, a Cr streak appeared around the blood vessel in hippocampus of 5 month-old transgenic mouse (shown by arrow in Figure 4.27, Row B1). The Cr crystal deposits were smaller in 8 and 14 month-old Tg mice (indicated by arrow in Figure 4.27, Row B2-3). No Cr was found in the blood vessel in hippocampus region of 17 month-old TgCRND8 mice (Figure 4.27, Row B4). The Figure 4.427 Row C1-4 & D1-4 display symmetric CH_2 and lipid carbonyl distribution in the blood vessel area in hippocampi of

these Tg mice, respectively. As shown in Figure 4.27, no correlation was found between Cr deposits and lipid distribution.

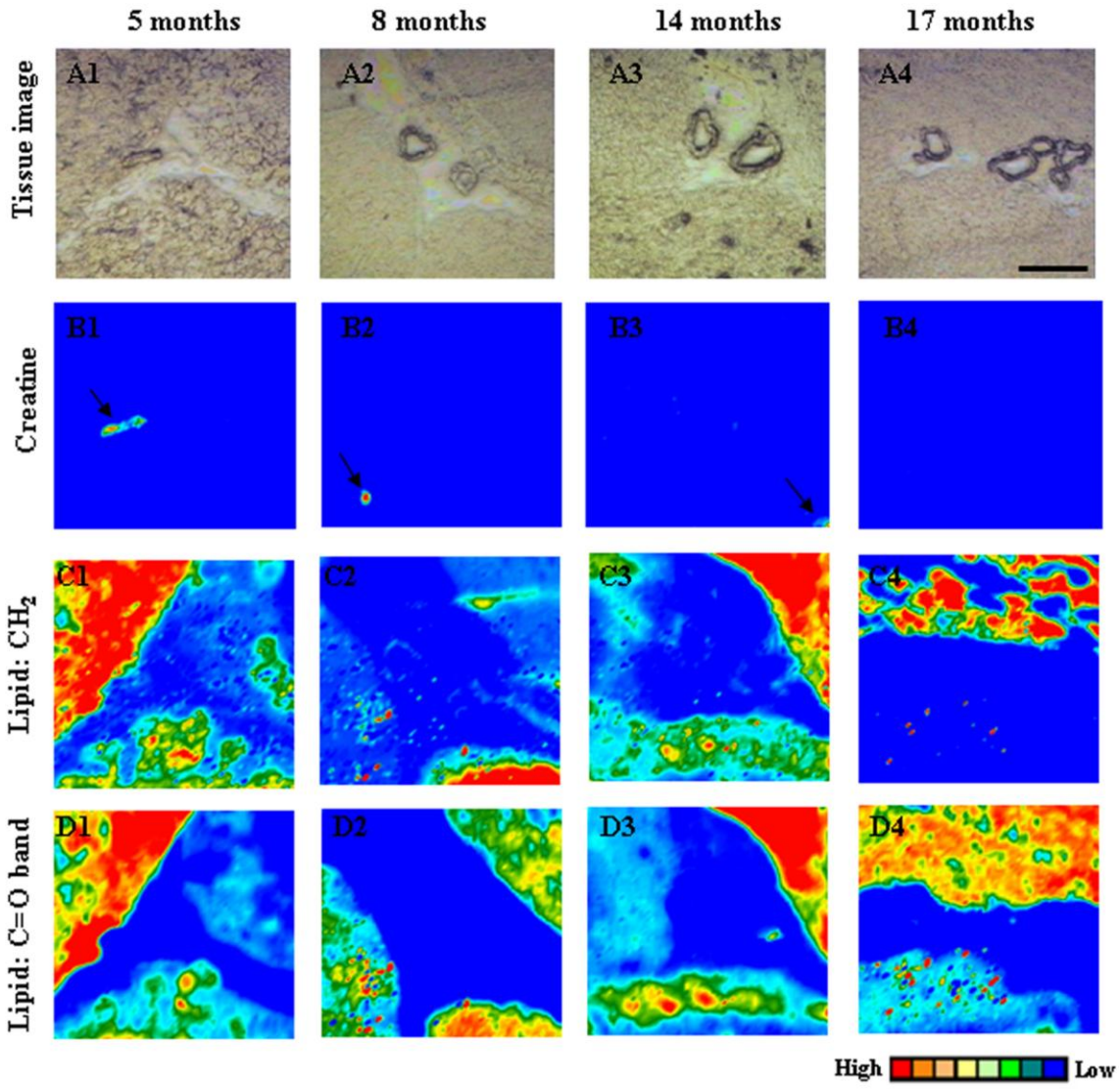

Figure 4.27: IR maps of blood vessel in mouse hippocampi through age (8, 11, 14, 17 months-old). (Row A1-4) illustrate blood vessel in hippocampus region of transgenic mice at 5, 8, 14 and 17 month-old. IR maps were processed for Cr (Row B1-4), for lipid symmetrical CH_2 stretching band of lipid (Row C1-4) and for lipid carbonyl (Row D1-4). Map area = 350 x 350 µm. Acquisition time = 53 min. Scan number = 1028. Colour scale: red corresponds to high intensity, dark blue to no signal. Scale bar = 100 µm.

To probe whether any Cr was within the blood vessel in hippocampus, the depth profile analysis were undertaken by Raman Microscope in serial sections of 14 months-old. IR and Raman are compatible if the sample is on a gold substrate; the same section can be mapped by FTIR and then by Raman, repeatedly. The Raman spectra can be obtained at higher spatial resolution (1-2 μm for Raman compared to 5.5 μm for FPA-FTIR). Figure 4.28-36A illustrate blood vessel in hippocampi through nine consecutive serial sections (A14 (10-19)) from 14 month-old TgCRND8 mounted on gold coated silicon chip slide. A14 (10-17) were serial to one another, and A14 (19) section was separated by only one missing section. These areas were mapped by Raman InVia Renishaw. Streamline maps were acquired for each section with the spectral resolution 1 cm^{-1}/pixel and spatial resolution of 2 μm, using 50x objective. The exposure time for all the maps was 300 seconds to improve S/N ratio. In order not to create any charcoal, 10% laser 785 nm was used. Raman spectra were recorded across a spectral range of 685 to 1075 cm^{-1} (centred at 880 cm^{-1}) detected by (CCD) detector. These Raman maps were processed for sphingomyelin (CN^+ stretching mode at 730 cm^{-1}) (Figure 4.28-36B), and for Cr (symmetric band CN_3^+ band at 830 cm^{-1}) (Figure 4.28-36C). As illustrated in Figure 4.56, just a few Cr deposits came through blood vessel in hippocampus of A14(19). No significant Cr deposits were noticed in any other sections. The collected maps were analyzed and some other peaks correspond to phospholipids (phosphate group at 900 and 960 cm^{-1}), phosphodiesters (at 900 and 820 cm^{-1}), lipid band (=CH bending of unsaturated lipid at 980 cm^{-1}) and phenylalanine (at 1003 cm^{-1}) was observed within most of the mapped blood vessel. (Figure 4.28-36).

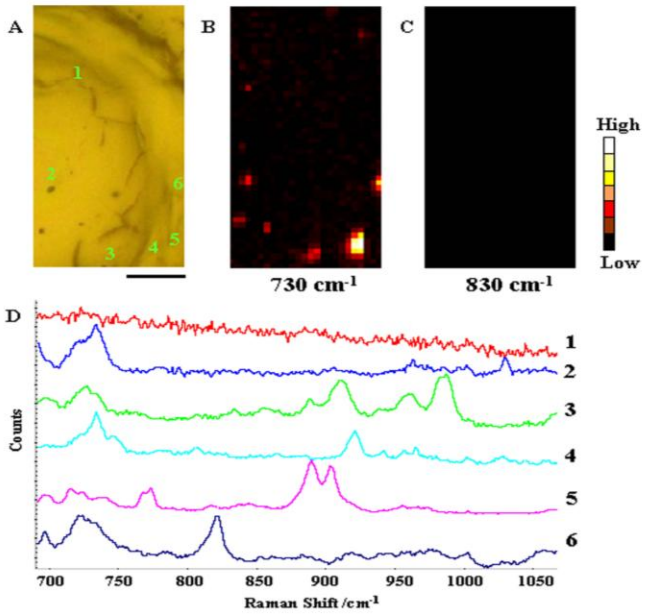

Figure 4.28: Depth Profile of blood vessel in hippocampus through A14(10) section of transgenic 14-month-old mouse brain. (A) Close-up of the mapped blood vessel in hippocampus. Processed map for (B) sphingomyelin (CN^+ stretching mode at 730 cm^{-1}), (C) Cr (symmetric band CN_3^+ band at 830 cm^{-1}). Map area = 1275 points. Acquisition time = 270 min. Colour scale: White corresponds to high intensity, black to no signal. Scale bar = 10 µm. (D) spectra (1-6) were correspond to the points illustrated in tissue image. Spectrum (1): just noise. Spectrum (2): sphengomyelin (C-N mode at 730 cm^{-1}); phenylalanine. Spectrum (3): broad band at 730 cm^{-1} due to C-N mode of choline; phosphate peaks at 900 and 960 cm^{-1}; peak at 980 cm^{-1} assigned to =CH bending of lipid; 925 cm^{-1} assigned to *v* (C-C) stretching probably in amino acids proline. Spectrum (4): sphingomyelin and unsaturated lipid at 720 and 920 cm^{-1}. Spectrum (5): C-N mode of choline at 730 cm^{-1}; doublet at 765-775 cm^{-1} assigned to phosphate group; strong doublet band at 885-905 cm^{-1} assigned to proteins. Spectrum (6): phenylalanine at 690 and 1003 cm^{-1}; C-N mode of choline at 730 cm^{-1}; 1060 cm^{-1} due to C-C stretching in lipids; 820 cm^{-1} due to phosphodiesters.

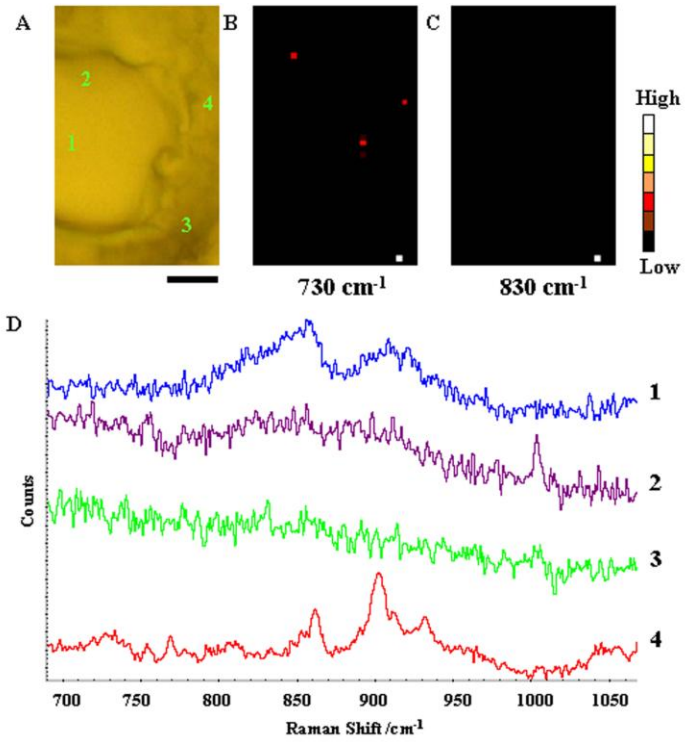

Figure 4.29: Depth Profile of blood vessel in hippocampus through A14(11) section of transgenic 14-month-old mouse brain. (A) Close-up of the mapped blood vessel in hippocampus. Processed map for (B) sphingomyelin (CN^+ stretching mode at 730 cm^{-1}), (C) Cr (symmetric band CN_3^+ band at 830 cm^{-1}). Map area = 1334 points. Acquisition time = 297 min. Colour scale: White corresponds to high intensity, black to no signal. Scale bar = 10 µm. (D) spectra (1-6) were correspond to the points illustrated in tissue image. Spectrum (1): broad band at 840 and 900 cm^{-1} assigned to glucose. Spectrum (2): phenylalanine peak at 1003 cm^{-1}. Spectrum (3): just noise. Spectrum (4): strong band at 860 and 900 cm^{-1} assigned to phosphate group of phospholipids and phosphodiesters, respectively.

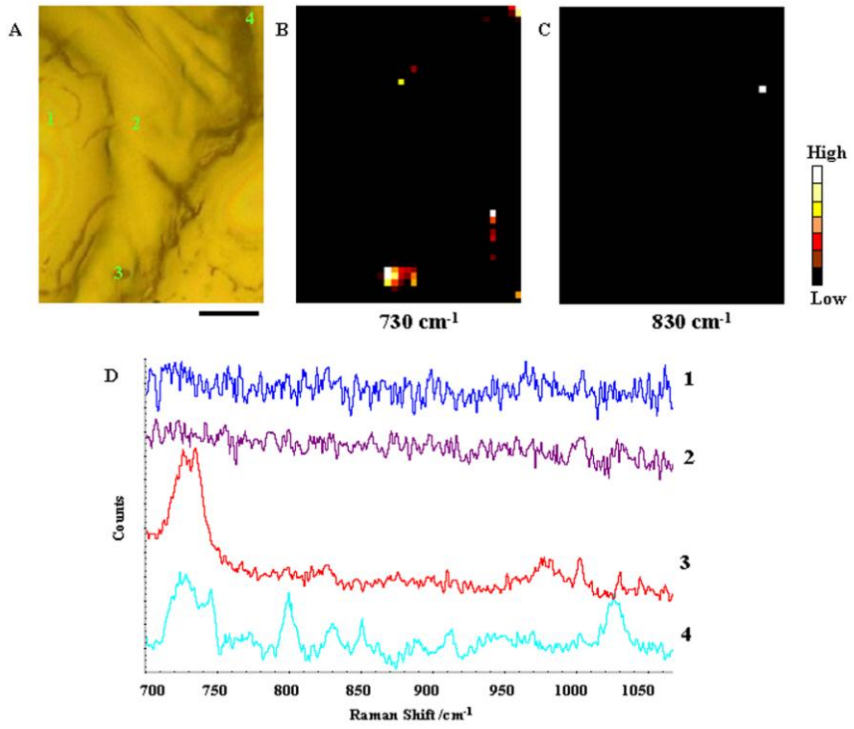

Figure 4.30: Depth Profile of blood vessel in hippocampus through A14(12) section of transgenic 14-month-old mouse brain. (A) Close-up of the mapped blood vessel in hippocampus. Processed map for (B) sphingomyelin (CN^+ stretching mode at 730 cm^{-1}), (C) Cr (symmetric band CN_3^+ band at 830 cm^{-1}). Map area = 1715 points. Acquisition time = 309 min. Colour scale: White corresponds to high intensity, black to no signal. Scale bar = 10 µm. (D) spectra (1-6) were correspond to the points illustrated in tissue image. Spectrum (1,2): just noise. Spectrum (3): strong band at 730 cm^{-1} assigned to CN^+ mode of sphengomyelin. Spectrum (4): band at 730 cm^{-1} assigned to CN mode of sphengomyelin; phosphate bandat 800 cm^{-1} correspond to phosphodieters; two peaks at 850 and 1030 cm^{-1} correspond to phenylalanine of collagen.

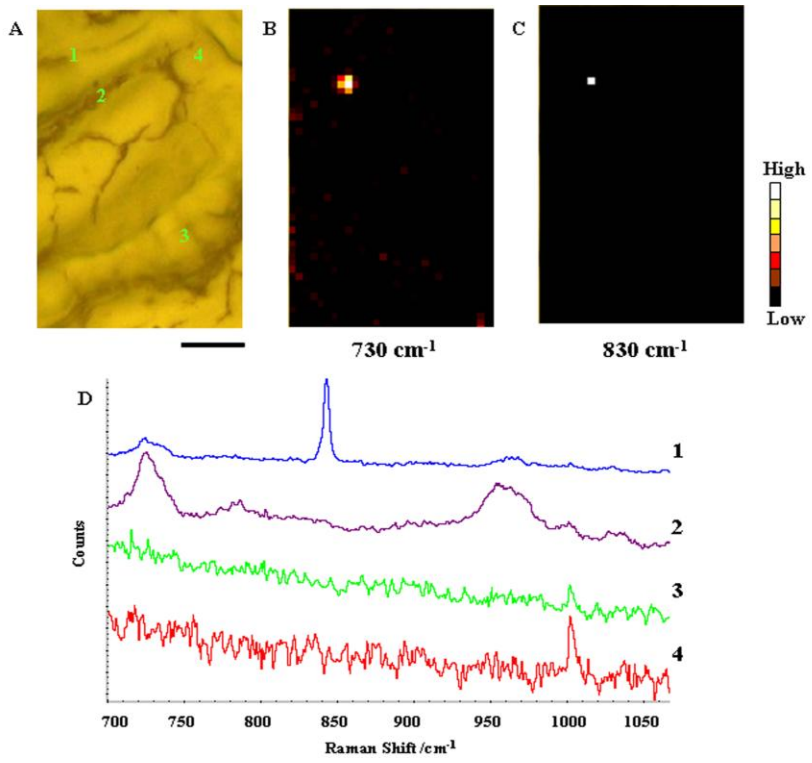

Figure 4.31: Depth Profile of blood vessel in hippocampus through A14(13) section of transgenic 14-month-old mouse brain. (A) Close-up of the mapped blood vessel in hippocampus. Processed map for (B) sphingomyelin (CN^+ stretching mode at 730 cm^{-1}), (C) Cr (symmetric band CN_3^+ band at 830 cm^{-1}). Map area = 1500 points. Acquisition time = 320 min. Colour scale: White corresponds to high intensity, black to no signal. Scale bar = 10 µm. (D) spectra (1-6) were correspond to the points illustrated in tissue image. Spectrum (1): strong band at 840 cm^{-1} assigned to glucose. Spectrum (2): CN^+ stretching mode at 730 cm^{-1} correspond to shingomyelin; broad band at 950 cm^{-1} most probably to $\nu(CH_3)$ of α-helix. Spectrum (3): just phenylalanine at 1003 cm^{-1}. Spectrum (4): strong phenylalanine band at 1003 cm^{-1}.

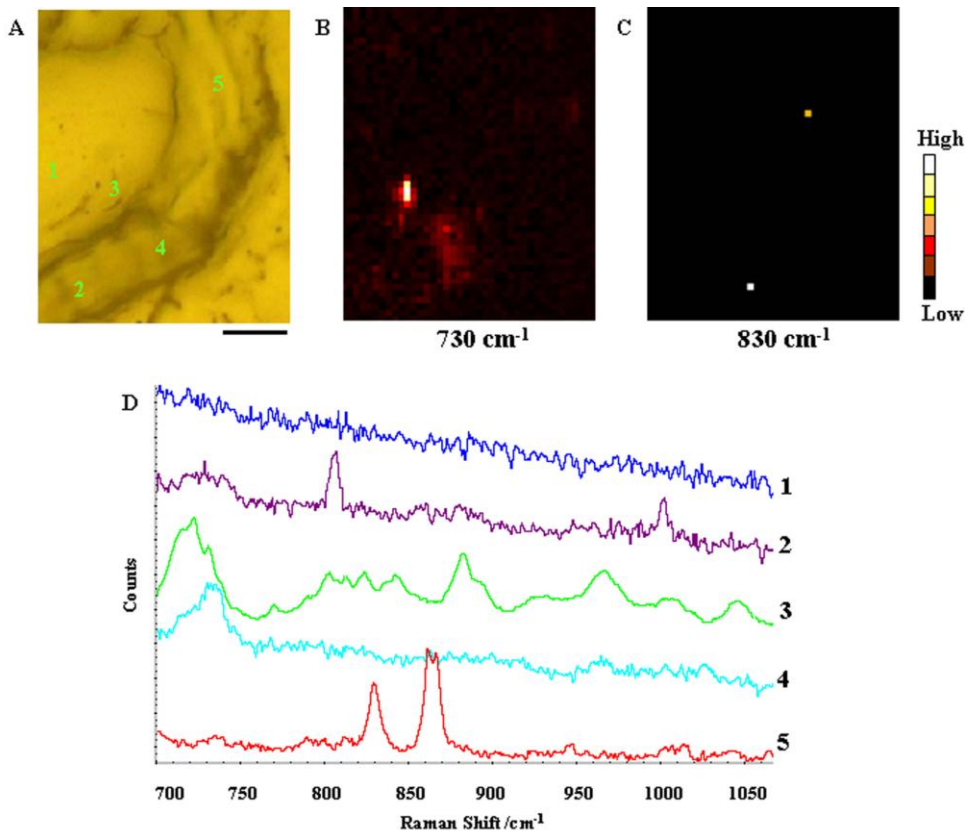

Figure 4.32: Depth Profile of blood vessel in hippocampus through A14(14) section of transgenic 14-month-old mouse brain. (A) Close-up of the mapped blood vessel in hippocampus. Processed map for (B) sphingomyelin (CN^+ stretching mode at 730 cm^{-1}), (C) Cr (symmetric band CN_3^+ band at 830 cm^{-1}). Map area = 2040 points. Acquisition time = 432 min. Colour scale: White corresponds to high intensity, black to no signal. Scale bar = 10 µm. (D) spectra (1-6) were correspond to the points illustrated in tissue image. Spectrum (1): just noise. Spectrum (2): band at 795 cm^{-1} due to nucleic acids; phenylalanine at 1003 cm^{-1}. Spectrum (3) band at 720-730 cm^{-1} assigned to CN^+ stretching mode of sphingolmyelin; band at 830-840 due to phosphate group in phospholipids . Spectrum (3): CN^+ stretching mode in 730 cm^{-1} correspond to sphingomelin. Spectrum (4): strong band at 720-730 cm^{-1} assigned to CN^+ symmetric mode of sphingomyelin. Spectrum (5): strong peaks at 830 cm^{-1} and doublet in 855-865 cm^{-1} assigned to phosphate group in phospholipids.

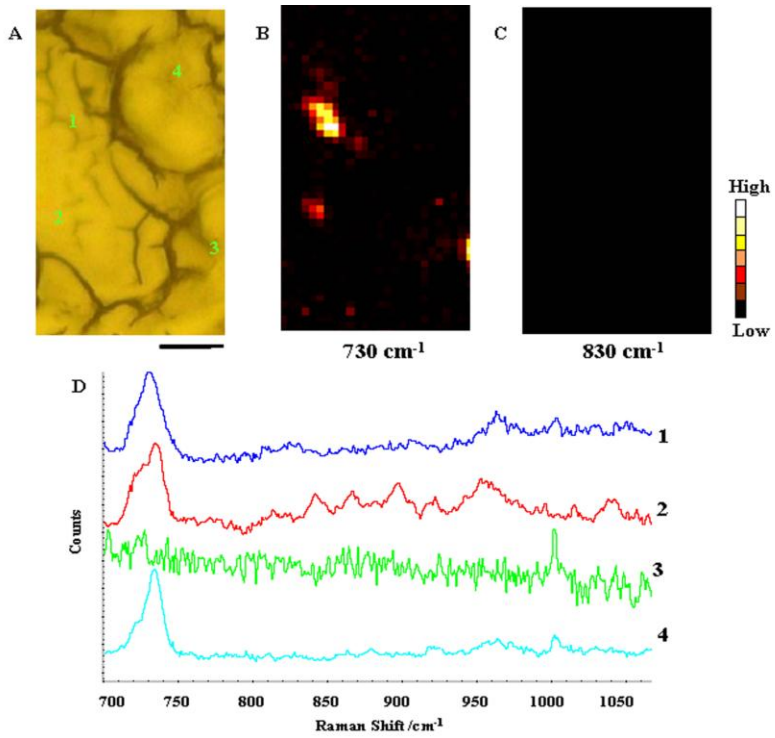

Figure 4.33: Depth Profile of blood vessel in hippocampus through A14(15) section of transgenic 14-month-old mouse brain. (A) Close-up of the mapped blood vessel in hippocampus. Processed map for (B) sphingomyelin (CN^+ stretching mode at 730 cm^{-1}), (C) Cr (symmetric band CN_3^+ band at 830 cm^{-1}). Map area = 1300 points. Acquisition time = 288 min. Colour scale: White corresponds to high intensity, black to no signal. Scale bar = 10 µm. (D) spectra (1-6) were correspond to the points illustrated in tissue image. Spectrum (1,2): strong band at 730 cm^{-1} assigned to CN^+ symetric mode in sphingomyelin. Spectrum (3): phenylalanine peak at 1003 cm^{-1}. Spectrum (4): CN^+ symmetric mode at 730 cm^{-1} correspond to sphingo-myelin; phenylalanine peak at 1003 cm^{-1}.

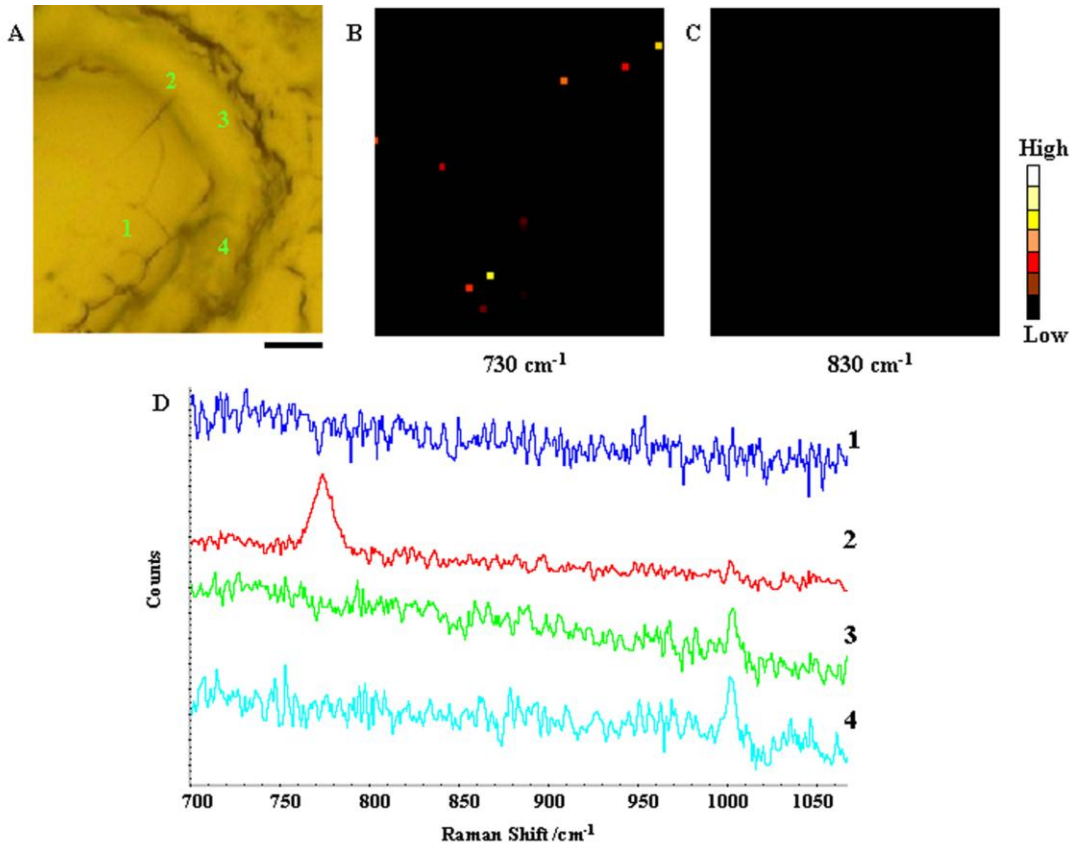

Figure 4.34: Depth Profile of blood vessel in hippocampus through A14(16) section of transgenic 14-month-old mouse brain. (A) Close-up of the mapped blood vessel in hippocampus. Processed map for (B) sphingomyelin (CN^+ stretching mode at 730 cm^{-1}), (C) Cr (symmetric band CN_3^+ band at 830 cm^{-1}). Map area = 3380 points. Acquisition time = 709 min. Colour scale: White corresponds to high intensity, black to no signal. Scale bar = 10 µm. (D) spectra (1-6) were correspond to the points illustrated in tissue image. Spectrum (1): just noise. Spectrum (2): strong band at 760 cm^{-1} assigned to protein. Spectrum (3,4): just phenylalanine peak at 1003 cm^{-1}.

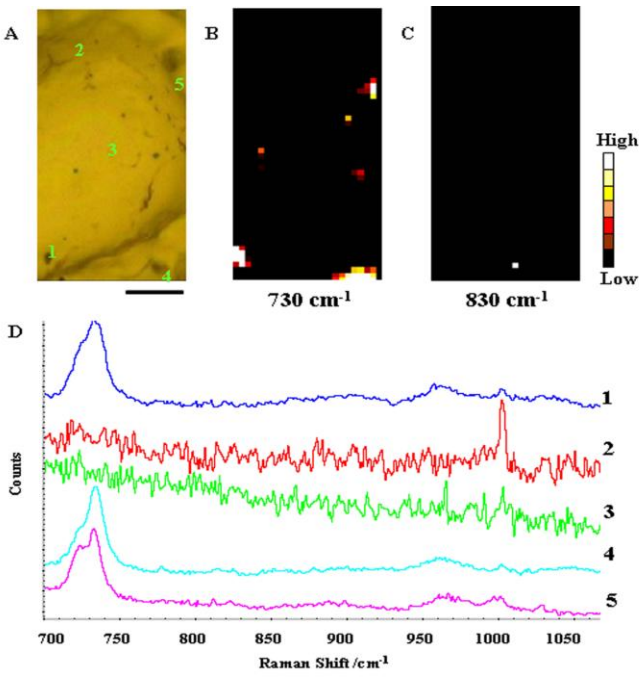

Figure 4.35: Depth Profile of blood vessel in hippocampus through A14(17) section of transgenic 14-month-old mouse brain. (A) Close-up of the mapped blood vessel in hippocampus. Processed map for (B) sphingomyelin (CN^+ stretching mode at 730 cm^{-1}), (C) Cr (symmetric band CN_3^+ band at 830 cm^{-1}). Map area = 1310 points. Acquisition time = 274 min. Colour scale: White corresponds to high intensity, black to no signal. Scale bar = 10 µm. (D) spectra (1-5) were correspond to the points illustrated in tissue image. Spectrum (1): strong band at 720-730 cm^{-1} assigned to CN^+ symmetric mode in sphingomyelin. Spectrum (2): strong phenylalanine band at 1003 cm^{-1}. Spectrum (3): just noise. Spectrum (4,5): CN^+ symmetric mode at 730 cm^{-1} correspond to sphingomyelin.

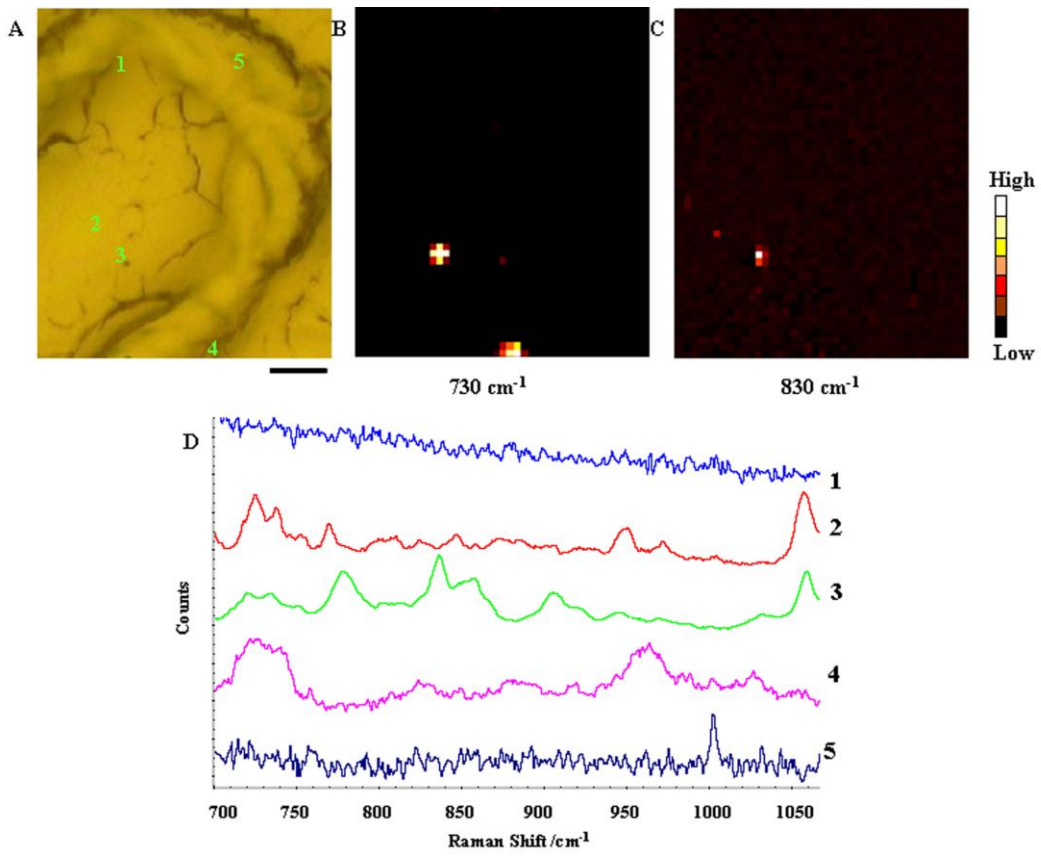

Figure 4.36: Depth Profile of blood vessel in hippocampus through A14(19) section of transgenic 14-month-old mouse brain. (A) Close-up of the mapped blood vessel in hippocampus. Processed map for (B) sphingomyelin (CN^+ stretching mode at 730 cm^{-1}), (C) Cr (symmetric band CN_3^+ band at 830 cm^{-1}). Map area = 3172 points. Acquisition time = 724 min. Colour scale: White corresponds to high intensity, black to no signal. Scale bar = 10 µm. (D) spectra (1-5) were correspond to the points illustrated in tissue image. Spectrum (1): just noise. Spectrum (2): CN^+ symmetric mode of choline at 730 cm^{-1} correspond to; phenylalanine peak at 1003 cm^{-1}; lipid band at 1060 cm^{-1}. Spectrum (3): broad band at 770 cm^{-1} assigned to protein; peak at 840 cm^{-1} assigned to glucose; band at 1060 cm^{-1} correspond to lipid. Spectrum (4): band at 730 cm^{-1} assigned to CN^+ symmetricmode in sphingomyelin; 960 cm^{-1} assigned to symmetric stretching vibration of PO_4^{3-} in phospholipids. Spectrum (5): phenylalanine peak at 1003 cm^{-1}.

4.4.2 Depth profile of Cr and environs on Tg mouse serial sections

Depth profiling data, by analysis of serial sections, was undertaken in an effort to determine whether any other biochemical signatures can be identified as being localized with the Cr deposits. Since Aβ aggregation is one of the most important pathological hallmarks of Alzheimer disease (Querfurth et al, 2010; Nerelius et al, 2009; Gotz et al, 2008; Tanzi et al, 2005; Reddy et al, 2005), an Aβ plaque located in CA4 region of hippocampus was selected to map through serial sections. As shown in Figure 4.37-54, the map of tissue of nine consecutive sections (A14 (10-19)) of 14 month-old TgCRND8 mouse brain were taken with Raman microscope. A14 (10-17) were serial to one another, and A14 (19) section was separated by only one missing section. The plaque located in hippocampus region was selected because Cr deposit was detected in IR maps of this area. The IR data collection was already done by Veena Agrawal and Alex Kuzyk (other members of Dr. Gough's research group) on the same plaque and published in JBC 2010 (Kuzyk et al, 2010). As the IR and Raman imaging techniques are compatibale, the same plaque was mapped with Raman microscope at higher spatial resolution to understand any co-localization between creatine deposits and either lipid, amyloid plaque or lipid. These maps were analyzed to investigate the association of Cr deposit with any other spectral markers such as sphingomyelin, phospholipid, nucleic acid, and phenylalanine.

Two streamline maps were acquired for each section with spectral resolution 1 cm^{-1}/pixel and spatial resolution of 2 μm because of using 50x objective. The exposure time for all the maps was 300 second to improve S/N ratio. In order not to get any charcoal band, 10% laser 785 nm was used. Raman spectra were recorded across a spectral range of 685 to 1075 cm^{-1} (centred at 880 cm^{-1}) and the other map across a spectral

range of 1410 to 1750 cm^{-1} (centred at 1580 cm^{-1}). These Raman maps were processed for sphingomyelin (CN^+ symmetric mode at 730 cm^{-1}) (Figure 37-54C), for Cr (symmetric CN_3^+ band at 830 cm^{-1}) (Figure 37-54D), lipid (CH_2 deformation band at 1440 cm^{-1}) (Figure 4.37-54E), and amyloid plaque (antiparallel β-sheet protein at 1670 cm^{-1}) (Figure 4.37-54F).

The processed A14 (10) map shows no creatine and β-sheet Amide I (Figure 4.37D&F). This area was surrounded by lipid (Figure 4.37E) and a few CN stretching mode from the choline of sphingomyelin (Figure 4.37C). The collected map was analyzed and some other peaks corresponded to amine group, phosphodiesters and lipid were observed (Figure 4.38).

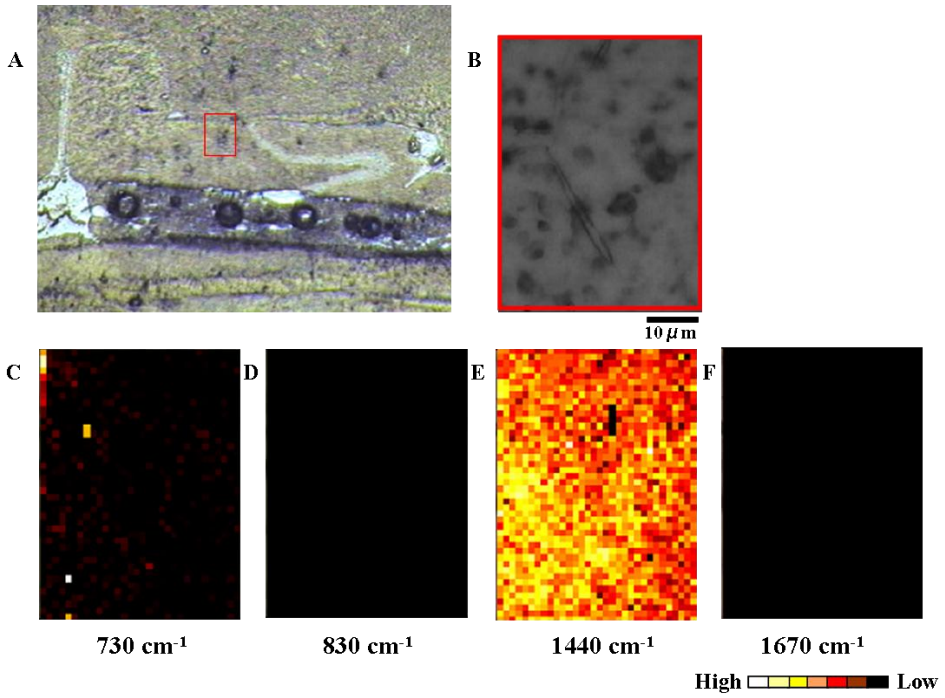

Figure 4.37: Depth Profile of Aβ plaque through A14(10) section of transgenic 14-month-old mouse brain. (A) The plaque in brain tissue. (B) Close-up of the mapped plaque. Processed map for (C) sphingomyelin (at 730 cm^{-1}), (D) Cr (at 830 cm^{-1}), (E) Lipid (at 1440 cm^{-1}), and (F) Aβ plaque (antiparallel β-sheet protein at 1670 cm^{-1}). Map area = 1376 points. Acquisition time = 376 min. Colour scale: White corresponds to high intensity, black to no signal. Scale bar = 10 μm.

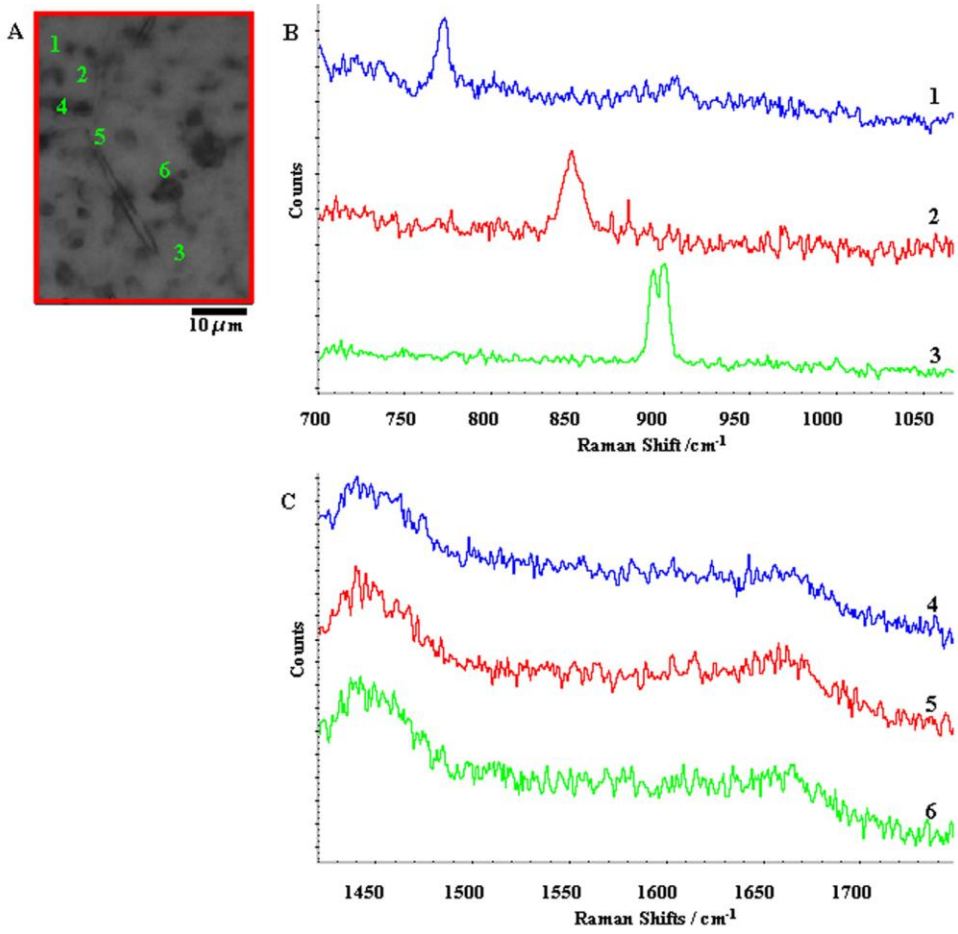

Figure 4.38: Spectra correspond to the pixels marked in the (A) mapped plaque in hippocampus of A14(10) section of transgenic 14 month-old mouse brain. Raman spectra in the region between (B) 700-1050 cm^{-1} and between (C) 1400-1750 cm^{-1}. Spectrum (1): strong band at 765 cm^{-1} assigned to proteins. Spectrum (2): strong peak at 840 cm^{-1} assigned to glucose and deformation vibration of amine group. Spectrum (3): Doublet in 890-900 cm^{-1} assigned to saccharide and phosphodiesters. Spectrum (4,5,6): broad band at 1450 cm^{-1} assigned to lipid.

The Aβ plaque was identified in A14 (11) and its appearance can be observed by dark area (Figure 4.39F). This plaque core was completely encased in lipid (Figure 4.39E). No Cr was present in this section (Figure 4.39D). As shown in Figure 4.40, The other distinct peaks found directly surrounding the Aβ plaque were assigned to amino acids mostly phenylalanine and lipid bands.

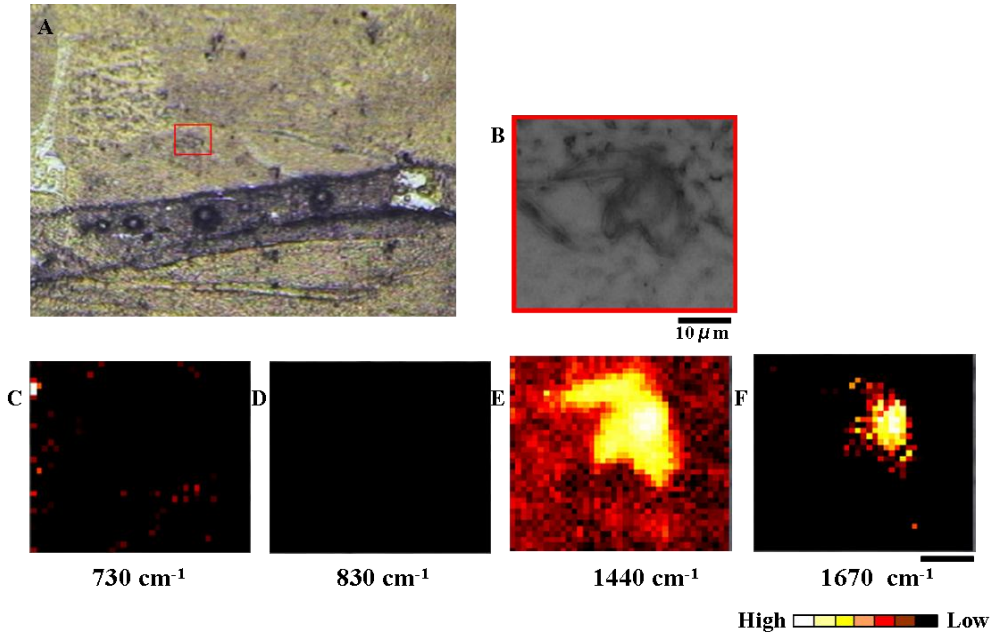

Figure 4.39: Depth Profile of Aβ plaque through A14(11) section of transgenic 14-month-old mouse brain. (A) The plaque in brain tissue. (B) Close-up of the mapped plaque. Processed map for (C) sphingomyelin (CN^+ symmetric mode at 730 cm^{-1}), (D) Cr (symmetric CN_3^+ band at 830 cm^{-1}), (E) Lipid (CH_2 deformation band at 1440 cm^{-1}), and (F) Aβ plaque (antiparallel β-sheet protein at 1670 cm^{-1}). Map area = 1326 points. Acquisition time = 347 min. Colour scale: White corresponds to high intensity, black to no signal. Scale bar = 10 µm.

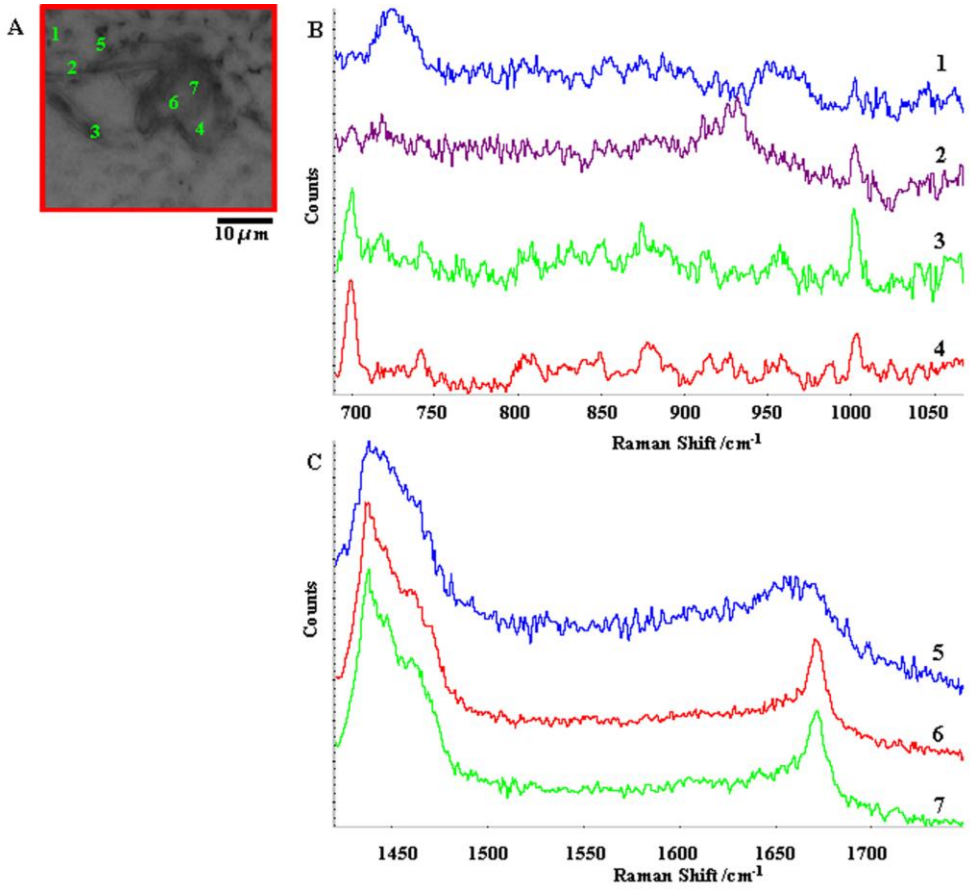

Figure 4.40: Spectra correspond to the pixels marked in the (A) mapped plaque in hippocampus of A14(11) section of transgenic 14 month-old mouse brain. Raman spectra in the region between (B) 700-1050 cm^{-1} and between (C) 1400-1750 cm^{-1}. Spectrum (1): strong band at 720-730 cm^{-1} assigned to symmetric stretch CN^{+} characteristic for sphingomyelin; strong band at 1003 cm^{-1} correspond to phenylalanine. Spectrum (2): broad band at 960-970 cm^{-1} assigned to lipids; strong band at 1003 cm^{-1} due to phenylalanine. Spectrum (3): 690 and 1003 cm^{-1} assigned to phenylalanne. Spectrum (4): 690 cm^{-1}, 740 cm^{-1} assigned to phenylalanine and adistinct band corresponding to DNA, respectively; weak band at 880 cm^{-1} assigned to proteins; strong band at 1003 cm^{-1} assigned to phenylalanine. Spectrum (5): strong lipid band at 1430-1440 cm^{-1}. Spectrum (6,7): strong lipid band at 1430-1440 cm^{-1}; broad band at 1450 cm^{-1} due to CH_2 bending of proteins and lipids; strong band at 1670 cm^{-1} assigned to anti-parallel β-sheet.

As shown in Figure 4.41D, some Cr deposits were identified in this section (A14(12)) surrounded by an area of lipid. These Cr deposits were not in the vicinity of β-sheet Amide I in this mapped area (Figure 4.41F). The majority of the thick dark area was found to be characteristic of phospholipids (phosphate bands at 1040-1050 cm^{-1}), protein (C-N stretch mode of protein), lipid (=CH bending mode of unsaturated lipid at 970-990 cm^{-1}), and amino acids (bands at 740, 870 and 920 cm^{-1}) (Figure 4.42).

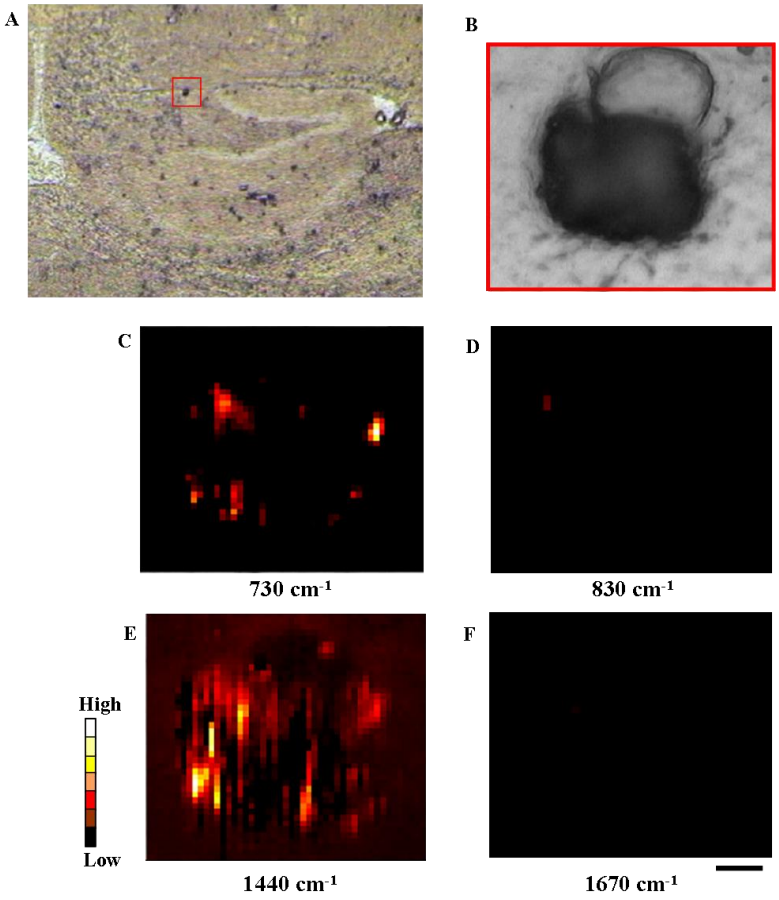

Figure 4.41: Depth Profile of Aβ plaque through A14(12) section of transgenic 14-month-old mouse brain. (A) The plaque in brain tissue. (B) Close-up of the mapped plaque. Processed map for (C) sphingomyelin (CN^+ symmetric mode at 730 cm^{-1}), (D) Cr (symmetric CN_3^+ band at 830 cm^{-1}), (E) Lipid (CH_2 deformation band at 1440 cm^{-1}), and (F) Aβ plaque (antiparallel β-sheet protein at 1670 cm^{-1}). Map area = 2150 points. Acquisition time = 495 min. Colour scale: White corresponds to high intensity, black to no signal. Scale bar = 10 µm.

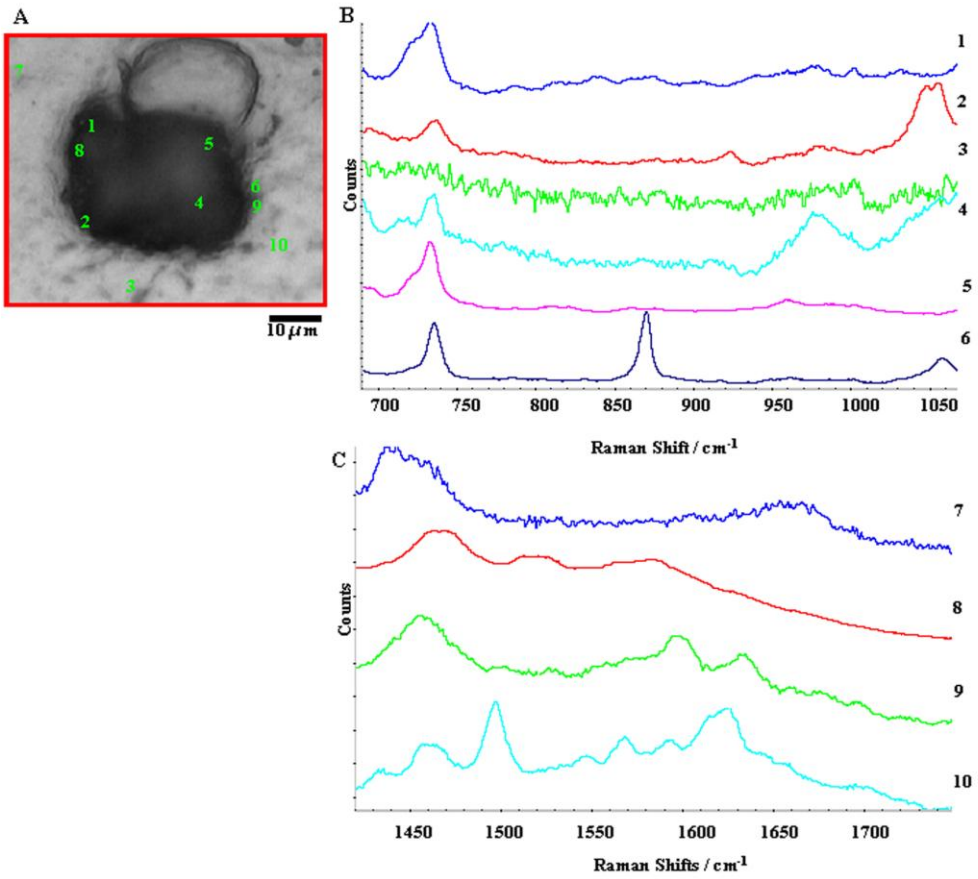

Figure 4.42: Spectra correspond to the pixels marked in the (A) mapped plaque in hippocampus of A14(12) section. Spectrum (1): broad doublet peaks around 720-740 cm^{-1} assigned to symmetric CN^{+} mode characteristic for sphingomyelin; weak phenylalanine peak at 1003 cm^{-1}. Spectrum (2): broad phosphatidylcholine band at 720-730 cm^{-1}; weak band at 920 cm^{-1} assigned to C-C stretching mode probably in amino acids proline; strong band at 1040-1050 cm^{-1} assigned to phosphate. Spectrum (3): phenylalanind band at 1060 cm^{-1}. Spectrum (4): phosphatidylcholine band at 720-730 cm^{-1}; phenylalanine band at 690 cm^{-1}; broad band at 970-990 cm^{-1} assigned to =CH bending (lipids). Spectrum (5): just broad symmetric $N^{+}(CH_3)_3$ at 720-740 cm^{-1} correspond to sphingomyelin . Spectrum (6): strong choline peak at 720 cm^{-1}; strong amino acids peak at 870 cm^{-1}; broad lipid band at 1060 cm^{-1}. Spectrum (7): just broad band at 1430-1450 cm^{-1} characterized to lipids. Spectrum (8): broad band at 1450-1470 cm^{-1} due to proteins. Spectrum (9): broad lipid band at 1430-1450 cm^{-1}; C=C deformation of phenylalanine band at 1590 cm^{-1}; broad band at 1630 cm^{-1} assigned to Amide I. Spectrum (10): strong band at 1495 cm^{-1} assigned to C-N stretching vibration of amino acids; broad band at 1570 cm^{-1} assigned to nucleic acids; peak at 1620 cm^{-1} due to protein carbonyl band.

Figure 4.43D shows some CN stretching mode from the choline of sphingomyelin and lipid (Figure 4.43C). No Cr and β-sheet bands were present in this section. As illustrated in Figure 4.44, the spectral markers detected in thick dark area were phenylalanine (bands at 1003 and 1610 cm^{-1}) and 980 cm^{-1} due to =CH bending of lipid (=CH bending of unsaturated lipid at 980 cm^{-1}).

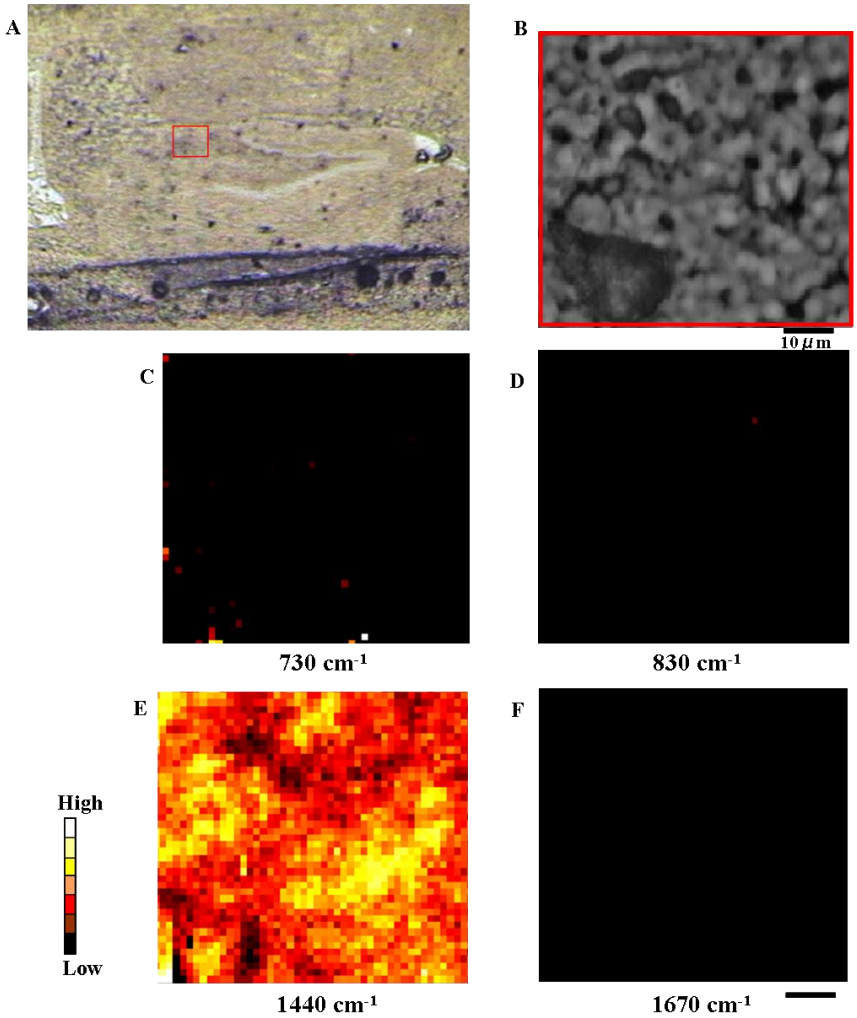

Figure 4.43: Depth Profile of Aβ plaque through A14(13) section of transgenic 14-month-old mouse brain. (A) The plaque in brain tissue. (B) Close-up of the mapped plaque. Processed map for (C) sphingomyelin (CN^+ symmetric mode at 730 cm^{-1}), (D) Cr (symmetric CN_3^+ band at 830 cm^{-1}), (E) Lipid (CH_2 deformation band at 1440 cm^{-1}), and (F) Aβ plaque (1670 cm^{-1}). Map area = 2806 points. Acquisition time = 695 min. Colour scale: White corresponds to high intensity, black to no signal. Scale bar = 10 µm.

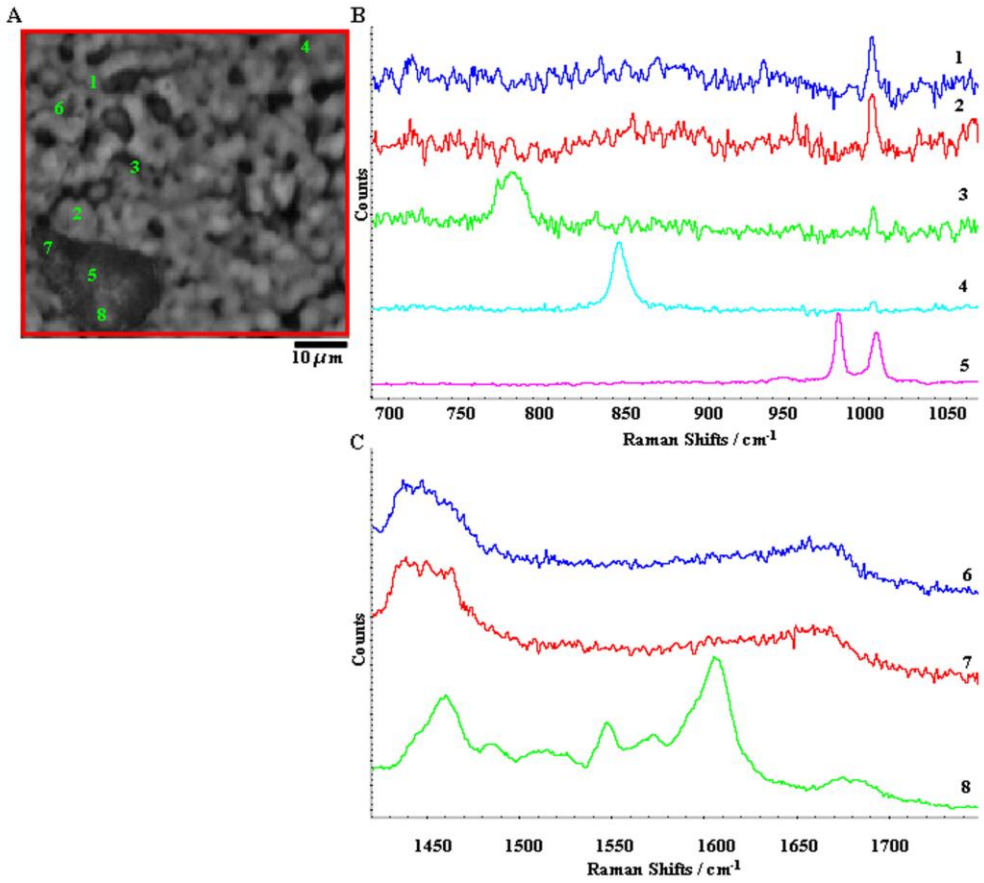

Figure 4.44: Spectra correspond to the pixels marked in the (A) mapped plaque in hippocampus of A14(13) section of transgenic 14 month-old mouse brain. Raman spectra in the region between (B) 700-1050 cm^{-1} and between (C) 1400-1750 cm^{-1}. Spectrum (1): weak choline band at 720 cm^{-1} assigned to symmetric stretch vibration of choline group $N^{+}(CH_3)_3$, characteristic for sphingomyelin; α-helix at 930 cm^{-1}; strong band at 1003 cm^{-1} due to phenylalanine. Spectrum (2): weak band at 960 cm^{-1} assigned to phosphate group; strong band at 1003 cm^{-1}. Spectrum (3): broad band at 770-780 cm^{-1} assigned to amino acids; phenylalanine band at 1003 cm^{-1}. Spectrum (4): strong band at 845 cm^{-1} assigned to amino acids and polysaccharide. Spectrum (5): strong band at 980 cm^{-1} assigned to =CH bending of lipid; 1003 cm^{-1} characterized to phenylalanine. Spectrum (6,7): broad lipid band at 1430-1440 cm^{-1}; α-helix peak at 1660 cm^{-1}. Spectrum (8): strong lipid band at 1430-1450 cm^{-1}; 1540 cm^{-1} characterized to Amide II; strong band at 1610 cm^{-1} assigned to C=C of phenylalanine.

As displayed in Figure 4.45D, Cr deposits were identified in the vicinity of some β-sheet Amide I and surrounded by an area of CN stretching mode of choline (Figure 4.45C) and CH_2 deformation band of lipid (Figure 4.45E). Like the other sections, in section A14 (14), the plaque was surrounded by elevated lipid distribution (Figure 4.45E&F). As shown in Figure 4.46, the spectra of dark accumulation were analyzed and shows that this area contains protein (CH_3 symmetric vibration mode of protein and α-helix at 930-940 cm^{-1}), phospholipids (phosphate group at 860 cm^{-1}) and phenylalanine (bands at 900, 930, 1003 cm^{-1}).

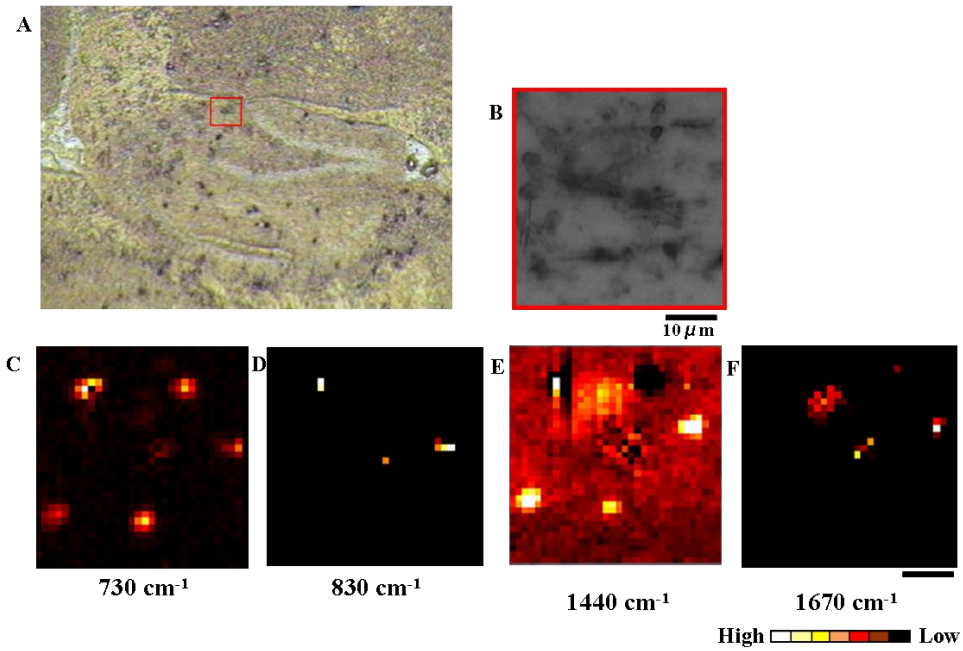

Figure 4.45: Depth Profile of Aβ plaque through A14(14) section of transgenic 14-month-old mouse brain. (A) The plaque in brain tissue. (B) Close-up of the mapped plaque. Processed map for (C) sphingomyelin (CN^+ symmetric mode at 730 cm^{-1}), (D) Cr (symmetric CN_3^+ band at 830 cm^{-1}), (E) Lipid (CH_2 deformation band at 1440 cm^{-1}), and (F) Aβ plaque (antiparallel β-sheet protein at 1670 cm^{-1}). Map area = 1190 points. Acquisition time = 310 min. Colour scale: White corresponds to high intensity, black to no signal. Scale bar = 10 µm.

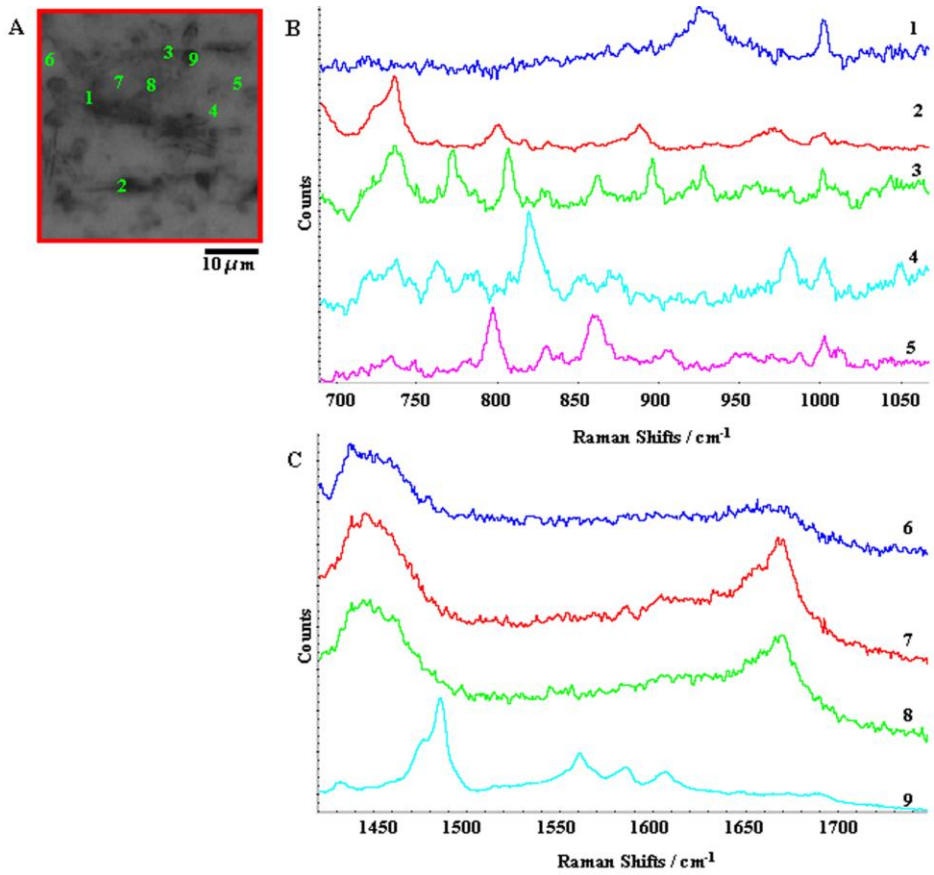

Figure 4.46: Spectra correspond to the pixels marked in the (A) mapped plaque in hippocampus of A14 (14) section. Raman spectra in the region between (B) 700-1050 cm^{-1} and between (C) 1400-1750 cm^{-1}. Spectrum (1): broad band at 930 and 1003 cm^{-1} assigned to *v*(C-C) stretching probably in amino acids praline and phenylalanine, respectively. Spectrum (2): peak at 880 cm^{-1} assigned to CH_2 bending mode (protein assignment); 1003 cm^{-1} characterized to phenylalanine. Spectrum (3): strong CN^+ symmetric mode at 720-730 cm^{-1} correspond to sphingomyelin; strong band at 810 cm^{-1} assigned to phosphodiesters; phosphate group in phospholipids at 860 cm^{-1}; Phenylalanine bands at 900, 930, and 1003 cm^{-1}. Spectrum (4): CN mode of choline at 720-730 cm^{-1}; Cr band at 830, 916, 1052 cm^{-1}; phenylalanine spectrum at 1003 cm^{-1}. Spectrum (5): strong band at 790 cm^{-1} assigned to phosphate band in DNA; broad band at 860 cm^{-1} assigned to phosphate group; phenylalanine band at 1003 cm^{-1}. Spectrum (6): lipid band at 1430-1440 cm^{-1}. Spectrum (7,8): lipid band at 1430-1440 cm^{-1}; anti-parallel β-sheet at 1670 cm^{-1}. Spectrum (9): doublet in 1470-1480 cm^{-1} assigned to Amide II (largely due to a coupling of CN stretching and in-plane bending of the N-H group); bands at 1560, 1580, 1610 cm^{-1} assigned to C=C of phenylalanine.

In Figure 4.47D, no Cr deposit was present in section A14 (15). The appearance of Aβ plaque core can be seen in the tissue image by dark area (Figure 4.47B&F). The Aβ plaque was surrounded by sphingomyelin (CN^+ symmetric mode at 730 cm^{-1}) and lipid (CH_2 deformation band at 1440 cm^{-1}). In the vicinity of this dark area, some other bands were observed that correspond to phenylalanine (bands at 960, 980, 1030 cm^{-1}), and lipid (975 and 1060 cm^{-1}) (Figure 4.48).

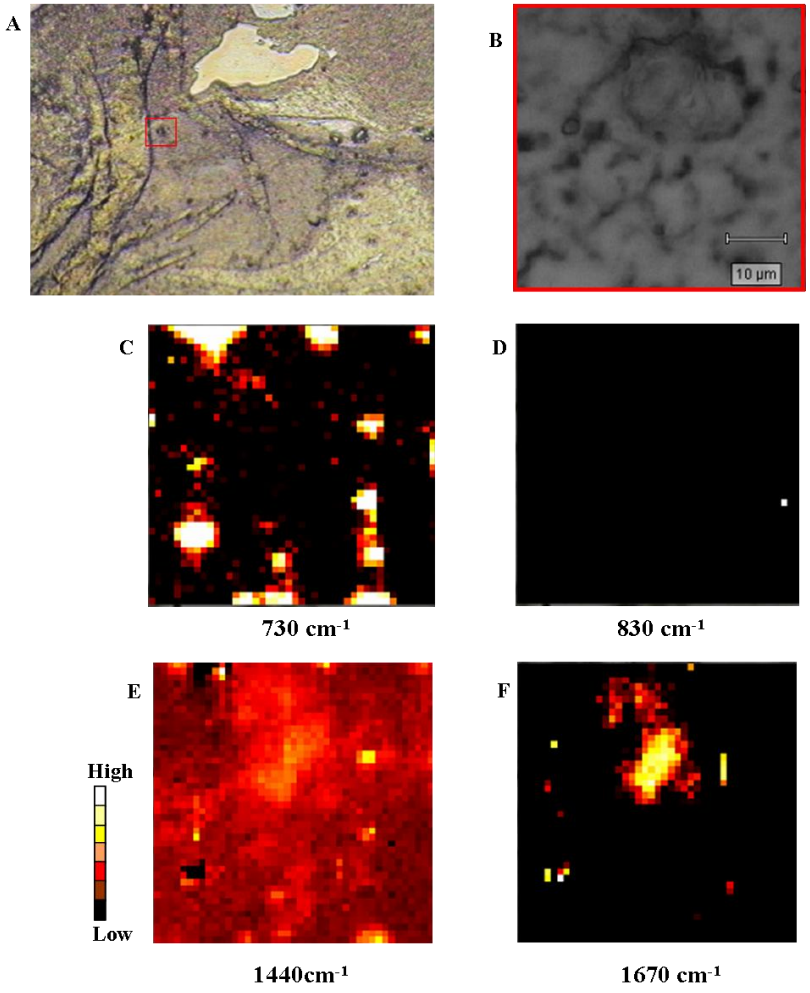

Figure 4.47: Depth Profile of Aβ plaque through A14(15) section of transgenic 14-month-old mouse brain. (A) The plaque in brain tissue. (B) Close-up of the mapped plaque. Processed map for (C) sphingomyelin (CN^+ symmetric mode at 730 cm^{-1}), (D) Cr (symmetric CN_3^+ band at 830 cm^{-1}), (E) Lipid (CH_2 deformation band at 1440 cm^{-1}), and (F) Aβ plaque (β-sheet protein at 1670 cm^{-1}). Map area = 1936 points. Acquisition time = 440 min. Colour scale: White corresponds to high intensity, black to no signal. Scale bar = 10 µm.

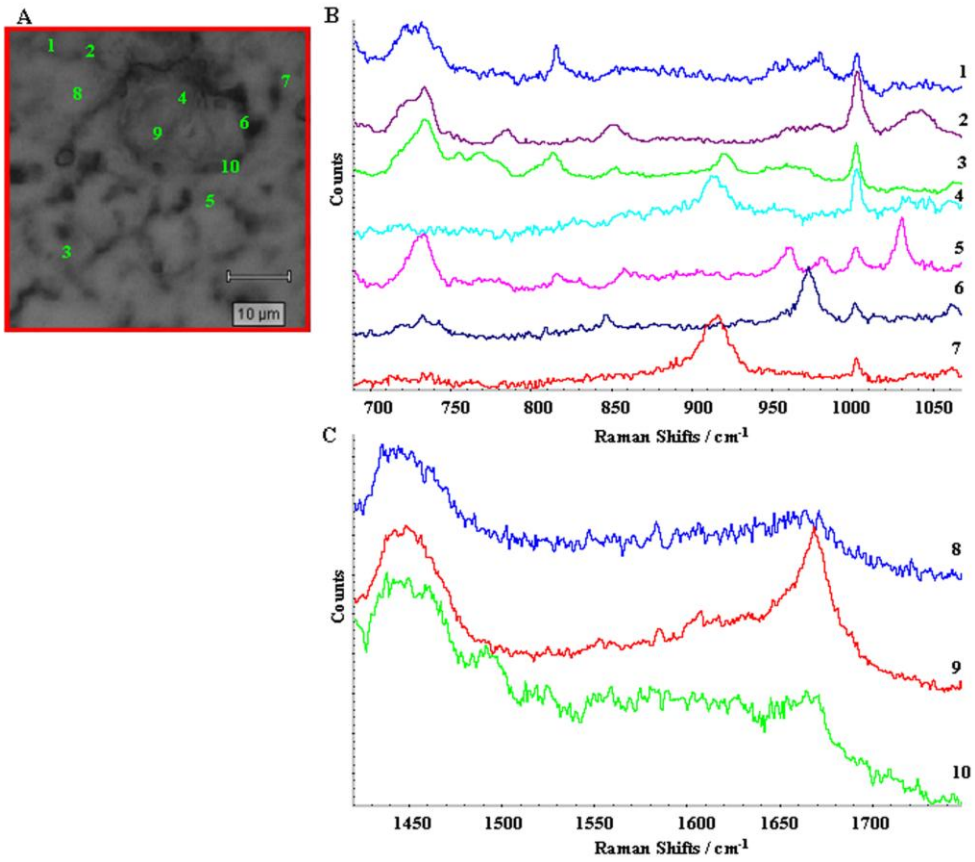

Figure 4.48: Spectra correspond to the pixels marked in the (A) mapped plaque in hippocampus of A14(15) section of transgenic 14 month-old mouse brain. Raman spectra in the region between (B) 700-1050 cm^{-1} and between (C) 1400-1750 cm^{-1}. Spectrum (1): strong band at 720-730 cm^{-1} assigned to symmetric CN^{+} mode of sphingomyelin; strong band at 810 cm^{-1} assigned to phosphodiesters; peak at 1003 cm^{-1} correspond to phenylalanine. Spectrum (2): CN^{+} symmetric mode of sphingomyelin at 730-740 cm^{-1}; broad band at 845 cm^{-1} assigned to stretch mode of the amino acids; phenylalanine bands at 1003 and 1030 cm^{-1}. Spectrum (4): broad band at 920 cm^{-1} characterized to amino acids; phenylalanine band at 1003 cm^{-1}. Spectrum (5): broad band at 720-730 cm^{-1} assigned to CN^{+} mode in sphingomyelin; phenylalanine bands at 960, 980, 1003 and 1030 cm^{-1}. Spectrum (6): strong lipid band at 975 cm^{-1}; phenylalanine band at 1003 cm^{-1}; lipid band at 1060 cm^{-1}. Spectrum (7): strong band at 915-920 cm^{-1} (one of the distinct RNA modes) and amino acids group; 1003 cm^{-1} due to phenylalanine. Spectrum (8): just lipid band at 1430-1460 cm^{-1}. Spectrum (9): lipid band at 1430-1460 cm^{-1} and anti-parallel β-sheet band at 1670 cm^{-1}. Spectrum (10): lipid band and very weak anti-parallel β-sheet band.

The processed map of plaque area at A14(16) section shows no sphingomyelin (CN^+ stretching mode 730 cm^{-1}) (Figure 4.49C) and Cr (symmetric CN_3^+ band at 830 cm^{-1}) (Figure 4.49D), respectively. The black area composed of phenylalanine (band at 1003 cm^{-1}) (Figure 4.50) and just a few β-sheet (antiparallel β-sheet protein at 1670 cm^{-1}).

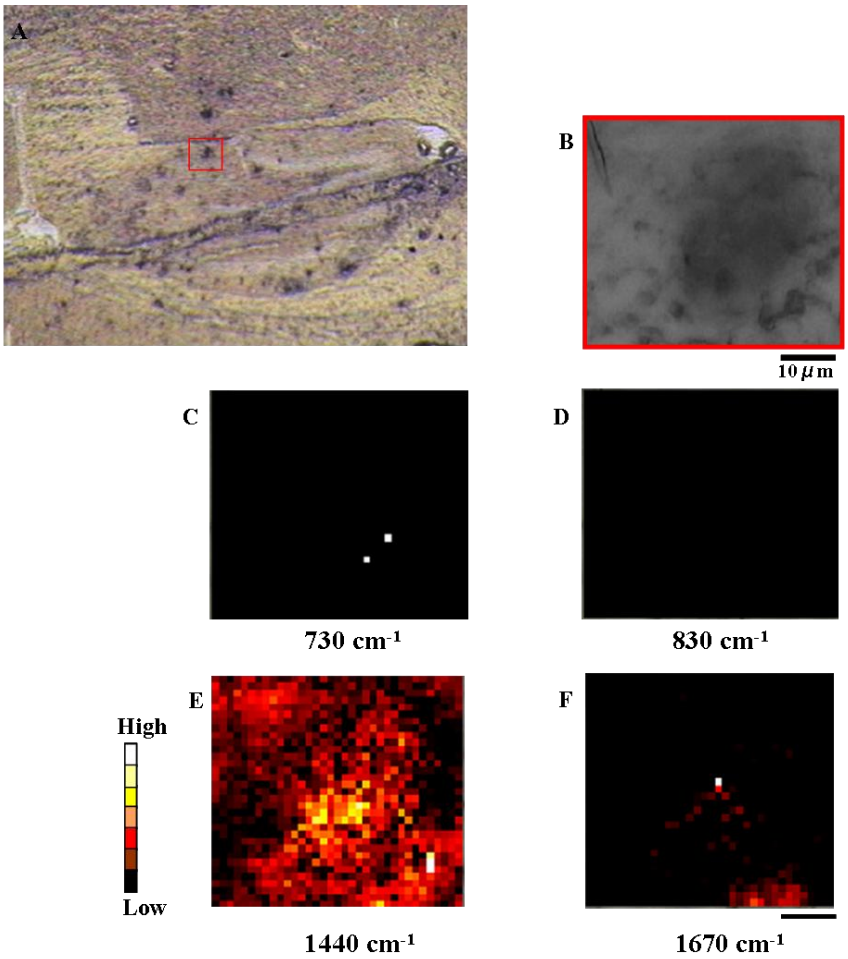

Figure 4.49: Depth Profile of Aβ plaque through A14(16) section of transgenic 14-month-old mouse brain. (A) The plaque in brain tissue. (B) Close-up of the mapped plaque. Processed map for (C) sphingomyelin (CN^+ symmetric mode at 730 cm^{-1}), (D) Cr (symmetric CN_3^+ band at 830 cm^{-1}), (E) Lipid (CH_2 deformation band at 1440 cm^{-1}), and (F) Aβ plaque (antiparallel β-sheet protein at 1670 cm^{-1}). Map area = 1184 points. Acquisition time = 320 min. Colour scale: White corresponds to high intensity, black to no signal. Scale bar = 10 µm.

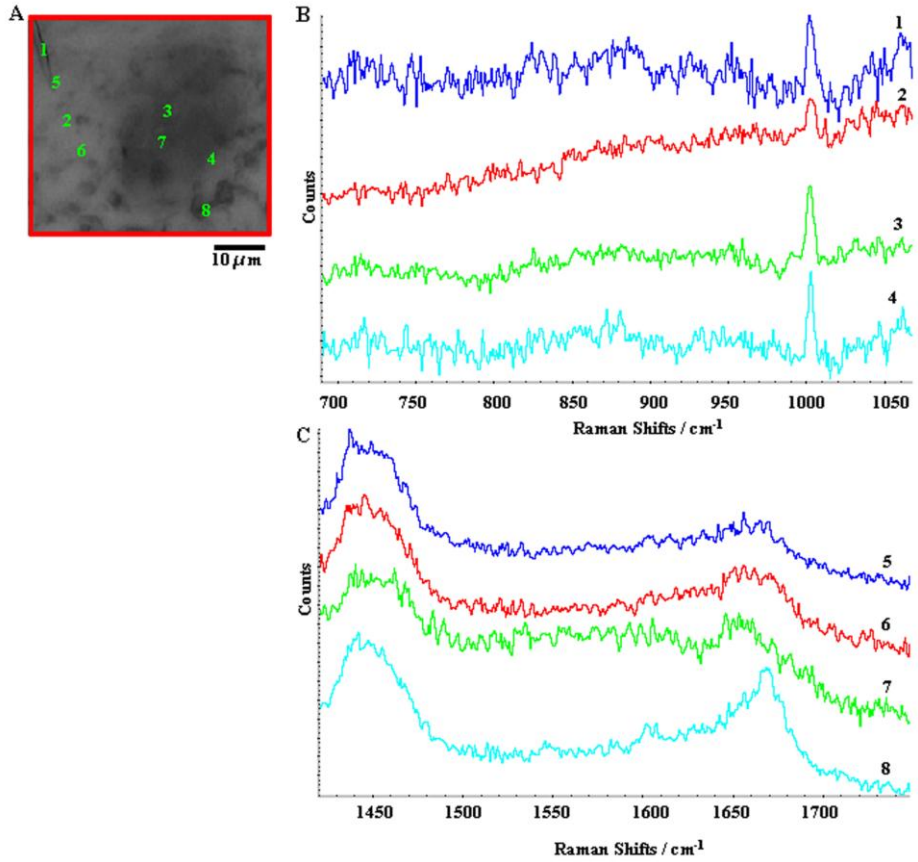

Figure 4.50: Spectra correspond to the pixels marked in the (A) mapped plaque in hippocampus of A14(16) section of transgenic 14 month-old mouse brain. Raman spectra in the region between (B) 700-1050 cm^{-1} and between (C) 1400-1750 cm^{-1}. Spectrum (1): strong phenylalanine bands at 1003 and 1060 cm^{-1}. Spectrum (2,3,4): strong phenylalanine band at 1003 cm^{-1}. Spectrum (5,6,7): lipid band at 1420-1430 cm^{-1}; α-helix band at 1550-1560 cm^{-1}. Spectrum (8): lipid and anti-parallel β-sheet bands at 1430 and 1670 cm^{-1}, respectively.

As displayed in Figure 4.51D, Cr was present in this map surrounded by CN stretching mode at 730 cm^{-1} (Figure 4.51C), CH_2 deformation of lipid at 1440 cm^{-1} (Figure 4.51E) and β-sheet Amide I at 1670 cm^{-1} (Figure 4.51). As shown in Figure 4.52, in the vicinity of Aβ plaque, some sharp lipid (=CH bending of unsaturated lipid at 985 cm^{-1}) and phenylalanine (bands at 695, 1003, 1585 cm^{-1}) were identified.

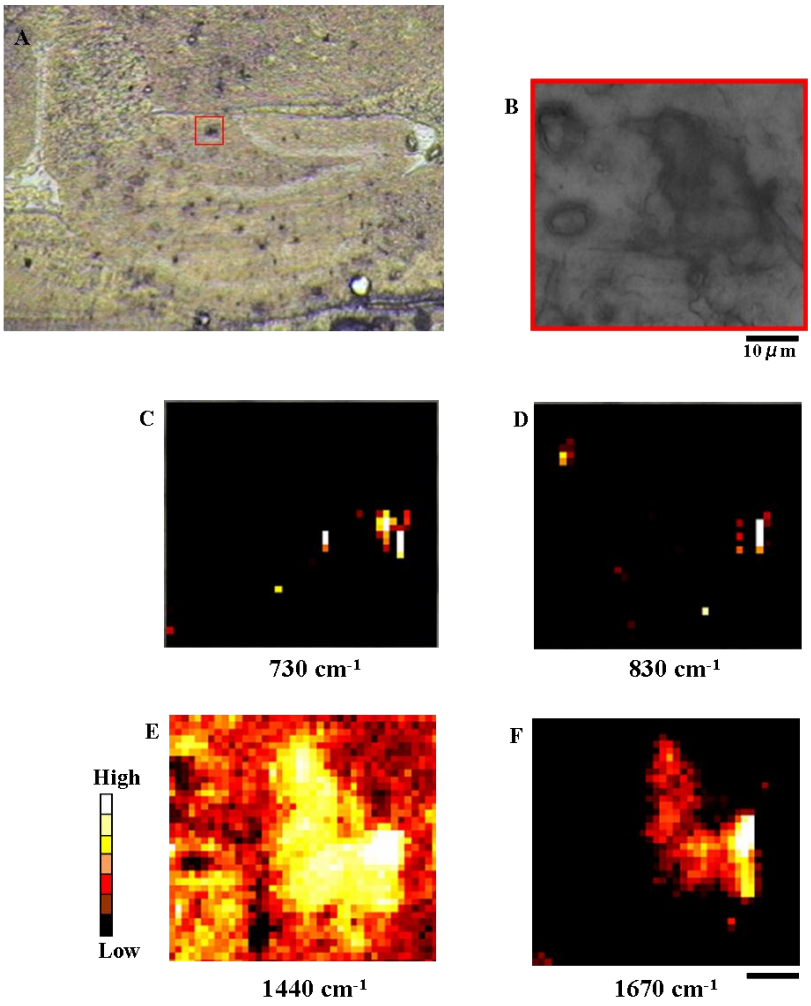

Figure 4.51: Depth Profile of Aβ plaque through A14(17) section of transgenic 14-month-old mouse brain. (A) The plaque in brain tissue. (B) Close-up of the mapped plaque. Processed map for (C) sphingomyelin (CN^+ symmetric mode at 730 cm^{-1}), (D) Cr (symmetric CN_3^+ band at 830 cm^{-1}), (E) Lipid (CH_2 deformation band at 1440 cm^{-1}), and (F) Aβ plaque (antiparallel β-sheet protein at 1670 cm^{-1}). Map area = 1680 points. Acquisition time = 356 min. Colour scale: White corresponds to high intensity, black to no signal. Scale bar = 10 µm.

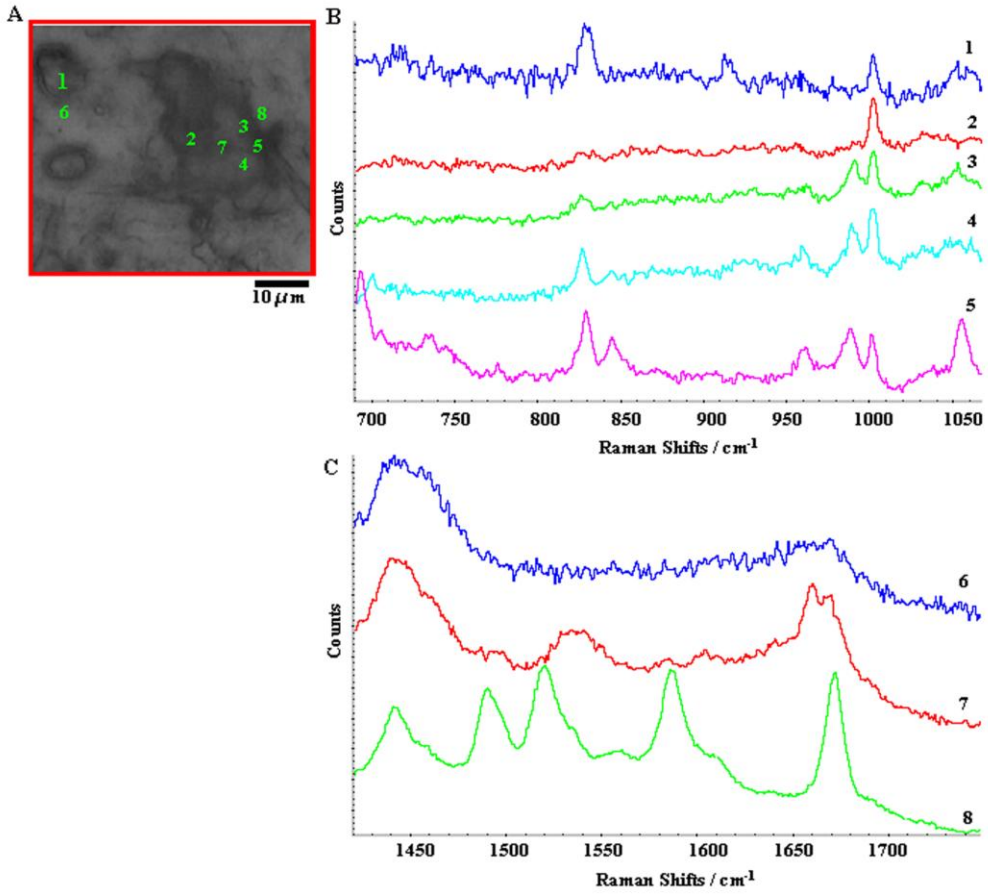

Figure 4.52: Spectra correspond to the pixels marked in the (A) mapped plaque in hippocampus of A14(17) section of transgenic 14 month-old mouse brain. Raman spectra in the region between (B) 700-1050 cm^{-1} and between (C) 1400-1750 cm^{-1}. Spectrum (1): Cr bands at 830, 916, 1052 cm^{-1}; phenylalanine peak at 1003 cm^{-1}. Spectrum (2): just phenylalanine. Spectrum (3): lipid band at 880 cm^{-1}; weak Cr bands; phenylalanine at 1003 cm^{-1}. Spectrum (4): Cr bands; phenylalanine at 690 and 1003 cm^{-1}. Spectrum (5) Cr bands at 830, 916, 1052 cm^{-1}; phenylalanine at 690 cm^{-1} and 1003 cm^{-1}. Spectrum (6): lipid band at 1420-1430 cm^{-1}. Spectrum (7): lipid band at 1420-1430 cm^{-1}; broad band at 1530 cm^{-1} assigned to Amide I; α-helix and anti-parallel β-sheet peaks at 1650-1660 and 1670 cm^{-1}, respectively. Spectrum (8): strong lipid band at 1420-1430 cm^{-1}; strong band at 1525 cm^{-1} due to Amide I; phenylalanine peak at 1585 cm^{-1}; strong band at 1670 cm^{-1} assigned to antiparallel β-sheet protein.

Figure 4.53D illustrates Cr deposit surrounded by CN stretch mode at 730 cm^{-1} and CH_2 deformation of lipid (Figure 4.53C,E). In the vicinity of these Cr deposits, some Aβ plaques were identified (Figure 4.53F). The background fluorescence intensity in the dark area was very strong and no Raman signal could be detected. As illustrated in Figure 4.54, in the vicinity of this dark area some sharp band were detected correspond phenylalanine (920, 760, 850 and1003 cm^{-1}) and phospholipids (O-P-O symmetric stretching mode at 760 and 835 cm^{-1}).

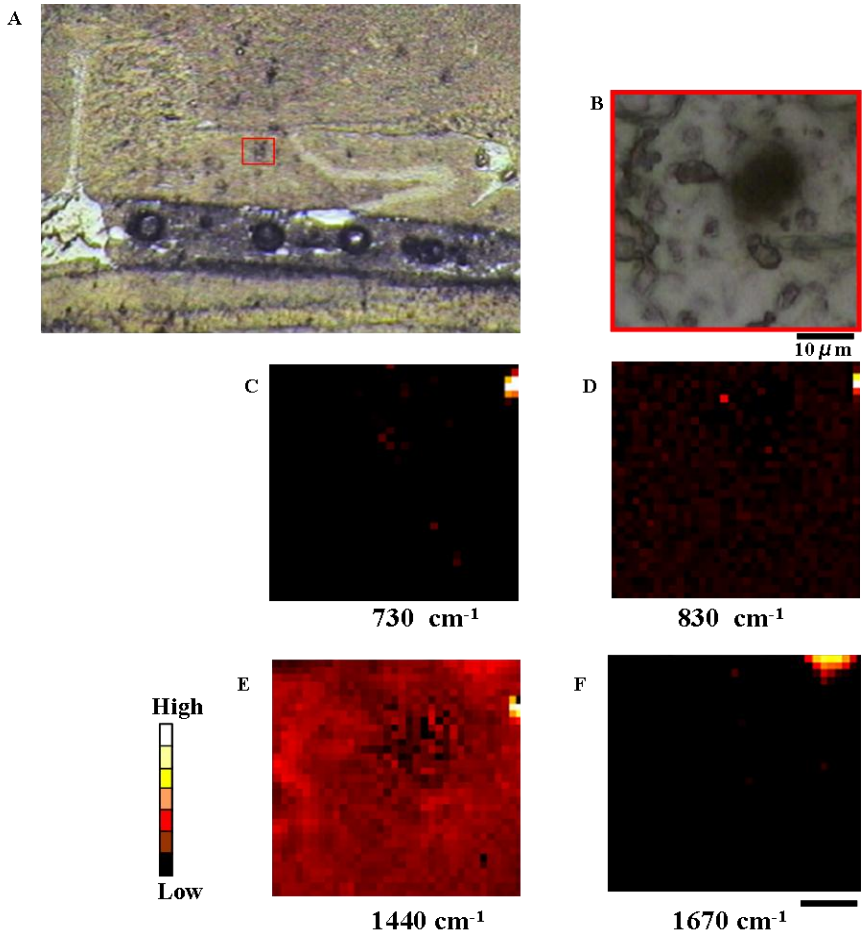

Figure 4.53: Depth Profile of Aβ plaque through A14(19) section of transgenic 14-month-old mouse brain. (A) The plaque in brain tissue. (B) Close-up of the mapped plaque. Processed map for (C) sphingomyelin (CN^+ symmetric mode at 730 cm^{-1}), (D) Cr (symmetric CN_3^+ band at 830 cm^{-1}), (E) Lipid (CH_2 deformation band at 1440 cm^{-1}), and (F) Aβ plaque (at 1670 cm^{-1}). Map area =1155 points. Acquisition time = 295 min. Colour scale: White corresponds to high intensity, black to no signal. Scale bar = 10 µm.

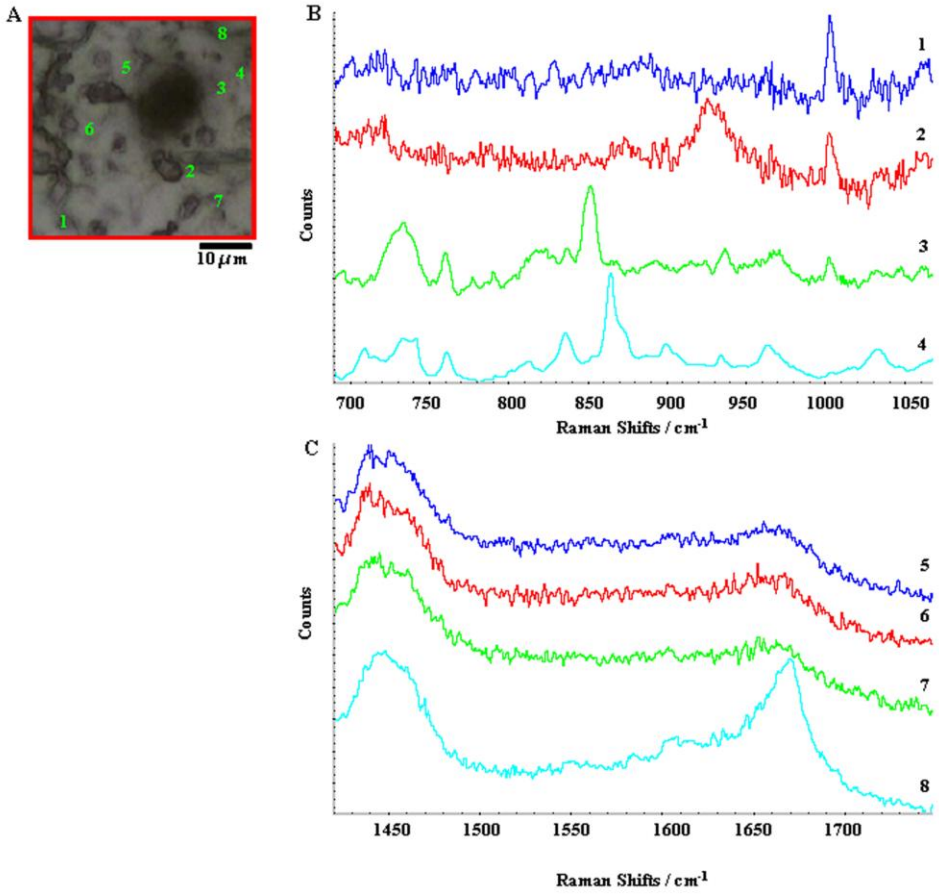

Figure 4.54: Spectra correspond to the pixels marked in the (A) mapped plaque in hippocampus of A14(19) section of transgenic 14 month-old mouse brain. Raman spectra in the region between (B) 700-1050 cm^{-1} and between (C) 1400-1750 cm^{-1}. Spectrum (1): broad band at 730 cm^{-1} assigned to CN mode of choline; phenylalanine peak at 1003 cm^{-1}; lipid band at 1060 cm^{-1}. Spectrum (2): broad band at 920 cm^{-1} due to *ν*(C-C) stretching mode probably in amino acids; strong phenylalanine peak at 1003 cm^{-1}; lipid band at 1060 cm^{-1}. Spectrum (3): broad band at 730 cm^{-1} due to CN^{+} symmetric stretching mode correspond to sphingomyelin; amino acids bands at 760 and 850 cm^{-1}; weak band at 930 cm^{-1} assigned to α-helix; phenylalanine and lipid peaks at 1003 and 1060 cm^{-1}, respectively. Spectrum (4) CN^{+} stretching mode at 730 cm^{-1}; asymmetric O-P-O stretching mode at 760 and 835 cm^{-1}; *ν* (C-C) protein assignment at 855 cm^{-1}; α-helix peak at 940 cm^{-1}. Spectrum (5,6,7): just lipid band at 1430-1440 cm^{-1}. Spectrum (8): lipid band at 1430-1440 cm^{-1}; anti-parallel β-sheet peak at 1670 cm^{-1}.

On conclusion, processed maps of amyloid plaque in serial sections of 14 month-old transgenic mouse, Cr deposits were observed in A14(14), A14(17) and A14(19). The appearance of Aβ plaque core in tissue sections A14(11), A14(14), A14(15), and A14(17) was much more distinctive. In these sections, the Aβ plaque was surrounded by elevated lipid distribution and sometimes near by deposits of Cr. The Cr deposits associated with plaques were not large in size. Lipid distribution was observed in all consecutive serial sections.

4.4.3 Creatine deposits in Caudate

The caudate of five transgenic mice and littermate controls were mosaic mapped with FPA-FTIR through 5, 8, 11, 14 and 17 month-old to explore any creatine distribution in the caudate region. Infrared spectra were collected with a Varian FPA-FTIR microscope, at 4 cm^{-1} spectral resolution, using Happ-Genzel apodization. An average of 128 spectra was co-added for each spectrum. In order to take the whole caudate area map, a mosaic was created. This technique involves combining a motorized stage to collect high resolution data from larger sample areas. The mosaic capability involves mapping the FPA image across a large field of view, whereby the images are tiled together to form a larger overall image consisting of many individual single tiles each 64 x 64 pixels. To collect the mosaic map, the center of the area of interest was selected and the mosaic map was taken first with 4 scan to make sure the collected mosaic was perfectly matched with the assigned area; then, the mosaic was collected with 128 scan per tile to increase the S/N ratio. IR maps were processed for Cr at 1410-1384 cm^{-1} (Figure 4.55B-62B), lipid symmetric CH_2 stretching band at 2853 cm^{-1} (Figure 4.55C-62C) and lipid carbonyl at 1733

cm^{-1} (Figure 4.55D-62D). In the colour scale, red corresponds to high intensity, and dark blue to no signal.

Areas of localized lipid elevation were observed in the caudate of almost all sections. Cr deposits were identified in sections A25(4), and A14(2) transgenic mice caudate tissue(Figure 4.57B&59B). Areas with strong absorption of the lipid band were located near Cr deposits (Figure 4.60B). Few Cr deposits were observed in the 14 month control mouse caudate (Figure 4.60C&D), but the size and amount of Cr deposits was greater in the same age transgenic section. No Cr was observed in 17 month-old Tg mouse (Figure 4.61B). It may be explained that the caudate region of most of the brain tissue sections was distorted at the time of sectioning. As shown in Figure 4.59B&60B, some Cr deposits were present in the caudate region of both Tg and non-Tg 14 month-old which the assigned region had been not folded and torn.

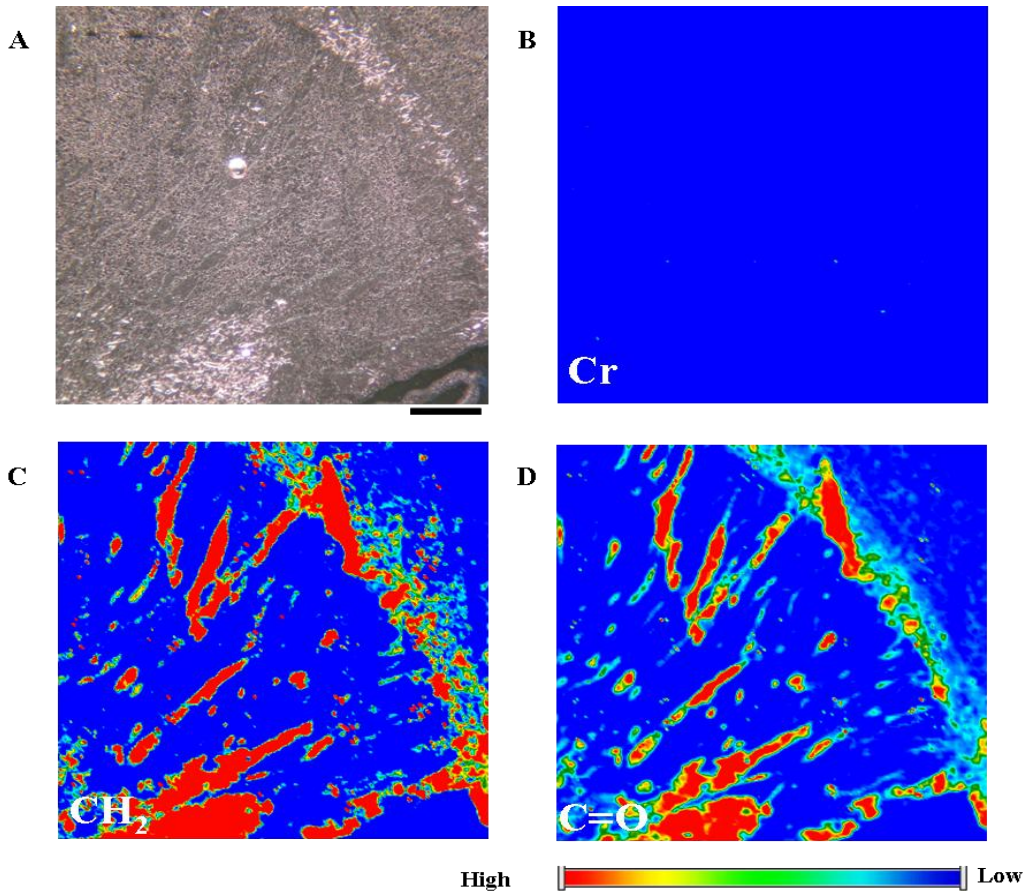

Figure 4.55: Creatine and lipid distribution in the caudate of Tg7(3), 5 months old Tg mouse. (A) Unstained hippocampi on MirrIR slide. (B) IR map of the caudate tissue processed for Cr, (C) IR map processed for the symmetrical CH_2 stretch, and (D) for lipid carbonyl. Spectral resolution 4 cm^{-1}/ pixel, spatial resolution 5.5 x 5.5 µm . Scale bar = 250 µm. Multiple mosaic map area = 5 x5. Spectra generated = 102400. Acquisition time = 182 min. Colour scale: red corresponds to high intensity, dark blue to no signal.

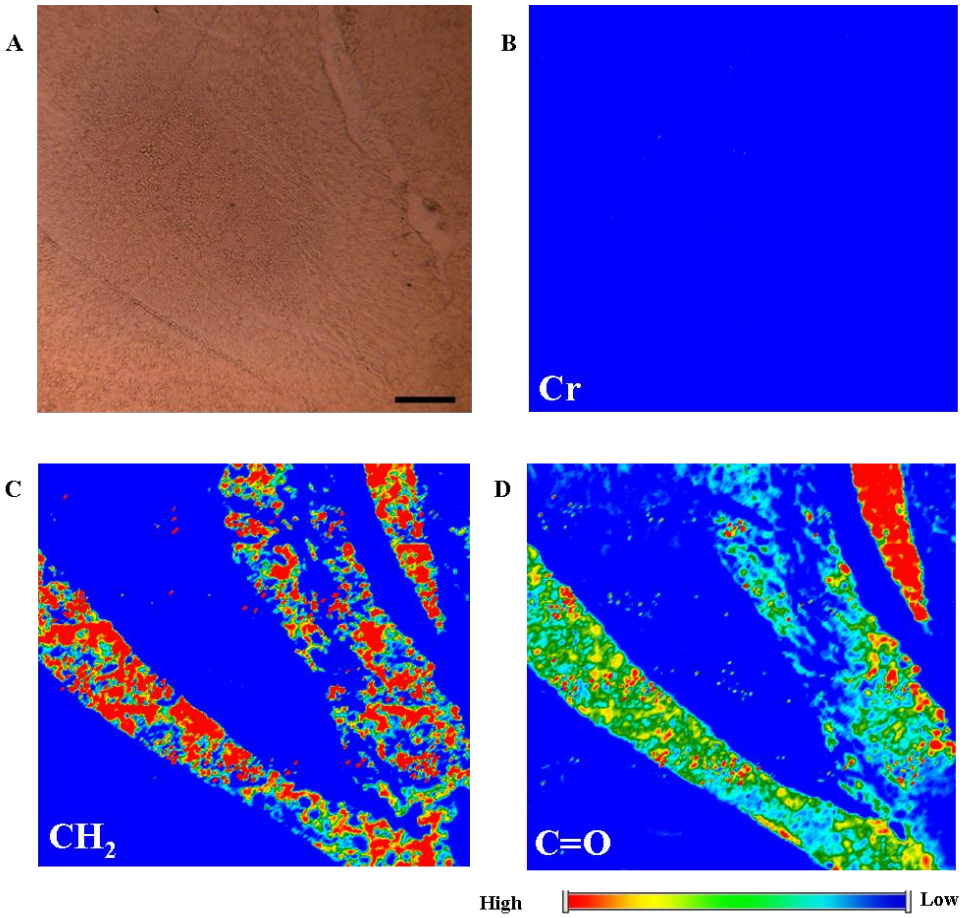

Figure 4.56: Creatine and lipid distribution in the caudate of TgADF 15(5c), 5 months old non-Tg control litter mate mouse. (A) The surveyed region of the caudate mounted on MirrIR slide. (B) IR map of the caudate tissue processed for Cr, (C) IR map processed for the symmetrical CH_2 stretch, and (D) for lipid carbonyl. Spectral resolution 4 cm^{-1}/ pixel, spatial resolution 5.5 x 5.5 . Scale bar = 250 µm . Multiple mosaic map area = 5 x5. Spectra generated = 102400. Acquisition time = 182 min. Colour scale: red corresponds to high intensity, dark blue to no signal.

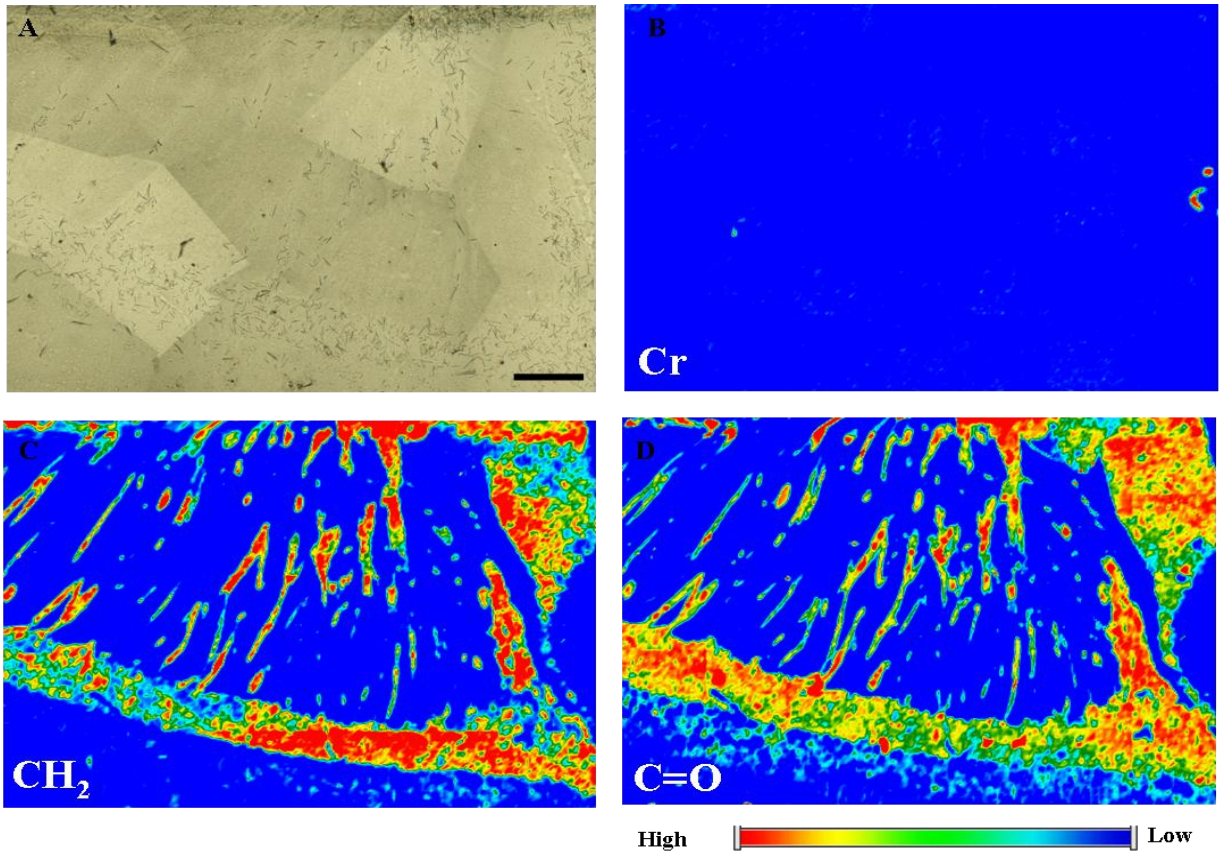

Figure 4.57: Creatine and lipid distribution in the caudate of A25(4), 8 months old Tg mouse . (A) The surveyed region of the caudate mounted on MirrIR slide.(B) IR map of the caudate tissue processed for Cr, (C) IR map processed for the symmetrical CH_2 stretch, and (D) for lipid carbonyl. Spectral resolution 4 cm^{-1}/ pixel, spatial resolution 5.5 x 5.5 µm . Scale bar = 250 µm. Multiple mosaic map area = 7 x 5. Spectra generated = 143,360. Acquisition time = 254 min. Colour scale: red corresponds to high intensity, dark blue to no signal.

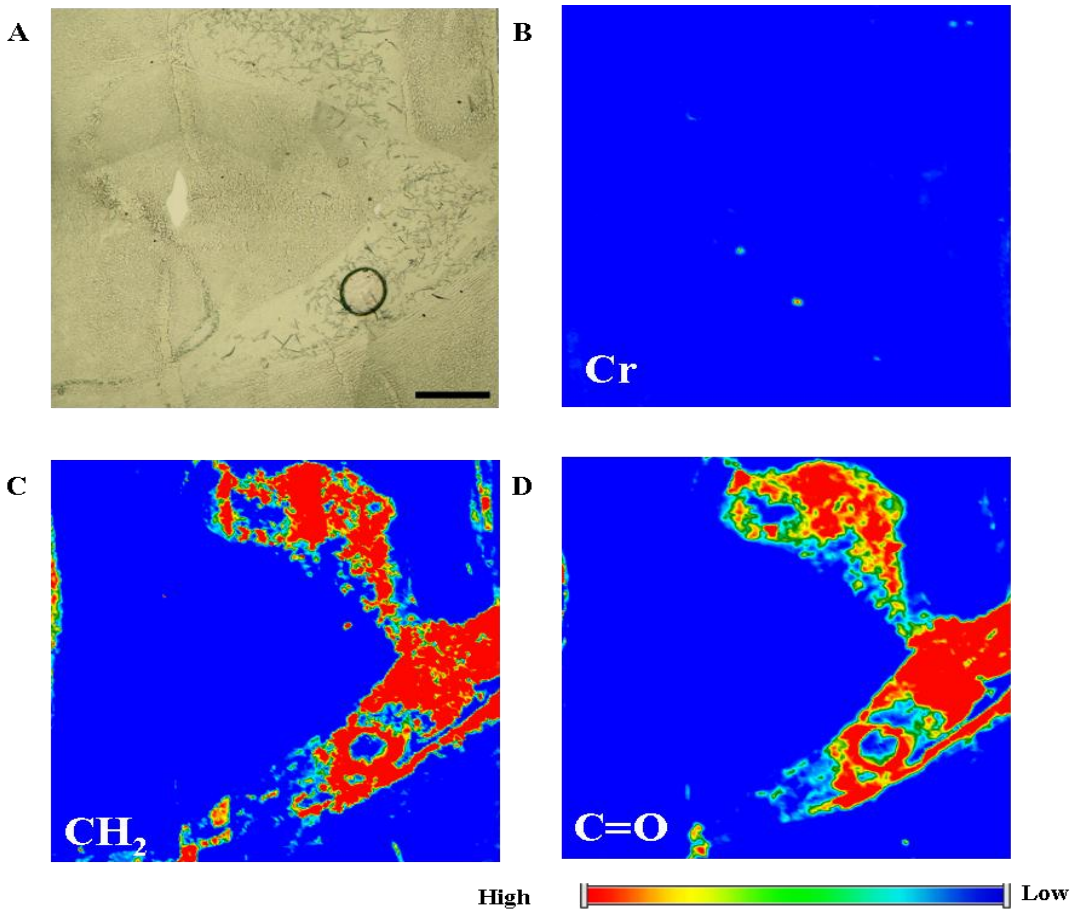

Figure 4.58: Creatine and lipid distribution in the caudate of A24(4), 8 months old non-Tg mouse. (A) The surveyed region of the caudate mounted on MirrIR slide. (B) IR map of the caudate tissue processed for Cr, (C) IR map processed for the symmetrical CH_2 stretch, and (D) for lipid carbonyl. Spectral resolution 4 cm^{-1}/ pixel, spatial resolution 5.5 x 5.5 . Scale bar = 250 µm. Multiple mosaic map area = 5 x5 μm^2. Spectra generated = 102400. Acquisition time = 182 min. Colour scale: red corresponds to high intensity, dark blue to no signal.

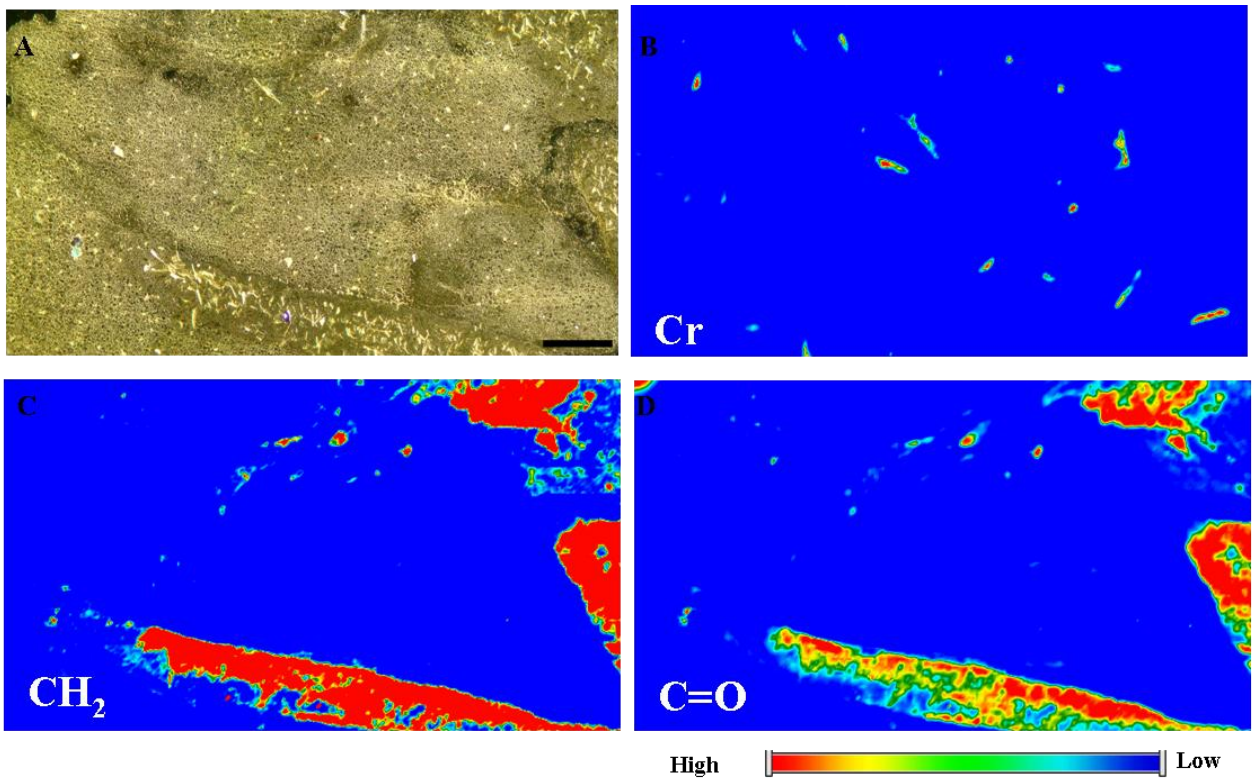

Figure 4.59: Creatine and lipid distribution in serial sections from the caudate of A14(2), 14 month-old Tg mouse. (A) The surveyed region of the caudate mounted on gold slide. (B) IR map of the caudate tissue processed for Cr, (C) IR map processed for the symmetrical CH_2 stretch, and (D) for lipid carbonyl. Spectral resolution 4 cm^{-1}/ pixel, spatial resolution 5.5 x 5.5 μm^2. Scale bar = 250 µm. Multiple mosaic map area = 7 x4. Spectra generated = 114,688. Acquisition time = 198 min. Colour scale: red corresponds to high intensity, dark blue to no signal.

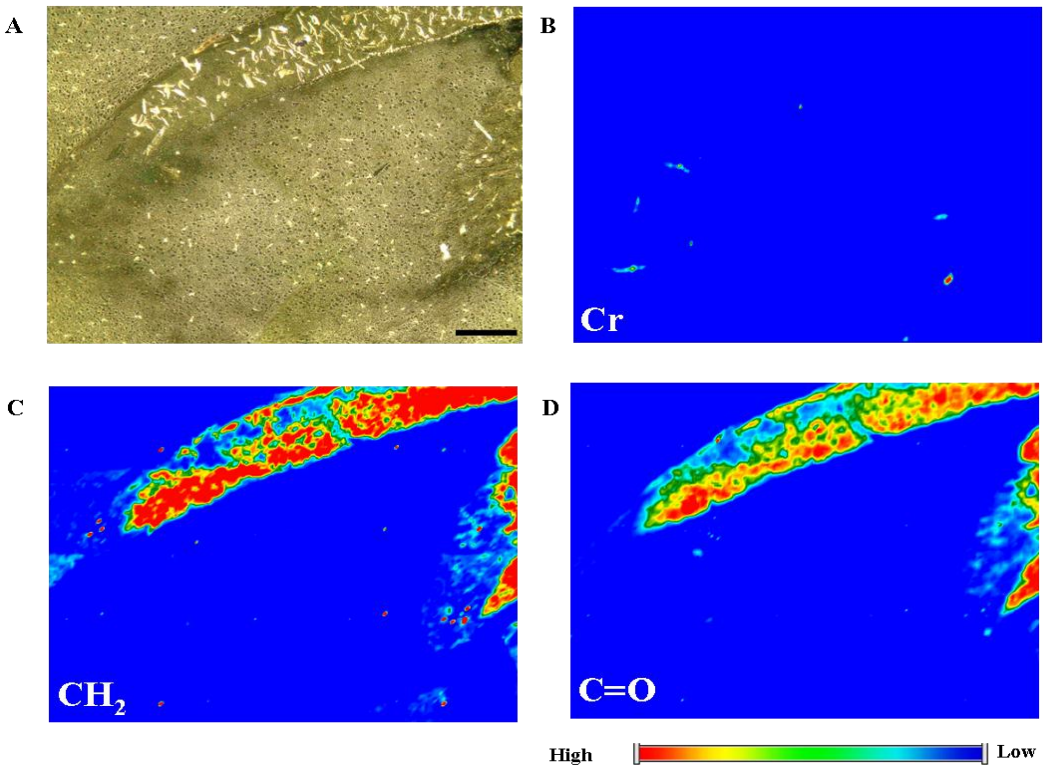

Figure 4.60: Creatine and lipid distribution in the caudate of A13(2), 14 month-old non-Tg mouse. (A) The surveyed region of the caudate mounted on gold silicon chips slide. (B) IR map of the caudate tissue processed for Cr, (C) IR map processed for the symmetrical CH_2 stretch, and (D) for lipid carbonyl. Spectral resolution 4 cm^{-1}/ pixel, spatial resolution 5.5 x 5.5 μm^2. Scale bar = 250 µm. Multiple mosaic map area = 5x4. Spectra generated =819,20. Acquisition time = 136 min. Colour scale: red corresponds to high intensity, dark blue to no signal.

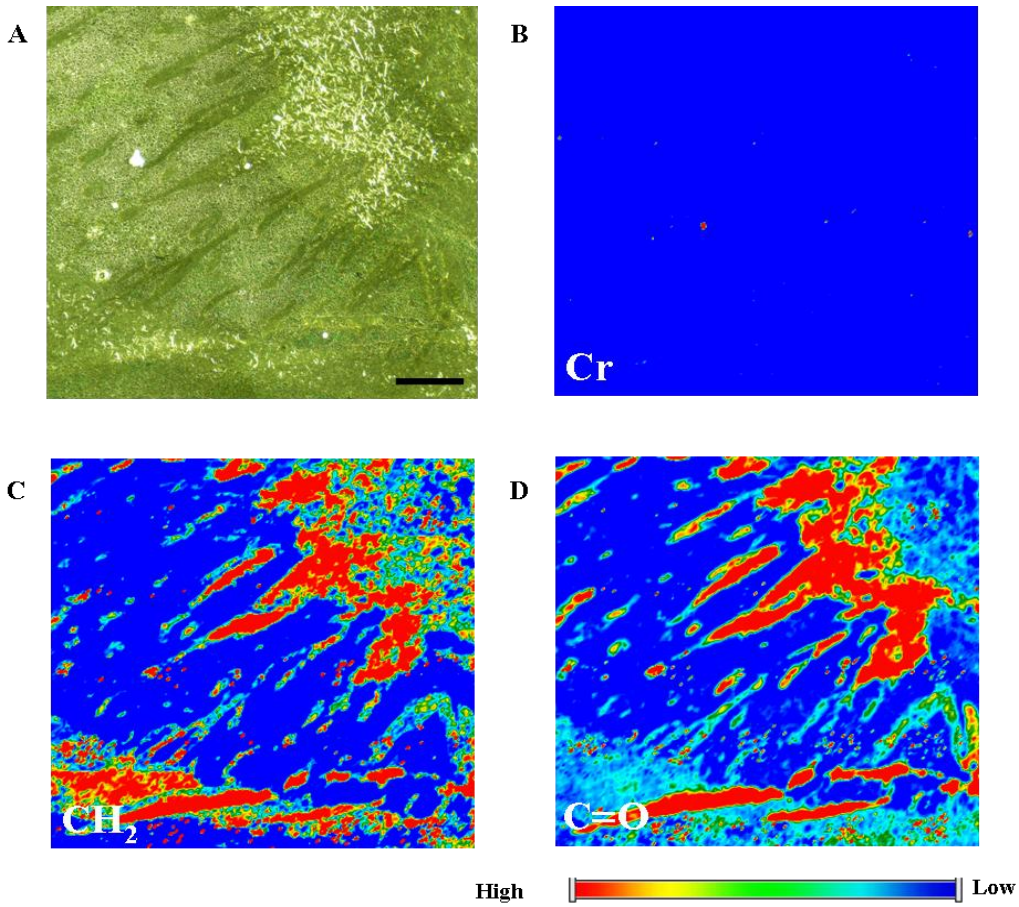

Figure 4.61: Creatine and lipid distribution in the caudate of A03(5), 17 months old Tg mouse. (A) The surveyed region of the caudate mounted on gold silicon chips slide. (B) IR map of the caudate tissue processed for Cr, (C) IR map processed for the symmetrical CH_2 stretch, and (D) for lipid carbonyl. Spectral resolution 4 cm^{-1}/ pixel, spatial resolution 5.5 x 5.5 μm^2. Scale bar = 250 µm. Multiple mosaic map area = 5 x5. Spectra generated = 102400. Acquisition time = 182 min. Colour scale: red corresponds to high intensity, dark blue to no signal.

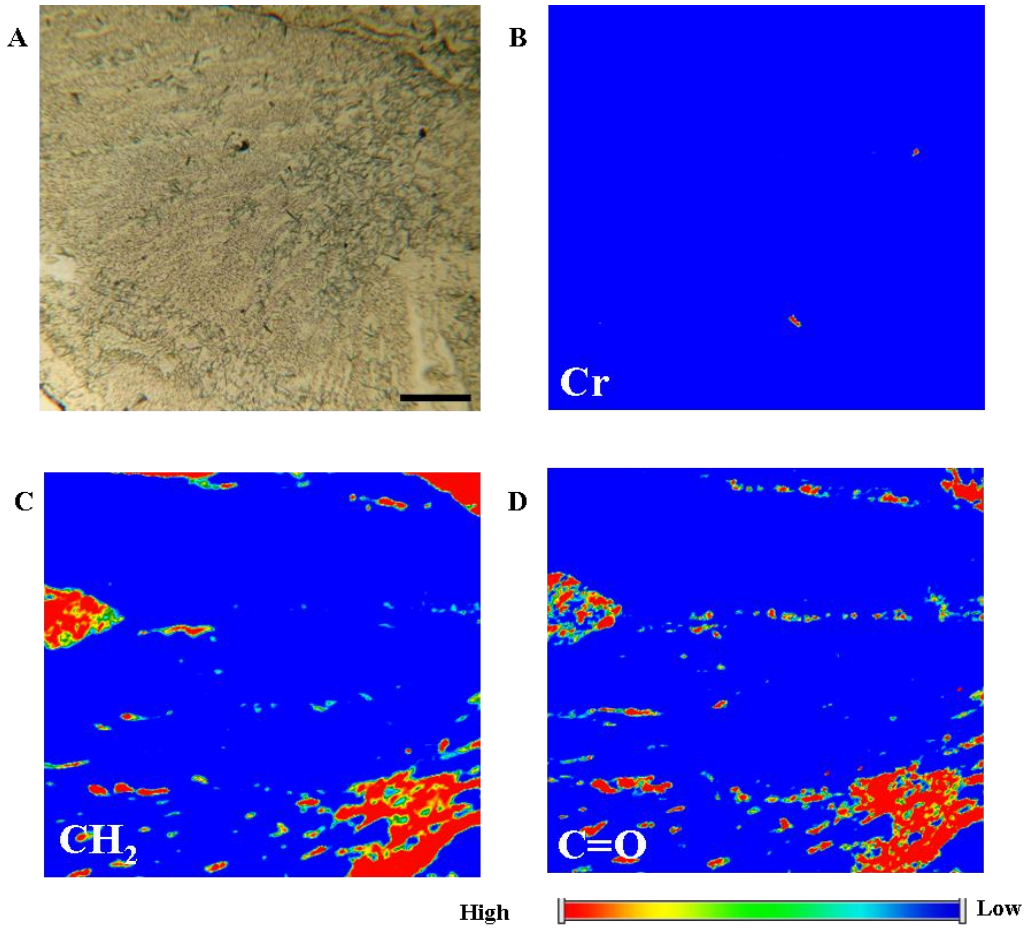

Figure 4.62: Creatine and lipid distribution in the caudate of A04(4), 17 month-old non-Tg mouse. (A) The surveyed region of the caudate mounted on MirrIR and gold. (B) IR map of the caudate tissue processed for Cr, (C) IR map processed for the symmetrical CH_2 stretch, and (D) for lipid carbonyl. Spectral resolution 4 cm^{-1}, spatial resolution 5.5 x 5.5 μm^2. Scale bar = 250. Multiple mosaic map area = 5 x5. Spectra generated = 102400. Acquisition time = 182 min. Colour scale: red corresponds to high intensity, dark blue to no signal.

Caudate Raman maps

The Raman maps was undertaken with higher spatial resolution in an effort to determine whether any other biochemical signatures can be identified as being localized with the Cr deposits found in caudate region of 14 month-old TgCRND8 mouse.

Raman maps were taken at 1 cm^{-1} spectral resolution with a Renishaw InVia Raman Microscope, using 785 nm excitation wavelength. The exposure time was 300 second to ensure a good signal to noise ratio. 10% laser power was used to prevent burning tissue.

Figure 4.63 shows Cr deposits in the caudate region of 14 month-old TgCRND8 mouse. The processed map displays that Cr deposit was surrounded by phenylalanine (Figure 4.63C&D). The selected spectra (1 to 8) illustrated Cr bands are shown in Figure 4.63D. These spectra correspond to the pixels marked with a box in the processed Raman map (Figure 4.63E). The strong symmetric CN^{+} stretch band at 830 cm^{-1} was chosen to illustrate the Cr distribution in brain tissue. As spectra 1 to 8 show, the only other sharp band that appeared was at 1003 cm^{-1} due to symmetric stretching vibration of the phenyl group of phenylalanine (Figure 4.63F). The other band which we were concern was Raman band at 730 cm^{-1} assigned to the symmetric stretching mode of the three $C\text{-}N^{+}$ bonds of choline for sphingomyeline which is predominantly found in cells of the nervous system. Oligodendrocytes which plays an important role to synthesize Cr in brain are rich in sphingomyelin; therefore, it could be possible a connection between some of the Cr deposits and these cells. In these spectra no band was observed at 730 cm^{-1}.

As shown in Figure 4.64, the dark area located in the left bottom of this map was found to be characteristic of phenylalanine band at 1003 cm^{-1} and ν(C-C) stretching mode, probably in amino acids proline because of sharp bands at 915 cm^{-1}.

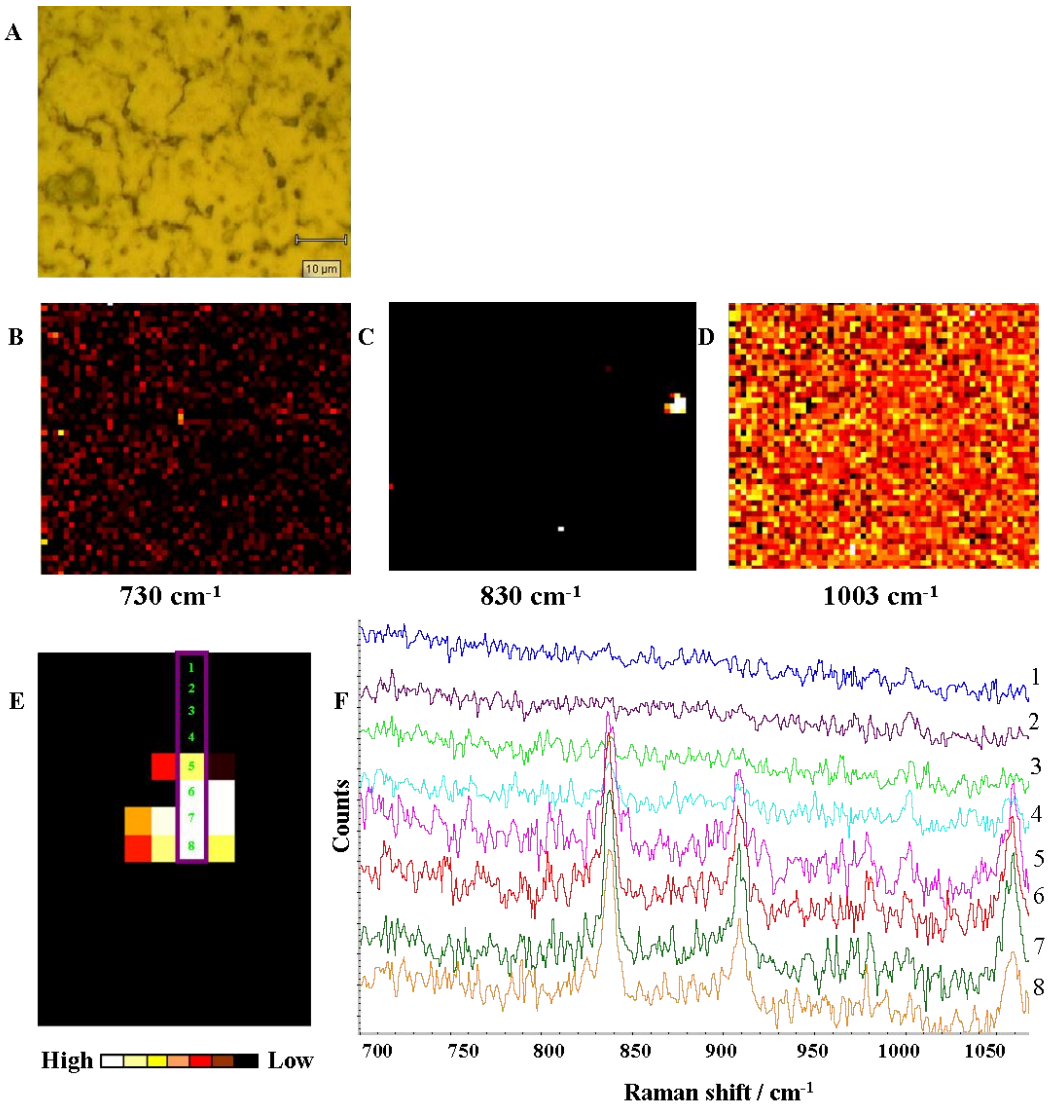

Figure 4.63: Raman map of an area in caudate of 14 month-old TgCRND8 mouse. (A) The photomicrograph of selected region in caudate. Scale bar = 10 µm. Processed map for (B) sphingomyelin (CN^+ symmetric mode at 730 cm^{-1}), (C) Cr (symmetric CN_3^+ band at 830 cm^{-1}), (D) phenylalanine (1003 cm^{-1}). Map area = 3068 points. Acquisition time = 624 min. Colour scale: White corresponds to high intensity, black to no signal. Scale bar = 10 µm. (F) These spectra (1-8) were correspond to the pixels marked with a box in the (E) processed Raman map (points 2823 to 2830) and labelled from 1 to 8.

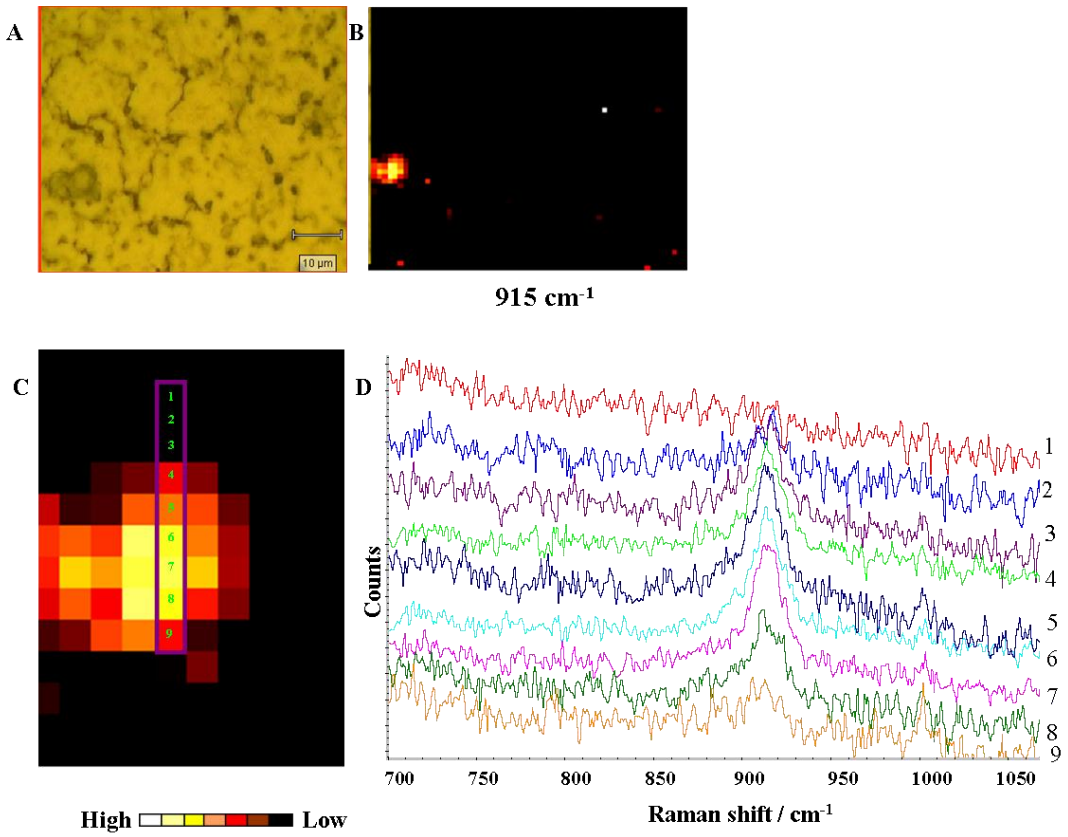

Figure 4.64: Raman map of an area in caudate of 14 month-old TgCRND8 mouse. (A) The photomicrograph of selected region in caudate. Scale bar = 10 µm. Processed map for (B) *v*(C-C) stretching mode, probably in amino acids proline because of sharp bands at 915 cm^{-1}. Map area = 3068 points. Acquisition time = 624 min. Colour scale: White corresponds to high intensity, black to no signal. Scale bar = 10 µm. (D) These spectra (1-9) were correspond to the pixels marked with a box in the (C) processed Raman map (points 289 to 297) and labelled from 1 to 9.

Figure 4.65 shows the mapped area in the caudate of 14 month-old transgenic mouse and processed for CN^+ stretching mode of choline head in sphingomyelin at 730 cm^{-1}, symmetric CN_3^+ stretch band of Cr at 830 cm^{-1}, and symmetric stretch mode of the phenyl group of phenylalanine at 1003 cm^{-1}. As the processed map displays, the Cr deposits were generally surrounded by phenylalanine without any remarkable elevation or depletion. The spectra of points to outline by a box in Figure 4.45 illustrated sharp Cr band along with phenylalanine band at 1003 cm^{-1} (Figure 4.65F).

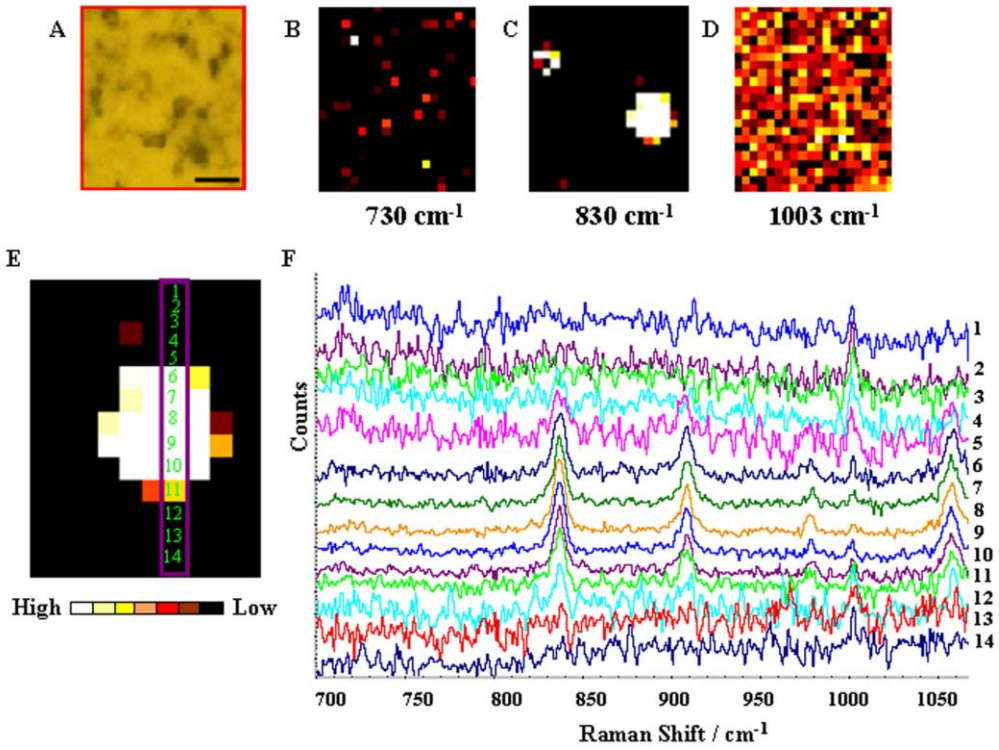

Figure 4.65: Raman map of an area in caudate of 14 month-old TgCRND8 mouse. (A) The photomicrograph of selected region in caudate. Scale bar = 10 µm. Processed map for (B) sphingomyelin (CN^+ symmetric mode at 730 cm^{-1}), (C) Cr (symmetric CN_3^+ band at 830 cm^{-1}), (D) phenylalanine (1003 cm^{-1}). Map area = 460 points. Acquisition time = 148 min. Colour scale: White corresponds to high intensity, black to no signal. Scale bar = 10 µm. (F) These spectra (1-14) were correspond to the pixels marked with a box in the (E) processed Raman map (points 265 to 352) and labelled from 1 to 14.

Figure 4.66 shows a Raman map recorded on the Cr rich area in caudate of 14 month-old TgCRND8 mouse. This area was first mapped by sFTIR microscope (Rak M, 2007) and FPA-FTIR, showed a large Cr deposit; then the Raman map was recorded and processed for CN mode of choline (Figure 4.66B), Cr (Figure 4.66C), and phenylalanine (Figure 4.66D). In map illustrated in Figure 4.66C, the number of pixels with Cr intensity was 580. It will be discussed more in section 4.5.3 that this Cr streak contains of a single crystal unit instead of several microcrystalline Cr deposits.

The selected spectra (1 to 14) illustrating Cr bands are shown in Figure 4.66D. These spectra correspond to the pixels marked with a box in the processed Raman map (Figure 4.66E). As illustrated in Figure 4.66F, the Cr band intensity increased gradually toward the centre of the aggregate (spectra 4-14 in Figure 4.66F). The band at 1003 cm^{-1} appeared in all these 14 spectra, and no peak was present at 730 cm^{-1}.

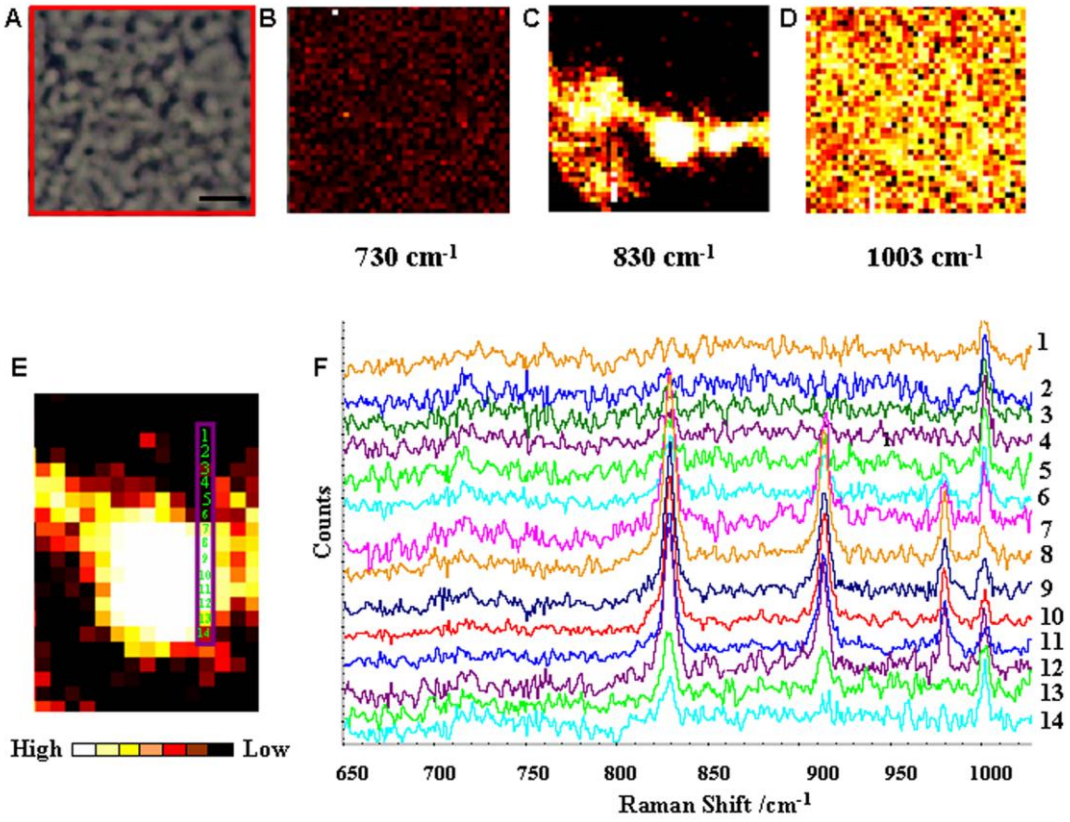

Figure 4.66: Raman map of an area in caudate of 14 month-old TgCRND8 mouse. (A) The photomicrograph of selected region in caudate. Scale bar = 10 µm. Processed map for (B) sphingomyelin (CN^+ symmetric mode at 730 cm^{-1}), (C) Cr (symmetric CN_3^+ band at 830 cm^{-1}), (D) phenylalanine (1003 cm^{-1}). Map area = 1886 points. Acquisition time = 411 min. Colour scale: White corresponds to high intensity, black to no signal. Scale bar = 10 µm. (F) These spectra (1-14) were correspond to the pixels marked with a box in the (E) processed Raman map (points 1082 to 1095) and labelled from 1 to 14.

4.5 Creatine crystal orientation effect

From the IR spectra collected at SRC, it was discovered by Veena Agrawal (summer student in Dr. Gough's lab) that those creatine spectra taken by synchrotron FT-IR spectromicroscopy gave different spectrum for various deposits.

Because the spectral markers were critical to identifying tissue components, a combined theoretical (collaboration with Fatemeh FarazKhorasani, graduate student in Dr. Gough's group) and experimental study was undertaken to better evaluate Cr crystal orientation in brain tissue. The combination of theoretical and experimental helped us make better interpretation of the experimental data.

After Cr monohydrate crystal prepared, the sFTIR spectra of three crystals in horizontal, 45° and vertical orientation (Figure 4.67A) were recorded across a spectral range of 2000 to 900 cm^{-1} on a Nicolet Magna 550 FTIR with Continuum microscope. The data collection was performed by Dr. Gough at SRC, University of Wisconsin (Madison, WI, USA, 2007).

As Figure 4.67C shows, the spectrum of horizontal Cr monohydrate crystal (red spectrum) reveals that the peak at 1405 cm^{-1} was present very strong, but the two other Cr peaks (1305, 1394 cm^{-1}) were totally disappeared. In the spectrum of pure Cr crystal at 45°, the peak at 1405 cm^{-1} was part of a doublet, with the second peak at a lower frequency of 1394 cm^{-1} and the peak at 1305 cm^{-1} was also strong (Figure 4.67C; green spectrum). However the spectrum obtained from a vertical Cr monohydrate crystal taken by sFTIR displays strong peak at 1305 cm^{-1} which is usually very distinct Cr peak from surrounding tissue. This peak was identified along with other peak at 1394 cm^{-1} and a small peak at 1422 cm^{-1} while the peak at 1405 cm^{-1} was not present (Figure 4.67C; blue

spectrum). This phenomenon is due to creatine deposits of different orientations interacting in the different ways with the polarized light of synchrotron.

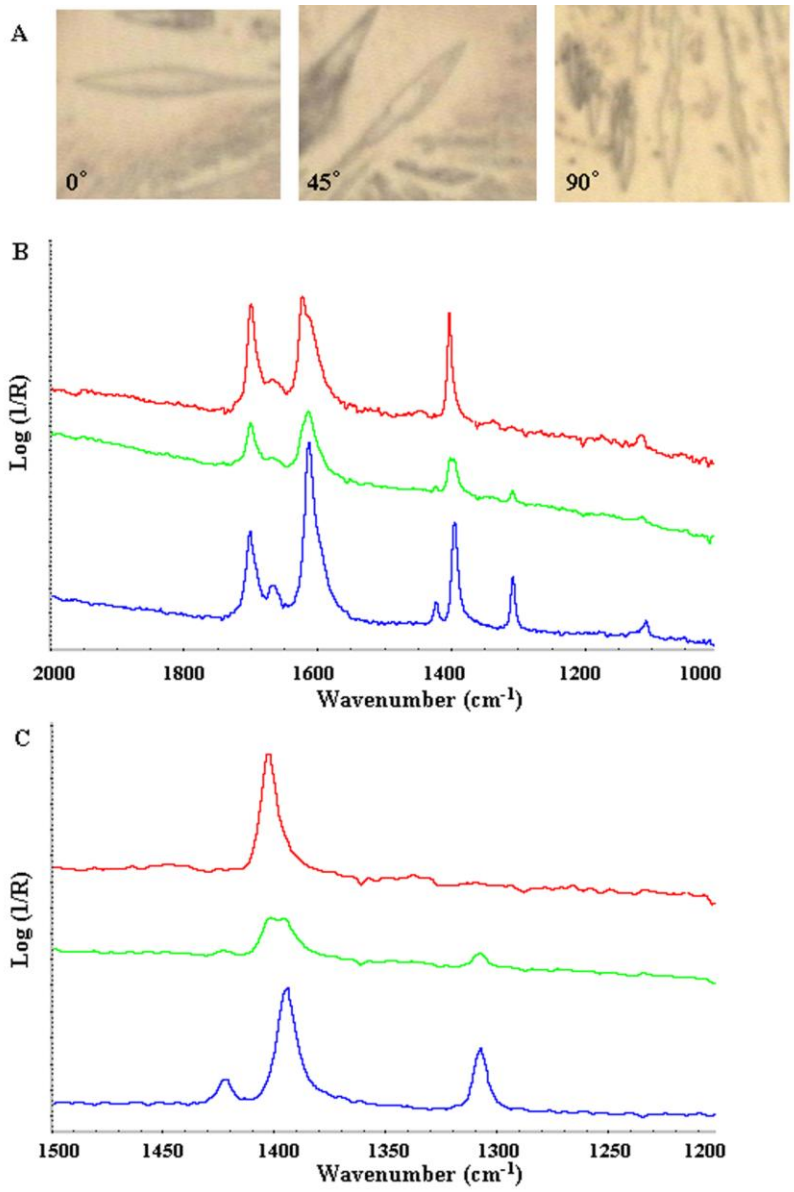

Figure 4.67: Creatine crystal with different orientation interact in the different ways with the polarized synchrotron light. (A) Pure creatine crystals prepared on gold coated silicon slide. a) Horizontal, b) 45°, and c) vertical crystal. (B) sFTIR spectra of horizontal crystals (red spectrum), 45° (green spectrum), and vertical (blue spectrum) taken by synchrotron light source with 512 san number between 2000-900 cm^{-1} and (C) Enlarged sFTIR between 1500-1200 cm^{-1}region. Data collection was performed by Dr. Gough at SRC, University of Wisconsin (2007).

4.5.1 Reprocessed previous sFTIR maps of serial sections

Previously, depth profiling of serial sections was undertaken in an effort to better characterize the creatine deposits and their distribution through the hippocampus of TgCRND8 mouse (Gallant, 2007). These maps were acquired across the hippocampus of each section using the Nicolet Continuum IR microscope at the Synchrotron Radiation Centre in Wisconsin and were processed for creatine at 1305 cm^{-1} (Figure 4.68 E,F,G,H) by Megan Gallant (former graduate student in Dr. Gough's lab). Meanwhile, it was discovered by Veena Agrawal (a summer student in Dr. Gough's group, 2007-2008) that creatine spectra taken by synchrotron FTIR spectromicroscopy gave different spectra for various deposits. Since the spectral markers were critical to identifying tissue components, these maps were reprocessed with Omnic/Atlμs software. The absorbance level at 1412 cm^{-1} and 1380 cm^{-1} were set as baseline values and the peak between 1408-1384 cm^{-1} was measured (Figure 4.68 I,J,K,L). The colors ranging from blue (low) to red (high) were assigned to display the distribution of creatine peaks on a colour scale. As shown in Figure 4.68 I,J,K,L, several horizontal deposits were appeared after reprocessing maps at 1408-1384 cm^{-1} that were not represented in maps processed at 1305 cm^{-1}.

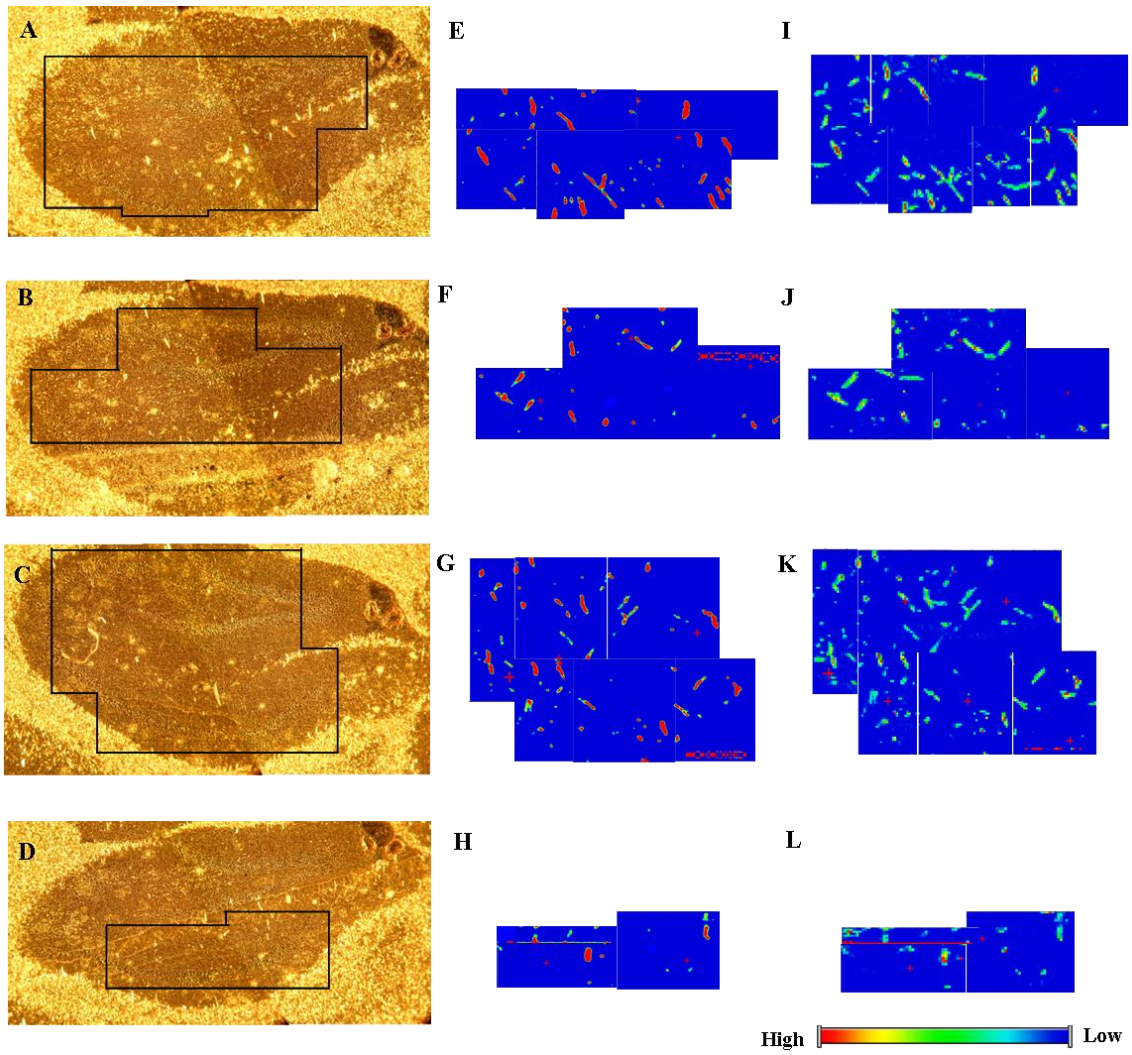

Figure 4.68: Comparison of the location of creatine deposits processed in only 1305 cm^{-1} and peaks between 1408 and 1384 cm^{-1} in serial sections of 14 month-old TgCRND mouse. (A,B,C,D) The region of the hippocampus surveyed. (E,F,G,H) sFTIR maps previously processed at 1305 cm^{-1} to identify Creatine distribution in serial sections. (I,J,K,L) These sections were reprocessed using the peaks between 1408 and 1384 cm^{-1}, rather than the peak centered at 1305 cm^{-1}. Several horizontal deposits appeared in the reprocessed maps.

Figure 4.69 shows the spectra from two points (A,B) in the synchrotron map (line green and aqua) and FPA map (blue and red) taken by Alex Kuzyk (summer student in Dr. Gough's lab). As illustrated in this Figure, spectrum A_1 which related to vertical Cr deposit shows the strong peaks at 1305, 1395 cm^{-1}; while, spectrum B_2 displays these two peaks were disappeared and only a strong band at 1405 was present. The spectra of the same points recorded by FPA-FTIR microscope shows that all Cr peaks at 1305, 1394 and 1405 cm^{-1} were appeared since the globar light is not polarized. These spectra clearly shows the effect of synchrotron polarized light on Cr crystal orientation.

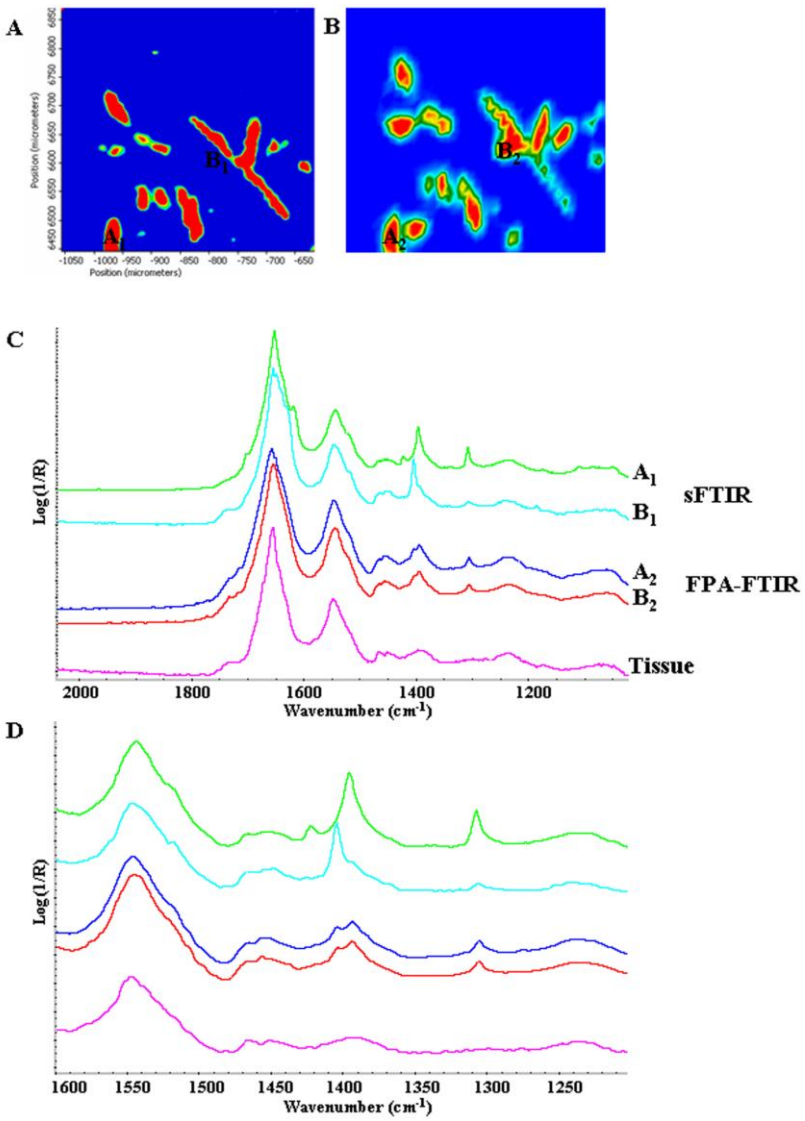

Figure 4.69: Comparison Cr spectra in hippocampus of 14 month-old TgCRND8 mouse. (A) sFTIR and (B) FPA-FTIR maps processed at 1305 cm^{-1}. C) IR spectra from points A_1 (green line), B_1 (aqua line) taken by synchrotron and spectra A_2, B_2 recorded by FPA-FTIR from the same region in hippocampus are shown in the region between 2000-1000 cm^{-1} and (D) enlarged between 1600-1200 cm^{-1}.

4.5.2 Spectra collected by IR and Raman from neat Cr crystal using polarizer

To evaluate the effect of polarized light on the spectra of crystalline Cr, several pure Cr monohydrate crystals were prepared and the best crystals were chosen for IR and Raman data collection. The reason that polarizer was applied is that globar light used as the light source of FPA-FTIR Microscope is not a polarized light; therefore, all the peaks to identify Cr deposits (1305, 1394, 1405 cm^{-1}) are appeared.

IR spectra of a pure Cr crystal, oriented horizontally on the gold silicon chips slide, were recorded with FPA detector and IR polarizer (0° and 90°) on the Varian Microscope (Figure 4.70). The Raman spectra of the same horizontal Cr crystal were collected using polarizer and polarizer + half-wave plate (Figure 4.71).

Single tile maps of neat creatine crystals prepared on gold slide were using polarizer (0° and 90°), then processed on the same peaks (1305 cm^{-1} and 1405 cm^{-1}), selected for brain tissue. FPA-FTIR data collection were obtained with the Varian 670/620 spectrometer. As shown in Figure 4.70, with using polarizer 0°, the polarizer light was perpendicular to the long axis of the crystal and by using polarizer 90°, the polarized light was parallel to the long axis of the crystal. The collected maps were processed at 1305 cm^{-1} to show the effect of polarized light on the crystalline Cr (Figure 4.70B). Figure 4.68D displays the spectra of pure horizontal Cr monohydrate crystal taken using polarizer 0° (blue spectrum) and 90° (red spectrum). As shown in the enlarged spectra between 1500-1200 cm^{-1}, when the polarization is perpendicular to the long axis of the horizontal Cr crystal, the peaks at 1305, 1394 and 1423 cm^{-1} appear and no peak was identified at 1405 cm^{-1}. Inversely, when the polarization is parallel to the long axis of the crystal, the

peak at 1405 and 1447 cm^{-1} were present. This result compared to the spectra taken at SRC from different Cr crystal orientation (Figure 4.67). The spectra obtained by using polarizer 0° on horizontal Cr crystal was exactly like the spectra of vertical pure Cr crystals taken by sFTIR Microscope and the spectra taken with using polarizer 90° was resemble to the spectra of horizontal pure Cr crystals taken by sFTIR Microscope. This similarity on the spectral behaviour could point that the the collected synchrotron radiation has more horizontal polarization.

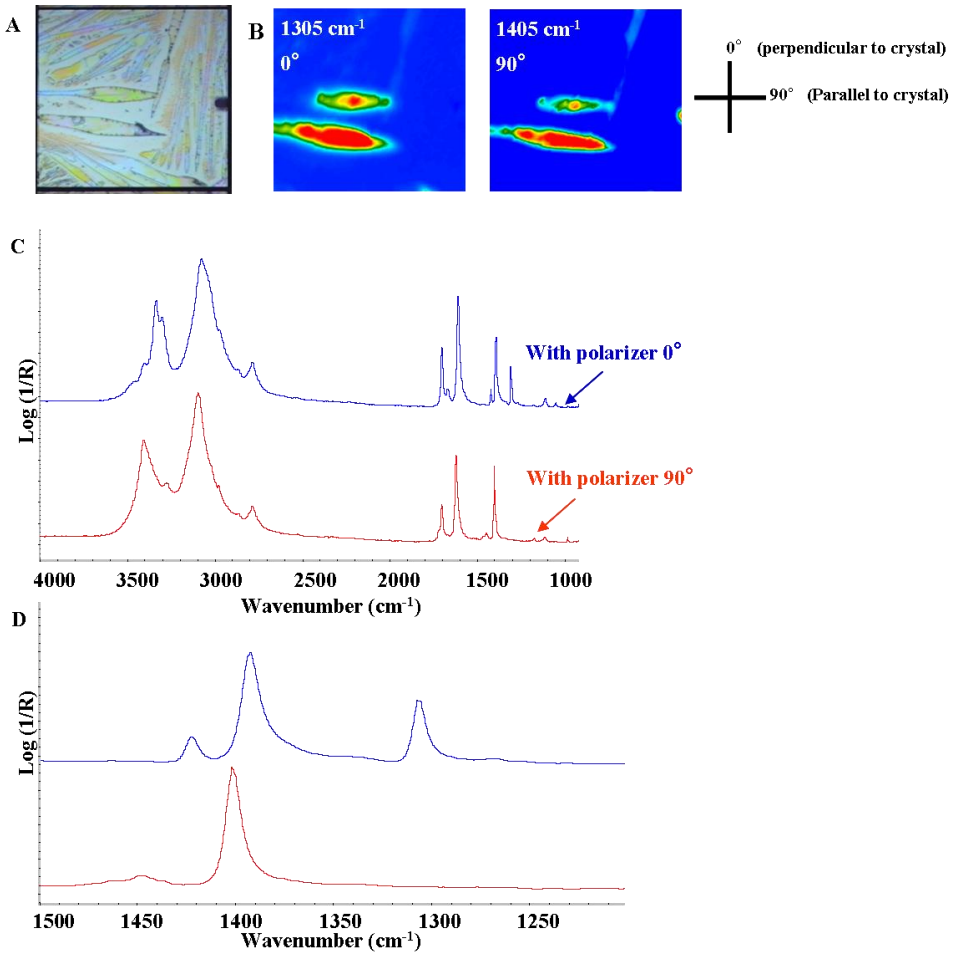

Figure 4.70: IR spectra of pure horizontal Cr crystal taken by FPA-FTIR Microscope. (A) The surveyed region of the pure Cr monohydrate crystal mounted on gold silicon chips slide. (B) Processed map at 1305 cm^{-1} and 1405 cm^{-1}. (C) IR spectra of pure Cr crystal taken by using polarizer at 0° (blue spectrum) and 90° (red spectrum) in the region between 4000-900 cm^{-1}, and (D) enlarged between 1500-1200 cm^{-1}.

Raman spectra of a small point of the same neat horizontal Cr monohydrate crystal outline in Figure 4.71A were recorded across a spectral range of 200-2000 cm^{-1} and detected by charge-coupled device (CCD). These spectra of pure Cr crystal were recorded with a polarizer and polarizer + half-wave plate. As displayed in Figure. 4.67C, the band at 830 cm^{-1} was very sharp in both Raman spectra taken with the polarizer (blue spectrum), and using polarizer & half-wave plate; therefore, the difference is between intensity of peak area at 912, 982, and 1054 cm^{-1}. As mentioned, in Raman spectrum, the band 830 cm^{-1} was selected for identification of Cr distribution. This band was always very strong, but as displayed in Figure 4.71C, the relative intensities of bands at 912, 982, and 1054 cm^{-1} were stronger with polarizer & half-wave plate compared to using polarizer. As with FT-IR, the selection rules for the polarizability derivatives govern the modes that will be active relative to the polarized laser light. The polarizability is defined as how easily the electron cloud becomes distorted. As the vectors *P* and *E* are not along one coordinate axis, the polarizability shown by polarizability tensor (α). The Raman intensity is related to the changes in the derivative of the polarizability tensor for each mode and these derivatives can be significantly large in different direction. This is the reason why all the Cr identified bands can be observed even by using polarizer and polarizer + half-wave plate. To get the effect of polarized light, all the data on brain tissue were recorded using FPA-FTIR microscope with polarizer through a wide range of angles.

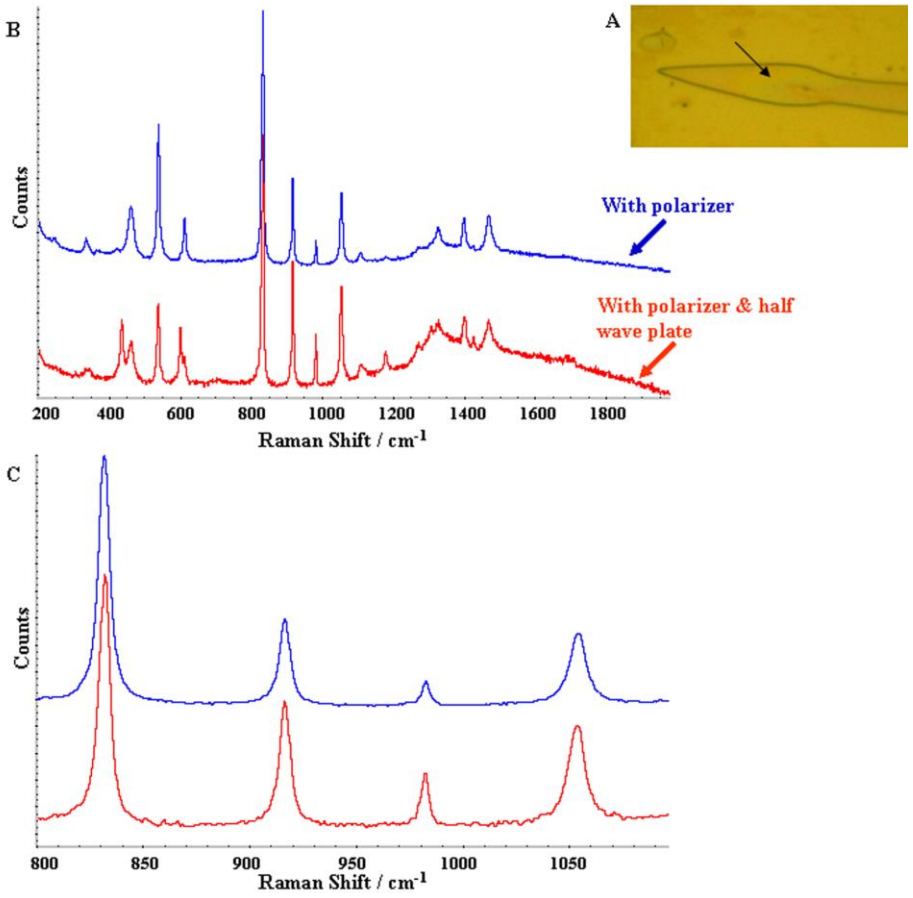

Figure 4.71: Raman spectra of pure horizontal Cr monohydrate crystal taken by Renishaw InVia Raman Microscope. (A) The surveyed region of the pure horizontal Cr monohydrate crystal mounted on gold silicon chips slide. (B) Raman spectra of pure horizontal Cr crystal taken by using polarizer (blue spectrum) and polarizer & half-wave plate (red spectrum) in the region between 200-2000 cm^{-1}, and (C) enlarged between 800-1100 cm^{-1}.

4.5.3 Maps collected by IR Microscope in different brain tissue regions using polarizer

To evaluate Cr crystal orientation and explore whether Cr deposits in brain tissue are composed of microcrystalline Cr deposits or a unit single crystal, single tile maps in caudate and hippocampus regions of 14 months-old transgenic mouse were recorded with the Varian FTIR microscope.

Figure 4.72 presents the caudate of 14 month-old transgenic mouse mapped with a 64 x 64 Focal Plane Array detector, at a range of polarizer angles from 0° to 180°, at 10° intervals. 19 maps were acquired with polarizer and one without polarizer. It took 7 min to collect each map with 128 scan number. FPA detector covered the IR spectral range from 4000 to 900 cm^{-1} at 4 cm^{-1} spectral resolution. All spectra were taken in reflection mode using Happ-Genzel apodization function.

For each of the maps, the background was taken with the same parameters and also same polarizer angle was applied. All data were processed with specific focus on peaks at 1305 cm^{-1} and 1405 cm^{-1}, as these exhibited extreme polarization effects and had less overlap with tissue bands compared to other Cr peaks.

As displayed in Figure 4.72C, the processed map at 1305 cm^{-1} shows that the Cr signal for Cr streak (a), located on the left bottom side of mapped area, was weak at 0° and started being strong at around 60° and gradually by increasing the polarizer angle started being weak again till for polarizer set at 150° disappeared, then at higher polarization of incident radiation, it started to appear again (Figure 4.72C).Conversely, the processed

map at 1405 cm^{-1} showed the Cr signal disappeared by applying 60° polarizer and was strong at around 150° (Figure 4.73C). As illustrated in Figure 4.70C, the processed map at 1305 cm^{-1} shows the Cr signal for Cr streak (b) increased from 0° to around 40° and extinguished at around 130° and then appeared again by utilizing higher polarizer angle (Figure 4.72C). Like to first Cr deposit, The Cr signal was inverse when the maps were processed at 1405 cm^{-1} (Figure 4.73C). This on and off in the Cr signal shows the orientation dependence of Cr crystal.

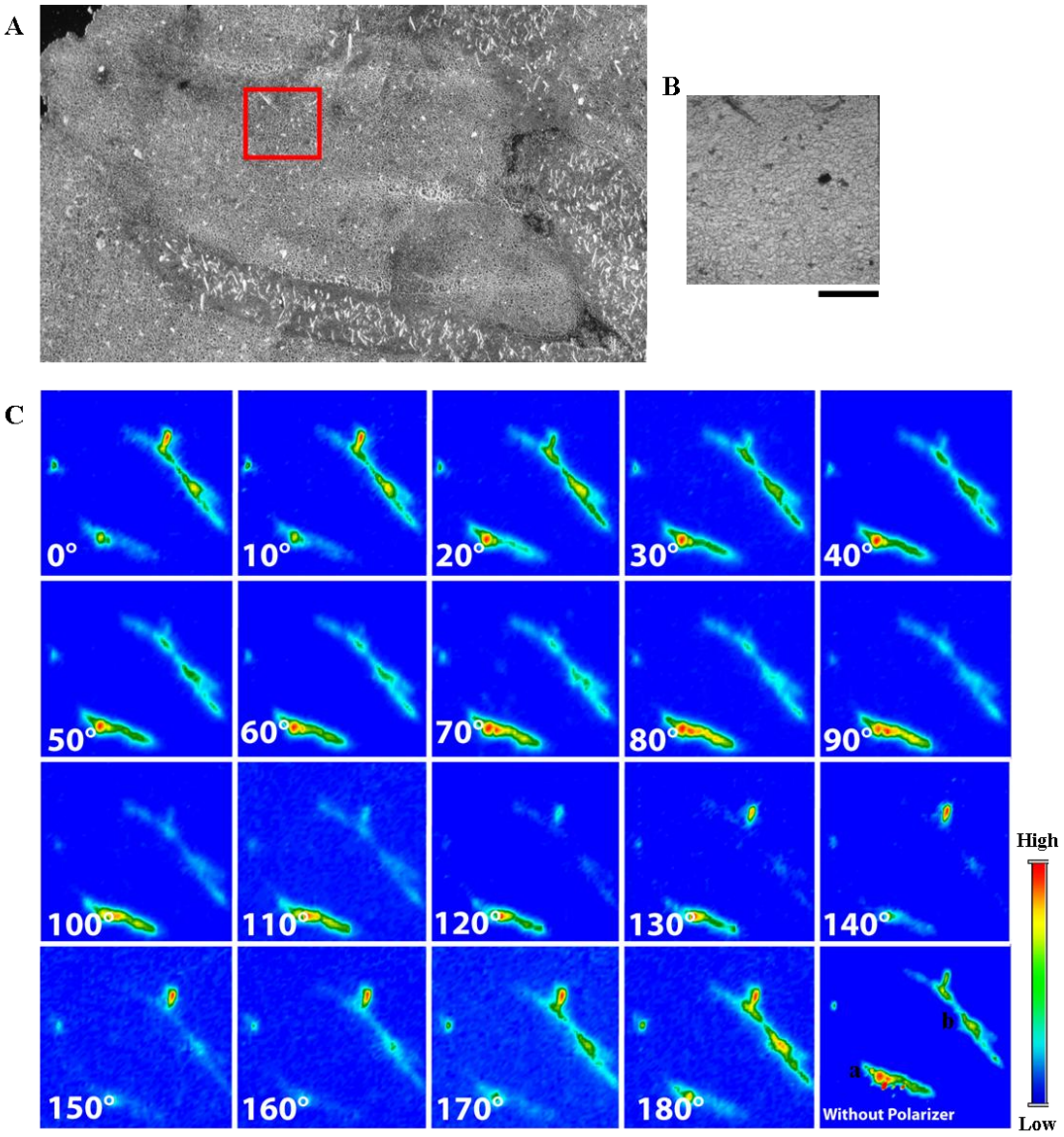

Figure 4.72: Maps processed at 1305 cm^{-1} in the caudate regions of 14 months-old transgenic mouse using polarizer angles of 0° to 180°, at 10° intervals. (A) The region of the caudate surveyed. (B) Close-up of the mapped area. (C) Maps recorded with a Varian FTIR microscope and a 64 x 64 Focal Plane Array detector, using polarizer through 0° to 180°, at 10° intervals and processed at 1305 cm^{-1}. Scale bar =100 µm. Single tile maps; spectra generated = 4096. Acquisition time = 7 min (for a single tile). Colour scale: red corresponds to high intensity, dark blue to no signal.

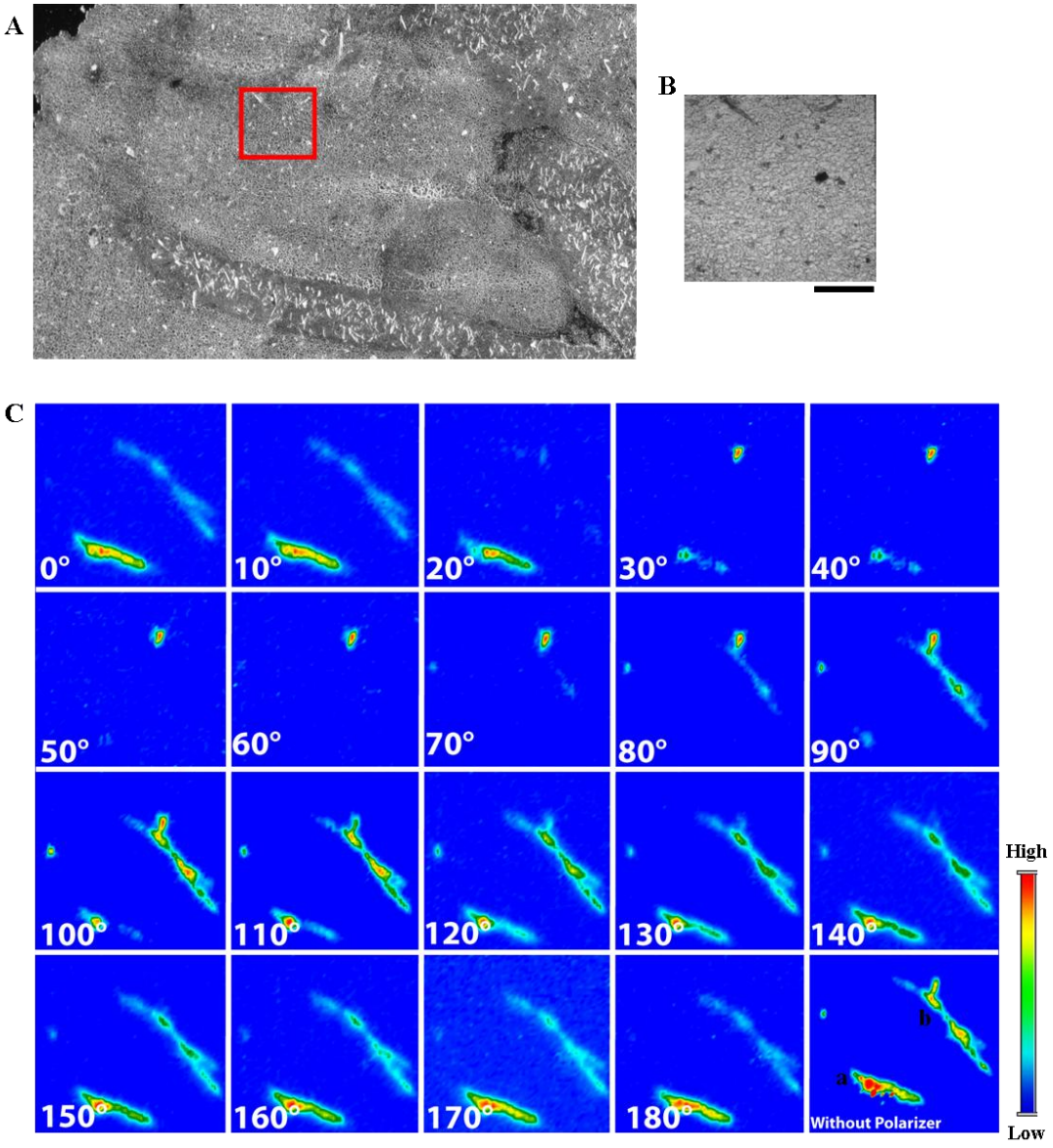

Figure 4.73: Maps processed at 1405 cm^{-1} in the caudate regions of 14 months-old transgenic mouse using polarizer angles of 0° to 180°, at 10° intervals. (A) The region of the caudate surveyed. (B) Close-up of the mapped area. (C) Maps recorded with a Varian FTIR microscope and a 64 x 64 Focal Plane Array detector, using polarizer through 0° to 180°, at 10° intervals and processed at 1405 cm^{-1}. Scale bar =100 µm. Single tile maps; spectra generated = 4096. Acquisition time = 7 min (for a single tile). Colour scale: red corresponds to high intensity, dark blue to no signal.

In the next step, the spectra of different points on the Cr streak (a,b) were examined by Varian Resolution-Pro software through the range of polarizer angles. Figures 4.74, 4.73 show the absorption intensity versus the polarization angle processed at 1305 and 1405 cm^{-1} for these two Cr streaks mapped by FPA-FTIR Microscope.

As presented in Figure 4.74, the intensity of four points marked in the Cr streak (a) has its maximum around 40° and gets to its minimum around 130° when analyzed at 1305 cm^{-1} (Figure 4.74C), while the intensity at 1405 has its minimum around 40° and gets to its maximum around 130° (Figure 4.74D).

As shown in Figure 4.75, five points in Cr streak (b) were chosen and the absorption intensity versus the polarization angle was probed for processed maps at 1305 and 1405 cm^{-1}. It can be seen that the intensity at 1305 cm^{-1} has its maximum around 60° and gets to its minimum around 150° (Figure 4.75C). In contrast, the intensity at 1405 cm^{-1} has its minimum around 60° and gets to its maximum around 150° (Figure 4.75D).

The same maximum and minimum intensity was obtained for examined points on each Cr streak. It shows that the along a Cr streak, the orientation dependency are similar and hence these points belong to a single crystal instead of composing several microcrystalline Cr crystal deposits.

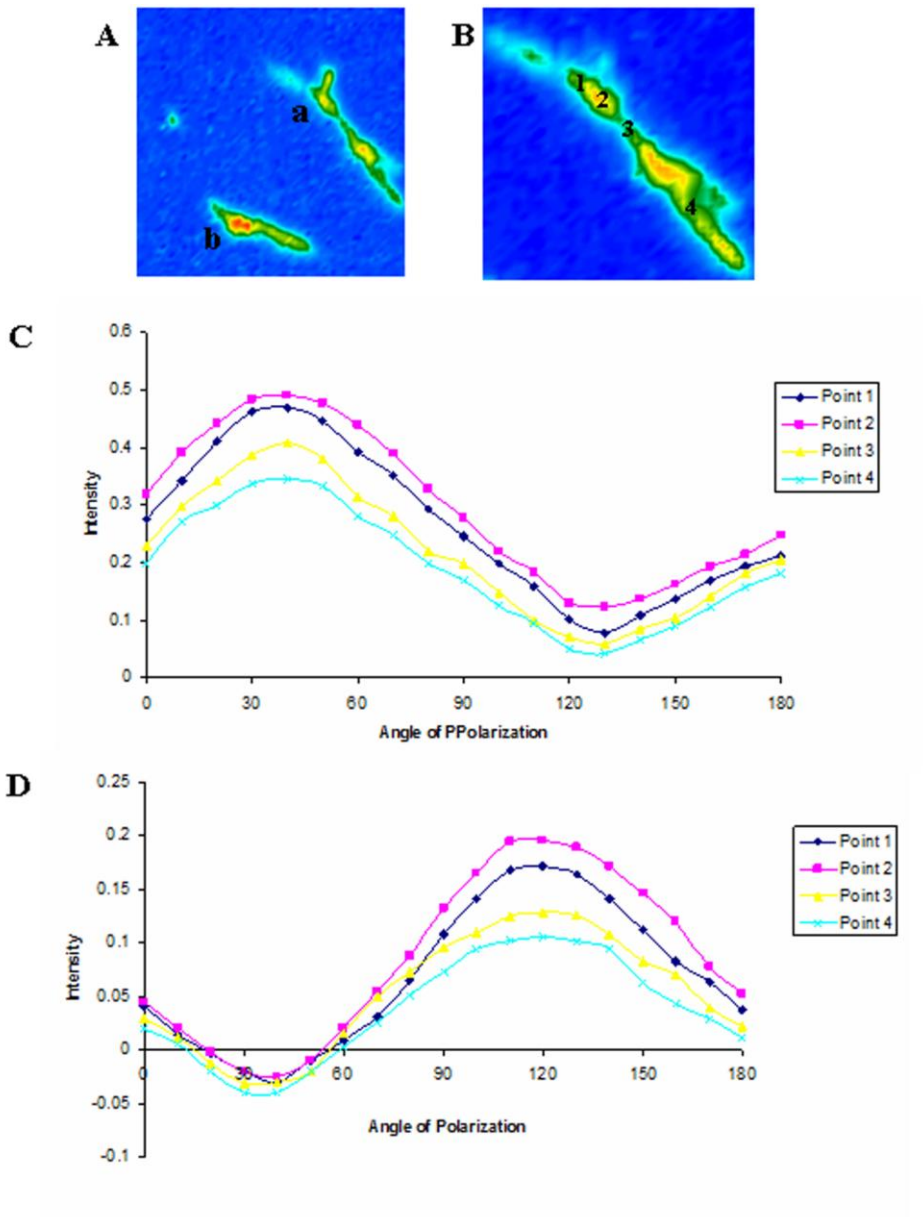

Figure 4.74: The absorption intensity versus polarization angle in the mapped caudate region. (A) Processed map of 14 month-old TgCRND8 mouse. (B) Close-up to indicate four points in Cr streak (a). The absorption intensity versus polarization angle to compare the processed map at (C) 1305 cm^{-1} and (D) 1405 cm^{-1}. The intensity at 1305 cm^{-1} has its maximum around 40° and gets to minimum around 130°, while the intensity at 1405 cm^{-1} has its minimum around 40° and gets to maximum around 130°.

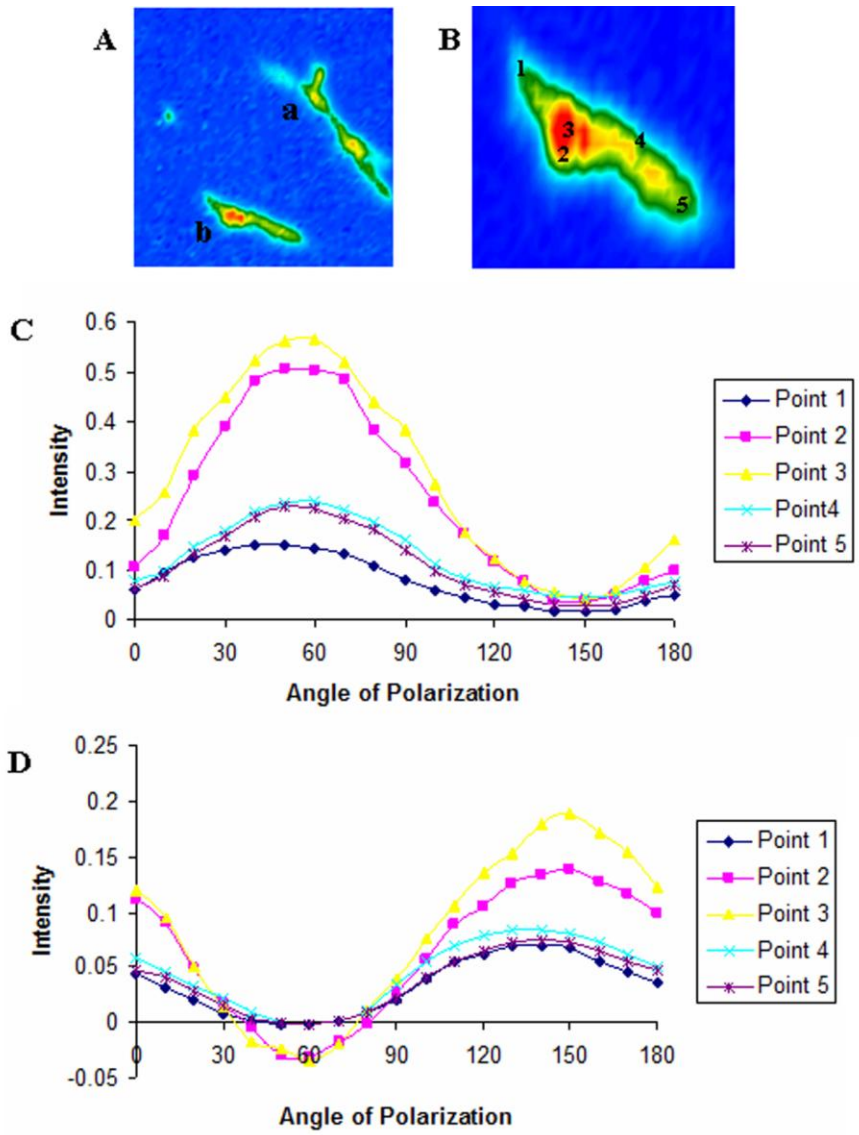

Figure 4.75: The absorption intensity versus polarization angle in the mapped caudate region. (A) Processed map of 14 month-old TgCRND8 mouse. (B) Close-up to indicate four points in Cr streak (B). The absorption intensity versus polarization angle to compare the processed map at (C) 1305 cm^{-1} and (D) 1405 cm^{-1}. The intensity at 1305 cm^{-1} has its maximum around 60° and gets to minimum around 150°, while the intensity at 1405 cm^{-1} has its minimum around 60° and gets to maximum around 150°.

To obtain more experimental evidence, the polarization angle dependence of FPA-FTIR maps was studied on CA4 area of hippocampus of 14 month-old transgenic mouse mounted on gold silicon slides. The data collection parameters were the same as those ones used for mapping the caudate.

The processed map at 1305 cm^{-1} shows that the Cr signal of Cr streaks (a) indicated in the mapped area started being strong at around 20° and gradually by increasing the polarizer angle started being weak again and around 120° it became disappeared and at higher polarization of incident radiation, it started to appear again (Figure 4.76C). However, the Cr signal at 1405 cm^{-1} was converse (Figure 4.77).

For Cr deposits (b,c), the analyzed maps at 1305 cm^{-1} display that Cr signal was minimum at around 30° and increased to get the maximum at around 120° (Figure 4.76C). In contrast, for processed maps at 1405 cm^{-1}, these two Cr deposits (b,c) show maximum and minimum Cr signal at 30° and 120°, respectively(Figure 4.77C).

As displayed in Figure 4.76C, the processed map at 1305 cm^{-1} shows that the Cr signal for Cr streak (d) was weak at 0° and started being strong at around 60° and gradually by increasing the polarizer angle started being weak again till for polarizer set at 170° disappeared, then at higher polarization of incident radiation, it started to appear again (Figure 4.76C). In contrast, the processed map at 1405 cm^{-1} showed the inverse results (Figure 4.77C).

Figure 4.76C, the processed map at 1305 cm^{-1} shows the Cr signal for Cr streak (e) increased from 0° to around 60° and extinguished at around 150° and then appeared again

by utilizing higher polarizer angle. Like the other Cr deposits, the Cr signal was converse when the maps were processed at 1405 cm^{-1} (Figure 4.77C).

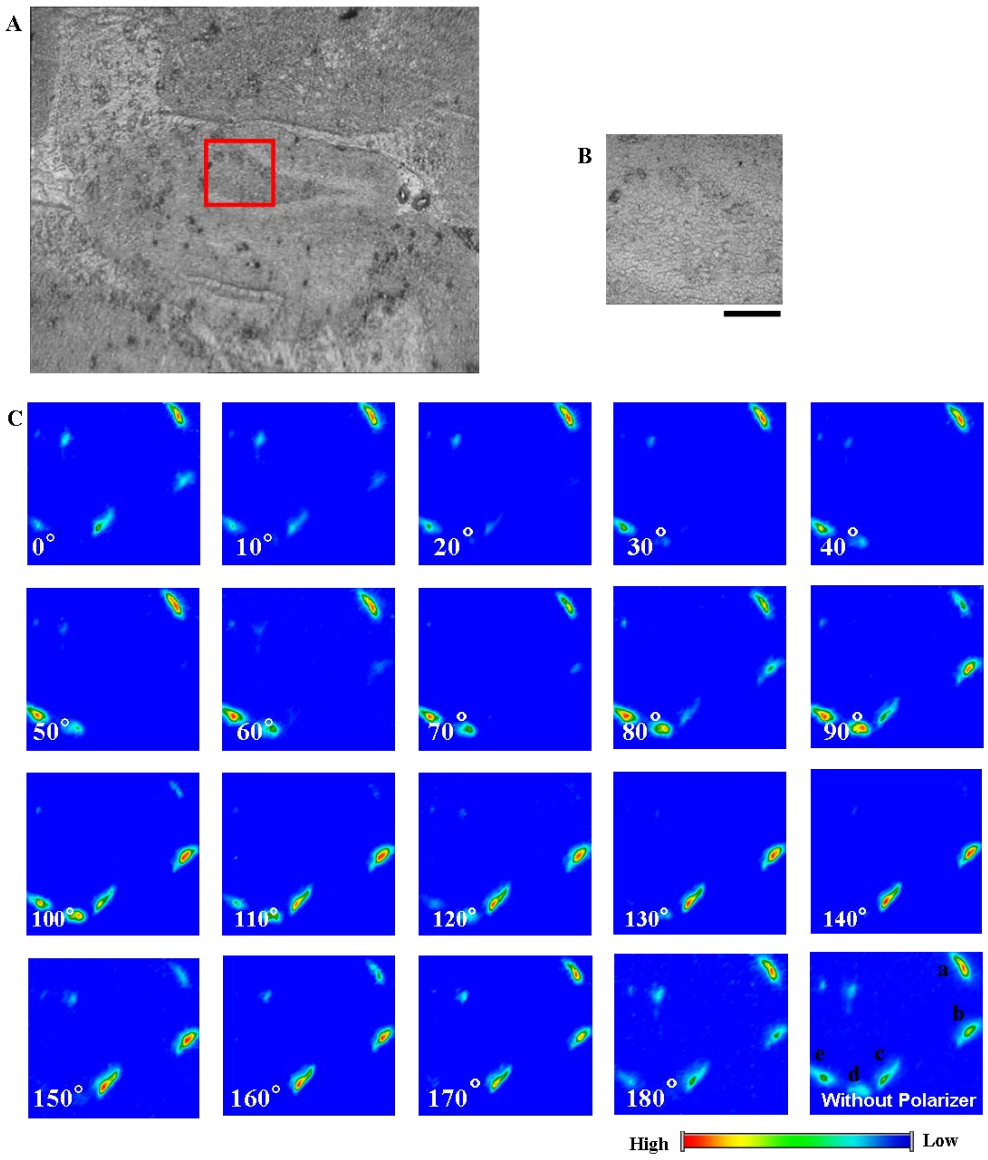

Figure 4.76: Maps processed at 1305 cm^{-1} in the hippocampus regions of 14 months-old transgenic mouse using polarizer angles of 0° to 180°, at 10° intervals. (A) The region of the hippocampus surveyed. (B) Close-up of the mapped area. (C) Maps recorded with a Varian FTIR microscope and a 64 x 64 Focal Plane Array detector, using polarizer angles of 0° to 180°, at 10° intervals and processed at 1305 cm^{-1}. Scale bar =100 μm. Single tile maps; spectra generated = 4096. Acquisition time = 7 min (for a single tile map). Colour scale: red corresponds to high intensity, dark blue to no signal.

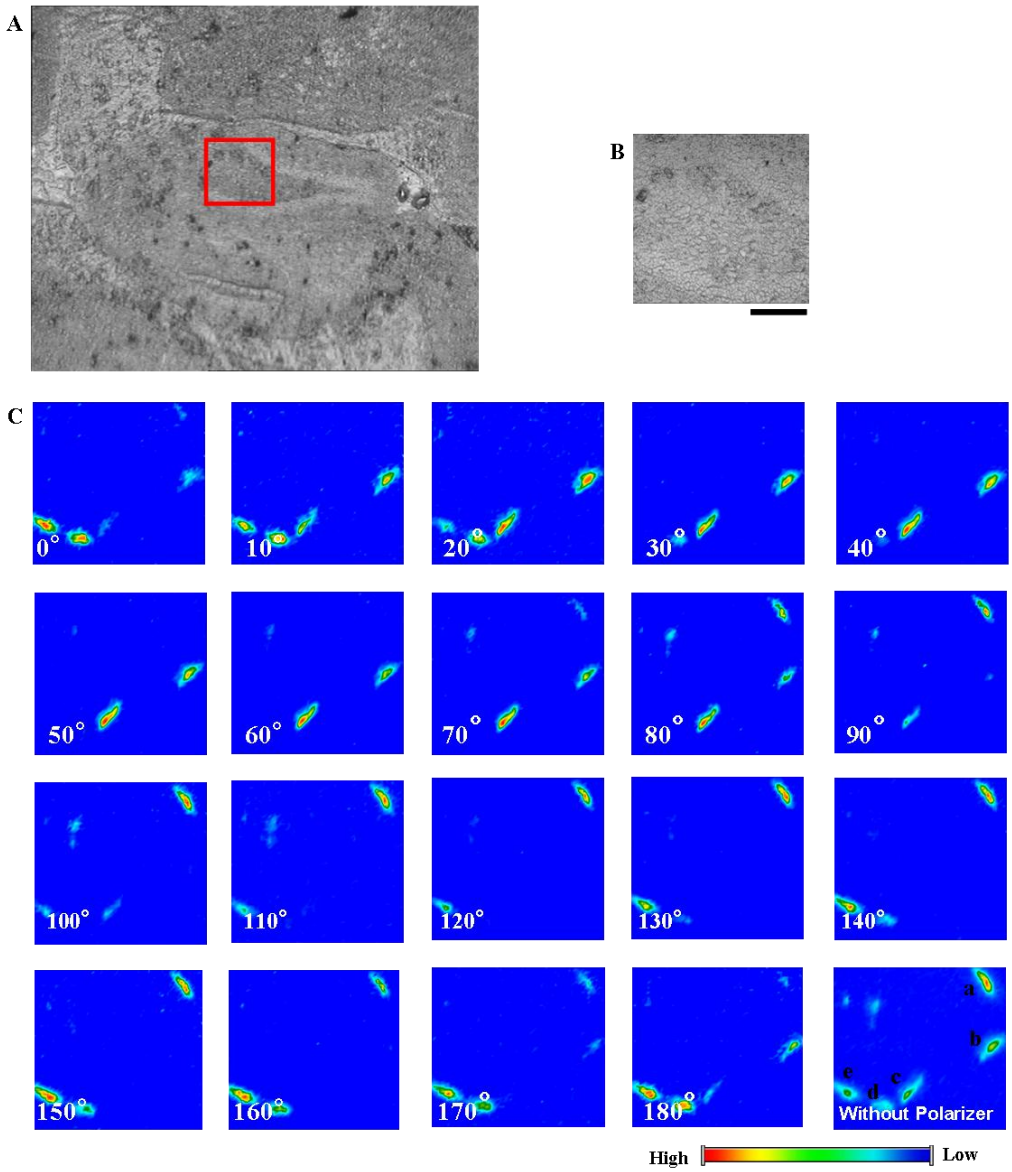

Figure 4.77: Maps processed at 1405 cm^{-1} in the hippocampus regions of 14 months-old transgenic mouse using polarizer angles of 0° to 180°, at 10° intervals. (A) The region of the hippocampus surveyed. (B) Close-up of the mapped area. (C) Maps recorded with a Varian FTIR microscope and a 64 x 64 Focal Plane Array detector, using polarizer angles of 0° to 180°, at 10° intervals and processed at 1405 cm^{-1}. Scale bar =100 µm. Multiple mosaic map area = 5 x5. Spectra generated = 4096. Acquisition time = 7 min (for a single tile map). Colour scale: red corresponds to high intensity, dark blue to no signal.

Like maps taken on caudate region, the spectra of different points located on various Cr streak (a, b, c, d, e) were examined through the range of polarizer angles 0° to 180° at a step of 10° (Figure 4.78-82).

Figure 4.78 shows the absorption intensity versus the polarization angle processed at 1305 and 1405 cm^{-1} for three different points marked on mapped Cr deposit (a). It can be seen that the intensity at 1305 cm^{-1} has its maximum around 20° and gets to its minimum around 120° (Figure 4.78C), while the intensity at 1405 cm^{-1} has its minimum around 20° and gets to its maximum around 120° (Figure 4.78D).

As shown in Figure 4.79, 4.80 three points in each Cr streak (b,c) were chosen and the absorption intensity versus the polarization angle were probed for processed maps at 1305 and 1405 cm^{-1}. It can be seen that the intensity at 1305 cm^{-1} has its minimum at around 30° and gets to its maximum around 120° (Figure 4.79, 4.80C). In contrast, the intensity at 1405 cm^{-1} has its maximum around 30° and gets to its maximum around 120° (Figure 4.79, 4.80D).

Figure 4.81C shows the intensity for Cr deposit (d) which was processed at 1305 cm^{-1} was got maximum at around 80° and minimum at around 170°. The intensity obtained from three points in Cr streak (d) processed at 1405 got the highest amount at 170° and lowest amount at 80° (Figure 4.81D).

Figure 4.82C shows the intensity versus angle of polarization for three points marked on Cr deposit (e). The processed map at 1305 cm^{-1} shows the highest intensity at around 60° and lowest intensity at around 150° (Figure 4.82D). By processing at 1405 cm^{-1}, the maximum and minimum intensity was at 60° and 150°, respectively (Figure 4.82D).

Like the maps taken on caudate region, the same maximum and minimum intensity was obtained for examined points on each Cr streak. It shows that the along a Cr streak, the orientation dependency are similar and hence these points belong to a single crystal instead of composing several microcrystalline Cr crystal deposits.

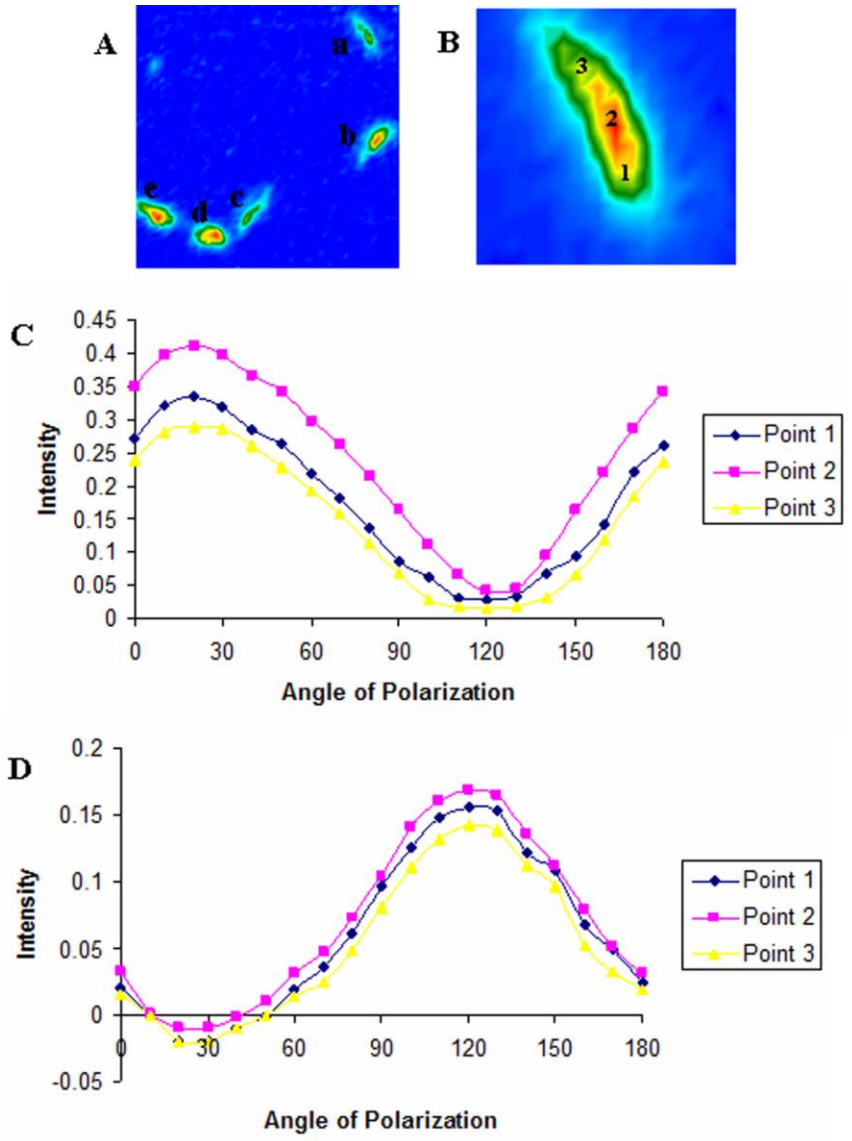

Figure 4.78: The absorption intensity versus polarization angle in the mapped hippocampus region. (A) Processed map of 14 month-old TgCRND8 mouse. (B) Close-up to indicate three points in Cr streak a (B). The absorption intensity versus polarization angle to compare the processed map at (C) 1305 cm^{-1} and (D) 1405 cm^{-1}. The intensity at 1305 cm^{-1} has its maximum around 20° and gets to minimum around 120°, while the intensity at 1405 cm^{-1} has its minimum around 20° and gets to maximum around 120°.

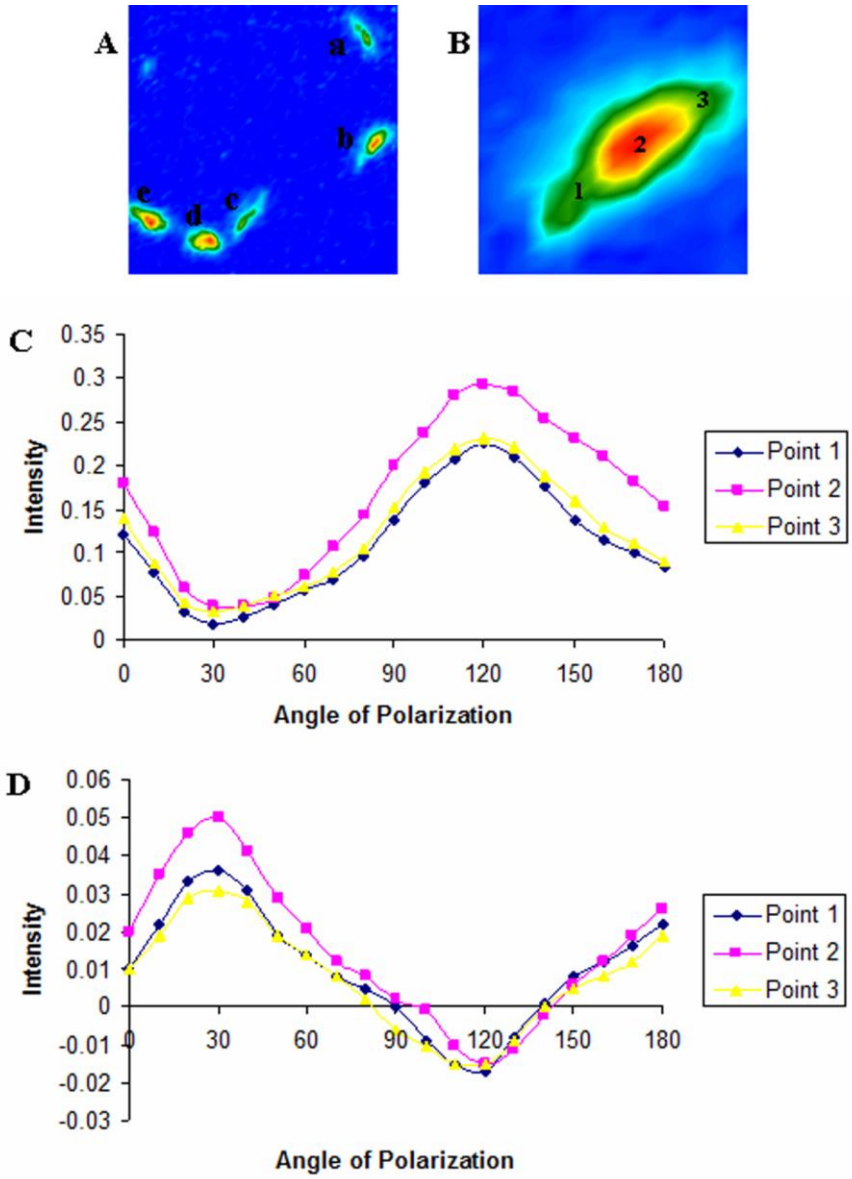

Figure 4.79: The absorption intensity versus polarization angle in the mapped hippocampus region. (A) Processed map of 14 month-old TgCRND8 mouse. (B) Close-up to indicate four points in Cr streak b (B). The absorption intensity versus polarization angle to compare the processed map at (C) 1305 cm^{-1} and (D) 1405 cm^{-1}. The intensity at 1305 cm^{-1} has its maximum around 120° and gets to minimum around 30°, while the intensity at 1405 cm^{-1} has its minimum around 120° and gets to maximum around 30°.

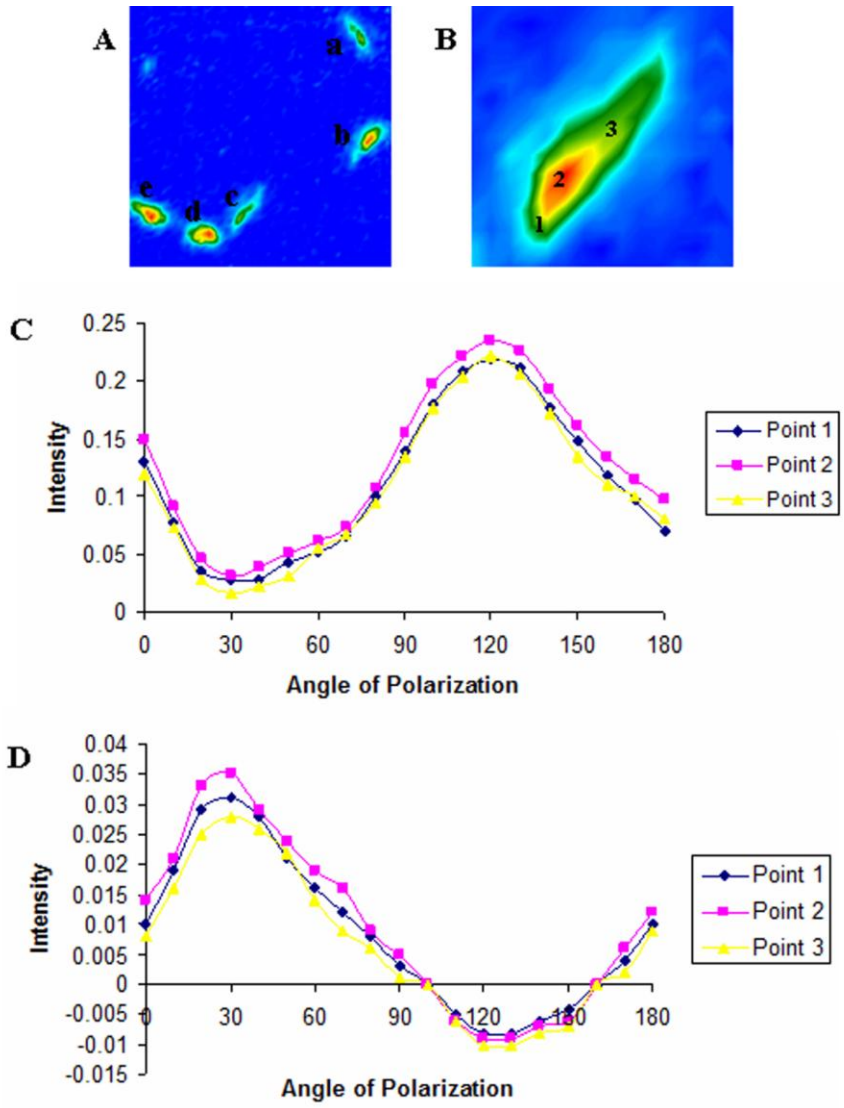

Figure 4.80: The absorption intensity versus polarization angle in the mapped hippocampus region. (A) Processed map of 14 month-old TgCRND8 mouse. (B) Close-up to indicate four points in Cr streak c (B). The absorption intensity versus polarization angle to compare the processed map at (C) 1305 cm^{-1} and (D) 1405 cm^{-1}. The intensity at 1305 cm^{-1} has its maximum around 30° and gets to minimum around 120°, while the intensity at 1405 cm^{-1} has its minimum around 120° and gets to maximum around 30°.

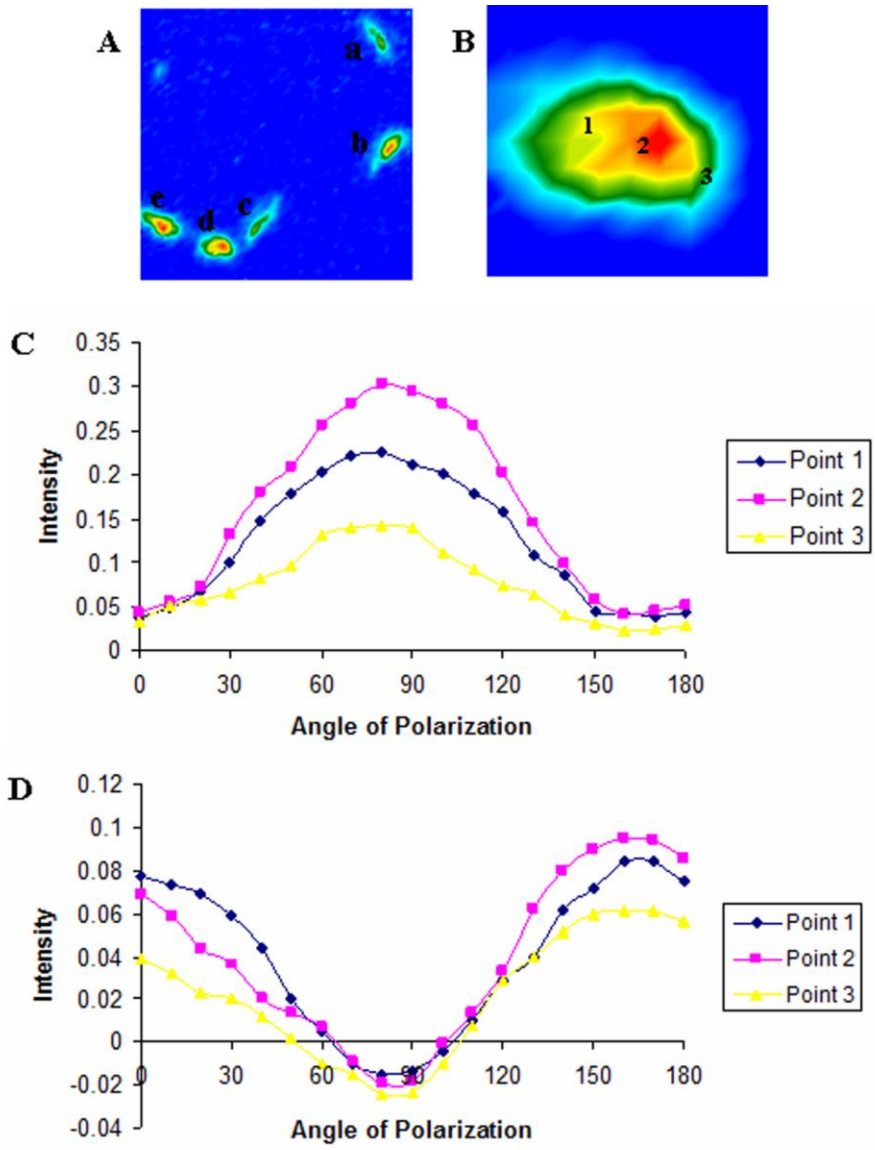

Figure 4.81: The absorption intensity versus polarization angle in the mapped hippocampus region. (A) Processed map of 14 month-old TgCRND8 mouse. (B) Close-up to indicate four points in Cr streak d (B). The absorption intensity versus polarization angle to compare the processed map at (C) 1305 cm^{-1} and (D) 1405 cm^{-1}. The intensity at 1305 cm^{-1} has its maximum around 80° and gets to minimum around 170°, while the intensity at 1405 cm^{-1} has its minimum around 80° and gets to maximum around 170°.

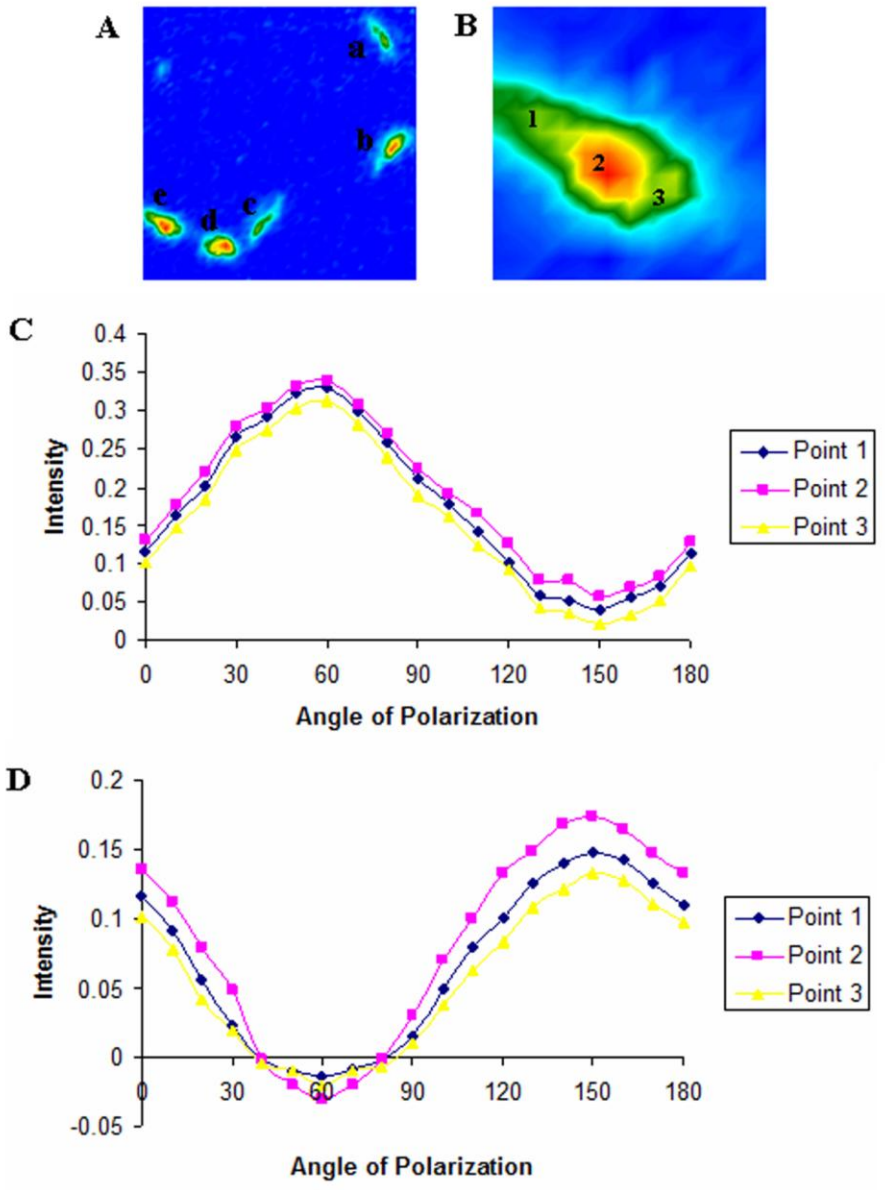

Figure 4.82: The absorption intensity versus polarization angle in the mapped hippocampus region. (A) Processed map of 14 month-old TgCRND8 mouse. (B) Close-up to indicate four points in Cr streak e (B). The absorption intensity versus polarization angle to compare the processed map at (C) 1305 cm^{-1} and (D) 1405 cm^{-1}. The intensity at 1305 cm^{-1} has its maximum around 60° and gets to minimum around 150°, while the intensity at 1405 cm^{-1} has its minimum around 60° and gets to maximum around 150°.

Chapter 5.

Discussion

5.1 Questions to be addressed about FTIR and Raman microspectroscopy of Tg mice

In this project, two imaging techniques, FTIR and Raman microscopy, were used to examine Cr deposits and surrounding tissue. The ability to detect Cr deposits and other biochemical signatures in tissue sections at micron level spatial resolution is specific to vibrational microspectroscopy of sections as prepared by snap freezing of unfixed tissues, method employed in this thesis. The reason that all IR and Raman spectra corresponded to Cr not PCr is that all PCr would be depleted at death, leaving Cr as the only existing form.

These spectroscopic techniques have some advantages compared to other standard visualization techniques. For instance, staining methods, commonly used to study tissue sections, involve various solvent treatments; therefore, small soluble molecules like Cr would not be detected because of being washed away. Sample preparation for both IR and Raman methods involves snap freezing of tissue excised at time of animal sacrifice,

cryosectioning and then desiccation of the sections; therefore, water is the only component removed, and no new components are added. In these techniques, a chemical map can be created by representing the distribution and intensity of peaks of interest on a color scale. These techniques are also non-destructive (note that illumination with infrared or visible light at very low power does not damage tissue), thus the sections remain suitable for further analysis such as X-ray fluorescence imaging (XRF) or staining.

FTIR and Raman imaging techniques are compatible; that means the same section can be mapped by FTIR and then by Raman, repeatedly. The Raman spectra can be obtained at higher spatial resolution (1-2 μm for Raman compared to 5-10 μm for FTIR) by an order of magnitude; therefore, FPA-FTIR microspectroscopy could be used for large area surveys to find elevated Cr deposits in hippocampus and caudate regions in order to do faster data collection and then the smaller areas identified to contain Cr deposits could be mapped by Raman microscopy to understand any association between creatine deposits and any other biochemical signatures, with 1-2 μm spot size.

It has been noted that substantial impairment of energy metabolism in the brains of patients with AD was found in numerous imaging studies, such as Magnetic Resonance Spectroscopy (MRS) (Mandal, 2008; Mandal, 2007; Morene-Torres et al, 2005). These studies reported higher variation of the total Cr (PCr and Cr) concentration in the gray matter than white matter of elderly individuals' brain. In the living brain, creatine may be crystalline or soluble and deposits may also be extra- or intracellular. These conditions can not be determined by MRS. One advantage of the MRS technique is that measurements can be made on living subjects. However, the spatial resolution is quite

low (1-8 cm^3 for ^{1}H-MRS, and 15-40 cm^3 for ^{31}P-MRS); therefore, this technique does not offer the spatial resolution provided by IR and Raman microspectroscopy. Several MRS studies have used total creatine levels as the internal standard when levels of other metabolites such as glutamate-glutamine complex, and choline are investigated (Godbolt et al, 2006). So far, the creatine distribution was assumed to be homogeneous, that is evenly distributed throughout the brain tissue.

Previous members of the Dr. Gough's group showed the in situ detection of crystalline Cr deposits in Tg mouse brain and in post mortem AD brain tissue, by IR micospectroscopy (Kuzyk et al, 2010; Rak, 2007; Gallant, 2007; Gallant et al, 2006).

The principal goal in this thesis was to find clues to the origin of creatine in transgenic mouse brain. As the creatine deposits were found in frozen and desiccated brain tissue, it was important to investigate whether these creatine crystals were formed after snap freezing and desiccation of brain tissue or there is any other possibility like synthesizing in situ or carrying out cross blood brain barrier (BBB).

Since Cr can be endogenously synthesized in kidney and liver, and carried out through the blood brain barrier by Cr transporters to get into the brain, blood vessels in the hippocampus of transgenic mice were analyzed by IR and Raman to discover whether any co-localization could be found between these Cr deposits and the blood vessels.

Depth profiling data, by analysis of serial sections, was undertaken in an effort to determine whether any association could be detected between Cr deposits and either palque or lipid. These maps were analyzed for other spectral markers such sphengomyelin, phospholipid, nucleic acids, and phenylalanine to investigate whethere these biochemical signatures were localized with the Cr deposits. Since Raman spectra can be ob-

tained at higher spatial resolution (1-2 μm for Raman compared to 5-10 μm for FTIR), all the depth profile analysis were performed by this spectroscopic technique.

To investigate whether Cr deposits distribute ubiquitously in brain tissue, it is necessary to collect IR maps from different brain tissue areas. It was shown that (Kuzyk et al, 2010) creatine was found more abundantly in hippocampus of mouse brain compared to their non-transgenic littermates and increased in size and number with age. In this thesis, the caudate of Tg and non-Tg mice at different ages were IR mapped, in order to evaluate whether focally elevated creatine levels detected in the hippocampus of transgenic mice are found in other parts of the brain.

To better evaluate Cr crystal structure and orientation, we undertook a combined theoritical and experimental study into the effect of polarized light on the spectra of crystalline Cr in both pure Cr and brain tissue deposits. Vibrational modes and intensities for both Raman and IR creatine spectra were calculated by density functional theory (DFT). Pure Cr crystals, prepared on gold silicon chip slide, were analyzed by FPA-FTIR microscope adjusted with polarizer, and by Raman microscope with polarizer and a polarizer+ half wave plate. In order to estimate Cr crystal form, orientation and dimension, several Cr deposits in hippocampus and caudate of TgCRND8 mouse brain tissue sections were imaged by FTIR with polarizer, setting from a wide range of angles (0° to 180°).

5.2 Calculation peaks assignment and polarization

The theoritical calculation, density functional theory (DFT), gives both frequency and polarization information to make a more detailed interpretation of the Cr spectra.

For IR spectra, six modes were calculated to lie in the region of experimental interest at 1247, 1275, 1321, 1332, 1455, and 1478 cm^{-1}. The observed 1305 and 1405 cm^{-1} peaks might be assigned to CH_2 deformation + NH_2 rocking and CH_3 deformation that appear in theoritical calculation at 1275 and 1455 cm^{-1}, respectively (Table 4.3). These two bands are the most affected bands when polarizer was put into the optical path. The experimental peak at 1392 cm^{-1} and 1423 cm^{-1} and 1448 cm^{-1} are corresponded to symmetric vibration of C4O8O9 + CH_2 wagging; CH_2 deformation + CN stretching, NH_2 rocking; CH_2 scissoring which can be seen at 1321, 1331 cm^{-1}, and 1478 cm^{-1} in the theoretical calculations, respectively. From the optimized, it was found that the guanidine and carboxylic portions of creatine monohydrate molecule are nearly perpendecular to each other. This intrinsic feature of creatine structure may cause the effect of polarized light on the spectra of crystalline creatine. As explained in section 5.7, this polarization dependence of creatine vibrational modes helped us better estimate the creatine form, orientation and dimension.

From the theoritical calculation, it was found that the very strong Raman band at 830 cm^{-1} is assigned to the symmetric stretching mode of the three CN^{+} bonds. This mode was very distinctive in the Raman spectra of brain tissues; therefore, it was selected for identification of Cr distribution, and pure Cr crystal. The relative intensities of bands at 912, 982, and 1054 cm^{-1} were stronger with polarizer & half-wave plate compared to using polarizer. These Cr bands (912, 982, 1054 cm^{-1}) are assigned to symmetric vibration of C3C4OO^{-}, CH_2 deformation, and symmetric vibration of CN_3 + CH_3 rocking, respectively. These Raman peaks were present at 812, 853, 964, 1040 cm^{-1} in theoretical calculation, respectively.

The vibrational energies calculated with DFT are generally overestimated compared to experimental values. In the theoretical calculation, one isolated Cr monohydrate molecule was regarded as being in gas phase, while the experimental analysis was in solid phase. Another effective parameter is the formation of molecular hydrogen bonding. The supermolecular lattice of the Cr monohydrate crystal allows for a network of six hydrogen bonds between each creatine molecule and its neighbours. However, in the theoretical process, just a single unit Cr monohydrate was calculated. To reduce the vibrational energies calculated by theoretical process, it has been suggested to apply a scale factor, one for the fingerprint region (0.9846 for wavenumbers below 1800 cm^{-1}) and the other one (0.9544 for wavenumbers above 1800 cm^{-1}). However, in this work, no scale factor was used, because it was proposed that the vibrational modes will probably be similar, although the intensities might be altered by the environment.

5.3 Raman parameters that were optimized

Before taking Raman maps, some parameters must be optimized for successfully mapping brain tissue, such as; laser wavelength, spatial resolution, exposure time and laser power. These parameters were determined to permit Raman mapping of Cr deposits and environs with higher S/N ratio in tissue sections from mice. With Raman, the fluorescence is generated very easily. It happens on the same time scale as Raman. The Raman scattering happens with very low probability (one in a million), while the fluorescence happens with very high probability (99.99% compared to Raman scattering). Fluorescence is really strong particularly when the biological samples like brain tissue are examined. Generally, conjugated systems, connecting p-orbital in compounds with alternat-

ing single and multiple bonds, are high fluoresce. Since brain tissue composed of different organic compounds like nucleic acids, amino acids, lipids and proteins, which have p-orbital as a source to maintain conjugation, can be more sensetive to fluorescence. It is important to choose a proper laser wavelength to get less fluorescence to be able to see Raman peaks in brain tissue. In this thesis, both laser 633 nm and 785 nm were tested. The laser at 785 nm is selected because the laser with longer wavelength, lower energy can not excite the molecule to higher excited electronic state; therefore, the probability of causing fluorescence is less compared with He-Ne laser (633 nm) and Ar ion laser (514 nm). (See section 4.1 for more information about optimization to take Raman data).

In this thesis, all Raman images were taken by streamline map which permits fast data collection compared to point by point map particularly when a large area is required to be mapped. All Raman maps were recorded with 300 second exposure time. For single spectra a sum of 10 accumulations with exposure time of 30 seconds was chosen to improve S/N ratio. The 785 nm laser at 10% power was used for excitation to prevent burning the sample and the appearance of charcoal bands at 1589 cm^{-1} and 1324 cm^{-1}.

The 50x objective, having the best quality, was used for mapping of all the mouse brain samples; therefore, the all spectra were measured with spectral resolution 1cm^{-1}/pixel and spatial resolution of 2 μm. Since the spot size for the diode laser was actually a line; therefore, the spot size as determined by the microscope was slightly blurred in the y direction.

5.4 IR data thermal source FPA and synchrotron source single pixel data

One of the most important advantages of FPA-FTIR microscopy is to collect mosaic maps in order to image a large area in brain tissue in very short time compared to single pixel raster scan data collection by using synchrotron FTIR.

With sFTIR microscope that was used in the previous research work in Dr. Gough's group, many maps had to be acquired separately and then manually pasted together to cover a full hippocampus. The time needed to acquire sufficient maps was at least 4 days to collect IR maps with synchrotron source with 10 x10 μm pixel size, for a single hippocampus section.

The Varian FPA-FTIR microscope combines a motorized stage to rapidly collect high spatial resolution data (5-10 μm) from larger sample areas. The mosaic capability involves moving the sample under the field of view of the FPA, collecting a series of tiles. The tiles are stitched together to form a single larger overall image consisting of many individual single tiles. The FPA detector contains an array of 64 x 64 elements; 4096 spectra are collected simultaneously from an area of analysis of 350 x 350 μm with spatial resolution of about 5.5 x 5.5 μm, to collect a single tile map.

Although this technique is very useful for acquisition of the mosaic image in a short time, it is not suitable to detect amyloid plaques. Unlike spectra taken by sFTIR microscope, it is not easy to observe the β-sheet shoulder, related to β-sheet Amide I (at 1630-1620cm^{-1}) and to α-helix Amide I (at 1662-1665cm^{-1}). At first time, it was assumed

that this problem probably happened because the brightness of globar light source is quite low. As noted in chapter 2, synchrotron radiation is 1000 times brighter than a globar light source. It is important to note that its brightness is because the effective source size is very small and the light is emitted into a narrow range of angles (Salzer, 2009; Miller, 2005).

In this thesis, all of the sFTIR data were acquired at SRC previously, and I just re-processed the data for creatine deposits. The only FTIR images taken for this thesis were thermal source FPA-FTIR images from the Varian at University of Manitoba. The sFTIR spectra of dense core Aβ plaque could be marked by a distinct amide I doublet but even by taking the FPA-FTIR map of plaques with highest intensity of globar light, it was not easy to see any β-sheet shoulder. This has now been attributed in part to the software image belnding on the Varian Resolution-Pro software (K. M. Gough & J. B. Morison, University of Manitoba). This might cause to see a braod band instead of seeing double band correspond to α-helix and β-sheet.

5.5 IR and Raman spectra of blood vessel

Processed IR maps reveal that almost all of the larger deposits, found in older transgenic mice, took the form of streaks and these larger deposits were not usually associated with plaques. Since Cr can be endogenously synthesized in liver and kidney and carried out through the blood brain barrier by Cr transporters to get into the brain, this could point to an association with blood vessels. To detect whether any Cr was coming through the blood vessel in hippocampus, two blood vessels in hippocampi of four transgenic mice were mapped in different ages (5, 8, 14, 17 months-old) by FPA-FTIR micro-

scope (Figure 4.27). The processed IR maps show that a Cr streak appeared nearby the blood vessel in the hippocampus of the 5 month-old transgenic mouse (Figure 4.27, Row B1). The Cr crystal deposits were smaller in 8 and 14 month-old Tg mice (Figure 4247, Row B2-3). No Cr was found in the blood vessel in hippocampus region of 17 month-old TgCRND8 mice (Figure 4.27, Row B4). The symmetric CH_2 and lipid carbonyl distribution was obsereved nearby the blood vessels (Figure 4.27, Row C1&D1). The processed depth profile Raman maps in serial sections of 14 month-old TgCRND8 mouse illustrate that just a few Cr deposits came through blood vessel in hippocampus of A14 (19) (Figure 4.36). No significant Cr deposits were found in any other sections. In all depth profile maps, sphingomyelin (CN^+ stretching mode at 730 cm^{-1}) and phenylalanine (distinct band at 1003 cm^{-1}) were detected. The depth profile data were analyzed and some other biochemical signatures were observed (Figure 4.28-36). In section A14(10) and A14(19), lipid (C-C stretching mode at 1060 cm^{-1} and =CH bending mode at 980 cm^{-1}) were identified (Figure 4.28, 36). In sections A14(10), A14(11), A14(12), A14(14) and A14(19), phospholipid (stretching vibration of PO_4^{3-} of phospholipid at 840-900 cm^{-1} and 960 cm^{-1}) was observed (Figure 4.28, 29, 30, 32, 36). Depth profile Raman maps shows no association has been obtained between Cr deposits and blood vessels so far. Therefore, detected Cr deposits were formed within brain tissue and not transported across the blood brain barrier.

5.6 Investigation of creatine distribution in brain tissue

As mentioned, the principal goal of this thesis is to explore the Cr origin in transgenic mice.

In this thesis, Depth profiling data, by analysis of serial sections, was undertaken in hippocampus in an effort to determine whether lipid membrane and amyloid plaques can be identified to be localized with Cr deposits. These images were also analyzed to see whethere any other biochemical signatures such as sphengomyelin, phospholipid, nucleic acids, sugar, and phenylalanine can be detected with the Cr deposits.

In order to evaluate whether focally elevated creatine levels detected in the hippocampus of transgenic mice are found in other parts of the brain, the caudate of Tg and non-Tg mice at different ages were IR mapped. Some Cr deposits detected in cauadte were recorded by Raman microscopy with higher spatial resolution to find whether any other biochemical signatures were observed to be co-localized with these deposits.

5.6.1 Depth profile plaque in hippocampus

In order to determine whether any other biochemical signatures could be identified as being specifically localized with the creatine deposits, the hippocampus and caudate regions in brain tissue transgenic mice were mapped by FTIR and Raman microscopy.

Since Aβ aggregation is one of the most important pathological hallmarks of Alzheimer disease, an Aβ plaque located in CA4 region of hippocampus was selected to map through serial sections. The plaque located in hippocampus region was selected because Cr deposit was detected in IR maps of this area (Kuzyk, 2010). The IR data collection was already done by Alex Kuzyk (member of Dr. Gough's research group) on the same plaque and published (Kuzyk et al, 2010). As the IR and Raman imaging techniques are compatible, the same plaque was mapped with the Raman microscope at higher spatial

resolution to search for co-localization between creatine deposits and any other bio-chemical signatures.

The processed Raman maps of amyloid plaque (antiparalell β-sheet protein at 1670 cm^{-1}) in serial sections of 14 month-old transgenic mouse revealed that Cr deposits were detected in A14(14), A14(17) and A14(19). Although Cr deposits were present in the vicinity of some amyloid plaques, so far no association was found between them.

Lipid was detected in all consecutive serial sections. From the processed Raman maps for lipid (CH_2 deformation band at 1440 cm^{-1}), it was found out that β-sheet aggregation was identified in areas where lipid appeared, and no β-sheet was found without lipid bands (Figure 4.39, 45, 47, 51). A lipid connection to AD has been proposed by other groups (Florent-Bechard et al, 2009; Bevhard et al, 2009; Debomay et al, 2008; Hartmann et al, 2007). The aggregation of Aβ is due in part, to hydrophobic nature of the peptides; therefore, lipids may have a physical role in the aggregation reaction because of their affinity to hydrophobic surfaces (Verdier et al, 2004). In addition, a study has demonstrated that lipid can revert aggregated Aβ fibrils into neurotoxic protofibrils, and that injection of such reverted protofibrils into mice causes the same memory impairment as protofibrils formed from monomeric Aβ (Martins et al, 2008). Those authors concluded that the step from protofibril to fibril formation can be reversible. The role of lipid distribution to AD is beyond the scope of this project.

All of the Raman maps were processed for sphingomyelin (CN^+ stretching mode at 730 cm^{-1}). Sphingomyelin is a type of sphingolipid that is found in animal cell membranes especially in the myelin sheath surrounding nerve cell axons. Since oligodendro-

cytes are rich in sphingomyelin and synthesize creatine in large amounts in brain, the Raman data could indicate a possible connection between some of the Cr deposits and sphingomyelin. Apart from section A14(11) and A14(16), CN^+ mode at 730 cm^{-1} was detected in all other serial sections. Although this band was present in the vicinity of some of the Cr deposits in sections A14(14), A14(17) and A14(19), no specific association between Cr deposits and C-N^+ bond of choline at sphengomyelin was observed particulary in maps collected in caudate region. It could be concluded that probably no co-localization is between large Cr streaks and axons.

The collected maps were analyzed to see any other biochemical signatures in brain tissue. The processed A14(10) map shows spectral markers of proteins (CN deformation of amine group at 840 cm^{-1}) and phosphodiesters (doublet bands in 890-900 cm^{-1}) (Figure 4.41). In section A14(11), the distinct phenylalanine (at 1003 cm^{-1}), lipid (broad band at 960-970 cm^{-1}; CH_2 bending of proteins and lipids), and protein (weak band at 880 cm^{-1}) were present (Figure 4.42). The majority of the thick dark area in section A14(12) was detected with phospholipids (phosphate bands at 1040-1050 cm^{-1}; =CH bending mode of unsaturated lipid at 970-990 cm^{-1}), protein (C-N stretch mode of protein; protein carbonyl band at 1620 cm^{-1}), and amino acids (bands at 740, 870, 920 cm^{-1}, C-N stretching vibration of amino acids at 1630 cm^{-1} and C=C deformation of phenylalanine band at 1590 cm^{-1}) , and nucleic acids (broad band at 1570 cm^{-1}) (Figure 4.43). The thick dark area in A14(13) was found to be characteristic of phenylalanine (at 1003 and 1610 cm^{-1}) and lipid membrane (=CH bending at 980 cm^{-1}). The other distinct peaks in this section were α-helix (symmetric CH_3 band at 930 cm^{-1}), phospholipids (weak band at 960 cm^{-1} assigned to phosphate group in phospholipids), amino acids (broad band at 770-780 cm^{-1};

strong band at 845 cm^{-1} assigned to amino acids (Figure 4.44). The spectra of dark accumulation in section A14(14) consist of α-helix (symmetric CH_3 band at 930-940 cm^{-1}), phospholipids (phosphate group at 860 cm^{-1}) and phenylalanine (at 900, 930, 1003, 1560, 1610 cm^{-1}). The other biochemical markers in this section include protein (CH_2 bending mode of protein at 880 cm^{-1}; CN stretching and in-plane bending of the N-H group at 1470-1480 cm^{-1}), phosphodiesters (strong band at 810 cm^{-1}), and DNA (strong band at 790 cm^{-1} assigned to phosphate band) (Figure 4.46). In the vicinity of amyloid plaque in section A14(15), some other bands were observed that correspond to phenylalanine (at 960, 980, 1030 cm^{-1}), and lipid (bands at 975 and 1060 cm^{-1}), amino acids (broad band at 845 and 920 cm^{-1}), RNA (strong band at 915-920 cm^{-1}) (Figure 4.48). The processed map of plaque area at A14(16) was composed of phenylalanine (band at 1003 cm^{-1}), α-helix (at 1550-1560 cm^{-1}) (Figure 4.49). In the vicinity of Aβ plaque in section A14(17), some sharp bands of of lipid (=CH bending at 985 cm^{-1}) and phenylalanine (bands at 695, 1003, 1585 cm^{-1}) were detected (Figure 4.51). In section A14(19), some sharp bands were found corresponding to amino acids mostly phenylalanine (at 920, 760, 850 and 1003 cm^{-1}), phospholipids (asymmetric O-P-O stretching mode at 760 and 835 cm^{-1}), protein (ν(C-C) at 855 cm^{-1} and α-helix protein at 940 cm^{-1}).

In conclusion, these processed depth profile maps from selected plaque in hippocampal tissue shows that Aβ plaque was enveloped by elevated lipid. Although, the Aβ plaque was found sometimes nearby deposits of Cr, no specific association was indicated between them. It could point to this fact that there is no possible interaction among detected Cr deposits, and either dense core plaque or lipid in the progression of AD. So far,

no specific association was obtained between Cr peaks and any other biochemical signatures in brain tissue.

5.6.2 Creatine distribution in caudate of transgenic mice

Of four Tg and non-Tg mice, ages through 5, 8, 14, and 17 month-old, analyzed for creatine distribution in caudate, the sections of both Tg and non-Tg mice from 14 month-old displayed creatine deposits, and it was illustrated that creatine was found more abundantly in size and number in caudate of transgenic mouse brain compared to its non-transgenic littermate (Figure 4.59, 4.60). The size of Cr deposits in the caudate of 14 month-old Tg mouse was recorded between 50-200 μm. It is important to note that caudate of these two tissue samples were not torn or folded at all. Apart from some small Cr deposits appeared in A25(4), 8 month-old Tg mouse (Figure 4.57), no Cr was detected in any other mice even in the oldest one, 17 month-old Tg mouse (Figure 4.61). Despite these sections being selected based on the quality of the samples, apart from A14(2) and A13(2), Tg and non-Tg 14 month-old mice sections show folding that would have occurred on sectioning. At the time of crysectioning, the most important part to examine was the hippocampus, not the caudate region. This suggests that any compression of the sample may prevent detection of Cr deposits; therefore, it is hard to draw any conclusion concerning the Cr distribution through different ages in caudate region with these samples.

The Raman maps were recorded with higher spatial resolution in an effort to determine whether any other biochemical signatures can be identified as being localized with the Cr deposits found in caudate region of 14 month-old TgCRND8 mouse. The proc-

essed map displays that Cr deposits were surrounded by phenylalanine without any remarkable elevation or depletion (Figure 4.63, 65, 66 C&D). All the maps were processed for sphengomyelin (symmetric stretching mode of the CN^+ at 730 cm^{-1}). No distinctive band was observed at 730 cm^{-1} in these processed maps. As noted, sphingomyelin is found in the myelin sheath surrounding axons. Since oligodendrocytes synthesizing Cr in brain are rich in sphingomyelin, it suggests to this fact that no co-localization is between detected Cr deposits and axons.

5.7 Exploration of creatine crystal structure with polarized Raman and IR Microspectroscopy

It was discovered by Veena Agrawal (a summer student in Dr. Gough's group) that creatine spectra taken by synchrotron FT-IR spectromicroscopy gave different spectra for various deposits because synchrotron radiation is polarized, and some vibrational modes are only excited if the molecule is oriented correctly relative to the polarized light. From the maps taken previously by M. Gallant (former Master student) and processed at 1304 cm^{-1} to examine Cr distribution in serial sections from the hippocampus of 14 month-old Tg, it was revealed that several horizontal deposits, not represented in maps processed at 1305 cm^{-1}, appeared after reprocessing maps at 1408-1384 cm^{-1} (Figure 4.68 I,J,K,L). It was perfectly matched with the spectra of pure Cr crystal prepared and mapped by sFTIR (Figure 4.70). Since the spectral markers were critical to identifying tissue components, a combined experimental and theoretical study was undertaken (See section 5.2 for more details about theoritical results).

In order to better evaluate creatine crystal orientation, we undertook a combined theoritical and experimental studies into the effect of polarized light on the spectra of crystalline Cr. Pure creatine monohydrate crystals were pepared and analyzed by FTIR microspectroscopy with FPA detector and IR polarzier adjusted through a wide range of angles, and by Raman microspectroscopy with a polarizer and polarizer + half wave plate. (Figure 4.70, 71).

When the polarizer and half-wave plate were used, the light was rotated by 90°. It is important to note that the vibrational modes are Raman active when the molecular polarizability changes, not the dipole moment. The spectra taken with polarizer and with polarizer + half-wave plate presented a very strong Raman band at 830 cm^{-1}. This band which corresponds to the symmetric stretching mode of the three CN^{+} bonds, does not change with polarizer orientation. Three other affected bands were the peak at 916 cm^{-1}, assigned to symmetric vibration of (C-COO^{-}) and NH_2 wagging, the peak at 982 cm^{-1} assigned to CH_2 rocking, and a peak at 1054 cm^{-1} assigned to asymmetric vibration of CN, and CH_3 twisting. These assignments were acquired from theoritical calculation (See Table 4.3). The depolarization ratios from the calculation for these three bands were 0.07, 0.27, 0.10, respectively. A Raman band with the depolarization ratio less than 0.75 is a polarized band. Although the intensity of these bands was different when the light was rotated by 90°, all of these bands were seen in all spectra for Cr crystals. This is because Raman intensities arise from changes in the derivative of the molecular polarizability tensor for each mode. These derivatives are reasonably large in each direction; therefore, no bands are completely extinguished at any direction. To get the effect of polarized light,

all the data on brain tissue were recorded using FPA-FTIR microscope with polarizer through a wide range of angles (0° to 180°).

From the IR spectra of Cr crystals in mouse brain tissue obtained with FPA-FTIR microscope (Kuzyk et al, 2010) and sFTIR (Gallant, 2007), Spectra from points A and B illustrate that unlike the sFTIR, all Cr peaks at 1305, 1394 cm^{-1} and 1405 cm^{-1} appeared because the globar light is not polarized (Figure 4.69). These spectra clearly illustrate the effect of synchrotron polarized light on Cr crystal orientation. When the polarization is perpendicular to the long axis of the Cr crystal, the bands at 1305, 1395 and 1423 cm^{-1} are observed and the bands at 1405 and 1447 cm^{-1} are disappeared. Conversely, when the polarization is parallel to the long axis of the crystal, only the peaks at 1405 and 1447 cm^{-1} appear and the other peaks vanish (Figure 4.70). Spectra from horizontal pure creatine crystals examined at SRC show the same behaviour, without using any polarizer (Figure 4.67). It could point that the collected radiation has more horizontal rather than vertical orientation.

Generally, the electrical field of unpolarized light oscillates in all possible directions. When a polarizer is put into the optical path, only one plane of oscillation passes through. The polarization dependence of the modes was used to identify the presence of Cr in tissue. To estimate crystal form, orientation and dimension, single tile maps in caudate and hippocampus regions of 14 months-old transgenic mouse were recorded with a 64 x 64 Focal Plane Array detector, using polarizer at settings from 0° to 180°, at 10° intervals. As explained, Cr peaks at 1305 cm^{-1} and 1405 cm^{-1} exhibit extreme polarization effects and have less overlap with tissue bands compared to other Cr peaks. Since the light

source of FPA-FTIR microscope was globar radiation which generated unpolarized light, all the Cr vibrational modes could be excited irrespective of Cr deposits in different orientations. The polarization filter provided the capability to study the creatine crystals (Figure 4.72, 4-73, 4.76, 4.77). The absorption intensity versus the polarization angle processed at 1305 and 1405 cm^{-1} for different points marked on mapped Cr deposit in caudate and hippocampus of Tg mouse show similar orientation for all analyzed points in a large creatine streak (Figure 4.74, 75, 76-82). From these results it was found that Cr streaks were formed of a single crystal unit instead of multiple microcrystalline deposit.

So far, the form and location of the Cr deposits in vivo is unknown. The sharp IR bands of Cr prove that it is a crystalline structure, but as the tissue desiccated, the crystallization could be artifact, formed after death.

All of these results along with the absence of any specific association between detected Cr deposits and any other biochemical signatures indicate that Cr crystals were formed after snap-freezing and desiccation of brain tissue.

5.8 Some speculation for the cause of creatine deposits in AD brain tissue

As mentioned in section 1.5, the pathological hallmarks of AD involve Aβ plaques, neurofibrillary tangles, inflammation, synaptic dysfunction and neuronal death. Discovery of creatine deposits in the brains of transgenic mice raises many questions about the role of Cr in this neurodegenerative disorder. Decreased energy metabolism is always associated with AD (Andres et al, 2008; Parihar et al, 2006). The role of Cr/PCr

system in energy metabolism has been recognized (Andres, 2008; Bürklen et al, 2006). IR and Raman maps enabled the identification of numerous Cr deposits in the transgenic mouse brain. Some Aβ plaques and lipids were detected in the vicinity of the Cr deposits in the Raman maps, but so far no specific correlation was identified between them.

The Cr deposits may be intra or extracellular. If they are located intracellular, they may be compartmentalized in mitochondria in addition to cytosol. The current Raman and IR images illustrated a large range in size for the Cr crystal deposits. These deposits could be generated either by Cr leakage from dying nerve cells or by impaired Cr trafficking between glial cells (actrocytes and oligodandrocytes) and neurons (Bürklen et al, 2006).

Cr may be associated with a particular cell types like neurons and microglial cells. Activated microglia is generally believed to be involved in AD-associated inflammatory response (Moore, 2010; Schlachetzki et al, 2009; Heneka et al, 2007). As noted, microglia cells can synthesize Cr in brain, and one of the pathological hallmarks of AD is activated microglia cells (Moore 2010; Schlachetzki et al, 2009; Bürklen et al, 2006); Therefore, inflammation and an increase in the number of glial cells can provide additional source of Cr because more Cr can be produced and released in the extracellular space (Bürklen et al, 2006).

Cr deposits were found in post mortem AD brain tissue and in Tg mouse brain (Gallant et al, 2006). Although the Cr deposits were sometimes found in the most aged control mice, those were fewer and much smaller compared to those observed in Tg mouse brain (Kuzyk et al, 2010). They could be result of a process associated with nor-

mal aging. The energy impairment in diseased and elderly brain has been intensively investigated during the last decades (Andres et al, 2008; Griffiths et al, 2008; Bürklen et al, 2006; Parihar et al, 2006). Mitochondrial dysfunction often leads to the excessive generation of free radicals and subsequent oxidative damage which can contribute to the age process (Lustbader et al, 2004). It is conceivable that increased oxidative modification of brain proteins may disturb neuronal functions by decreasing activities of key metabolic enzymes and affecting cellular signalling systems (Aksenov et al, 2000). Brain energy metabolism is characterized by high and fluctuating rates of ATP synthesis. High levels of CK, catalyzing the reversible transfer of the phosphate group of PCr to ADP in order to regenerate ATP, were found in the brain. The PCr level was found to decrease in the brains of patients with AD. PCr/Cr/ATP level are regulated by the enzyme CK. The interplay between cytosolic and mitochondrial CK isoenzymes accomplishes multiple roles in cellular energy homeostasis (Braissant et al, 2007; Bürklen et al, 2006). It was concluded that damage of CK function may be an important part of a neurodegenerative pathway that lead to neuronal loss in the brain (Aksenov et al, 2000). From that study by Bürklen, it was shown that BB-CK is significantly inactivated by oxidation in AD patients, and is one of the biochemical markers of the Central Nervous System (CNS) cell damage in AD. A direct connection between AD and uMt-CK was discovered by showing that uMt-CK can interact with the short cytoplasmic tail of APP family proteins; therefore, this interaction can affect the correct import of uMtCK into mitochondria and thus would negatively interfere with cellular energetic (Li et al, 2006). The inactivation of PCr causes an increase in the level of Cr, which may then form the deposits (Bürklen et al, 2006).

Although there is some speculation for the cause of Cr deposits in AD brain, no clear reason for the existences of the Cr deposits exists at this time.

5.9 The correlation between creatine deposits in AD brain tissue and activated microglial cells is still unknown

Most of the Cr deposits in the serial sections were elevated in CA1 area of hippocampus (Kuzyk et al, 2010). As neuronal activity in CA1 region of hippocampus has been strongly linked to memory formation (Walsh et al, 2004), this region in hippocampus was shown susceptible to Aβ pathology in both AD patients and transgenic mouse model (Rodrigues et al, 2010). It has been reported that the formation of amyloid plaques is concurrent with the appearance of activated microglial cells and shortly followed by the clustering of activated astrocytes around Aβ plaques (Dudal et al, 2004). Activation of microglia results in altered morphology of these cells, and increased secretion of cytokines, reactive oxygen intermediates all of which contribute to neuronal dysfunction and ultimately cell death (Schlachetzki et al, 2009). It was reported that the earliest reduction in neuronal counts was observed in CA1 region of hippocampus (West et al, 2004).

Cr biosynthesis involves two sequential steps catalyzed by two enzymes AGAT and GAMT (Braissant et al, 2005). The immunoreactivity of GAMT is very strong in oligodendrocytes, moderate in astrocytes, and not detected in neurons (Bürklen et al, 2006; Braissant et al, 2005). It might be hypothesized that discovered creatine deposits were originated from microglial cells.

When the processed maps of younger transgenic mice were investigated, Cr deposits were observed in hippocampus and the size and numbers was much lower com-

pared to older ones (Kuzyk et al, 2010). Although it is generally accepted that Aβ aggregation is a potent glial activator, activation of microglia and astrocytes could be an early event in the disease, occurring even in the absence of focal Aβ aggregation (Nunomura et al, 2001). It has been reported that in 3 months old APP transgenic mice, both cognitive deficits and focal glial cytokine production has been observed well before Aβ plaque deposition (Heneka et al, 2005). It means at least at the beginning of the disease, the senile plaques do not cause glial activation, and the neuroprotective effect of glial cells is a response against Aβ oligomers or protofibrils instead of senile plaques (Schlachetzki et al, 2009; White et al, 2005).

To investigate the possible correlation between Cr deposits and activated microglia, more data collection of even older mice, along with a staining will be needed. However, the required antibodies are not commercial stains, so they need to be created. From the publications, staining methods like preparing monoclonal OX-6 antibody (Bellucci et al, 2006) and Mac-1 antibody (Rodrguez et al, 2010) were reported to do staining microglial cells. From that study by Rodrguez, it was shown the activated microglial cells stained with Mac-1 antibody were normally present in multiple clusters, revealing an activity against amyloid plaques as shown by a high co-localization with Aβ (Rodrguez et al, 2010). Moreover, from the published paper by Belluci, it was illustrated that staining with OX-6 antibodies in TgCRND8 mouse brain shows clusters of large round-shaped microglial cells, surrounded Aβ plaques (Bellucci et al, 2006). Since most of the creatine deposits were reported in CA1 region of hippocampus, it makes this question that creatine might be originated from microglial cells. However, the processed data in CA1 area of hippocampus of older transgenic mouse shows most of these deposits were large

streaks (100-200 μm) (Kuzyk et al, 2010). Comparison of creatine dimension to the size of activated microglial cells stained by OX-6 and Mac-1 antibodies (10-30 μm) (Rodrguez 2010; Bellucci, 2006) remains this question that the origin of these large creatine streaks may not be from activated glial cells. However, the IR (Kuzyk et al, 2010) and Raman depth profile analysis show the creatine deposits co-localized with plaque in CA4 area of hipocapus of 14 month-old TgCRND8 mouse were small in size (10-80 μm). With these data, it is hard to draw any conclusion whethere the origin of identified creatine deposits may or may not be from activated microglial cells.

5.10 The neuroprotective or neurotoxic effect of creatine in AD is still unknown

Neuroprotective effects of Cr supplementation as a treatment of Alzheimer disease have been examined with different research groups (Bruno et al, 2010; Adhihetty et al, 2008; Andres et al, 2008). Cr supplementation has been shown to protect neurons against glutamate and Aβ toxicity (Adhihetty et al, 2008; Nivaggioli et al, 2007; Tarnopolsky et al, 2000). In addition, it has been reported that it can involve maintenance of mitochondrial function and preservation of ATP levels. This is due to the fact that newly entered Cr is phosphorylated inside the neurons by the catalytic activity of CK, leading to an increasing PCr/ATP ratio. Therefore, a higher energy charge in the cell. However, it can not happen if CK is damaged by oxidative stress. It has been speculated that Cr supplementation at an early time point of the disease may prevent or delay the course of this neurodegenerative disorder (Bürklen et al, 2006). With discovery of Cr deposits in the brain of transgenic mice, there is a concern whether Cr plays a neuroprotective or neuro-

toxic role in Alzheimer disease. Since the cause of Cr deposits in AD brain tissue is still not very clear, it is difficult to draw any conclusion about positive or negative effect of Cr in this neurodegenerative disorder. This part is beyond the scope of this thesis.

Conclusions

The discovery of creatine deposits in the brains of TgCRND8 mice raises many questions about the possible role of Cr in this neurodegenerative disorder. In this thesis, the principal goal was to find clues to the origin of creatine in transgenic mouse brain by analyzing IR and Raman microscopic images.

Since Cr can be endogenously synthesized in liver and kidney and transferred through the blood brain barrier by Cr transporters to get into the brain, blood vessels in the hippocampus of transgenic mice were analyzed by IR and Raman microscopy. The processed data show no createin could be detected in or around theses vessels, hence no association was identified between Cr deposits and blood vessels. Therefore, it can be concluded that these Cr deposits were most likely formed within brain tissue and not transported across the blood brain barrier.

The processed Raman depth profile maps confirm results, already seen in IR, that Aβ plaque was surrounded by lipid. Serial sections were analyzed for Cr (symmetric CN_3^+ band at 830 cm^{-1}), lipid (CH_2 deformation band at 1440 cm^{-1}), and amyloid plaque (anti-parallel β-sheet protein at 1670 cm^{-1}). No specific association between Cr deposits and either Aβ plaques or lipid membrane was detected. The maps were analyzed for other spectral markers such as sphingomyelin (CN^+ stretching mode at 730 cm^{-1}), nucleic acids (symmetric PO_2 band of DNA and RNA at 790, 1085 cm^{-1}; and a distinct band corre-

sponding to RNA at 920 cm^{-1}), phospholipids (symmetric PO_2 band of phospholipids at 860, 1098 cm^{-1}; =CH bending of unsaturated lipid at 980 cm^{-1}) and amino acids mostly phenylalanine (distinct bands correspond to phenylalanine at 930, 1003 cm^{-1}; C=C deformation of phenylalanine 1590 cm^{-1}). No correlation was found between Cr deposits and these biochemical signatures

To investigate whether Cr deposits are distributed ubiquitously in brain tissue, the caudate of Tg and non-Tg mice at different ages were imaged with IR. Cr was observed in the caudate of two 14 month-old mice, one TgCRND8 and its non-Tg littermate. The size and number of detected Cr streaks were much greater in Tg compared to non-Tg.

Another student (Veena Agrawal) discovered that some Cr bands in synchrotron IR images appeared or disappeared completely. This resulted from the effect of polarized synchrotron light. To better understand Cr crystal structure and orientation, combined theoretical and experimental studies were undertaken into the effect of polarized light on the spectra of crystalline Cr in both pure Cr and tissue deposits. Theoretical calculation conducted by Fatemeh Faraz Khorasani gave both frequency and polarization information to enable a more detailed interpretation of the Cr spectra. As the IR bands are dependent on crystal orientation, polarized IR images were used to estimate the form, orientation and dimension of crystalline Cr deposits in tissue. IR images of large Cr streaks in hippocampus and caudate of 14 months-old TgCRND8 mouse were recorded with FPA-FTIR microscope, using a polarizer at settings from 0° to 180°, at 10° intervals. The absorption intensity, processed at 1305 cm^{-1} and 1405 cm^{-1}, versus polarization angle shows similar orientation for all analyzed points in a single large creatine streak. The same maximum and minimum intensity obtained for points examined along each Cr streak shows that

these Cr streaks must exist as a single crystal unit instead of multiple microcrystalline deposits. While the state of the Cr in the living mouse and the causes for these deposits are still unclear, it can be concluded that Cr could have been intracellular or extracellular and formed as crystal deposits after snap-freezing and desiccating of brain tissue. Therefore, it can be speculated from this research that Cr might be exist in solution form in vivo.

In Magnetic Resonance spectroscopy (MRS) studies, the Cr/PCr signal has been used as an internal standard to obtain the relative concentrations of other components such as glutamate-glutamine complex, and choline. Because of the focally elevated creatine levels already detected in the hippocampus and some cortex and now found in caudate of TgCRND8 mice, the use of creatine as an internal standard should be reconsidered. If Cr is used as internal standard when levels of other metabolites are investigated, errors may occur.

Cr deposits were identified in the brain of transgenic mice and increased in size and number with age. Evidence above suggests that it is formed in the brain and is found throughout hippocampus and caudate. The questions remain as to why the Cr is there whether it has any active role in the progression of the disease, and whether the role of Cr is neurotoxic or neuroprotective.

Future work

Further of large regions mapping in mice of different ages should be performed to investigate whether or not creatine deposits are common features in other regions of brain, such as cerebellum, thalamus and olfactory bulb, regions typically developing Aβ plaques in TgCRND8 mouse.

To investigate the possible correlation between Cr deposits and activated microglia, more data collection from even older mice is recommended, along with the staining of microglia and actrocytes through different ages of Tg and non-Tg mice. It should be mentioned that the required antibodies are not commercial stains, so they need to be created.

Staining for enzymes AGAT and GAMT involving in the synthesis of creatine can be performed to probe whether any changes in these enzymes is a factor in the increased creatine deposits observed in TgCRND8 mice. Two CK isoenzymes, uMt-CK and BB-CK, can be stained to determine whether the levels are altered, as they might play a role to increase the Cr levels. In Dr. Gough's lab, 5 antibodies to detect enzymes including AGAT, GAMT, BB-CK, uMt-CK, and CrT were donated and stained by Fred Zeiler (summer 2006). The only antibody that showed any slight indication of positive results was the uMt-CK. The antibodies my have been too old.

Mapping different brain tissue regions by IRENI (InfraRed ENvironmental Imaging), combining 12 brilliant synchrotron source beams with multi-element detection, can be

used to obtain chemical images with excellent S/N at 0.54 μm pixel resolution in minutes. This technique can be performed to record data at higher spatial resolution from serial sections, previously imaged by FTIR and Raman in order to investigate whether any other biochemical signature can be identified to be localized with Cr deposits.

X-ray Fluorescence Imaging (XRF) can be performed to probe metal distribution in different brain tissue regions. The results from XRF can be compared with IR and Raman processed for Aβ plaque aggregation and Cr deposits to determine whether there is any co-localization between them. So far, these techniques have not been addressed by other groups in order to investigate Cr origin in transgenic mouse brain.

References

Adhihetty, P. J., & Beal, M. F. (2008) Creatine and its potential therapeutic value for targeting cellular energy impairment in neurodegenerative diseases. *NeuroMolecular Medicine*, 10, 4, 275-290.

Aksenov, M., Aksenov, M., Butterfield, D. A., & Markesbery, W. R. (2000) Oxidative modification of creatine kinase BB in Alzheimer's disease brain. *Journal of Neurochemistry*. 74**,** 6, 2520-2527.

Alonso, A. D. C., Li, B., Grundke-Iqbal, I., & Iqbal, K. (2008) Mechanism of tau-induced neurodegeneration in Alzheimer disease and related tauopathies. *Current Alzheimer Research*, 5, 375-384.

Andres, R. H., Ducray, A. D., Schlattner, U., Wallimann, T., & Widmer, H. R. (2008) Functions and effects of creatine in the central nervous system. *Brain Research Bulletin*, 76, 329-343.

Ansari, M. A., & Scheff, S. W. (2010) Oxidative Stress in the Progression of Alzheimer Disease in the Frontal Cortex. *Journal of Neuropathology & Experimental Neurology*. 69(2), 155-167.

Apostolova, L. G., & Cummings, J. L. (2007) The pathogenesis of Alzheimer's disease: General overview. *Protein overviews*, 6, 3-29.

Bandyopadhyay, B., Li, G., Yin, H., & Kuert. (2007) Tau aggregation and toxicity in a cell culture model of tauopathy, *Journal of Biological Chemistry*, 282, 16454-16464.

Barth, A. (2007) Review: Infrared Spectroscopy of proteins. *Biochemica et Biophysica Acta*. 1767, 1073-1101.

Beard, E., & Braissant, O. (2010) Synthesis and transport of creatine in the CNS: importance for cerebral functions. *Journal of Neurochemistry,* 115(2), 297-313.

Belluci, A., Cristina, M., Grossi, C., Fiorentini, A., Lucccarini, I., & Casamenti, F. (2007) Abnormal processing of tau in the brain og aged TgCRND8 mice. *Neurobiology of Disease*, 27, 328-338.

Bellucci, A., Luccaraini, I., Scail, C., Prosperi, C., Giovannini, M. G., Pepeu, G., & Casamenti, F. (2006) Cholinergic dysfunction, neuronal damage and axonal loss in TgCRND8 mice. *Neurobiology of Disease*, 23, 260-272.

Bernhardy, R. V. (2007) Glial cell dysregulation: A new perspective on Alzheimer Disease. *Neurotoxicity Research*, 12, 4, 215-232.

Bettens, K., Sleegers, K., & Broeckhoven, C. V. (2010) Current status on Alzheimer disease molecular genetics: from past, to present, to future. *Human Molecular Genetics*, 19, 1, R4-R11.

Bharadwaj, P. R., Dubey, A. K., Masters, C. L., Martins, R. N., & Macreadie, I. G. (2009) *Journal of Cellular and Molecular Medicine.* 13(3), 412-421

Bhargava, R., & Levin, I. W. (2005) Spectrochemical analysis using Infrared Multichannel detectors. *Blackwell Publishing*. Pages: 311.

Billings, L. M., Green, K. N., McGough, J. L., & LaFerla, F. M. (2007) Learning dcreases amyloid beta 56 an dtau pathology and ameliorates behavioural decline in 3xTg-AD mice. *The Journal of Neuroscience*, 24, 4, 751-761.

Bista, R. K., Bruch, R. F., & Convington, A. M. (2009) Reviews: Vibrational spectroscopic studies of newly developed synthetic. *Biopolymers*. Vol. 93, No. 5, 403-41.

Blass, J., Gibson, G. E., & Hoyer, S. (2002) The role of the metabolic lesion in Alzheimer's disease. *J. Alziemer's Disease*, 2, 225-232.

Braissant, O., Henry, H., Villard, A. M., Speer, O., Wallimann, T., & Bachmann, C. (2005) Creatine synthesis and transport during rat embryogenesis: Spatitomporal expression of AGAT, GAMT and CTI. *BMC Developmental Biology*. 4, 5-9.

Braissant, O., Henry, H., Villard, A., Speer, O., Wallimann, T., & Bachmann, C. (2005) Creatine synthesis and transport during rat embryogenesis. *BMC Development Biology*, 5:9, 1-16.

Brent, C., & Landreth, G. E. (2010) Inflammation, microglia, and Alzheimer's Disease. *Neurobiology of Disease*, 37, 503-509.

Brewer, G. J., & Wallimann, T. W. (2000) Protective effect of the energy precursor creatine against toxicity of glutamate an dbeta-Amyloid in rat hippocampal neurons. *J of Neurochemistry*, 74, 1968-1978.

Brosnan , M. E., Edison, E. E., Da Silva, R., & Brosnan, J. T. (2007) New insights into creatine function and synthesis. *Advan. Enzyme. Regul*, 47, 252-260.

Bruno, E., Quattrocchi, G., Nicoletti, A., Le Pira, F., Maci, T., Mostile, G., Andreoli, V., Quattrone, A., & Zappia, M. (2010) Lack of interaction between LRP1 and A2M polymorphisms for the risk of Alzheimer disease. *Neuroscience Letters*, 482, 2, 112-116.

Bürklen, T. S., Schlattner, U., Homayouni, R., Gough, K., Rak, M., Szeghalmi, A., & Wallimann, T. (2006) The creatine kinase/creatine connection to Alzheimer's disease: CK inactivation, APP-CK complexes, and focal creatine deposits. *J of Biomed & Biotech*, 1-11

Busciglio, J., Pelsman, A., Wong, C., Pigino, G., Yuan, M., Mori, H., & Yankner, B. A. (2002) Altered metabolism of the amyloid precursor protein is associated with mitochondrial dysfunction in Down's syndrome. *Neuron*, 33, 677-688.

Butterfield, D. A, Drake, J., Pocernich, C., & Castegna, A. (2001) Evidence of oxidative damage in Alzheimer's disease brain: central role for amyloid beta-peptide. *Trends in molecular medicine*, 7(12), 548-54.

Cagin, A., Gerhard, A., & Banati, R. (2002) In vivo imaging of neuroinflammation. Eur Neuropsychopharmacol. 12(6) 581-586

Casely, C. S., Canevari, L., Lan, J, M., Clark, J. B., & Sharpe, M. A. (2002) Beta-Amyloid inhibits integrated mitochondrial respiration and key enzyme activities. *J Neurochem*, 80, 91-100.

Cerpa, W., Dinamarca, M. C., & Inestrosa, N. C. (2009) Structure-function implications in Alzheimer's disease: Effect of Aβ oligomers at central synapses. *Current Alzheimer Research*. 5, 233-243

Cerpa, W., Dinamarca, M. C., & Inestrosa, N. C. (2008) Structure-function implications in Alzheimer's Disease: Effect of amyloid beta oligomers at central synapses. *Current Alzheimer's Research*, 5, 233-243.

Chan, J. W., Taylor, D. S., Zwerdling, T., Lane, S. T., Ihara, K., & Huse, T. (2006) Micro-Raman spectroscopy detects individual neoplastic and normal hematopoietic cells. *Biophysical Journal*, 90, 648-656.

Chishti, M. A., Yang, D. S., Janus, C., Phinney, A. L., Horne, P., Pearson, J., Strome, R., Zuker, N., Loukides, J., French, J., Turner, S., Lozza, G., Grilli, M., Kunicki, S., Morissette, C., Paquette, J., Gervais, F., Bergeron, C., Fraser, P. E., Carlson, G. A., St. George-Hyslop, P., & Westaway, D. (2001) Early-onset amyloid deposition and cognitive deficits in transgenic mice expressing a double mutant form of amyloid precursor protein 695. *Journal of Biological Chemistry*, 276(24), 21562-21570.

Christensen, D. Z., Bayer, T.A., & Wirths, O. (2009) Formic acid is essential for immunohistochemical detection of aggregated intarneuronal amyloid beta peptides in mouse models of Alzheimer's Disease. *Brain Research*, 1301, 116-125.

Coleman, P., Federoff, H., & Kurlan, R. (2004) A focuse on the synapse for neuroprotection in Alzheimer disease and other dementias. *Neurology*. 63, 1155-1162.

Combs, A. K. (2009) Inflammation and microglia actions in Alzheimer's Disease. *Journal of Neuroimmune Pharmacology*, 4, 380-388.

Conde, J. R., & Streit, W. J. (2006) Microglia in the aging brain. *J. Neuropathol. Exp. Neurol*, 65, 199-203.

Courch, P. J., Harding, S. E., White, A. R., Camakaris, J., Bush, A. I., & Masters, C. L. (2008) Mechanisms of amyloid beta mediated neurodegeneration in Alzheimer's disease. *IJBCB*. 40, 181-198.

D'Andrea, M. R, Nagele, R. G, Wang, H. Y, Peterson, P. A, & Lee, D. H .(2001) Evidence that neurones accumulating amyloid can undergo lysis to form amyloid plaques in Alzheimer's disease. *Histopathology*. 38, 120

Debomay, L. D. (2008) Current Alzheimer research: Update on lipids, estrogen, neurotrophins and the roles in neurodegeneration. Current Alzheimer Research, 5, 1, 1-3.

De Felic, F.G., Wu, D., Lamber, M. P., Fernandez, S. J., Velasco, P. T., Lacor, P. N., Bigio, E. H., Jerecic ,J., Acton, P. J., Shughure, P. J., Kinney, G. G., & Klein., W. L. (2008) Alzheimer's disease – type neuronal tau hyperphosphorylation induced by Aβ oligomers. *Neurobiology of aging*. 29, 1334-1347

Dovebeshko, G. I., Girdina, N. Y., Kruglova, E. B., & Pashchuk, O. P. (2000) FTIR spectroscopy studies of nucleic acid damage. *Talanta*, 53, 233-246.

Dudal, S., Krzywkowski, P., Paquette, J., Morissette, C., Lacombe, D., Tremblay, P., & Gervais, F. (2004) Inflammation occurs early during the amyloid beta depostion process in TgCRND8 mice. *Neurobiology of aging*, 25, 861-871.

Dumas, P., & Miller, L. (2004) The use of synchrotron infrared microspectroscopy in biological and biomedical investigations. *Vibrational Spectroscopy*. 32, 3-21.

Duyckaerts, C., & Dickson, D. W., (2003). Neuropathology of Alzheimer's disease. The molecular pathology of dementia and movement disorders. ISN Neuropath Press, *Basel*, pp. 47-65.

Ellepola, S. W., Choi, S. M., Philips, D. L., & Ma. C. Y. (2006) Raman spectroscopics study of rice globulin. *Journal of Cereal Science*, 43, 85-93.

Fabian, H., Jackson, M., Murphy, L., Watson, P. H., Fichtner, I., & Mantsch, H. H. (1995) A comparative infrared spectroscopic study of human breast tumors and breast tumor cell xenografts. *Biospectroscopy*, 1, 1, 37-45.

Ferraro, J. R., Nakamoto, K., & Brown, C. W. (2003) Introductory Raman Spectroscopy, *Elsevier*. 434 pp.

Fetler, L., & Amigorena, S. (2005) Neuroscience brain under surveillance. *The microglia patrol Science*, 309, 392-393.

Florent- Bechard, S. F., Desbene, C., Garcia, P., Allouche, A., Youssef, I., Escayne, M. C., Koziel, V., Hanse, M., Malaplate-Armand, C., Stenger, C., Krein, B., Yen-Potin, F. T., Oliver, J. L., Pillot, T., & Oster, T. (2009) The essential role of lipids in Alzheimer's disease. *Bichimie*, 91, 804-809.

Friedrich, R. P., Tepper, K., Roenicke, R., Soom, M., Westermann, M., Reymann, K., Kaether, C., & Faendrich, M. (2010) Mechanism of amyloid plaque formation suggests an intracellular basis of Amyloid beta pathogenicity. *Proceedings of the National Academy of Sciences of the United States of America*, 1-6.

Funato, H., Enya, M., Yoshimaro, M., & Ihara, A. M. (1999) Presence of sodium dodecyl sulfate-stable amyloid beta-protein dimers in the hippocampus CA1 not exhibiting neurofibrillary tangle formation. *The American Journal of Pathology*, 155, 1, 23-28.

Gallant, M., Rak, M., Szeghalmi, A., Del Bigio, M. R., Westaway, D., Yang, J., Julian, R., & Gough, K. M. (2006) Focally elevated creatine detected in amyloid precursor protein (APP) transgenic mice and Alzheimer's disease brain tissue. *The Journal of Biological Chemistry*, 281(1), 5-8.

Gallant, M. (2007) Infrared Microspectroscopy of focally elevated creatine in brain tissue from Amyloid Precursor Protein (APP) Transgenic mioce, *M.Sc. Thesis*, University of Manitoba.

Gasparani, L., Gouras, G. K., Wang, R., Gross, R. S., Beal, M. F., Greengard, P., & Xu, H. (2001) Stimulation of beta-amyloid precursor protein trafficking by insulin reduces intraneuronal beta- amyloid and requires mitogen-activated protein kinase signalling. *The Journal of Neuroscience*, 21(8), 2561-70.

Godbolt, A. K., Waldman, A. D., MacManus, D. G., Schott, J. M., Frost, C., Cipolotti, L., Fox, N. C., & Rossor, M. N. (2006) MRS shows abnormalities before symptoms in familial Alzheimer disease. *Neurology*, 66, 718-722.

Gotz, L., Ittner, L. M., Schonrock, N., & Cappai, R. (2008) An update on the toxicity of amyloid beta in Alzheimer's disease. *Neuropsychiatric Disease and Treatment*, 4, 6, 1033-1042.

Green, P. S., & Simpkins, J.W. (2000) Estrogens and estrogen-like non-feminizing compounds: Their role in the prevention and treatment of Alzheimer's disease. *Annals of the New York Academy of Sciences*, 924, 93-98.

Griffiths, H. H., Morten, I. J., & Hooper, N. M. (2008) Emerging and potential therapies for Alzheimer's disease. *Expert Opinion on Therapeutic Targets*, 12, 6, 693-704.

Griffiths, P. (2007) Fourier Transform Infrared Spectroscopy. *Wiley*. Pages. 704.

Gong, C., Grundke-Iqbal, I., & Iqbal, K. (2010) Targeting tau protein in Alzheimer's disease. *Drugs & Aging*. 27(5), 351-365.

Gotz, J., Ittner, L. M., Schonrock, N., & Cappai, R. (2008) An update on the toxicity of A.beta. in Alzheimer's disease. *Neuropsychiatric Disease and Treatment*, 4(6), 1033-1042

Guido, K., & John, R. C. (2000) Mitochondrial control of cell death. *Nal. Med*, 6 (5) 513-519.

Hammes, G. G. (2005) Spectroscopy for the biological sciences. *Wiely*, Pages: 179.

Hardy, J., & Selkoe, D. J. (2002) The amyloid hypothesis of Alzheimer's disease: preogress and problems on the road to therapeutics. *Science*, 297, 353-356.

Hardy, J. A., & Higgins, G. A. (1992) Alzheimer siease: the amyloid cascade hypothesis. *Science*, 256 (5054). 184-185 1992

Heneka, M. T., & O'Banion, M. K. (2007) Inflammatory processes in Alzheimer's disease. *J. Neuroimmunology*. 184, 69-91.

Heneka, M. T., Sastre, M., Dumitrescu-Ozimek, L., Dewachter, I., Walter, J., & Klockgether, T. (2005) Focal glial activation coincides with increased BACE1 activation and precedes amyloid plaque deposition in APP[V717I] transgenic mice. *J. Neuroinflammation*, 2, 22.

Herringa, A., Yasin, H., Ambree, O., Sachser, N., Paulus, W., & Keyvani, K. (2008) Enviromental enrichment counteracts Alzheimer's neurovascular dysfunction in TgCRND8 mice. *Brain Pathology*, 18, 32-39.

Herz, J. (2007) Overview: The long and winding road to understand Alzheimer's disease. *Neuron*, 53, 477-79.

Iwata, N., Mizukami, H., Shirotni, K., Takaki, Y., Muramatsu, S. I., Lu, B., Gerard, N. P., Gerard, C., Ozawa, K., & Saido, T. C. (2004) Presynaptic localization of Neprilysin contributes to efficient clearance of amyloid beta peptide in mouse brain. *The Journal of Neuroscience*, 81, 2, 742-66.

Jan, a., Gokce, o., Luthi-Carter, r., & Lashuel, H. A. (2008) The Ratio of monomeric to aggregated forms of Amyloid-Beta 40 and Amyloid-Beta 42 is an important determinant of amyloid-.beta. aggregation, fibrillogenesis, and toxicity. *Journal of Biological Chemistry*, 283, 42, 28176-28189.

Jakob-Roetne, R., & Jacobsen, H. (2009) Alzheimer's Disease: From pathology to therapeutic appoaches. Angewandte Chemie, International Edition. 48(17), 3030-3059.

Kateinen, E., Elomaa, M., Laakkonen, U. M., Sippola, E., Niemela, P., Suhonen, J., & Jarninen, K. (2007) Qualification of the amphetamine content in seized street samples by Ramn spectroscopy. *Journal of Forensic Science*, 52, 1, 88-92.

Kawahara, M., Negishi-Kato, M., & Sadakane, Y. (2009) Calcium dyshomeostasis and neurotoxicity of Alzheimer's beta-amyloid protein.

Kawarabayashi, T., Shoji, M., Younkin, L. H., Dikson, D. W., & Younkin, S. G. (2004) Dimeric amyloid-β protein rapidly accumulates in lipid rafts followed by apolipoprotein E and phosphorylated tau accumulation in the Tg2576 mouse model of Alzheimer's disease. *Journal of Neuroscience*, 24, 3801-3809.

Kayad, R., Head, E., Thompson, J. L., McIntire, T. M., Milton, S. C., Cotman, C. W., & Glabe, C. G. (2003) Common structure of soluble amyloid oligomers implies common mechanism of pathogenesis. *Science*. 300, 486-489.

Klein, W. L., Stine, J. R., & Teplow, D. B. (2004) mall assemblies of unmodified amyloid -β protein are the proximate neurotoxin in Alzheimer's disease. *Neurobiology of Aging*, 25, 569-80.

Kobayashi, K,. Nakano, H., & Hayashi, M. (2003) Association of phosphorylation site of tau protein with neuronal apoptosis in Alzheimer's disease. *J Neurol Sci*, 208(1–2):17–24

Köehler, M., Machill, S., Salzer, R.,& Krafft, C. (2009) Characterization of lipid extracts from brain tissue and tumors using Raman spectroscopy and mass spectrometry. *Analytical and Bioanalytical Chemistry*, 393, 5, 1513-1520.

Kolijenovice, S., Scut, T. B., Vincent, A., Kros, J. M., & Pupples, G. J. (2005) Detection of meningioma in dura mater by Raman spectroscopy. *Analytical Chemistry*, 77, 24, 7958-7965.

Koppenal, C., Finefrock, A. E., Bush, A. I., & Doraiswamy, P. M. (2004) Copper, iron and zinc as therapeutic targets in Alzheimer's disease. *Research and Practice in Alzheimer's Disease*, 9, 250-255.

Kosik, K. S., Joachim, C. L., & Selkoe, D. J. (1986) Microtubule-associated protein tau is a major antigenic component of paired helical filaments in Alzheimer disease. *Proc Natl Acad Sci*, 83, 4044-4048

Krafft, C., Knetschke, T., Funk, R. H. W., & Salze, R. (2006) Studies on stress-induced changes at the subcellular level by Raman Microspectroscopic mapping. *Analytical. Chemistry*, 78, 4424-4429.

Krafft, C., Sobottka, S. B., Schackert, G., & Salzer, R. (2005) Near Infrared Raman Spectroscopic mapping of native brain tissue and intracranial tumors. *Analyst*, 130, 1070-1077.

Krafft, C., Neudert, L., Simat, T., & Salzer, R. (2005) Near Infrared Raman spectra of human brain lipids. *Spectrochimica Acta*, Part A, 61, 1529-1535.

Kraftt, C. (2004) Bioanalytical applications of Raman Spectroscopy. *Analytical Bioanalytical Chemistry*, 378: 60-62.

Kuzyk, A., Kastyak, M., Agrawal, V., Gallant, M., Sivakumar, G., Rak, M., Del Bigio, M. R., Westaway, D., Julian, R., & Gough, K. M. (2010) Association among amyloid plaque, lipid, and creatine in hippocampus of TgCRND8 mouse model for Alzheimer disease. *The Journal of biological chemistry*, 285(41), 31202-7.

Lakshimi, R. J., Kartha, V. B., Krishna, C. M., Solomon, J. G. R., Ullas, G., & Devi, U. (2002) Tissue Raman spectroscopy for the study of radiation damage: Brain irradiation of mice. *Radiation Research*, 157, 175-182.

Lee, Y. B., Nagai, A., & Kim, S. U. (2002) Cytokines, chemokines, and cytokine receptors in human microglia. *Journal of Neuroscience Research*, 69, 94-103.

Lepoirve, M., Flaman, J.M., Bobe, P., Lemaire, G., & Henry, Y. (1994) Quenching of the tyrosyl free radical of ribonucleotide reductase by nitric oxide. *Journal of Biological. Chemistry*. 269, 21891-21897

Li, X., Bürklen, T, Yuan, X., Schlattner, U., Desiderio, D. M., Wallimann, T., & Homayouni, R. (2006) Stabilization of ubiquitous mitochondrial creatine kinase preprotein by APP family proteins. *Molecular and Cellular Neuroscience*, 31, 263-272.

Li, R., Lindholm, K., Yang, L., Yue, X., Citon, M., Yan, R., Beach, T., Sue, L., Sabbagh, M., Cai, H., Wong, P., Price, D., & Shen, Y. (2004) Amyloid beta peptide load is correlated with increased beta secratse activity in sporadic Alzheimer's disease patients. *PNAS*, 101, 10, 3632-3637.

Lustbader, J. W., Cirilli, M., & Lin, C. (2004). ABAD directly links Abeta to mitochondrial toxicity in Alzheimer's disease. *Science*, 304, 448-452.

Lucas, J. J., Hernandez, F., & Gomez-Ramos, P. (2001) Decreased nuclear beta-catenin, tau hyperphosphorylation and neurodegeneration in GSK-3beta conditional transgenic mice. *EMBO J*, 20(1–2):27–39

Maccioni, R. B., Farias, G., Morales, I., & Navarrete, L. (2010) The revitalized tau hypothesis on Alzheimer's disease. *Archives of Medical Research*, 41, 226-231.

Magistretti, P. J., & Pellerin, L. (1999) Cellular mechanisms of brain energy metabolism and their relevance to functional brain imaging. *Biological Science*, 1977, 55, 637-653.

Malini, R., Venkatarkrishma, K., & Kurien, J. (2006) Discrimination of normal, inflammatory, premalignant, and malignant oral tissue: A Raman spectroscopy study, *Biopolymers*, 81, 3, 179-193.

Mancuso, M., Orsucci, D., Siciliano, G., & Murri, L. (2008) Mitochondria, mitochondrial DNA and Alzheimer's disease. What comes first? *Current Alzheimer Research*, 5, 5, 457-468.

Mandal, P. K. (2008) Magnetic resonance spectroscopy (MRS) and its application in Alzheimer's disease. *Bridging Education and Research*, 32A, 5, 407.

Mandal, P. K., (2007) Magnetic resonance spectroscopy (MRS) and its application in Alzheimer's disease. *Bridging Education and Research*, 30A(1) 40-64

Martinez , A., Portero-Otin, M., Pamplona, R., & Ferre, I. (2010) Protein targets of oxidative damage in human neurodegenerative disease with abnormal protein aggregates. *Brain Pathology*, 20, 281-297.

Martins, I. C., Kuperstein, I., Wilkinson, H., Maes, E., Mieke V., Jonckheere, W., D'Hooge, R., De Strooper, B., Schymkowitz, J., & Rousseau. A. (2008) Lipids revert inert amyloid beta fibrils to neurotoxic protofibrils that affect learning in mice. *The EMBO Journal*, 27, 224-233.

Matteson, M. P. (2004) Ways towards and away from Alzheimer's disease. *Nature*, 430, 631-639.

McGown, E. J., & Erksend, A. (2006) A decade of modeling Alzheimer's disease in trasgneic mice. *Trends Genet*, 22, 5, 281-289

Miller, L. M., & Smith, R. J. (2005) Synchrotron versus golbars, point-detectors versus focal plane arrays: Selecting the best source and detector for specific infrared microspectroscopy and imaging applications. *Vibrational Spectroscopy*. 38, 237-240.

Moreno-Torres, A., Pujol, J., Soriano-Mas, C., Deus, J., Iranzo A., & Santainaria, J. (2005) *Neurobiology of Aging*. 26, 1051-1059.

Moore, A. H., Bigbee, M. J., Boynton, G. E., Wakeham, C. M., Rosenheim, H. M., Staral, C. J., Morrissey, J. L., & Hund, A K. (2010) Non-steroidal anti-inflammatory drugs in Alzheimer's disease and Parkinson's disease: reconsidering the role of neuroinflammation. *Pharmaceuticals*, 3, 1812-1841.

Movasaghi, Z., Rehman, S., & Rehman, I. U. (2007) Fourier Transform Infrared (FTIR) Spectroscopy of biological tissues. *Applied Spectroscopy Reviws*, 43: 134-179.

Movasaghi, Z., Rehman, S., & Rehman, I. U. (2007) Raman Spectroscopy of biological tissues. *Applied Spectroscopy Reviws*, 42: 493-541.

Mucke, L., Msliah, E., Yu, G. O., Mallory, M., Rockenstein, E. M., Tatsuno, G., Kholodenko, D., & McConologue, L. (2000) High-level neuronal expression of amyloid beta 1-42 in wild-type human APP transgenic mice: Synaptotoxicity without plaque formation. *Journal of Neuroscience*, 20, 4050-4058.

Napoli, I., & Neumann, H. (2009) Microglial clearance function in health and disease. *Neuroscience*, 158, 1030-1038.

Nelson, P. T., Abner, E. L., Schmitt, F. A., Kryscio, R. J., Jicha, G. A., Santacruz, K., Smith, C., Patel, E., & Markesbery, W. R. (2008) Brains with medial temporal lobe neurofibrillary tangles but no neuritic amyloid plaques are a diagnostic dilemma but have pathogenetic aspects distinct from Alzheimer disease. *Journal of Neuropathology and Experimental Neurology*, 68, 7, 774-784.

Nerelius, C., Johnsson, J., & Sandegren, A. (2009) Amyloid beta-peptide aggregation. What does it result in and how can be prevented? *Frontiers in Bioscience*, 14, 1716-1729.

Nivaggioli, B. T. (2007) Methods for treating a neurological disorder with creatine monohydrate. *U.S. Pat. Appl*. Publ, 16pp.

Nunomura, C., Tamoki, T., Tanaka, K., Motohashi, N., Nakamura, M., Hayashi, T., Yamaguchi, H., Shimohama, S., Lee, H., Zhu, X., Smith, M. A., & Perry, G. (2010) Intraneuronal amyloid β accumulation and oxidative damage to nucleic acids in Alzheimer disease. *Neurobiology of Disease*, 37, 731-737.

Nunomura, A., Perry, G., Aliev, G., Hirai, K., Takeda, A., Balraj, E. K., Jones, P. K., Petersen, R. B., & Smith, M. A., (2007) Oxidative damage is the earliest event in Alzheimer disease. *J. Neuropathol. EXP. Neurol*, 60, 759-767.

Ogg, M. (2002) Vibrational Microspectroscopy of Alzheimer Diseased Hippocampus tissue. *M.Sc. Thesis*, University of Manitoba.

Ohtsuki, S., Tachikawa, M., & Takanaga, H. (2002) The blood-brain barrier creatine transporter is a major pathway for supplying creatine to the brain. *J. of Cerebral Blood Flow and Metabolism*, 22, 11, 1327-1335.

Ohyagi, Y. (2008) Intracellular amyloid .beta.-protein as a therapeutic target for treating Alzheimer's disease. *Current Alzheimer Research*, 5(6), 555-561.

Ong, C. W., Shen, Z. X., Lee, Y., & Tang, S. H. (1999) Raman Microspectroscopy of the brain tissues in the substantia nigra and MPTP-induced parkinson's disease. *J of Raman Spectroscopy*, 30, 91-96.

Ozaki, Y. Y. (2008) Introduction to Raman spectroscopy. *Pharmaceutical applications of Raman spectroscopy*, 1, 28, 1-28.

Panza, F., Solfrizzi, V., Frisardi, V., Capurso, C., D'Introno, A., Colacicco, A. M., Vendemiale, G., Capurso, A. I., & Bruno, P. (2009) Disease-Modifying Approach to the *Treatment of Alzheimer's Disease. Drugs & Aging*, 26 - Issue 7, 537-555.

Parachikova, A., Agadjanyan, M., & Cribbs, D. (2006) Inflammatory changes parallel the early stages of Alzheimer disease. *Neurobiol Aging*. 28 (12) 1821- 1833

Parihar, M. S., & Brewer, G. J. (2007) Mitoenergetic failure in Alzheimer disease. *AM J Physiol Cell Physiol*, 292: C8-C23.

Patterson, C., Feighter, J. W., Garcia, A., Hsiung, G. R., Macknight, C., & Sadovink, D. (2008) Diagnosis and treatment of dementia: Risk assessment and primary prevention of Alzheimer disease. *CMAJ*, 26, 178(5), 548-586.

Pereira, C., Agostinbo, P., Moreira, P. I., Cardoso, S. M., & Oliveira, C. R. (2005) Alzheimer's disease-associated neurotoxic mechanisms and neuroprotective strategies. *Current Drug Targets-CNS & Neurological Disorders*, 4, 383-403.

Pierrot, N., & Octave, J. (2008) Processing of amyloid precursor protein and amyloid peptide neurotoxicity. *Current Alzheimer Research*, 5(2), 92-99

Pimplikar, S. W. (2009) Reassessing the amyloid cascade hypothesis of Alzheimer's disease. *The international Journal of Biochemistry & Cell Biology*, 41, 1261-1268.

Pratico, D. (2008) Oxidative stress hypothesis in Alzheimer's disease: a reappraisal. *Trends in Pharmacological Sciences*, 29(12), 609-615.

Querfurth, H. W., & LeFerla, F. W. (2010) Mechanisms of disease; Alzheimer's disease. *The New England Journal of Medicine*, 362, 329-344.

Quiroz-Baeza, R., Emilio, R., & Clorinda, A. (2009) Oxidative stress promotes amyloidogenic processing of normally expressed human APP by differential modification of α-, β- and γ-secretase expression. *Neuroche Inter*, 55, 7, 662-670

Ramos, A., Diaz-Hernandez, M., Cuadros, R., Hernandez, R., & Ávila, J (2006) Extracellular tau is toxic to neuronal cells. *FEBS Lett*, 580:4842–4850.

Rankin, C. A., & Gamblin, T. C. (2008) Assessing the toxicity of Tau aggregation. *J of Alzheimer's Disease*, 14, 411-416.

Rak, M. (2007) Synchrotron infrared microspectroscopy of biological tissues: brain tissue from TgCRND8 Alzheimer's disease mice and developing scar tissue in rats. *Ph.D. Thesis*, University of Manitoba.

Rak, M., Del Bigio, M. R., Mai, S., Westaway, D., & Gough, K. M. (2007) Dense-core and diffuse Aβ plaques in TgCRND8 mice studies with synchrotron FTIR microspectroscopy. *Biopolymers*, 87, 4, 207-217.

Reddy, P. H., & Beal, M. F. (2005) Are mitochondria critical in the pathogenesis of Alzheimer's disease? *Brain Research Reviews*. 49, 618-632.

Rodriguez, J. J., Witton, J., Olabarria, M., Noristani, H. N., & Verkhratsky, A. (2010) Increase in the density of resting microglia precedes neuritic plaque formation and microglia activation in a transgenic model of Alzheimer's disease. *Cell Death and Disease*. 1, 10, 1038, 1-6.

Rogers, J., Lue, L. F., Walker, D. G., Yan, S. D., Stern, D., Strohmeyer, R., & Kovelowski, C. J. (2002) Elucidating molecular mechanisms of Alzheimer's disease in microglial cultures. *Ernst Schering Research Foundation Workshop*, 39 25-44.

Rouessac, F., & Rouessac, A. (2007) Chemical analysis. Modern instrumentation methods and techniques. *Wiley*. Pages. 574.

Ruan, L. (2009) Amyloid deposition and inflammation in APP/PS1 mouse model of AD. *Current Alziemer Research*, 6, 6, 531-540.

Salzer, R., Krafft, C. (2009) Infrared and Raman Spectroscopy Imaging. *Wiley*. Pages. 510.

Schlachetzki, J. C. M., & Hull M., (2009) Microglial activation in Alzheimer's disease. *Current Alzheimer Research*, 6, 6, 554-563.

Selkoe, D. J. (1991) The molecular pathology of Alzheimer's disease. *Neuron*, 6(4) 487-498

Shih, W., & Chuan, W. (2009) Quantitative biological Raman spectroscopy. *Handbook of optical sensing of Glucose in biological fluids and tissues*, 353-385.

Siedlak, S. L., Casadesus, G., Webber, K. M., Pappolla, M. A., Atwood, C. S., Smith, M. A., & Perry, G. (2009) Chronic antioxidant therapy reduces oxidative stress in a mouse model of Alzheimer's disease. *Free radical Research*, 43, 2, 156-164.

Simard, A. R., Soulet, D., Gowing, G., Julien, J. P., & Rivest, S. (2006) Bone marrow-derived microglia play a critical role in restricting senile plaque formation in Alzheimer's disease. *Neuron*, 49, 489-502.

Small, S. A., & Duff, K. (2008) Linking Aβ AND Tau in late-onset Alzheimer's disease: A dual pathway hypothesis. *Neurons*, 60, 534-542

Solano, D. C., Sironi, M., Bonfini, C., Solerte, B., Govoni, S., & Racchi, M. (2000) Insulin Regulates Soluble Amyloid Precursor Protein Release Via Phosphatidyl Inositol 3 Kinase-dependent Pathway. *The FASEB*, 14, 10115-1022.

Stampfer, M. J. (2006) Cardiovascular disease and Alzheimer's disease: common links. Journal of Internal Medicine, 260, 211-23. Risk of Alzheimer's disease and duration of NSAID use. *Neurology*, 48(3), 626-32.

Stoothoff, W. H., & Johnson, G.V. (2005) Tau phosphorylation: physiological and pathological consequences. *Biochem Biophys Acta*, 1739(2–3):280–297

Streijger F., Oerlemans F., Elenbroek BA., Jost C. R, & Wieringa, B. (2005) Structural and behavioural consequences of double deficiency for creatine kinases. *Behav Brain Res*, 157, 219-23

Stuart, B. (2004) Infrared Spectroscopy: Fundamentals and applications. *Wiley*. Pages. 203.

Szekely, C. A., & Zandi, P. P. (2010) Non-steroidal anti-inflammatory drugs and Alzheimer's disease: the epidemiological evidence. *CNS & Neurological Disorders: Drug Targets*, 9(2), 132-139.

Tachkawa, M., Fukaya, M., Terasaki, T., Ohtsuki, S., & Watanabe, M. (2004) Distinct cellular expressions of creatine synthetic enzyme GAMT and creatine kinases uCK-Mi and CK-B suggest a novel neuron-glia relationship for brain energy homeostasis. *The European Journal of Neuroscience*, 20, 144-160.

Takahashi, R. H., Capetillo-Zarate, E., Lin, M.T., Milner, T. A., &Gouras, G. K. (2010) Co-occurrence of Alzheimer's disease .beta.-amyloid and tau pathologies at synapses. *Neurobiology of Aging*, 31, 7, 1145-1152.

Tanzi, R. E. (2005) The synaptic Amyloid beta hypothesis of Alzheimer Disease. *Nat Neurosci*. 8(8), 977-979.

Tarnopolsky, M. A. (2000) The mitochondrial cocktail: Rationale for combined nutraceutical therapy in mitochondrial cytopanthies. *Advanced Drug Delivery Reviws*, 60, 1561-1567.

Terry, R. D., Gonatas, N. K.,& Weiss, M. (1964) The uktrastructure of the cerebral cortex in Alzheimer's disease. *Am Neuro Assoc*, 89, 12.

Tiraboschi, P., Hansen, L. A., Masliah, E., Thal, L., & Corey-Bloom, J. (2000) The decline in synapses and cholinergic activity is asynchronous in Alzheimer's disease. *Neurology*. 55, 1278-1283.

Tkahashi, R. H., Amedia, C. G., Keanery, P. F., Lin, M. T., Milner, T. A., & Gouras G. K. (2004) Oligomerization of Alzheimer's .beta.-amyloid within processes and synapses of cultured neurons and brain. *Journal of Neurscience*, 24, 3592-3599.

Urenjak, J., Williams, S. R., Gadian, D. G., & Noble, M. (1993) Protein nuclear magnetic resonance spectroscopy unambiguously identified different neural cell types. *J. Neurosci*, 13, 981-989.

Uttara, B., Singh, A. V., Zamboni, P., & Mahajan, R. T. (2009) Oxidative stress and neurodegenerative diseases: A review of upstream and downstream antioxidant therapeutic options. *Current Neuropharmacologu*, 7, 65, 74.

Verdier , Y., Zarandi, M., & Penke, B. (2004) Amyloid beta-peptide interactions with neuronal and glial cell plasma membrane: Binding sites and implications for Alzheimer's Disease. *Journal of Peptide Science*, (2004) 10, 229-248.

Walsh, D. M., & Selko, D. J., (2004) Deciphering the molecular basis of memory failure in Alzheimer's disease. *Neuron*, 44, 181-193.

Waldo, C. W., Dinamarca, M. C, & Inestrosa, N. C. (2008) Structure-function implications in Alzheimer's disease: Effect of amyloid beta oligomers at central synapses. *Cuurent Alzheimer Research*, 5, 233-243.

Wallimann, T., & Hermmer, W. (1994) III-2 creatine kinase in non-muscle tissue and cells. *Molecular and Cellular Biochemistry*, 133/134, 193-220.

Wallimann, T., Wyss, M., Brdiczka, D., Nicolay, K., & Eppenberger, H. M. (1992) Intracellular compartmentation, structure and function of creatine kinase isoenzymes in tissue with high and fluctuating energy homeostasis. *The Biochemical Journal*. 281, 21-40.

Walsh, D. M., Minogue, A. M., Frigerio, C. S., Fadeeva, J. V., Wasco, W., & Selkoe, D. J. (2007) The APP family of proteins: similarities and differences. *Biochhemical Society Transactions*, 35, part2, 416-420.

Walsh, D. M., & Selkoe, D. J. (2007) Amyloid beta oligomers-a decade of discovery. *Journal of Neurochemistry*, 101, 1172-1184.

Walsh, D. M., Klyubin ,G. M., Shankar, M., Townsend, J. V., Rowan, M. J., & Selkoe, D. J. (2005) The role of cell-derived oligomers of Aβ in Alzheimer's disease and avenues for therapeutic intervention. 33, 1087-1090

Walsh, D. M., Tseng, B. P., Rydel, R. E., Podisny, M. B., & Selkoe, D. J. (2000) The oligomerization of amyloid beta-protein begins intracellular in cells derived from human brain. *Bio Chem*, 39, 10831-10839.

Watson, D., Castano, E., Kokjohn, T. A., Kuo, Y., Lyubchenko, Y., Pinsky, D., Connolly, E. S., Esh, C., Luehrs, D. C., Stine, W. B., RowseM, L. M., Emmerling, M. R., & Roher, A. E. (2005) Physiolochemical characteristics of soluble oligomeric amyloid beta an dtheir pathologic role in Alzheimer's disease. *Neurol Res*, 27, 869-881.

West, M. J., Kawas, C. H., Stewart, W. F., Rudow, G. L., & Troncoso, J. C. (2004) Hippocampal neurons in pre-clinical Alzheimer's disease. *Neurobiol Aging*, 25, 1205-1212.

White, J. A., Maneli, A. M., Holmberg, K. H., & Ladu, M. J. (2005) Differential eefects of oligomeric and fibrillar amyloid-beta 1-42 on astrocyte-mediated inflammation. Neurobiol. Dis, 18, 459-465.

Wirths, O., Multhaup, G., & Bayer, T. A. (2004) Amodified beta-amyloid hypothesis: INtraneuronal accumulation of the beta-amyloid peptide-th efirst step of fatal cascade. *Journal of Neurochemistry*, 91, 513-520.

Wirths, O., Breyhan, H., Marcello, A., Cotel, M. C., Bruck, W., & Bayer, T. A. (2008) Inflammatory of changes are tightly associated with neurodegeneration in the brain and spinal cord of the APP/PS1K1 mouse model of Alzheimer's disease. *Neurobiol. Aging*, 31, 747-757.

Wirths , O., Multhaup, G., & Bayer, T. A. (2004) A modified beta-amyloid hypothesis: Intraneuronal accumulation of the beta-amyloid peptide-the first step of a fatal cascade. *Journal of Neurochemistry*, 91, 513-520.

Wood, B. R., Quinn, M. A., Tait, B., Ashdown, M., Hislop, T., Romeo, M., & McNaughton, D. (1998) FTIR microspectroscopic study of cell types and potential confounding variables in screeing for cervical malignancies. Biospectroscopy, 4, 75, 91.

Woodhouse, A., Vickers, J. C., Aldard, P. A., & Dickson, T. C. (2009) Dystrophic neuritis in TgCRND8 and Tg2576 mice mimic human pathological brain aging. Neurobiology of Aging, 30, 864-874.

Wyss, M., & Kaddurah, R. (2000) Creatine and creatine metabolism. Physiol Rev, 80, 1107-1213.

Xu, H., Wang, H., Zhuang, L., Yan, B., Yu, Y., Wei, Z., Zhang, Y., Dyck, L., Steven, J., He, J., Jiming, L,. & Xin, M. (2008) Demonstration of an anti-oxidative stress mechanism of quetiapine: Implications for the treatment of Alzheimer's disease. FEBS Journal, 275(14), 3718-3728.

Yoshida, S., Miyazaki, M., Sakai, K., Takeshita, M., Yuasa, S., Sato, A., Kobayashi, T., Watanabe, S., & Okuyama, H. (1997) Fourier transform infrared spectroscopic analysis of rat brain microsomal membranes modified by dietary fatty acids: possible correlation with altered learning behavior. Biospectroscopy, 3, 281-290.

Yu, L., Edalji, R., Harlan, J. E., Holzman, T. F., Pereda, L. A., Labkovsky, B., Hillen, H., Barghorn, S., Ebert, U., Richardson, P. L., Miesbauer, L., Solomon, L., Bartley, D., Walter, K., Johnson, R. W., Hajduk, P. J., & Olejniczak, E. T. (2009) Biochemistry, 48(9), 1870-1877

Zhao, L., Teter, B., Morihara, T., Lim, G. P., Ambegaokar, S. S., Ubeda, O., Frautschy, S. A., & Cole, G. M. (2004) Insulin-degrading enzyme as a downstream target of insulin receptor signalling cascade: implications for Alzheimer’s disease intervention. The Journal of Neuroscience, 8, 24(49), 11120-11126.